MFeS Clusters as Models for Complex Multimetallic Systems

Thesis by
Anna G. Scott

In Partial Fulfillment of the Requirements
for the Degree of Doctor of Philosophy

CALIFORNIA INSTITUTE OF TECHNOLOGY
Division of Chemistry and Chemical Engineering
Pasadena, California
2023
(Defended on May 5th, 2023)

Acknowledgements

My PhD could not have been accomplished without the many people in my life who have encouraged, supported, taught, and mentored me including family, friends, colleagues, mentors, teachers, collaborators, and more.

I would first like to thank my family who have provided an immeasurable amount of support and encouragement to pursue my passions throughout my life. Thank you Mom, Dad, Jenny, Nora, Ben, Luke, Aunt Leah, Uncle Pat, Noah, Res, Silas, Taylor, Lindsey, Grandpa Denis, Grandma Jackie, Chloe, Gabe, Masha, Jessie, Laura, and Roy. I am so fortunate to be part of a family where I can easily choose my path in life and be completely myself. My parents fostered in me a sense of curiosity and amazement about the world and thus my natural inclination towards science. My mother is the hardest working, caring, and selfless person I know. From her, I have learned that a good work ethic and resilience are ultimately what lead to success, but that being a kind and compassionate person is the most important achievement to strive for in this complicated world. My father is the most creative and curious person I know. His love for his work and the thoughtfulness with which he approaches his science and life has taught me that passion, attention to detail, and looking for inspiration in the exquisiteness and joy of the world around us are key to being a productive scientist and member of society as well as to living a full and happy life.

Next, I would like to thank the many teachers in my life who have shaped the way I approach learning and problem solving. My 2nd and 3rd grade teacher, Mr. Johnson, who organized a trip to visit a space history museum and our classmate that had moved all the way across the state, was truly inspiring. At Montana State University, there were many professors who piqued my interest in chemistry as well as in challenging myself to solve difficult but interesting scientific questions. Thank you to the following for your efforts to make the courses you taught outstanding: Professor Rob Walker, Professor Tim Minton, Professor Trevor Rainey, and Professor Erik Grumstrup.

My first experience in a research lab started when I was a freshman in college in the Broderick group. Professor Joan Broderick is not only an outstanding professor, but also an influential mentor, undergraduate research advisor, and female role model. She constantly encouraged me to apply for career opportunities and participate in scientific research, which had a large impact on my success and career opportunities. Early on I noticed her passion towards her group's research and as I worked in her lab I quickly understood her interest in the intricate nature of radical SAM enzymes. The first few years of working in Joan's lab catalyzed my passion for pursuing a career in chemistry. Others in the lab were also very influential. Dr. Jeremiah Betz taught me many biochemistry techniques and also served as a mentor and friend. I thank him for the great amount of time he spent training me and talking about science with me. Dr. Eric Shepard also served as a mentor and advisor in the Broderick lab and I am thankful for the exciting chats we had about science as well as the time he spent helping me with my projects in the group.

I had many opportunities to work at various scientific institutions as an undergraduate and am thankful to the advisors and mentors I had during these experiences. Dr. Kenneth McClellan welcomed me into his lab at LANL. Dr. David Mulder and Dr. Paul King served as wonderful mentors at NREL and helped me to work on my biochemical skill set. Dr. Stephen Lippard accepted me into his lab at MIT for a summer despite my lack of synthetic experience and gave me helpful career advice. Dr. Andrè Bessete spent much time while I was at MIT teaching me synthetic techniques as well as making my time at MIT fun and welcoming.

My time at Caltech has been challenging and testing, but in the end very beneficial and has helped me grow immensely as a scientist and person. For my graduate research, I was very interested in working on bioinorganic synthetic cluster chemistry. Not only did my advisor Theo accept me into his synthetic inorganic chemistry lab despite my lack of experience in the area, but he also let me work on the exact project I wanted. For this I am very grateful. His engagement and excitement in my chemistry throughout the years, as well as in everyone else's in the group, has been impressive and helped me to keep pursuing difficult projects even when I was disheartened. I have learned much from Theo about scholarship, scientific techniques, and designing approaches to research problems. I also had the opportunity to TA for one of Theo's classes and appreciated the opportunity to learn about teaching, designing course material, and engaging with the students.

I am also grateful to other faculty at Caltech who helped me during my PhD. My committee members Professor Ryan Hadt, Professor Garnet Chan, and Professor Jonas Peters have given me helpful feedback on my scientific writing and presenting skills and supported my development as a scientist for which I am thankful. Professor Harry Gray has also been a major inspiration in my time at Caltech and has always reminded me that the pursuit of science is exciting and that being wrong is alright, even if you are Harry Gray. His compassion is greatly appreciated by many graduate students.

I have had the opportunity to collaborate on some of my projects to be able to take exciting measurements on my compounds. Thank you to Isabel Bogacz and Dr. Junko Yano for XAS measurements. Thank you to Dr. Diogo Alves and Professor Muralle Murugesu for being excited about my clusters and your work on getting magnetism data on my Fe_{13} clusters.

I would like to thank Dr. Paul Oyala and Dr. David Vandevelde, facilities managers at Caltech who work tirelessly to keep the instruments running and are a wealth of knowledge about various spectroscopic techniques. Your work ethic is impressive and greatly appreciated. I would also like to thank Larry Henling who never lost patience with me no matter how terrible my crystals were early on in my PhD. Margarita Davis has been a great help many times during my PhD and is always happy to assist with any task. She was especially helpful in the end with reserving rooms for my proposals exam and defense. Thank you also to Ignacio Martini at UCLA for managing the MMPS instrument. Joe Drew, the facilities manager for the chemistry department, has also been great and provided help with any facilities problems promptly. Thank you to Dr. Nate Siladke of EHS for being open to discussing safety concerns and providing safety guidance. Also thank you to the staff of EHS who help with disposing of lab waste among many other important duties. Thank you to the Caltech staff who work hard to keep the lab and working spaces clean and running.

I would like to thank the colleagues and friends I have made while at Caltech. I am grateful to those in the group who have made my time at Caltech more fun and have encouraged and supported me. Nate, Charlie, and Chris were very helpful, especially in the beginning, teaching me many synthetic techniques and providing guidance on my project. Members of the cluster subgroup, Chris, Charlie, Angela, Linh, HB, Gwen, and Mike, always asked insightful questions and provided useful ideas. Mike has always been willing to listen to my crazy ideas and provide feedback, and coffee. Thank you to Sam, who has always showed much interest in my chemistry and been supportive during times of difficulty with my science. Linh has always been a very neat and generous bay and box mate for which I am greatful. Linh and Gwen worked hard with me on starting the FeS cluster project and my science would not have been possible without their efforts. I had the privilege of working with two Post Docs in the lab, Manar and Gwen, who were not only great sources of knowledge when I had questions about my chemistry, but also served as great friends and mentors for my career goals. Thanks to Gavin and newer members of the group, Matt and Fernando, who I have enjoyed chatting with about science around the lab. I am also greatful for other members of the lab I have had the chance to overlap with who have influenced my science and career: Adjeoda, Max, Masa, Mya, Priyo, Matthew, Alex H., Ryan, Arnaud, Josh, Jessica, Marcus, Till, Alex B., Naofumi, Miku, Hitoshi, Naoki, Davit, Meaghan, Vidyha, Sophie, Weixuan, and others. I have also enjoyed and appreciated working with others at Caltech including Dirk, Christian, Emily, and Rebecca.

Finally, I would like to thank the friends I have made while at Caltech who have helped me have fun and feel supported through stressful times. Thank you Axl, Jackie, Mike, Madison, Tina, Cullen, David, Madeline, Josh, Pat, Teddy, and the SGMC family.

Abstract

The impressive chemistry of the FeMco-factor of nitrogenase is still under intense study with many remaining mechanistic questions about the important transformation of N_2 to NH_3, including the role of the synthetically interesting carbide ligand and the complex structure of the octanuclear active site cluster. This thesis describes efforts to incorporate bridging carbon based ligands into synthetic MFeS clusters, which remains a significant synthetic challenge in inorganic chemistry. The subsequent characterization and reactivity studies of such clusters provide insight into how cluster structural properties, including ligand identity, metal identity, and cluster composition and geometry affect cluster electronic properties and reactivity.

Chapter II describes the synthesis of an unprecedented $WFe_3S_3(\mu_3\text{-carbyne})$ cluster and comparisons with a $WFe_3S_3(\mu_3\text{-S})$ cluster provide insight into the role of the bridging carbide in FeMco. The generality of the developed method for synthesis of $MFe_3S_3(\mu_3\text{-carbyne})$ clusters is also demonstrated. Characterization of the various carbyne clusters are discussed. Cleavage of the C-Si bond of $MFe_3S_3(\mu_3\text{-CSiMe}_3)$ clusters towards bridging methylidyne clusters is also demonstrated.

Chapter III discusses the synthesis of novel octanuclear (CH_n) bridged $Mo_2Fe_6S_6$ clusters and describes the reactivity of these bridges in the context of organometallic and nitrogenase chemistry.

Chapter IV describes spectroscopic data of an extensive family of MFeS cubane clusters that is currently lacking in the literature and provides important structure property benchmarking information for synthetic and biological FeS clusters.

Chapter V describes the synthesis of well-defined high nuclearity Fe_{13} clusters resulting from studies of WFeS clusters. These clusters exhibit high spin states and undergo well-defined reactivity with small molecules and thus provide an unprecedented atomically resolved study of reactivities of high-nuclearity transition metal clusters.

PUBLISHED CONTENT AND CONTRIBUTIONS

Parts of this thesis have been adapted from literature references and published articles co-written by the author.

Chapter I

Figure 1:

Qian, J.; An, Q.; Fortunelli, A.; Nielsen, R. J.; Goddard, W. A. III. Reaction Mechanism and Kinetics for Ammonia Synthesis on the Fe(111) Surface. *J. Am. Chem. Soc.* **2018**, *140* (20), 6288-6297. https://doi.org/10.1021/jacs.7b13409.

Bjornsson, R.; Neese, F.; Schrock, R. R.; Einsle, O.; Hu, Y; DeBeer, S. The discovery of Mo(III) in FeMoco: reuniting enzyme and model chemistry. *JBIC*. **2015**, *20*, 447-460. https://doi.org/10.1007/s00775-014-1230-6.

Figure 2:

Hoffman, B. M.; Lukoyanov, D.; Yang, Z.; Dean, D. R.; Seefeldt, L. C. Mechanism of Nitrogen Fixation by Nitrogenase: The Next Stage. *Chem. Rev*. **2014**, *114* (8), 4041-4062. 10.1021/cr400641x

A.G.S. and T.A. co-wrote the chapter.

Chapter II

The following article was reproduced in part with permission from the American Chemical Society:

Scott, A. G.; Agapie, T. Synthesis of a Fe_3–Carbyne Motif by Oxidation of an Alkyl Ligated Iron–Sulfur (WFe_3S_3) Cluster. *J. Am. Chem. Soc.* **2023**, *145* (1), 2–6. https://doi.org/10.1021/jacs.2c04826.

A.G.S. conducted all research and spectroscopic studies. A.G.S. and T.A. conceived and designed the research and co-wrote the manuscript and chapter.

Chapter III

A.G.S. conducted all research and spectroscopic studies. A.G.S. and T.A. conceived and designed the research and co-wrote the chapter.

Chapter IV

A.G.S., L.L.E, and G.B. conducted all research and spectroscopic studies. A.G.S., L.L.E, G.B., and T.A. conceived and designed the research and co-wrote the chapter.

Chapter V

A.G.S., D.A.G., and I. B. conducted all research and spectroscopic studies. A.G.S., D.A.G., I. B., J. Y., M. M., and T.A. conceived and designed the research and co-wrote the manuscript and chapter.

Appendix A

Figure 2:

Seefeldt, L. C.; Yang, Z.; Lukoyanov, D. A.; Harris, D. F.; Dean, D. R.; Raugei, S.; Hoffman, B. M. Reduction of Substrates by Nitrogenases. *Chem. Rev*. **2020**, *120* (12), 5082-5106. 10.1021/acs.chemrev.9b00556

A.G.S. conducted all research and spectroscopic studies. A.G.S. and T.A. conceived and designed the research and co-wrote the chapter.

Table of Contents

LIST OF FIGURES

Note: Figures listed below correspond to those included in the main text of each Chapter. Remaining figures can be found in the respective Experimental Sections.

Chapter I

Chapter II

Chapter III

Chapter IV

Chapter V

Appendix A

LIST OF TABLES

Note: Tables listed below correspond to those included in the main text of each Chapter. Remaining tables can be found in the respective Experimental Sections.

Chapter II

Chapter III

Chapter IV

Appendix A

Chapter I

GENERAL INTRODUCTION

Introduction

Multimetallic active sites are at the center of many essential catalytic processes in both industry and biology. In heterogeneous catalyst processes, which account for over 80% of industrial synthesis, different metal surfaces are used to activate and turnover small molecules.[1–7] For example, the Haber Bosch process uses an Fe surface to convert N_2 and H_2 into NH_3.[6] Computation and experiment have shown that certain Fe morphologies are more efficient at N_2 reduction, but the exact active site structure for N_2 and H_2 binding and subsequent NH_3 formation is still unknown (Fig. 1).[8,9] Nitrogen fixation in biology is carried out by the nitrogenase enzymes, which utilize protons and electrons instead of H_2.[1] The active site architecture of nitrogenase has been precisely determined to be a octametallic [M-7Fe-9S-C] cluster (FeMco), where M = Mo, Fe, or V (Fig. 1 and 2).[10–13] Much spectroscopic work has been carried out to determine the mechanism of N_2 turnover at FeMco, but questions still remain.[1,14] While heterogeneous and enzymatic systems are central to life on earth, they are inherently difficult to study. There are currently limited techniques in materials chemistry that allow for atomic scale

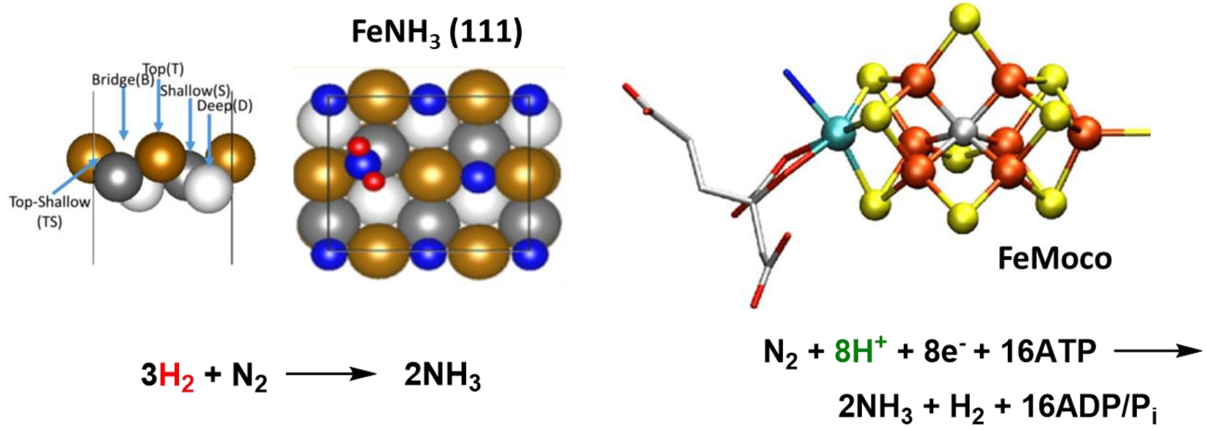

Figure 1: Schematic of Fe(111) surface for N_2 reduction[15] (left). Structure of FeMoco-factor responsible for N_2 fixation in nitrogenase enzymes[11] (right).

of single active sites on metal surfaces.[7,16,17] In biology, studies of enzymatic active sites are complicated by the complex protein machinery and the presence of other spectroscopically similar species that complicate characterization techniques of species of interest. Synthetic molecular metal clusters can help in understanding different aspects of these complex systems by taking advantage of atomically resolved molecular characterization techniques and synthetic tunability of model systems.

FeMco has been well studied in attempts to understand the electronic structure of the cluster and the catalytic mechanism of N_2 turnover;[1,14,18–20] however, the effects of certain structural aspects of the cluster on catalytic mechanism and reactivity are not fully understood.[14,19,20] Areas of interest include the role of the synthetically interesting μ_6-carbide ligand, the effects of Mo, Fe, and V in the different nitrogenases, the relevance of the octanuclear cluster structure, the fluxionality of the cluster during turnover, and the presence of conserved secondary sphere amino acid residues surrounding FeMco in the active site.

The relevance of some of these factors are illustrated in Fig. 2, which shows one proposed mechanism of N_2 turnover by FeMoco based on advanced spectroscopic techniques, DFT, and crystal structures of FeMco with small molecules bound.[1,12,14,21–24] The presence and organization of multiple Fe and sulfide sites allows for the accumulation of multiple reducing equivalents, which are stored as metal hydrides, and protons, while also providing a site for N_2 binding. While this particular mechanism implies that the fluxionality of the FeMco core is minimal, other proposals implicate greater fluxionality to accommodate and activate substrate, as shown in Fig. 3.[1,14,25]

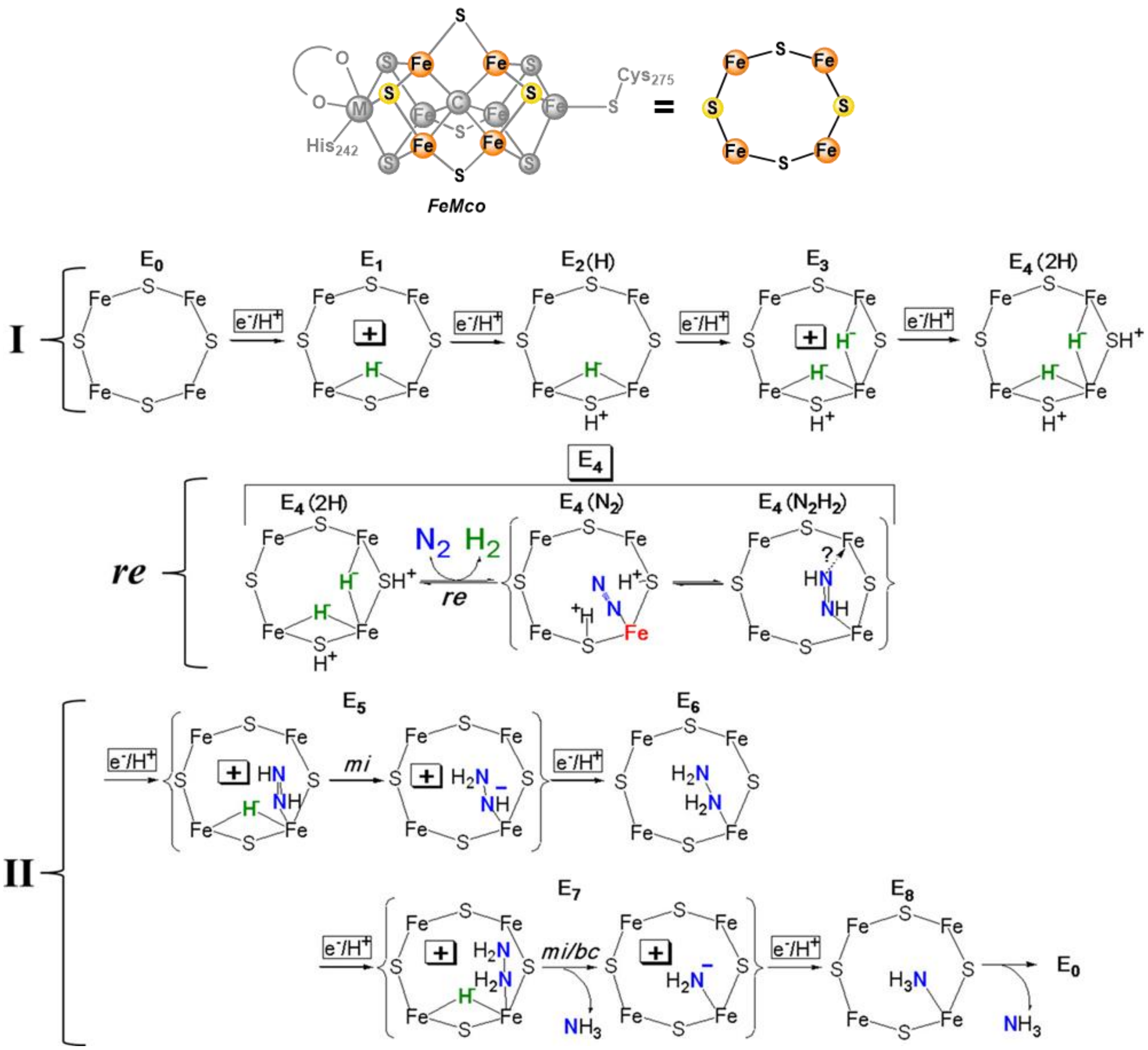

Figure 2: One proposed mechanism for N_2 reduction by FeMoco.[1]

The site of N_2 binding at FeMco is still under debate. Several structures with small molecules bound at FeMco have been reported and suggest that one belt sulfide can dissociate to accommodate ligand binding (Fig. 3 bottom left).[23,24,26–30] Activation of N_2 by mono-metallic Fe complexes provide evidence for N_2 binding to single Fe sites at FeMoco (Fig. 3, top).[31] DFT studies have also proposed that the central carbide can be protonated during N_2 binding and turnover implicating high fluxionality of the carbide ligand and a role of the carbide beyond electronic tuning and stabilization of the cluster (Fig. 3, bottom right).[21,32–37] Another interesting component of the FeMco-factors is the

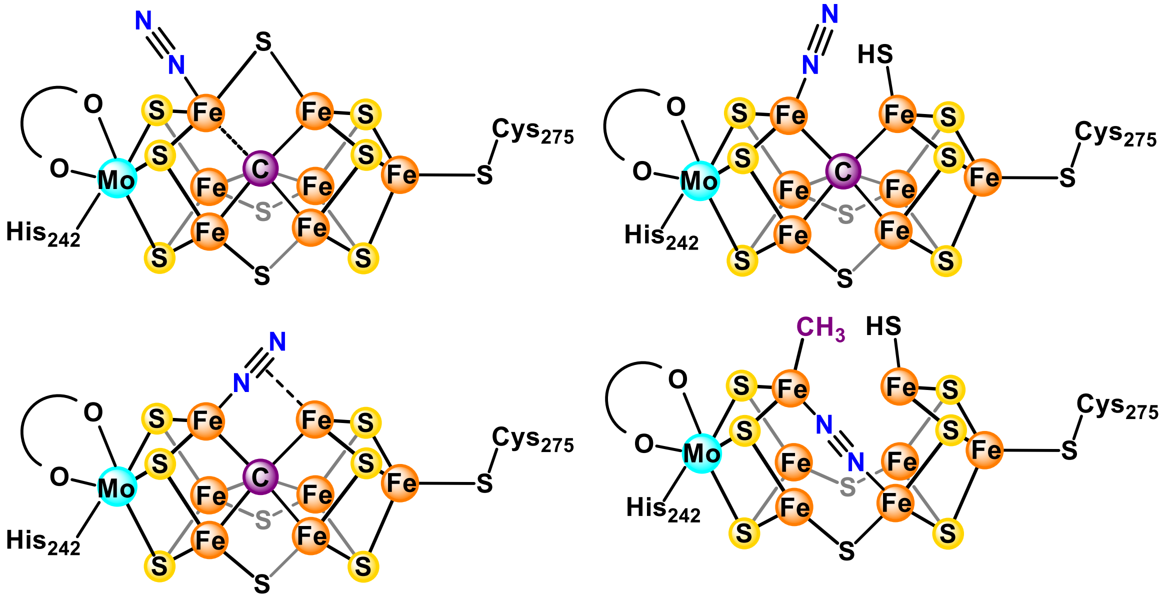

Figure 3: Proposed structures of N_2 binding at FeMoco.

variability of the M atom in different nitrogenases, which lead to reactivities with different small molecules and different product distributions.[12] While the M atoms are not proposed to be directly involved in substrate turnover, the electronic tuning by these remote metal centers clearly plays an important role in reaction mechanism.

The ability to make synthetic models of FeMco presents an opportunity to study how single point variations in clusters affect the different above mentioned properties and thus provide insight into the roles of the different components of the cluster. This thesis describes the development of well-defined cluster platforms that allow for systematic tunability of cluster properties for detailed studies on structure property relationships with a focus on the role of the carbide ligand of FeMco.

References

(1) Hoffman, B. M.; Lukoyanov, D.; Yang, Z.-Y.; Dean, D. R.; Seefeldt, L. C. Mechanism of Nitrogen Fixation by Nitrogenase: The next Stage. *Chemical reviews* **2014**, *114* (8), 4041–4062.

(2) Lubitz, W.; Ogata, H.; Rüdiger, O.; Reijerse, E. Hydrogenases. *Chem. Rev.* **2014**, *114* (8), 4081–4148. https://doi.org/10.1021/cr4005814.

(3) Can, M.; Armstrong, F. A.; Ragsdale, S. W. Structure, Function, and Mechanism of the Nickel Metalloenzymes, CO Dehydrogenase, and Acetyl-CoA Synthase. *Chem. Rev.* **2014**, *114* (8), 4149–4174. https://doi.org/10.1021/cr400461p.

(4) Bowker, M.; DeBeer, S.; Dummer, N. F.; Hutchings, G. J.; Scheffler, M.; Schüth, F.; Taylor, S. H.; Tüysüz, H. Advancing Critical Chemical Processes for a Sustainable Future: Challenges for Industry and the Max Planck–Cardiff Centre on the Fundamentals of Heterogeneous Catalysis (FUNCAT). *Angewandte Chemie International Edition* **2022**, *61* (50), e202209016. https://doi.org/10.1002/anie.202209016.

(5) Fuller, J.; An, Q.; Fortunelli, A.; Goddard, W. A. I. Reaction Mechanisms, Kinetics, and Improved Catalysts for Ammonia Synthesis from Hierarchical High Throughput Catalyst Design. *Acc. Chem. Res.* **2022**, *55* (8), 1124–1134. https://doi.org/10.1021/acs.accounts.1c00789.

(6) Deutschmann, O.; Knözinger, H.; Kochloefl, K.; Turek, T. Heterogeneous Catalysis and Solid Catalysts, 3. Industrial Applications. In *Ullmann's Encyclopedia of Industrial Chemistry*; John Wiley & Sons, Ltd, 2011. https://doi.org/10.1002/14356007.o05_o03.

(7) Friend, C. M.; Xu, B. Heterogeneous Catalysis: A Central Science for a Sustainable Future. *Acc. Chem. Res.* **2017**, *50* (3), 517–521. https://doi.org/10.1021/acs.accounts.6b00510.

(8) Ertl, G. Reactions at Surfaces: From Atoms to Complexity (Nobel Lecture). *Angewandte Chemie International Edition* **2008**, *47* (19), 3524–3535. https://doi.org/10.1002/anie.200800480.

(9) Fuller, J.; Fortunelli, A.; Iii, W. A. G.; An, Q. Reaction Mechanism and Kinetics for Ammonia Synthesis on the Fe(211) Reconstructed Surface. *Phys. Chem. Chem. Phys.* **2019**, *21* (21), 11444–11454. https://doi.org/10.1039/C9CP01611B.

(10) Spatzal, T.; Aksoyoglu, M.; Zhang, L.; Andrade, S. L. A.; Schleicher, E.; Weber, S.; Rees, D. C.; Einsle, O. Evidence for Interstitial Carbon in Nitrogenase FeMo Cofactor. *Science* **2011**, *334* (6058), 940–940. https://doi.org/10.1126/science.1214025.

(11) Lancaster, K. M.; Roemelt, M.; Ettenhuber, P.; Hu, Y.; Ribbe, M. W.; Neese, F.; Bergmann, U.; DeBeer, S. X-Ray Emission Spectroscopy Evidences a Central Carbon in the Nitrogenase Iron-Molybdenum Cofactor. *Science* **2011**, *334* (6058), 974–977. https://doi.org/10.1126/science.1206445.

(12) Jasniewski, A. J.; Lee, C. C.; Ribbe, M. W.; Hu, Y. Reactivity, Mechanism, and Assembly of the Alternative Nitrogenases. *Chem. Rev.* **2020**. https://doi.org/10.1021/acs.chemrev.9b00704.

(13) Burén, S.; Jiménez-Vicente, E.; Echavarri-Erasun, C.; Rubio, L. M. Biosynthesis of Nitrogenase Cofactors. *Chem. Rev.* **2020**, *120* (12), 4921–4968. https://doi.org/10.1021/acs.chemrev.9b00489.

(14) Seefeldt, L. C.; Yang, Z.-Y.; Lukoyanov, D. A.; Harris, D. F.; Dean, D. R.; Raugei, S.; Hoffman, B. M. Reduction of Substrates by Nitrogenases. *Chem. Rev.* **2020**. https://doi.org/10.1021/acs.chemrev.9b00556.

(15) Qian, J.; An, Q.; Fortunelli, A.; Nielsen, R. J.; Goddard, W. A. Reaction Mechanism and Kinetics for Ammonia Synthesis on the Fe(111) Surface. *J. Am. Chem. Soc.* **2018**, *140* (20), 6288–6297. https://doi.org/10.1021/jacs.7b13409.

(16) Du, X.; Jin, R. Atomically Precise Metal Nanoclusters for Catalysis. *ACS Nano* **2019**, *13* (7), 7383–7387. https://doi.org/10.1021/acsnano.9b04533.

(17) Cutsail III, G. E.; DeBeer, S. Challenges and Opportunities for Applications of Advanced X-Ray Spectroscopy in Catalysis Research. *ACS Catal.* **2022**, *12* (10), 5864–5886. https://doi.org/10.1021/acscatal.2c01016.

(18) Lee, S. C.; Lo, W.; Holm, R. Developments in the Biomimetic Chemistry of Cubane-Type and Higher Nuclearity Iron–Sulfur Clusters. *Chemical reviews* **2014**, *114* (7), 3579–3600.

(19) Tanifuji, K.; Ohki, Y. Metal–Sulfur Compounds in N2 Reduction and Nitrogenase-Related Chemistry. *Chem. Rev.* **2020**, *120* (12), 5194–5251. https://doi.org/10.1021/acs.chemrev.9b00544.

(20) Van Stappen, C.; Decamps, L.; Cutsail, G. E.; Bjornsson, R.; Henthorn, J. T.; Birrell, J. A.; DeBeer, S. The Spectroscopy of Nitrogenases. *Chem. Rev.* **2020**. https://doi.org/10.1021/acs.chemrev.9b00650.

(21) Dance, I. Computational Investigations of the Chemical Mechanism of the Enzyme Nitrogenase. *ChemBioChem* **2020**, *21* (12), 1671–1709. https://doi.org/10.1002/cbic.201900636.

(22) Burgess, B. K.; Lowe, D. J. Mechanism of Molybdenum Nitrogenase. *Chem. Rev.* **1996**, *96* (7), 2983–3012. https://doi.org/10.1021/cr950055x.

(23) Buscagan, T. M.; Rees, D. C. Rethinking the Nitrogenase Mechanism: Activating the Active Site. *Joule* **2019**, *3* (11), 2662–2678. https://doi.org/10.1016/j.joule.2019.09.004.

(24) Buscagan, T. M.; Perez, K. A.; Maggiolo, A. O.; Rees, D. C.; Spatzal, T. Structural Characterization of Two CO Molecules Bound to the Nitrogenase Active Site. *Angewandte Chemie International Edition* **2021**, *60* (11), 5704–5707. https://doi.org/10.1002/anie.202015751.

(25) Pérez-González, A.; Yang, Z.-Y.; Lukoyanov, D. A.; Dean, D. R.; Seefeldt, L. C.; Hoffman, B. M. Exploring the Role of the Central Carbide of the Nitrogenase Active-Site FeMo-Cofactor through Targeted 13C Labeling and ENDOR Spectroscopy. *J. Am. Chem. Soc.* **2021**, *143* (24), 9183–9190. https://doi.org/10.1021/jacs.1c04152.

(26) Spatzal, T.; Perez, K. A.; Einsle, O.; Howard, J. B.; Rees, D. C. Ligand Binding to the FeMo-Cofactor: Structures of CO-Bound and Reactivated Nitrogenase. *Science* **2014**, *345* (6204), 1620–1623. https://doi.org/10.1126/science.1256679.

(27) Spatzal, T.; Perez, K. A.; Howard, J. B.; Rees, D. C. Catalysis-Dependent Selenium Incorporation and Migration in the Nitrogenase Active Site Iron-Molybdenum Cofactor. *eLife* **2015**, *4*, e11620. https://doi.org/10.7554/eLife.11620.

(28) Sippel, D.; Rohde, M.; Netzer, J.; Trncik, C.; Gies, J.; Grunau, K.; Djurdjevic, I.; Decamps, L.; Andrade, S. L. A.; Einsle, O. A Bound Reaction Intermediate Sheds Light on the Mechanism of Nitrogenase. *Science* **2018**, *359* (6383), 1484–1489. https://doi.org/10.1126/science.aar2765.

(29) Kang, W.; Lee, C. C.; Jasniewski, A. J.; Ribbe, M. W.; Hu, Y. Structural Evidence for a Dynamic Metallocofactor during N2 Reduction by Mo-Nitrogenase. *Science* **2020**, *368* (6497), 1381–1385. https://doi.org/10.1126/science.aaz6748.

(30) Dance, I. How Feasible Is the Reversible S-Dissociation Mechanism for the Activation of FeMo-Co, the Catalytic Site of Nitrogenase? *Dalton Transactions* **2019**, *48* (4), 1251–1262. https://doi.org/10.1039/C8DT04531C.

(31) Del Castillo, T. J.; Thompson, N. B.; Peters, J. C. A Synthetic Single-Site Fe Nitrogenase: High Turnover, Freeze-Quench 57Fe Mössbauer Data, and a Hydride Resting State. *J. Am. Chem. Soc.* **2016**, *138* (16), 5341–5350. https://doi.org/10.1021/jacs.6b01706.

(32) George, S. J.; Barney, B. M.; Mitra, D.; Igarashi, R. Y.; Guo, Y.; Dean, D. R.; Cramer, S. P.; Seefeldt, L. C. EXAFS and NRVS Reveal a Conformational Distortion of the FeMo-Cofactor in the MoFe Nitrogenase Propargyl Alcohol Complex. *Journal of Inorganic Biochemistry* **2012**, *112*, 85–92. https://doi.org/10.1016/j.jinorgbio.2012.02.004.

(33) Jiang, H.; Ryde, U. Thermodynamically Favourable States in the Reaction of Nitrogenase without Dissociation of Any Sulfide Ligand. *Chemistry – A European Journal* **2022**, *28* (14), e202103933. https://doi.org/10.1002/chem.202103933.

(34) McKee, M. L. A New Nitrogenase Mechanism Using a CFe8S9 Model: Does H2 Elimination Activate the Complex to N2 Addition to the Central Carbon Atom? *J. Phys. Chem. A* **2016**, *120* (5), 754–764. https://doi.org/10.1021/acs.jpca.5b10384.

(35) Dance, I. The Stereochemistry and Dynamics of the Introduction of Hydrogen Atoms onto FeMo-Co, the Active Site of Nitrogenase. *Inorg. Chem.* **2013**, *52* (22), 13068–13077. https://doi.org/10.1021/ic401818k.

(36) Rao, L.; Xu, X.; Adamo, C. Theoretical Investigation on the Role of the Central Carbon Atom and Close Protein Environment on the Nitrogen Reduction in Mo Nitrogenase. *ACS Catal.* **2016**, *6* (3), 1567–1577. https://doi.org/10.1021/acscatal.5b02577.

(37) M. Siegbahn, P. E. The Mechanism for Nitrogenase Including All Steps. *Physical Chemistry Chemical Physics* **2019**, *21* (28), 15747–15759. https://doi.org/10.1039/C9CP02073J.

Chapter II

SYNTHESIS OF A $\mathrm{Fe_3}$-CARBYNE MOTIF BY OXIDATION OF AN ALKYL LIGATED IRON-SULFUR ($\mathrm{WFe_3S_3}$) CLUSTER

The text for this chapter was reproduced in part from:

Scott, A. G.; Agapie, T. *J. Am. Chem. Soc.* **2023**, *145* (1), 2–6.

ABSTRACT

The presence of a carbide ligand in the active site of nitrogenases remains an unusual example of organometallic chemistry employed by a protein. Carbide incorporation into the MFe_7S_9C cluster involves complex biosynthesis, but analogous synthetic methodologies are limited. Herein, we present a new synthetic strategy for incorporating carbon based bridging ligands into iron-sulfur clusters. Starting from a halide precursor, a WFe_3S_3 cluster displaying three terminal alkyl ligands and an open Fe_3 face was prepared. Oxidation results in loss of alkane and formation of a μ_3-carbyne. Characterization of these clusters and mechanistic studies are presented.

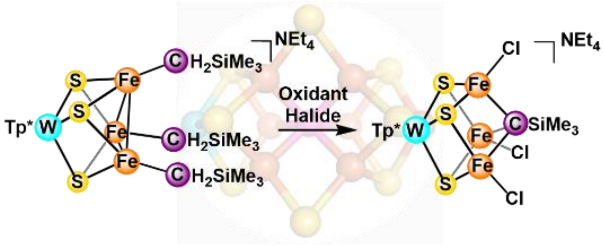

Introduction

Enzymatic active sites displaying complex metal clusters have prompted synthetic exploration towards models that can facilitate spectroscopic benchmarking and structure-function studies.[1–3] Nitrogenases display a remarkably complex inorganic active site with a MFe_7S_9C composition (FeMco, M = Mo, Fe, or V) that contains a biologically unique interstitial carbide moiety.[4–6] A complicated protein machinery is involved in the biosynthesis of this cluster, including the delivery of an alkyl-derived carbon center.[7] Despite significant efforts by synthetic chemists on modeling iron-sulfur cluster chemistry,[8–16] the structure of FeMco remains an outstanding challenge. Clusters that show substantial topological similarity have been prepared with interstitial O or S ligands,[8,17–20] but carbide -containing variants have been limited to CO ligated clusters which contrast with weak field sulfides found in biological clusters.[21,22]

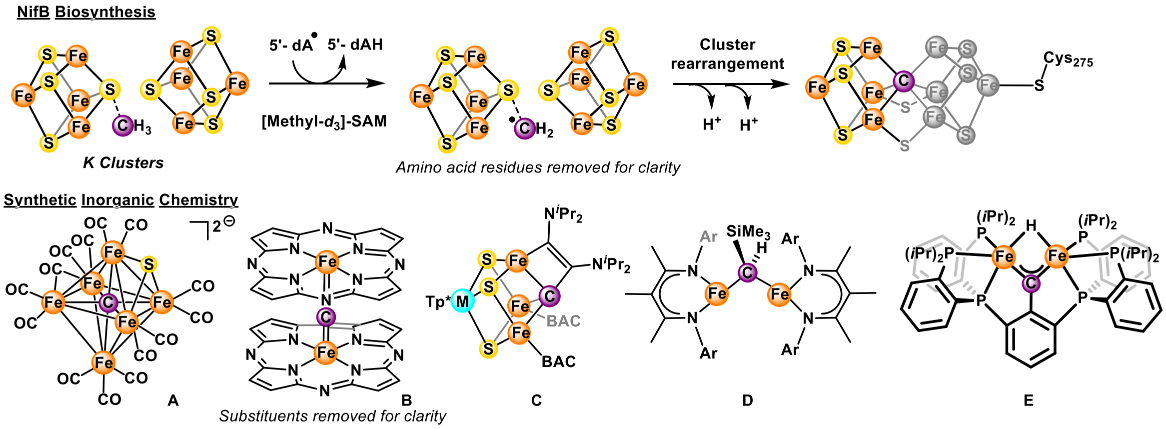

Figure 1: Top: NifB biosynthesis of carbide bridged [8Fe-8S-C] FeMco cluster precursor. Top right structure highlights the cubane subsite targeted in this work. Bottom: Selection of transition metal carbide, carbyne, and alkylidene complexes of Fe.[7,21,23–28] BAC = bis(diisopropylamino)cyclopropenylidene.

The biosynthesis of FeMco provides a potential blueprint for synthetic development.[7] The exact mechanism of carbide generation remains ill-defined, but isotopic labeling studies confirm that the source is a methyl group delivered from the radical S-adenosyl methionine (SAM) enzyme NifB.[29] Two [4Fe-4S] clusters are bound in close proximity (Fig. 1) within NifB.[30] A methyl group is transferred to one of the clusters upon cleavage of SAM at the sulfonium-methyl bond initiated by radical-SAM enzyme chemistry (Fig. 1),[29,31,32] followed by at least one more cycle of SAM chemistry to promote the abstraction of a hydrogen atom in an oxidative process.[29,33,34]

Synthetically, the incorporation of carbide moieties into Fe clusters is limited to CO rich systems (**A**, Fig 1).[21,22,27,28] For bimetallic Fe complexes (**B**), a μ_2 bridging carbide was delivered from $CHCl_3$ by activation of reactive C-Cl bonds.[26] The more common bridging carbyne (**C**) and carbene (**D**) ligands have been sourced from ring opening of the strained cyclopropenylidene moiety and from group transfer chemistry with diazoalkanes, respectively.[23,35] More closely related to the biosynthesis of FeMco, iron alkyl species can promote C-H activation to result in di-iron bridging carbynes (**E**).[24,25] Reminiscent of the

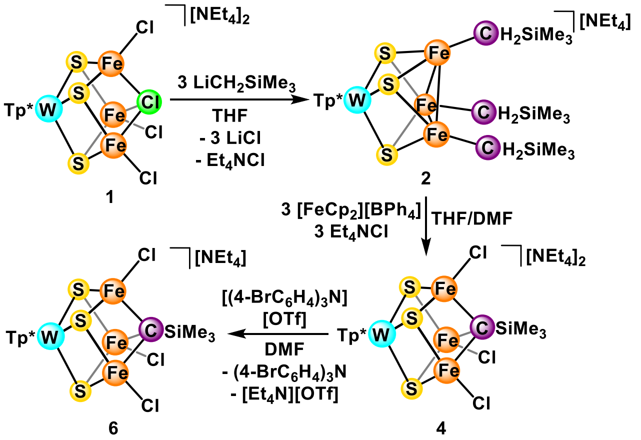

Figure 2: Synthesis of $[Et_4N][Tp^*WFe_3S_3(CH_2SiMe_3)_3]$ (**2**), $[Et_4N]_2[Tp^*WFe_3S_3(\mu_3\text{-}CSiMe_3)Cl_3]$ (**4**) and $[Et_4N][Tp^*WFe_3S_3(\mu_3\text{-}CSiMe_3)Cl_3]$ (**6**).

activation of the methyl group toward carbide generation in nitrogenase, preparations of terminal alkylidene and alkylidyne complexes are known for Ti and V via oxidative promotion of abstraction chemistry from polyalkyl precursors.[36,37] A suitable precursor for targeting FeMco is an iron sulfur cluster with multiple alkyl ligands.

Structurally characterized iron clusters with alkyl ligands are very rare.[38–42] An iron-alkyl cluster was prepared from Fe^{III} and methyl Grignard in a process that, notably, involves redox chemistry.[41] Site-differentiated Fe_4S_4 cubane clusters with three iron centers coordinated by ancillary ligands and one binding an alkyl group have been prepared by ligand substitution from halide precursors.[38–40] Conversion of cluster-bound alkyl ligands toward a bridging carbon based ligand has not been reported. Toward facilitating such a process, incomplete cubanes with an accessible Fe_3 face are appealing precursors. The cluster $[Et_4N]_2[Tp^*WFe_3S_3(\mu_3\text{-}Cl)Cl_3]$ (**1**, Fig. 2; Et_4N = tetraethylammonium, Tp* = tris(3,5-dimethyl-1-pyrazolyl)borate), has a μ_3-halide that can be substituted with other ligands, including sulfide, imide, and nitride.[43,44] These bridging ligands can also be incorporated via group transfer to an open Fe_3 face of incomplete iron sulfur cubanes.[35] Herein, the synthesis of a robust, open faced WFe_3S_3 cluster with three terminal alkyl ligands is described. Oxidation of this trialkyl ligated cluster leads to the formation of a bridging carbyne. This method demonstrates a new strategy for incorporating bridging, non-chelating carbon-based ligands into iron sulfur clusters via halide substitution and redox chemistry.

Results and Discussion

Treatment of **1** with $LiCH_2SiMe_3$ in tetrahydrofuran (THF) results in a dark brown solution. A single crystal X-ray diffraction (SC-XRD) study of the isolated product shows that substitution of the terminal chlorides with alkyl ligands and loss of the bridging chloride occurs in an overall redox neutral process (Fig. 2 and 3). This is in contrast to reactions with BAC ligands where only terminal chlorides are substituted and loss of the μ_3-Cl occurs with addition of reductant.[35] Compound **2** is notable given the scarcity of Fe clusters with multiple alkyl ligands.[41] Structurally, **2** is similar to the previously reported cluster with BAC ligands instead of alkyl $[Tp^*WFe_3S_3(BAC)_3][BPh_4]$ (**3**; BPh_4 = tetraphenylborate) that also displays an open Fe_3 face,[35] with the Fe-Fe distances averaging 2.563 Å and the C-Fe bonds averaging 2.009 Å. Cyclic voltammetry (CV) of **2** reveals two quasi-reversible redox features, one at -0.97 V (v. Fc/Fc^+, Fig. 3) assigned to $[WFe_3]^{9+/8+}$ which is more positive than for **3** ($[WFe_3]^{9+/8+}$ at -1.10 V. Fc/Fc^+), indicating lower reducing power despite the presence of anionic alkyl ligands in **2**. Electron paramagnetic resonance (EPR) of **2** is consistent with $S = 9/2$ (Fig. S32).

Targeting a bridging carbon-based ligand, heating was performed to promote hydrogen abstraction chemistry. Compound **2** is notably stable with no reactivity observed after heating at 80 °C for 24 hours (Fig. S7). It is well established that α-hydrogen abstraction can occur at high oxidation state metal polyalkyl complexes to form alkylidene[45] or bridging alkylidyne species,[46] depending on the steric bulk of the alkyl ligands, and oxidative chemistry has also been employed to promote this reaction.[36,37] Oxidation of **2** with silver triflate or tris(4-bromophenyl)ammoniumyl triflate ($[(4\text{-}BrC_6H_4)_3N][OTf]$) at -78 °C leads to the formation of multiple new species (Fig. S10, S11). Reaction products were characterized by SC-XRD studies, which all revealed formation of a bridging μ_3-$CSiMe_3$ carbyne, as desired, with differing terminal Fe ligands (Fig. S35).

However, these products were isolated in low yields (<1 mg) and alternate synthetic protocols were targeted.

The carbyne complexes characterized by SC-XRD indicate a multi-electron oxidation and a propensity for the Fe_3-carbyne motif to bind anionic ligands. Therefore, treatment with excess $[FeCp_2][BPh_4]$ ($FeCp_2$ = ferrocenium; 3 equivalents) followed by addition of Et_4NCl (3 equivalents) was investigated. After work up and recrystallization in *N,N*-dimethylformamide (DMF) with diethyl ether (Et_2O) vapor diffusion, dark rod like crystals were obtained in 65% yield. SC-XRD characterization shows formation of $[Et_4N]_2[Tp^*WFe_3S_3(\mu_3\text{-}CSiMe_3)Cl_3]$ (**4**, Fig. 3**)** displaying a μ_3-bridging carbyne ligand and three terminal chloride ligands with pseudo-C_{3v} symmetry. This compound is notable because of the unchelated nature of the carbyne incorporated into an iron sulfur cluster, in contrast to vinyl or amine chelation previously described.[35] The chelated carbyne containing WFe_3S_3 cluster (**C**) is supported by two BAC ligands displaying pseudo-C_s symmetry and has a formal charge of $[WFe_3]^{11+}$. Despite lower symmetry, the Fe-C bond lengths (1.943(3), 1.945(3), and 1.958(4) Å)[35] are all very similar. Compound **4** with the same redox state, $[WFe_3]^{11+}$, shows only very slightly shorter Fe-C distances (1.902(5), 1.931(5), and 1.932(4) Å) suggesting similar Fe-C interactions. These distances are shorter than observed in FeMoco (2.00 Å) where the C ligand bridges between six rather than three metal centers.[4] ^{1}H-NMR was used to probe the mechanism of formation of the bridging carbyne ligand of **4**. The only silyl-alkyl-derived reaction byproduct was identified as $SiMe_4$ consistent with hydrogen abstraction to generate the carbyne (Fig. S8). When the reaction was performed in *d8*-THF, the upfield shifted 1:1:1 triplet resonance for $DC\mathit{H}_2SiMe_3$ of *d1*-$SiMe_4$ was not observed by ^{1}H-NMR spectroscopy, indicating that the abstracted hydrogen does not originate from solvent (Fig. S9). Although abstraction from Tp* cannot be ruled out, a mechanism involving abstraction from the alkyl ligand resulting in carbyne is proposed based on precedent from monometallic systems.[36,37,45,46]

While the presence of oxidant is necessary for formation of the bridging carbyne, the electrochemistry of **2** indicates that $[FeCp_2][BPh_4]$ does not have a redox potential more positive than that of **2** (Fig. 3). To gain additional insight, CV and ^{1}H- NMR studies were performed on **2** with the addition of varying amounts of Et_4NCl (Fig. S21). Shifting of the

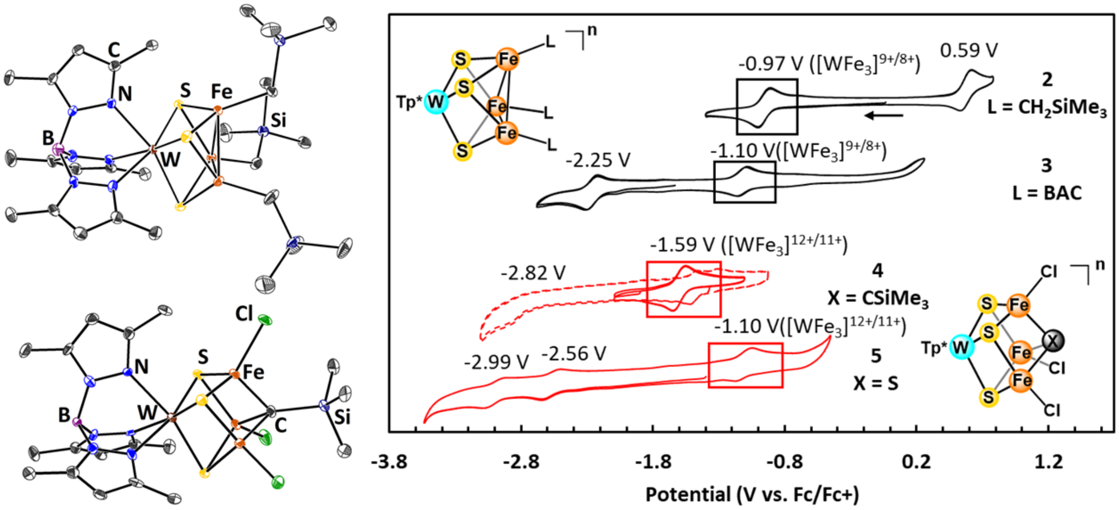

Figure 3: Crystal structures (left) of **2** (top) and **4** (bottom) with ellipsoids plotted at the 50% probability level. Solvent and counter ions omitted for clarity. Cyclic voltammograms (right) of WFe_3S_3 clusters **2**, **3**, **4**, and **5**, respectively, with varying terminal (black) and bridging ligands (red). Boxes indicate redox couples of WFe_3. Conditions: 250 mV/s, 2.5 mM cluster, CH_3CN (black) and DMF (red), 0.2 M $TBAPF_6$.

oxidative redox feature in the CV and significant broadening of the ^{1}H-NMR resonances of **2** indicate a dynamic process that is consistent with halide coordination or ligand exchange in solution (Fig. S13, S21). Chloride binding to **2** can therefore shift the redox potential such that oxidation with $[FeCp_2][BPh_4]$ is possible. While only two equivalents of oxidant are required to balance the stoichiometry for the formation of **4**, use of two rather than three equivalents of $[FeCp_2][BPh_4]$ led to 30% reaction yields, suggesting the presence of additional redox reactivity requiring excess oxidant for higher yields of **4**. The CW-EPR of **4** is consistent with S = 3/2 that can be explained with a ferromagnetically coupled high spin Fe^{III} and a non-Hund W^{III} that interact anti-ferromagnetically with a high spin mixed-valent Fe^{III}-Fe^{II} pair of S = 9/2.[47] These interactions are reminiscent of FeMoco and match those of a previously studied $[MoFe_3S_4]^{3+}$ cubane in the same redox state as **4** ($[WFe_3]^{11+}$).[47]

Access to carbyne **4** allows comparison of redox behavior to previously reported chelated carbynes and other bridging ligands. The CV of **4** reveals two quasi-reversible redox features at -2.82 and -1.48 V v. Fc/Fc$^+$ (Fig. 3) assigned as $[WFe_3]^{11+/10+}$ and $[WFe_3]^{12+/11+}$, respectively. The $[WFe_3]^{12+/11+}$ couple is shifted negatively by 480 mV compared to the sulfide bridged analogue $[Et_4N][Tp^*WFe_3S_3(\mu_3\text{-}S)Cl_3]$ **(5)** (-1.10 V v. Fc/Fc$^+$ for $[WFe_3]^{12+/11+}$) (Fig. 3). This is a smaller difference compared to **C**, with a chelating carbyne ligand, where the redox shift is nearly 2 V compared to the related sulfide analog, $[Tp^*WFe_3S_3(\mu_3\text{-}S)(BAC)_3][BPh_4]$, albeit one of the terminal ligands is also distinct.[35] The comparison between isostructural **4** and **5** provides a direct measure of the effect of the μ_3 ligand on the redox potentials, showing the significantly more reducing character of the C- vs S-bridged cluster.[48]

Chemical oxidation of **4** to form $[Et_4N][Tp^*WFe_3S_3(\mu_3\text{-}CSiMe_3)Cl_3$ (**6**) by one electron was achieved using $[(4\text{-}BrC_6H_4)_3N][OTf]$. Analysis of **6** using SC-XRD shows a shortening of Fe-S bond lengths (Fe-S average = 2.239 Å versus 2.282 Å in **4**) and Fe-C bond lengths (Fe-C average = 1.908 Å versus 1.949 Å in **4**) consistent with an increase in the oxidation state at Fe (Table 1). Comparison of Mössbauer data for **6** (δ = 0.34 mm/s and ΔEq = 0.62 mm/s, Fig S12) and **4** (two sites with δ = 0.43 and 0.58 mm/s and ΔEq = 0.84 and 0.90 mm/s with relative intensities of 1:2, respectively; Fig. S17)[49] is also indicative of an increased Fe oxidation state in **6**.[50]

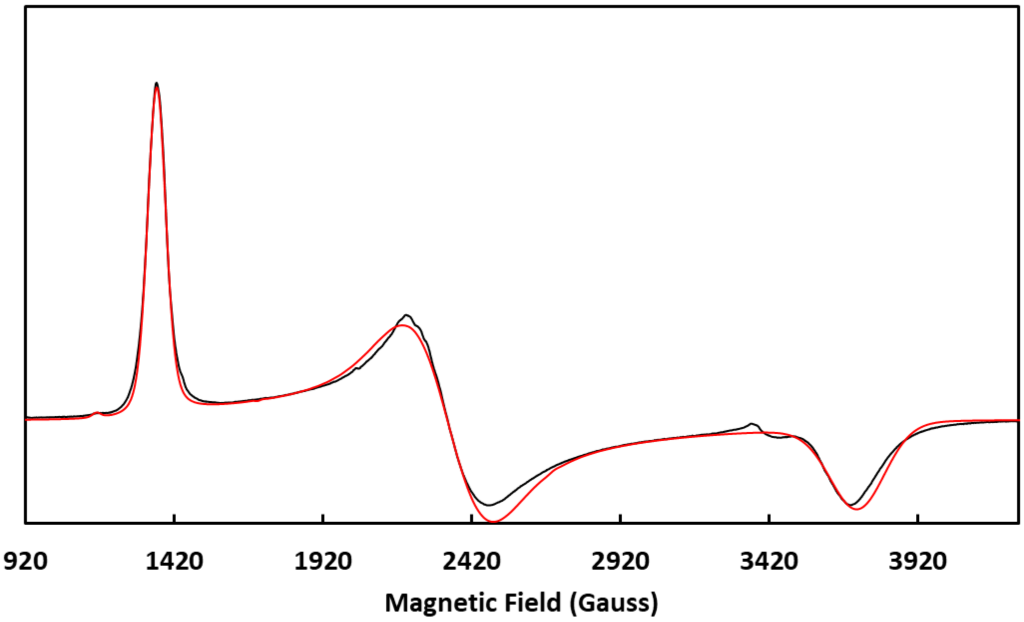

Figure 4: EPR spectrum of **4** in DMF (black) with simulation shown in red (*g* = 2.04, D = 1.44 cm-1 and E/D = 0.18). Data acquisition parameters: frequency = 9.6375 MHz, power = 2 mW, conversion time = 10.12 ms, and modulation amplitude = 8 G.

Investigations into the electronic structures of **4** and **6** were carried out using ^{1}H-NMR and EPR. **6** is diamagnetic (S = 0) based on ^{1}H-NMR spectroscopy. (Fig S5). The simulation of the EPR spectrum of **4** indicates an S = 3/2 species with *g* = 2.04, D = 4.76 cm^{-1}, and E/D = 0.18 (Fig. 4). A basic building block to describe the electronic structure of FeS clusters is the [2Fe-2S]$^{2+;1+}$ (Fe_3^{+2}; $Fe^{2+}Fe^{3+}$) dimer where the oxidation states of the Fe centers can generally be determined using Mössbauer spectroscopy and the spin states identified by EPR and/or magnetism measurements.[1,51–55] The coupling between the two Fe centers can be described as ferromagnetically ($S = 10; 9/2$) or antiferromagnetically coupled ($S = 0; 1/2$), where only $S = 0$, $1/2$, or $9/2$ FeS dimers have been observed.[55–59] This is because the ground spin state of such clusters is largely influenced by the Heisenberg exchange coupling value (J), where if $J < 0$ (antiferromagnetic coupling) the lowest possible spin state occurs and if $J > 0$ (ferromagnetic coupling) the highest possible spin state occurs.[60] Theoretically, however, if the double-exchange parameter (B) is significant, intermediate spin states (for $J < 0$; $S = 3/2, 5/2, 7/2$) can become the lowest in energy.[60] While not observed yet in FeS dimers, higher nuclearity clusters have been reported with intermediate spin states, such as $[4Fe\text{-}4S]^{1+}$ clusters with $S = 3/2$.[61–64]

In $[4Fe\text{-}4S]^{n}$ clusters, the electronic spin state results from the two ferromagnetically or antiferromagnetically coupled FeS dimers (Fig. 5). In biology, $[4Fe\text{-}4S]^{n}$ are commonly found in the following redox and spin states: $[4Fe\text{-}4S]^{3+}$ ($S = ½$), $[4Fe\text{-}4S]^{2+}$ ($S = 0$), and $[4Fe\text{-}4S]^{1+}$ ($S = ½$).[55,52,65,66] Less commonly observed redox and spins states include $[4Fe\text{-}4S]^{1+}$ ($S = 3/2$) and the all ferrous $[4Fe\text{-}4S]^{0}$ ($S = 0$ or 4).[67–69,65] The $[4Fe\text{-}4S]^{1+}$ ($S = 3/2$) electronic configuration is hypothesized to arise from significant contribution of B to the overall spin state manifold.[60] Similar coupling schemes can also be applied to [M-7Fe-7S] clusters. For example, $S = 0$ ground states have been observed in the all ferrous oxidation state of the P-cluster of nitrogenase ($M = Fe$)[70] and in the oxidized state of FeMoco (E_0; $M = Mo$).[71–74] The diamagnetic oxidation state of FeMoco has been assigned as $Mo^{IV}Fe^{II}{}_3Fe^{III}{}_4$,[75] which would require an intermediate spin state assignment of at least one unit of the octanuclear cluster. FeMoco cycles through nine distinct states (E_n) that are either half-integer Kramers states or integer non-Kramers states.[76] It has been difficult to understand the geometric and electronic structures of many of these states because of challenges isolating states of interest and identifying spectroscopic signals of interest that are convoluted by other FeS clusters in the nitrogenase assembly.[56,76,77] Nonetheless, a considerable amount of spectroscopic and computational work has been carried out on various E_n states, some of which can be freeze trapped.[1,5,56,70,76–81] These studies have helped to determine metal oxidation states, cluster spin states, coupling parameters and, ultimately, proposed geometric and electronic structures of the E_n states.

Synthetic models developed by Holm of half of FeMoco were determined to be useful spectroscopic benchmarks based on Mössbauer, XAS, EPR, and DFT.[47,82,83] These data, along with XAS and XMCD of FeMoco, identified the oxidation state of Mo as 3+ and that its non-Hund electron configuration.[84,85] Using similar approaches, as well as SpReAD, the oxidation states for each metal atom in the E_0, E_1, and E_4 states have been proposed.[47,70,74,86–89] Based on these assignments, the coupling schemes for the $MoFe_3$ subunit of each are shown in Fig. 5, assuming high spin Fe centers and a tetrahedral geometry about Fe.

The EPR of **4** indicates an $S = 3/2$ spin state, which can be explained with an oxidation state assignment of $W^{III}Fe^{III}_2Fe^{II}$ and a coupling scheme as shown in Fig. 6, where the W atom adopts a non-Hund electron configuration as is observed in some oxidation states of FeMoco.[56] In this case, an octahedral ligand field is assumed for W and a tetrahedral field is assumed for the Fe centers. Isolation of **6** provides the opportunity to investigate diamagnetic WFe_3S_3 clusters whose electronic structures are unprecedented in the literature,[49] in contrast to more common diamagnetic Fe_4S_4 clusters. Again, assuming a simplified d-orbital splitting and high spin states for all of the metal atoms, an $S = 0$ spin state would necessitate oxidation state assignments of

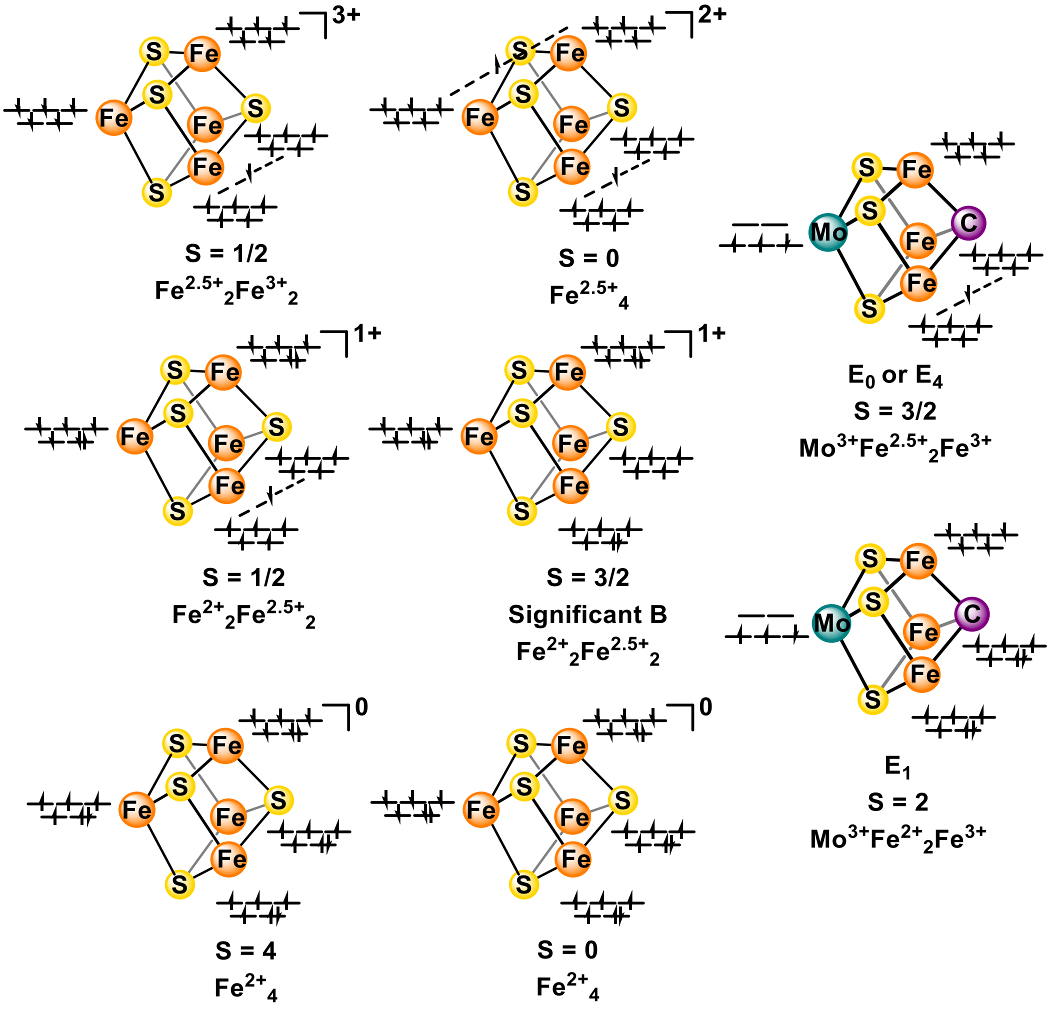

Figure 5: Electronic structures of FeS clusters.

$\mathrm{W^{II}Fe^{III}{}_2Fe^{IV}}$ (Fig. 6). However, as discussed above, there is a lack of precedent in the literature for the oxidations states of $\mathrm{W^{II}}$ or $\mathrm{Fe^{IV}}$ in FeS clusters.[56,90–93] Alternate electronic structures to rationalize an S = 0 spin state include $\mathrm{W^{III}Fe^{III}{}_3}$, where an intermediate spin state could be rationalized based on significant contributions of B. For example, if a S = 1/2 W center is antiferromagnetically coupled to a S = 5/2 Fe center intermediate spin states could be S = 2 or 3 for the $\mathrm{WFeS_2}$ dimer. If the remaining two S = 5/2 Fe centers are antiferromagnetically coupled intermediate spin states could be S = 1, 2, or 3. Therefore coupling of an intermediate spin $\mathrm{WFeS_2}$ dimer (S = 2 or 3) and an intermediate spin $\mathrm{Fe_2S_2}$ dimer (S = 2 or 3) could result in an overall S = 0 spin state. Alternately, one or more of the

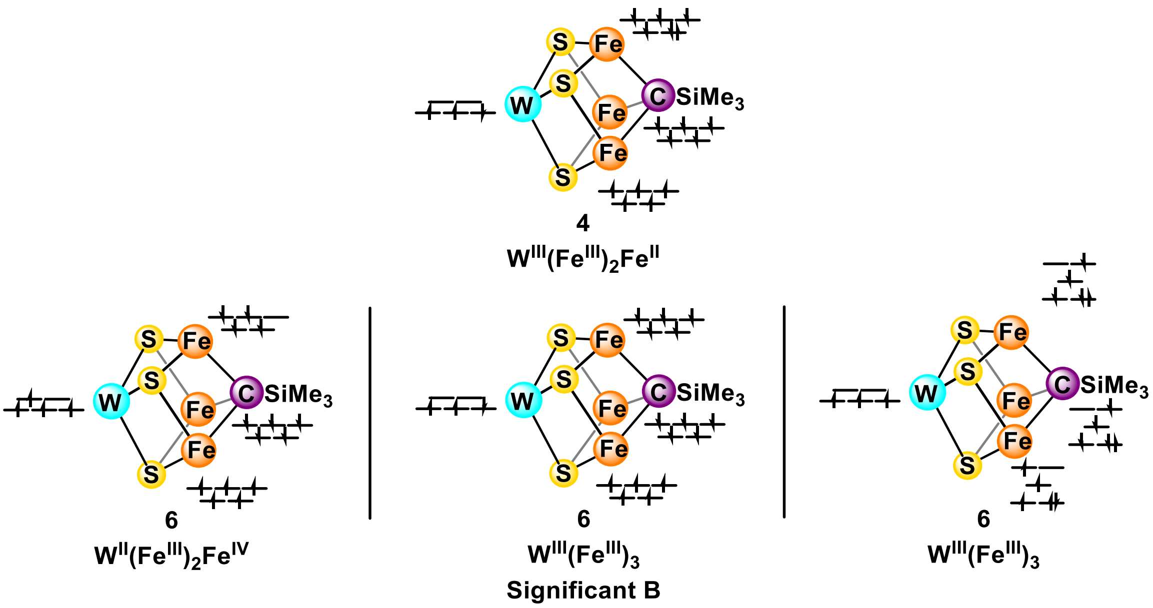

4
$W^{III}(Fe^{III})_2Fe^{II}$

6
$W^{II}(Fe^{III})_2Fe^{IV}$

6
$W^{III}(Fe^{III})_3$
Significant B

6
$W^{III}(Fe^{III})_3$

Figure 6: Possible electronic configurations for clusters **4** and **6**.

pseudotetrahedral Fe centers (bond angles range from 102°-116°) could adopt an intermediate spin, as depicted in Fig. 6, due to distortions from a tetrahedral geometry and differences in ligand field strengths of sulfide versus chloride versus carbyne ligands. While distortions from a tetrahedral ligand field have been implicated for FeS clusters,[94] intermediate spin states of single Fe centers have not been proposed based on the distortions. Further spectroscopic characterization of **6** is necessary to determine the factors that contribute to a spin state of $S = 0$.

Compared to enzymatic carbide formation on NifB, where a methyl from SAM cleavage is proposed to transfer to one of the sulfides of the cysteine ligated FeS clusters,[31,32] the bridging carbyne of **4** originates from a metal bound ligand. Ultimately, the alkyl group must be activated to form metal-carbon bonds in the biological system as well. An additional oxidation event, in the form of an H-atom transfer, has been supported experimentally.[32] Similarly, though not necessarily through the same mechanism, oxidation of **2** promotes multiple H-atom transfers and carbyne formation.

To determine if the method for the synthesis of **2** and **4** is general for other alkyl ligands as well as Mo analogues, clusters of the general composition

$[Et_4N][Tp^*MFe_3S_3(\mu_3\text{-}CR)Cl_3]$ were targeted, where M = W or Mo and R = $SiMe_3$, $SiMe_2Ph$, or $SiPh_3$. Mo analogues of **2**, **4**, and **6** were successfully synthesized using the same synthetic protocols as for the W analogues (Fig. 7). SC-XRD studies indicate similar bond lengths of **2-Mo**, **4-Mo**, and **6-Mo** to those of **2**, **4**, and **6** (Table 1).

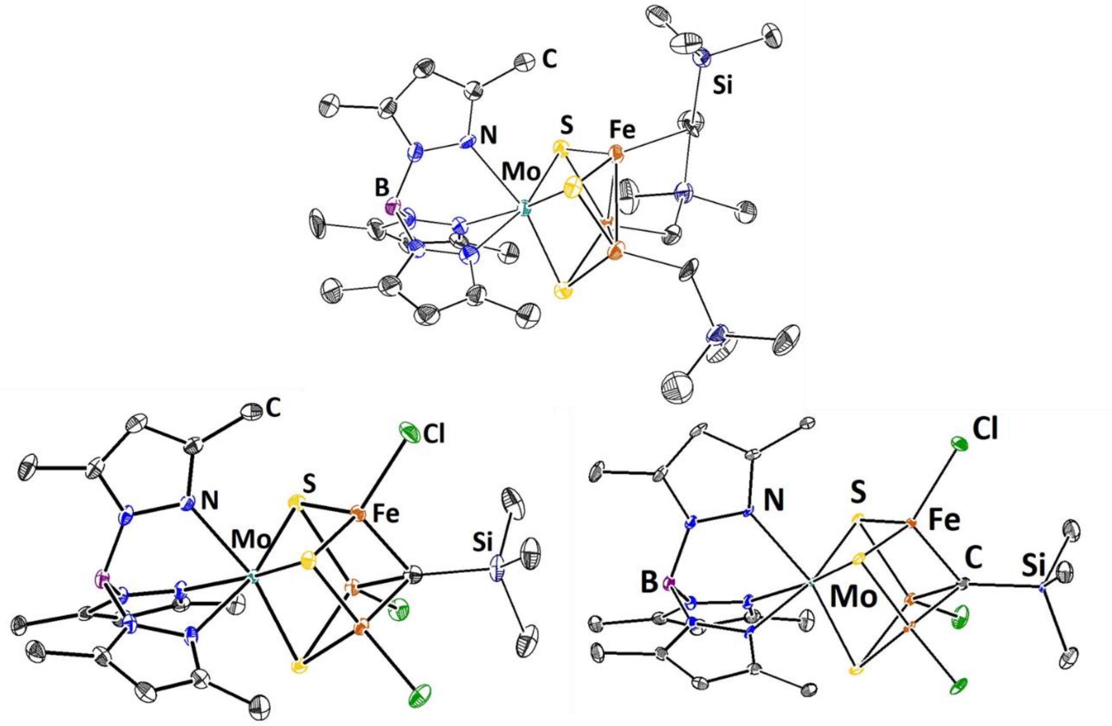

Figure 7: Crystal structures or **2-Mo** (top), **4-Mo** (bottom left), and **6-Mo** (bottom right) with ellipsoids plotted at the 50% probability level. Solvent and counter ions omitted for clarity.

Table 1: Average Bond Lengths ± S.D. (Å)

	2	**2-Mo**	**4**	**4-Mo**	**6**	**6-Mo**
M-S	2.385 ± 0.004	2.400 ± 0.002	2.360 ± 0.001	2.370 ± 0.001	2.351 ± 0.005	2.363 ± 0.004
Fe-S	2.260 ± 0.004	2.255 ± 0.005	2.282 ± 0.010	2.273 ± 0.002	2.238 ± 0.005	2.228 ± 0.005
Fe-C	2.010 ± 0.003	2.006 ± 0.016	1.921 ± 0.015	1.918 ± 0.011	1.910 ± 0.005	1.905 ± 0.002
Fe-Cl	N/A	N/A	2.258 ± 0.004	2.255 ± 0.003	2.213 ± 0.002	2.209 ± 0.003
Fe-Fe distance	2.563 ± 0.029	2.567 ± 0.025	2.520 ± 0.003	2.510 ± 0.002	2.545 ± 0.014	2.524 ± 0.001

To incorporate alternate bridging carbyne ligands, synthetic protocols analogous to the generation of **2** and **4** were developed using RMgCl salts instead of alkyl lithium salts (Fig. 8). The trialkyl clusters **7-Mo** and **8-Mo** were isolated and based on SC-XRD studies show partial occupancy of a bridging chloride ligand in the structures, which is in contrast to the open faced cubane **2** synthesized from $LiCH_2SiMe_3$ (Fig. 9). The average bond lengths of the Fe-alkly bonds in **7-Mo** and **8-Mo** (2.020 and 2.02 Å, respectively) are slightly elongated, but similar to that of **2-Mo** (2.006 Å), although it should be noted that the structure of **8-Mo** is not of high quality.

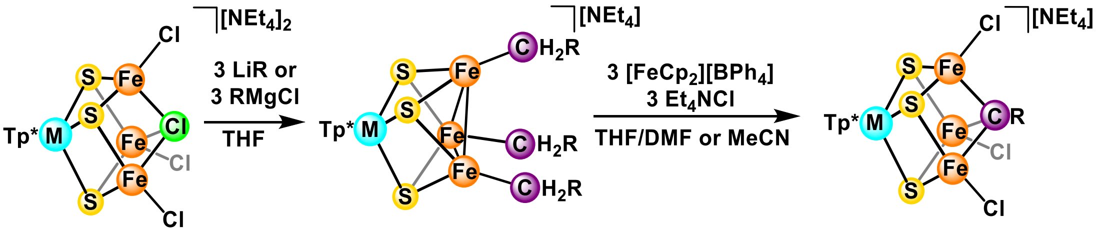

1 M = W
1-Mo M = Mo

2 M = W, R = $SiMe_3$
2-Mo M = Mo, R = $SiMe_3$
7-Mo M = Mo, R =$SiMe_2Ph$
8-Mo M = Mo, R = $SiPh_3$

6 M = W, R = $SiMe_3$
6-Mo M = Mo, R = $SiMe_3$
9-Mo M = Mo, R =$SiMe_2Ph$
10-Mo M = Mo, R = $SiPh_3$

Figure 8: General synthesis of carbyne bridged MFeS clusters. It should be noted that **7-Mo** and **8-Mo** contain partial occupancies of a bridging chloride, as shown in the crystal structures in Fig. 7.

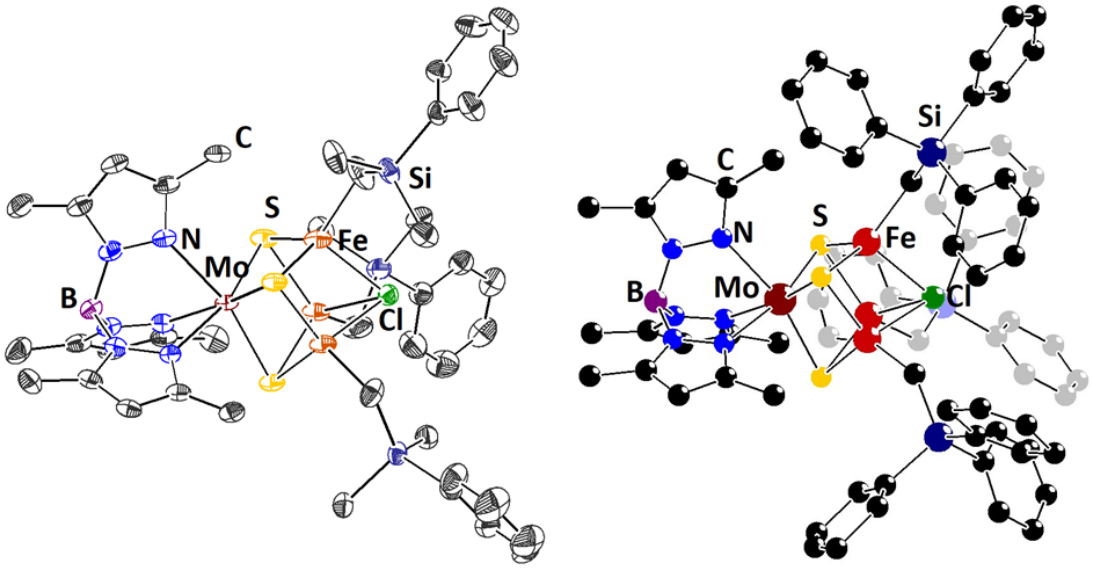

Figure 9: Crystal structures **7-Mo** (left) with ellipsoids plotted at the 50% probability level. The chloride atom has 64% occupancy. Connectivity structure of **8-Mo** (right). The chloride atom has 48% occupancy. Solvent and counter ions omitted for clarity.

Clusters **7-Mo** and **8-Mo**, with partial Cl occupancy, were used to generate the carbyne bridged clusters **9-Mo** and **10-Mo** using the same conditions as for the generation of **4** (Fig. 8), but were recrystallized from MeCN instead of DMF. SC-XRD studies show the formation of the desired carbyne cluster products with similar bond metrics as to those of **4** (Fig. 10). It should be noted that further characterization of **9-Mo** and **10-Mo** is required to confirm the preliminary structural assignments based on SC-XRD. With isolation of a number of $[Et_4N]_n[Tp^*MFe_3S_3(\mu_3\text{-}CR)Cl_3]$ the described method of carbyne formation using alkyl ligands of the type CH_2SiR_3 seems to be general.

With a number of $[Et_4N]_n[Tp^*MFe_3S_3(\mu_3\text{-}CH_2SiR_3)Cl_3]$ in hand, cleavage of the C-Si bond was targeted to synthesize a more structurally accurate model of FeMco. Reactions of **4**, **4-Mo**, **6**,

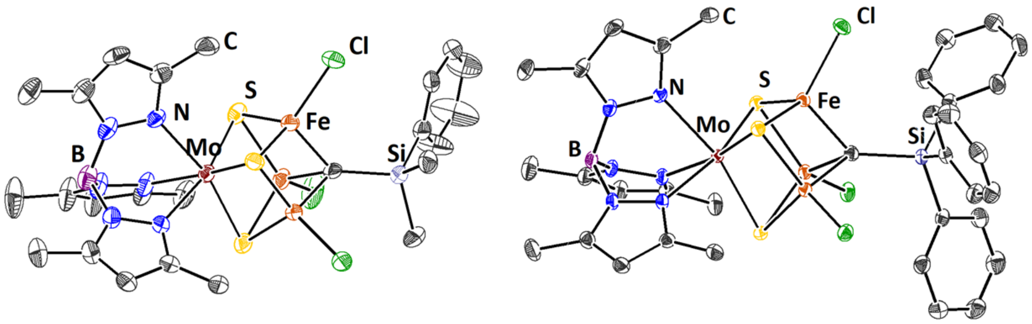

Figure 10: Crystal structures **9-Mo** (left) and **10-Mo** (right) with ellipsoids plotted at the 50% probability level. Solvent and counter ions omitted for clarity.

6-Mo, **9-Mo**, and **10-Mo** with tetrabutylammonium fluoride (TBAF; isolated or generated *in situ*, Fig. 11), CsF, AgF, iodosobenzene, $FeOC(O)CH_3$, NaOONa, and $NaOC(O)CH_3$ were carried out at room temperature and at reflux. In all cases, no silane products were detected using ^{1}H-NMR spectroscopy. Recrystallization attempts from the reaction mixtures generally resulted in isolation of the starting clusters. Excitingly, a methylidyne or carbide cluster **11** was isolated from reaction of **6** with TBAF generated *in situ* (Fig. 11). A bridging methylidyne ligand is proposed based on an elongated C ellipsoid (Fig. 12) and the average Fe-C bond lengths (1.975 Å), which are longer than the carbyne clusters described above, consistent with a more reduced carbyne cluster (Table 1). Additionally, reaction of **6-Mo** with TBAF generated *in situ* resulted in isolation of a carbyne cluster that indicates C-Si bond cleavage and further reaction with unreacted cyanofluorobenzene to form **12-Mo** (Fig. 11). Isolation of the dianionic **12-Mo** provides support for the assignment of **11** as a bridging methylidyne cluster. **11** and **12-Mo** were characterized using SC-XRD (Fig. 12). Unfortunately, the yields of **11** and **12-Mo** were extremely low and the synthesis was not reproducible. However, the isolation of these exciting clusters demonstrate the feasibility of the synthesis of methylidyne/carbide containing cubane clusters.

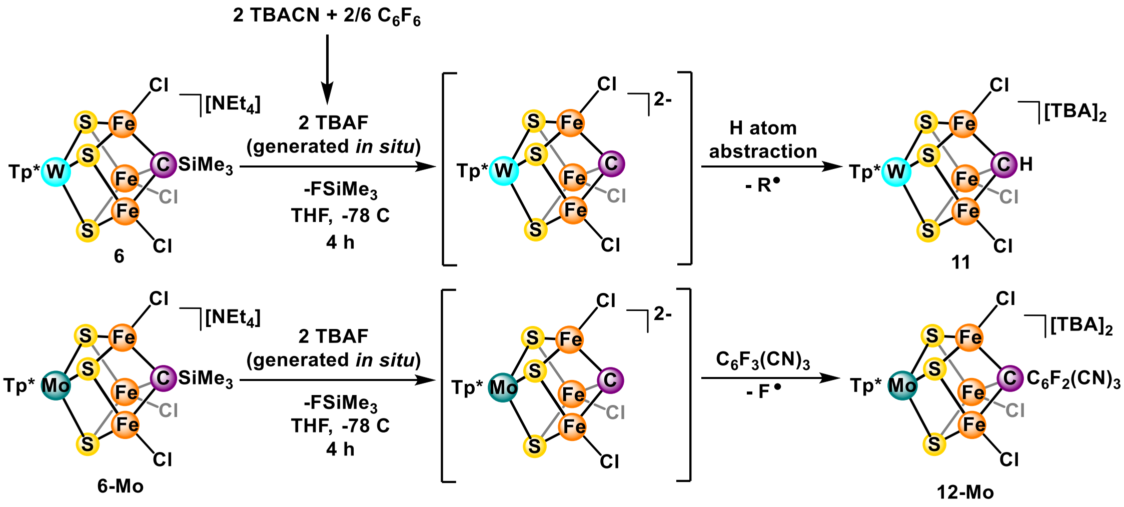

Figure 11: Reaction conditions for generations of **11** and **12-Mo**.

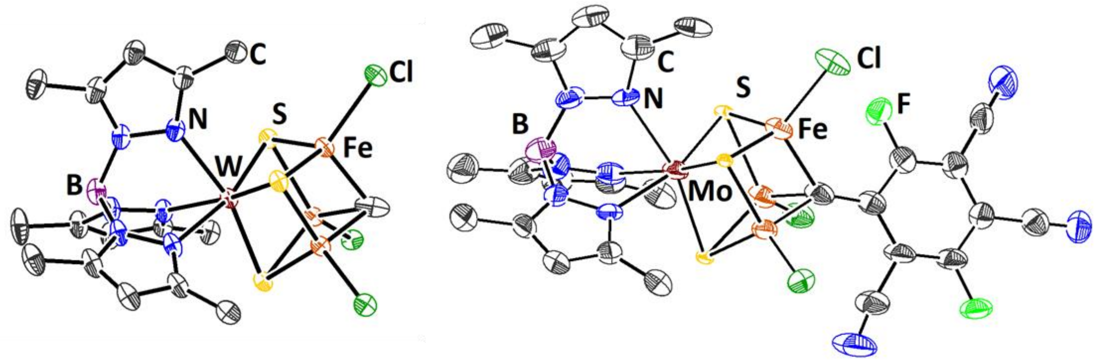

Figure 12: Crystal structures **11** (left) and **12-Mo** (right) with ellipsoids plotted at the 50% probability level. Solvent and counter ions omitted for clarity.

Conclusion

In summary, a WFe_3S_3 cluster has been synthesized with terminal alkyl ligands on each of the Fe centers and an open Fe_3 face. The cluster is stable upon heating, a notable feature given the scarcity of synthetic iron sulfur clusters with alkyl ligands, suggesting that high reactivity is not a general feature of this structural motif. Hydrogen abstraction occurs upon treatment with a mild oxidant in the presence of halide to form a bridging carbyne cluster. This system presents a new synthetic strategy for incorporation of carbon-based bridging ligands into iron sulfur clusters and is found to be general for other alkylsilane ligands. It also suggests a potential intermediate for biosynthesis of FeMco, whereby an alkyl radical is transferred to an Fe center. Carbon silicon bond cleave of a bridging carbyne ligand in W and Mo clusters is demonstrated, showing a promising route for methylidyne formation.

Experimental

General Considerations

All reactions were performed at room temperature in a N_2-filled M. Braun glovebox or using standard Schlenk techniques unless otherwise specified. Glassware was oven dried at 140 °C for at least 2 h prior to use, and allowed to cool under vacuum. Sodium tetrafluoroborate ($NaBPh_4$) was purchased in an anhydrous form and dissolved in acetonitrile (CH_3CN) and dried over 3 Å molecular sieves for 2 days before being filtered over Celite and dried in vacuo. $[Et_4N]_2[Tp^*WFe_3S_3(\mu_3\text{-}Cl)Cl_3]$[95] **(1)** (Tp* = tris(3,5-dimethyl-1-pyrazolyl)borate), $[Et_4N]_2[Tp^*WFe_3S_3(\mu_3\text{-}Cl)Cl_3]$ (**1-Mo**),[96] $[Et_4N]_2[Tp^*WFe_3S_3(\mu_3\text{-}S)Cl_3]$ **(5)**,[95] $[Tp^*WFe_3S_3(BAC)_3][BPh_4]$ **(3)**,[96] ferrocenium tetrafluoroborate $[FeCp_2][BPh_4]$,[97] tetrabutylammonium fluoride (TBAF),[98] and Ph_3SiCH_2Cl[99] were prepared according to literature procedures. Tetrahydrofuran (THF), diethyl ether (Et_2O), benzene (C_6H_6), toluene, CH_3CN, hexanes, and pentane were dried by sparging with nitrogen for at least 15 minutes, then passing through a column of activated A2 alumina under positive N_2 pressure and then degassed via several consecutive cycles of active vacuum and agitation on the Schlenk line before use.[100] Dimethylformamide was purchased in an anhydrous form from MiliporeSigma@, cannula-transferred to an oven dried Schlenk under N_2, degassed via several consecutive cycles of active vacuum and agitation on the Schlenk line, and then brought into the glovebox and dried over 3 Å molecular sieves for 48 h before use. ^1H and ^{31}P NMR spectra were recorded on a Varian 400 MHz spectrometer. ^1H-NMR spectra in proteo solvents were recorded on a Varian 400 MHz spectrometer using solvent suppression protocols. *d8*-THF, CD_3CN, and C_6D_6, were purchased from

Cambridge Isotope Laboratories, dried over calcium hydride, degassed by three freeze-pump-thaw cycles, and vacuum transferred prior to use. All other reagents were purchased from commercial sources in their anhydrous forms and used without further purification.

Synthetic Procedures

Synthesis of [Et_4N][$Tp^*WFe_3S_3(CH_2SiMe_3)_3$] (2). [$Et_4N$]$_2$[$Tp^*WFe_3S_3(\mu_3\text{-}Cl)Cl_3$] (100 mg, 0.087 mmol) was measured into a scintillation vial and suspended in THF (6 mL). $LiCH_2SiMe_3$ (0.63 ml of 0.7 M pentane solution, 0.44 mmol) was added to the stirring suspension dropwise at room temperature. The reaction suspension was allowed to stir at room temperature for 24 h. The suspension was filtered over a Celite pad and then the volatiles were removed under vacuum. After trituration three times with Et_2O, the solids were washed with Et_2O and then C_6H_6 until the filtrate was colorless. The desired product was extracted into a minimum of THF and crystallization was set up with vapor diffusion of 2x volume of pentane to yield dark needle like crystals. Finally, volatiles were removed under vacuum to yield 79.4 mg of the final product (80% yield). ^1H NMR (400 MHz, THF): δ 16.1 (br s), 7.0 (br s), -18.3 (s) ppm. Anal. calcd. (%) for C35H75BFe3N7S3Si3W: C, 36.98; H, 6.65; N, 8.63. Found: C, 37.13; H, 6.65; N, 8.71.

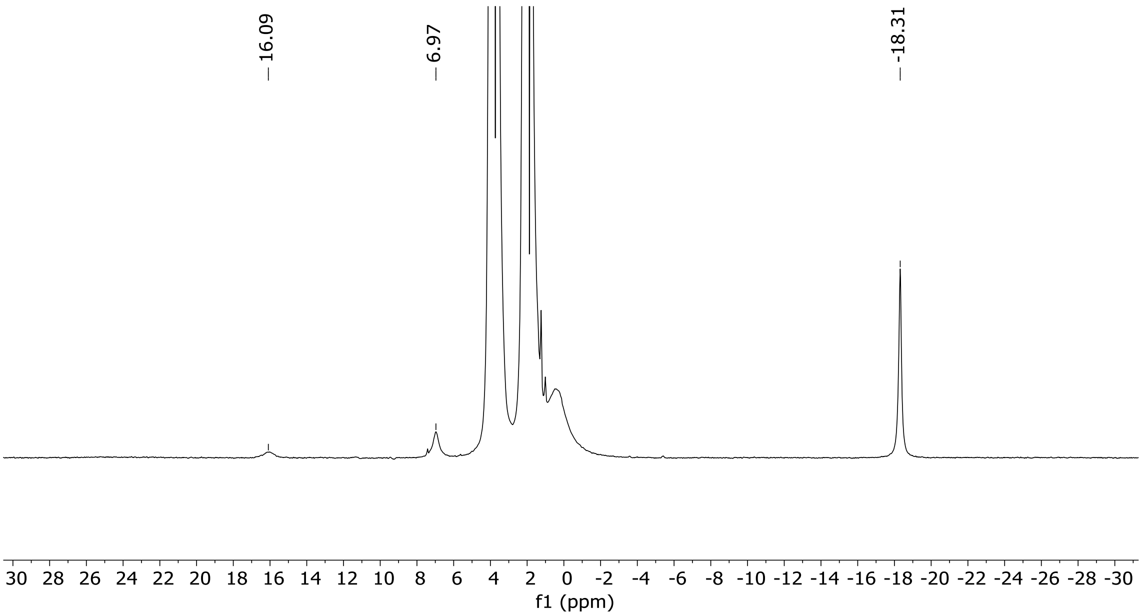

Figure S1: ^{1}H-NMR spectrum of $[Et_4N][Tp^*WFe_3S_3(CH_3SiMe_3)_3]$ in THF.

Synthesis of $[Et_4N][Tp^*MoFe_3S_3(CH_2SiMe_3)_3]$ (2-Mo). $[Et_4N]_2[Tp^*MoFe_3S_3(\mu_3\text{-}Cl)Cl_3]$ (100 mg, 0.095 mmol) was measured into a scintillation vial and suspended in THF (6 mL). $LiCH_2SiMe_3$ (0.41 ml of 0.7 M pentane solution, 0.285 mmol) was added to the stirring suspension dropwise at room temperature. The reaction suspension was allowed to stir at room temperature for 24 h. The suspension was filtered over a Celite pad and then dried *in-vacuo*. After trituration three times with Et_2O, the solids were washed with Et_2O and then C_6H_6 until the filtrate was colorless. The desired product was extracted into a minimum of THF and crystallization was set up with vapor diffusion of 2x volume of pentane to yield dark needle like crystals. Finally, the crystals were dried under vacuum to yield 64.8 mg of the final product (82% yield). ^{1}H NMR (400 MHz, THF): δ 19.7 (br s), 12.9 (s), -0.3 (s), -10.9 (s) ppm. Anal. calcd. (%) for C35H75BFe3N7S3Si3Mo: C, 40.08; H, 7.21; N, 9.35. Found: C, 40.11; H, 7.18; N, 9.08.

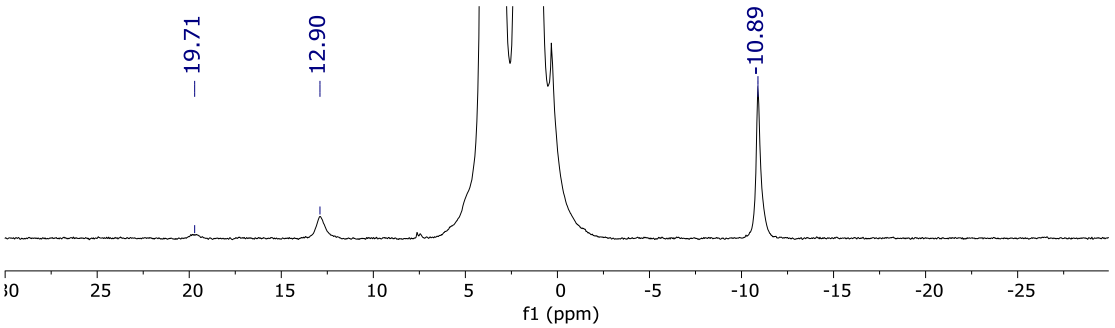

Figure S2: ^{1}H-NMR spectrum of $[Et_4N][Tp^*MoFe_3S_3(CH_3SiMe_3)_3]$ in THF.

Synthesis of $[Et_4N][Tp^*MoFe_3S_3(CH_2SiMe_2Ph)3(\mu_3\text{-}Cl_{64\%})]$ (7-Mo). $PhMe_2SiCH_2Cl$ (52.7 mg, 0.285 mmol) was added to a vigorously stirring suspension of activated Mg and stirred at room temperature for 24 h to generate $PhMe_2SiCH_2MgCl$. The reaction mixture was filtered and added to a suspension of $[Et_4N]_2[Tp^*MoFe_3S_3(\mu_3\text{-}Cl)Cl_3]$ (100 mg, 0.095 mmol) in THF (6 mL). The reaction suspension was allowed to stir at room temperature for 24 h. The suspension was filtered over a Celite pad and then dried *in-vacuo*. After trituration three times with Et_2O, the solids were washed with Et_2O and then C_6H_6 until the filtrate was colorless. The desired product was extracted into a minimum of THF and crystallization was set up with vapor diffusion of 2x volume of pentane to yield dark needle like crystals. Finally, the crystals were dried under vacuum to yield 71.7 mg of the final product (60% yield). ^{1}H NMR (400 MHz, THF): δ 19.1 (br s), 12.7 (s), 9.6 (s), -5.4 (br s), -12.0 (s) ppm.

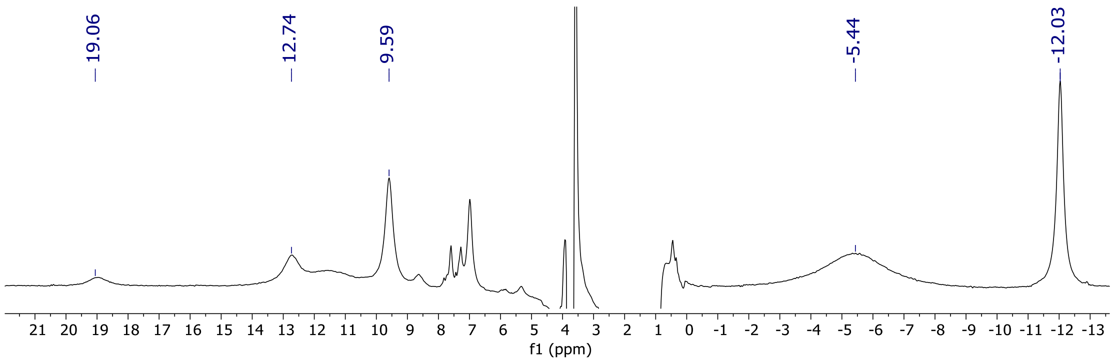

Figure S3: ^{1}H-NMR spectrum of $[Et_4N][Tp^*MoFe_3S_3(CH_2SiMe_2Ph)_3(\mu_3\text{-}Cl_{64\%})]$ in THF.

Synthesis of [Et_4N][$Tp^*MoFe_3S_3(CH_2SiPh_3)_3(\mu_3\text{-}Cl_{48\%})$] (8-Mo). Ph_3SiCH_2Cl (88 mg, 0.285 mmol) was added to a vigorously stirring suspension of activated Mg and stirred at room temperature for 24 h to generate $PhMe_2SiCH_2MgCl$. The reaction mixture was filtered and added to a suspension of $[Et_4N]_2[Tp^*MoFe_3S_3(\mu_3\text{-}Cl)Cl_3]$ (100 mg, 0.095 mmol) in THF (6 mL). The reaction suspension was allowed to stir at room temperature for 24 h. The suspension was filtered over a Celite pad and then dried *in-vacuo*. After trituration three times with Et_2O, the solids were washed with Et_2O and then C_6H_6 until the filtrate was colorless. The desired product was extracted into a minimum of THF and crystallization was set up with vapor diffusion of 2x volume of pentane to yield dark needle like crystals. Finally, the crystals were dried under vacuum to yield 64.8 mg of the final product (82% yield). ^{1}H NMR (400 MHz, THF): δ 15.4 (br s), 12.1 (br s), 9.4 (s), -4.7 (br s), -19.2 (s) ppm.

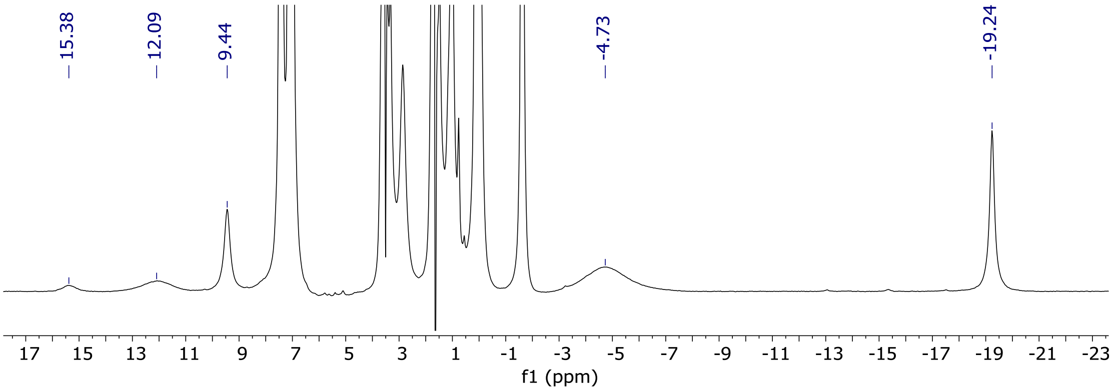

Figure S4: ^{1}H-NMR spectrum of [Et_4N][$Tp^*MoFe_3S_3(CH_2SiPh_3)_3(\mu_3\text{-}Cl_{48\%})$] in THF.

Synthesis of $[Et_4N]_2[Tp^*WFe_3S_3(\mu_3\text{-}CSiMe_3)Cl_3]$ (4). **2** (100 mg, 0.088 mmol) was measured into a scintillation vial and dissolved in THF (6 mL). The solution was cooled to -78 °C and $[FeCp_2][BPh_4]$ (133.3 mg, 0.26 mmol) was added and the solution was maintained at -78 °C for 2 h. Et_4NCl (43.1 mg, 0.26 mmol) was added to the solution and the reaction was brought to room temperature and stirred at room temperature for 3 h. It was then filtered over a Celite pad and volatiles were removed under vacuum. After trituration three times with Et_2O, the solids were washed with pentane, Et_2O, and then C_6H_6 until the filtrate was colorless. The product was extracted into a minimum of THF and crystallization was set up with vapor diffusion of 2x volume of Et_2O to yield dark block like crystals. The crystals were then dissolved in a minimum of DMF and crystallization was set up with vapor diffusion of 3x volume of Et_2O. Finally, volatiles were removed under vacuum to yield 68.5 mg of the final product (65% yield). ^{1}H NMR silent except for solvent peaks (DMF). Anal. calcd. (%) for C35H71BCl3Fe3N8S3SiW: C, 35.13; H, 5.98; N, 9.36. Found: C, 35.20; H, 5.99; N, 9.46.

Synthesis of [Et_4N][$Tp^*WFe_3S_3(\mu_3$-$CSiMe_3)Cl_3$] (6). **4** (100 mg, 0.084 mmol) was measured into a scintillation vial and dissolved in DMF (6 mL) and frozen. [(4-$BrC_6H_4)_3N$][OTf] (53.0 mg, 0.084 mmol) was added to the thawing DMF solution of **4**. The solution was stirred at room temperature for 30 minutes and then filtered over a Celite pad. 20x the volume of Et_2O was added and the solution was allowed to sit for at least 6 hours before dark needle like crystals formed. The crystals were dissolved in 2 mL of DMF and then filtered over a Celite pad and then 18 mL of Et_2O was added and the solution was allowed to sit for at least 6 hours before dark needle like crystals formed. This was performed 5x to achieve high purity. Finally, volatiles were removed under vacuum to yield 58.2 mg of the final product (65% yield). ^{1}H NMR (400 MHz, CD_3CN): δ 6.10 (s, 3H), 3.7 (s, 9H), 3.2 (q, 9H), 2.4 (s, 9H), 1.3 (td, 12H), 0.7 (s, 9H) ppm.Anal. calcd. (%) for C27H51BCl3Fe3N7S3SiW: C, 30.41; H, 4.82; N, 9.19. Found: C, 30.52; H, 4.84; N, 9.57.

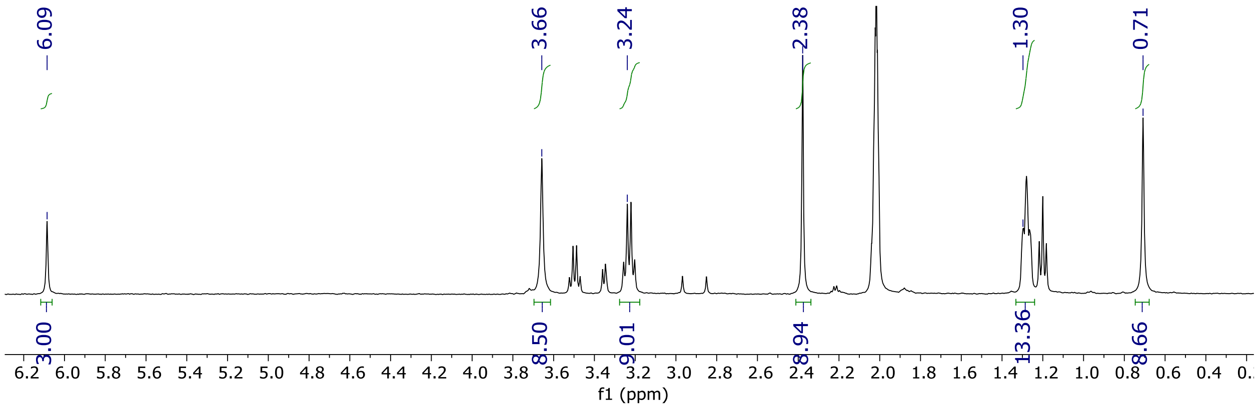

Figure S5: ^{1}H-NMR spectrum of $[Et_4N][Tp^*WFe_3S_3(\mu_3\text{-}CSiMe_3)Cl_3]$ in CD_3CN

Synthesis of $[Et_4N]_2[Tp^*MoFe_3S_3(\mu_3\text{-}CSiMe_3)Cl_3]$ (4-Mo). **2** (100 mg, 0.095 mmol) was measured into a scintillation vial and dissolved in THF (6 mL). The solution was cooled to -78 °C and $[FeCp_2][BPh_4]$ (133.3 mg, 0.29 mmol) was added and the solution was maintained at -78 °C for 2 h. Et_4NCl (43.1 mg, 0.29 mmol) was added to the solution and the reaction was brought to room temperature and stirred at room temperature for 3 h. It was then filtered over a Celite pad and dried *in-vacuo*. After trituration three times with Et_2O, the solids were washed with pentane, Et_2O, and then C_6H_6 until the filtrate was colorless. The product was extracted into a minimum of THF and crystallization was set up with vapor diffusion of 2x volume of Et_2O to yield dark block like crystals. The crystals were then dissolved in a minimum of DMF and crystallization was set up with vapor diffusion of 3x volume of Et_2O. Finally, the crystals were dried under vacuum to yield 68.5 mg of the final product (65% yield). ^{1}H NMR silent except for solvent peaks (DMF).

Synthesis of $[Et_4N][Tp^*MoFe_3S_3(\mu_3\text{-}CSiMe_3)Cl_3]$ (6-Mo). **4** (100 mg, 0.090 mmol) was measured into a scintillation vial and dissolved in DMF (6 mL). The solution was cooled to -78 °C and $[(4\text{-}BrC_6H_4)_3N][OTf]$ (56.9 mg, 0.090 mmol) was added. The solution was stirred at room temperature for 30 minutes and then filtered over a Celite pad. 20x the volume of Et_2O was added and the solution was allowed to sit for at least

6 hours before dark needle like crystals formed. The crystals were dissolved in 2 mL of DMF and then filtered over a Celite pad and then 18 mL of Et_2O was added and the solution was allowed to sit for at least 6 hours before dark needle like crystals formed. This was performed 5x to achieve high purity. Finally, the crystals were dried under vacuum to yield 59.8 mg of the final product (65% yield). ^1H NMR (400 MHz, CD_3CN): δ 6.01 (s, 3H), 3.6 (s, 9H), 3.2 (q, 9H), 2.3 (s, 9H), 1.2 (td, 12H), 0.6 (s, 9H) ppm.

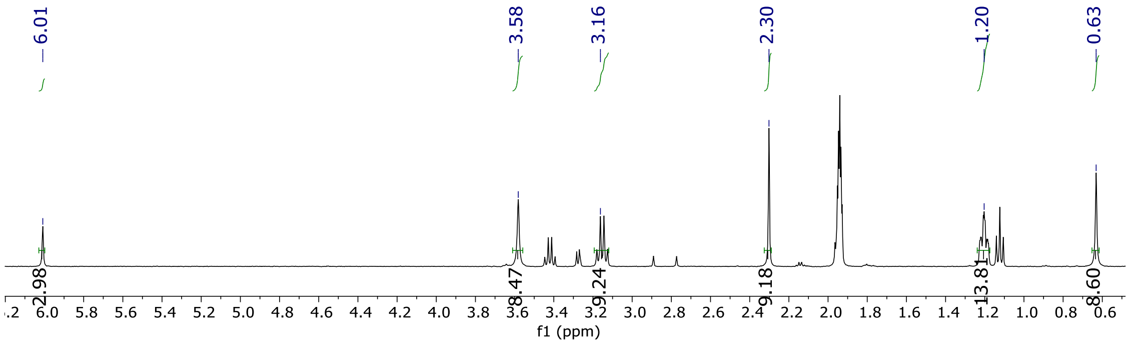

Figure S6: ^1H-NMR spectrum of $[Et_4N][Tp^*MoFe_3S_3(\mu_3\text{-}CSiMe_3)Cl_3]$ in CD_3CN.

Synthesis of $[Et_4N][Tp^*MoFe_3S_3(\mu_3\text{-}CSiMe_2Ph)Cl_3]$ (9-Mo). **7-Mo** (113 mg, 0.095 mmol) was measured into a scintillation vial and dissolved in THF (6 mL). The solution was cooled to -78 °C and $[FeCp_2][BPh_4]$ (133.3 mg, 0.29 mmol) was added and the solution was maintained at -78 °C for 2 h. Et_4NCl (43.1 mg, 0.29 mmol) was added to the solution and the reaction was brought to room temperature and stirred at room temperature for 3 h. It was then filtered over a Celite pad and dried *in-vacuo*. After trituration three times with Et_2O, the solids were washed with pentane, Et_2O, and then C_6H_6 until the filtrate was colorless. The product was extracted into a minimum of THF and crystallization was set up with vapor diffusion of 2x volume of Et_2O to yield dark block like crystals. The crystals were then dissolved in a minimum of MeCN and crystallization was set up with vapor diffusion of 3x volume of Et_2O. Finally, the crystals were dried under vacuum to yield 60.3 mg of the final product (61% yield). ^{1}H NMR silent except for solvent peaks (THF).

Synthesis of [Et_4N][$Tp^*MoFe_3S_3(\mu_3\text{-}CSiPh_3)Cl_3$] (10-Mo). **8-Mo** (154 mg, 0.095 mmol) was measured into a scintillation vial and dissolved in THF (6 mL). The solution was cooled to -78 °C and [$FeCp_2$][BPh_4] (133.3 mg, 0.29 mmol) was added and the solution was maintained at -78 °C for 2 h. Et_4NCl (43.1 mg, 0.29 mmol) was added to the solution and the reaction was brought to room temperature and stirred at room temperature for 3 h. It was then filtered over a Celite pad and dried *in-vacuo*. After trituration three times with Et_2O, the solids were washed with pentane, Et_2O, and then C_6H_6 until the filtrate was colorless. The product was extracted into a minimum of THF and crystallization was set up with vapor diffusion of 2x volume of Et_2O to yield dark block like crystals. The crystals were then dissolved in a minimum of MeCN and crystallization was set up with vapor diffusion of 3x volume of Et_2O. Finally, the crystals were dried under vacuum to yield 68.6 mg of the final product (62% yield). ^{1}H NMR silent except for solvent peaks (THF).

Synthesis of [TBA]$_2$[$Tp^*WFe_3S_3(\mu_3\text{-}CH)Cl_3$] (11). **6** (89.5 mg, 0.088 mmol) was measured into a scintillation vial and dissolved in THF (6 mL). The solution was cooled to -78 °C and TBAF (47.1 mg, 0.18 mmol) generated *in situ* was added and the solution was maintained at -78 °C for 2 h. It was then filtered over a Celite pad and volatiles were removed under vacuum. After trituration three times with Et_2O, the solids were washed with pentane, Et_2O, and then C_6H_6 until the filtrate was colorless. The product was extracted into a minimum of THF and crystallization was set up with vapor diffusion of 2x volume of Et_2O to yield a small amount of dark block like crystals.

Synthesis of [TBA]$_2$[$Tp^*MoFe_3S_3(\mu_3\text{-}CC_6F_2(CN)_3Cl_3$] (12-Mo). **6-Mo** (81.7 mg, 0.088 mmol) was measured into a scintillation vial and dissolved in THF (6 mL). The solution was cooled to -78 °C and TBAF (47.1 mg, 0.18 mmol) generated *in situ* was added and the solution was maintained at -78 °C for 2 h. It was then filtered over a Celite pad and volatiles were removed under vacuum. After trituration three times with Et_2O, the solids were washed with pentane, Et_2O, and then C_6H_6 until the filtrate was colorless. The product was extracted into a minimum of THF and crystallization was set up with vapor diffusion of 2x volume of Et_2O to yield a small amount of dark block like crystals.

Synthesis of Tp*$WFe_3S_3(\mu_3\text{-}CSiMe_3)(CH_2SiMe_3)_2(CH_3CN)$ (13). 2 (100 mg, 0.088 mmol) was measured into a scintillation vial and dissolved in THF (6 mL). The solution was cooled to -78 °C and $[(4\text{-}BrC_6H_4)_3N][OTf]$ (56.8 mg, 0.088 mmol) was added and the solution was maintained at -78 °C for 2 h. It was then filtered over a Celite pad and volatiles were removed under vacuum. After trituration three times with Et_2O, the solids were washed with pentane, Et_2O, and then C_6H_6 until the filtrate was colorless. The remaining solid was extracted into a minimum of THF and crystallization was set up with vapor diffusion of 2x volume of Et_2O to yield less than 1 mg of crystals.

Synthesis of Tp*$WFe_3S_3(\mu_3\text{-}CSiMe_3)Cl_2(THF)$ and Tp*$WFe_3S_3(\mu_3\text{-}CSiMe_3)(CH_2SiMe_3)_2(THF)$ (14 and 15). 2 (100 mg, 0.088 mmol) was measured into a scintillation vial and dissolved in THF (6 mL). The solution was cooled to -78 °C and AgOTf (23.1 mg, 0.088 mmol) was added and the solution was maintained at -78 °C for 2 h. It was then filtered over a Celite pad and volatiles were removed under vacuum. After trituration three times with Et_2O, the solids were washed with pentane, Et_2O, and then C_6H_6 until the filtrate was colorless. The remaining solid was extracted into a minimum of THF and crystallization was set up with vapor diffusion of 2x volume of Et_2O to yield less than 1 mg of crystals.

NMR Experiments

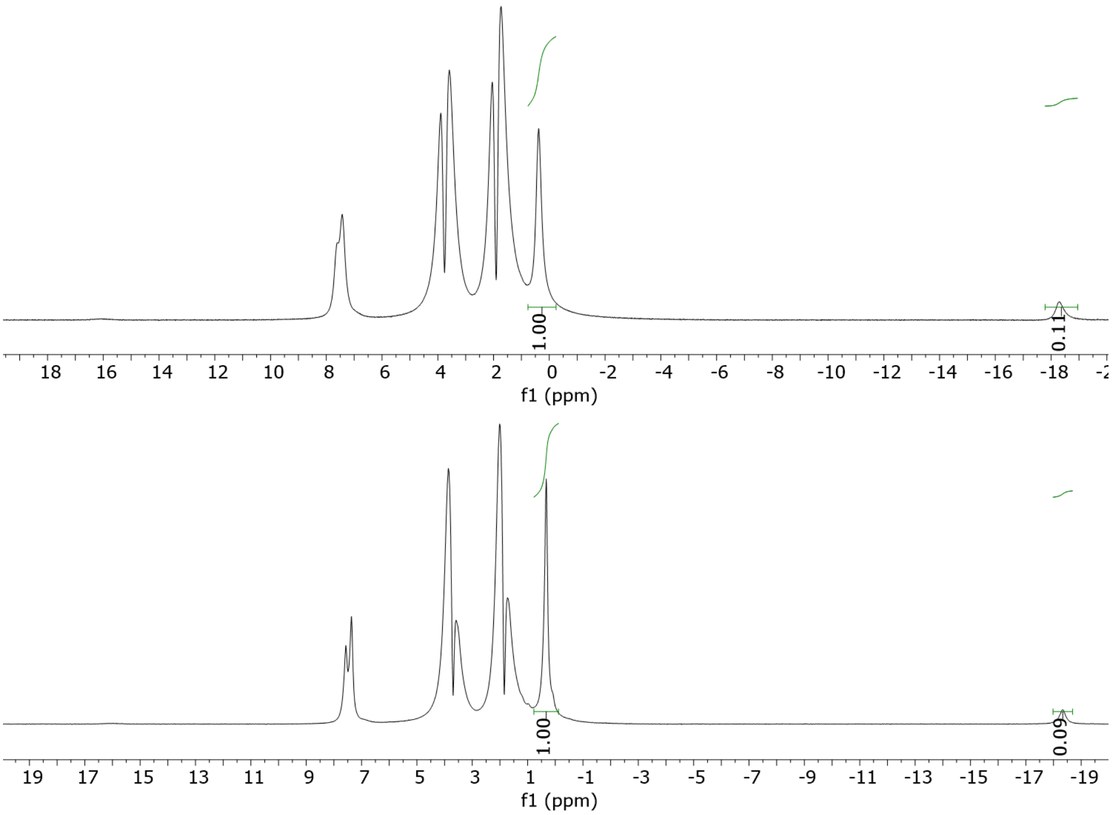

Figure S7: ^{1}H-NMR spectra of [Et_4N][$Tp^*WS_3Fe_3(CH_2SiMe_3)_3$] before (top) and after (bottom) heating at 80 ˚C for 24 hours in THF. $PhMe_3Si$, 0.3 ppm, was used as an internal standard and integrated as 1. The cluster peak at -18.4 ppm was used for integration for the cluster.

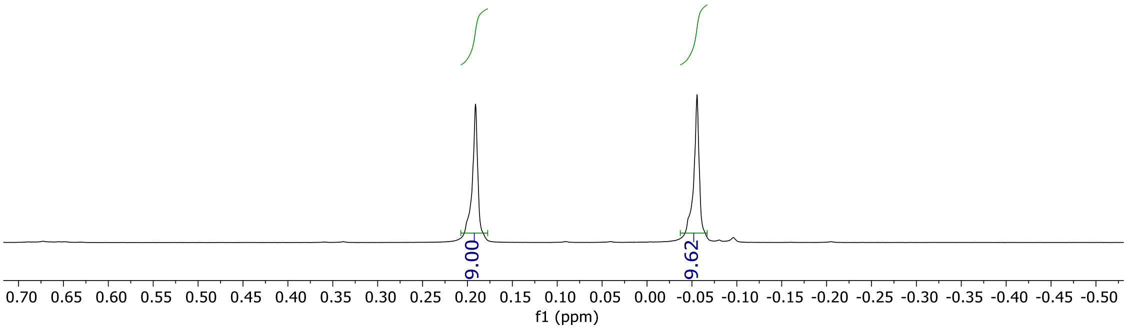

Figure S8: ^{1}H-NMR spectrum of the reaction mixture of the synthesis of **4** in THF with two equivalents of Me_3PhSi (0.2 ppm) used as an internal standard. Integration of Me_4Si (-0.05 ppm) generated during reaction indicates 1.6 equivalents are formed per cluster.

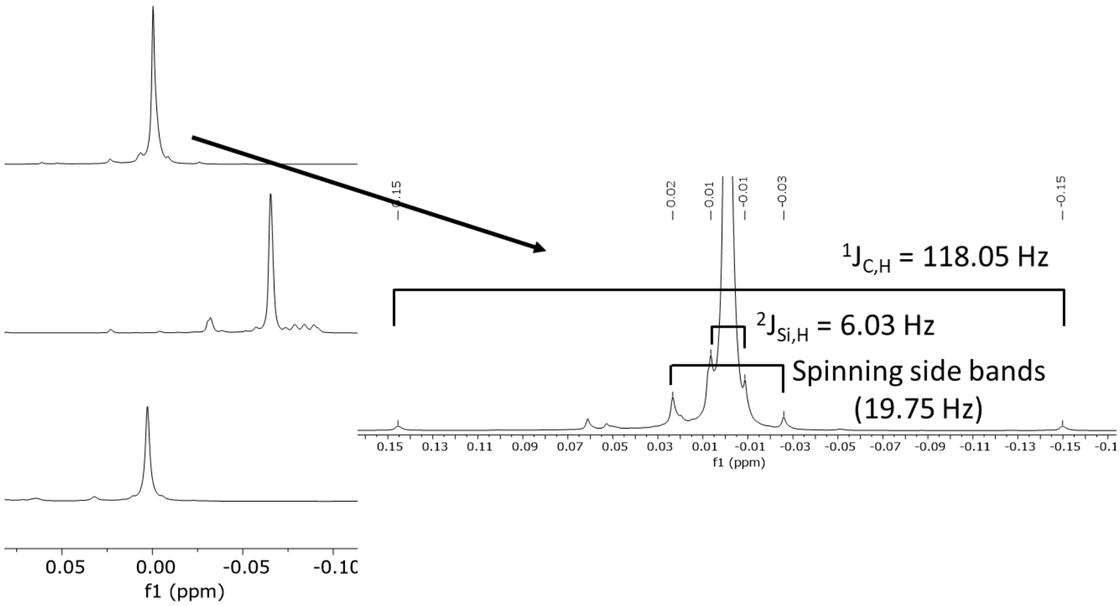

Figure S9: ^{1}H-NMR spectra of reaction performed in d_8-THF (bottom) and control samples showing $Si(CH_3)_4$ (top) and $DCH_2Si(CH_3)_3$ (middle) generated independently in d_8-THF from $LiCH_2SiMe_3$ and CH_3OH and CD_3OD, respectively.

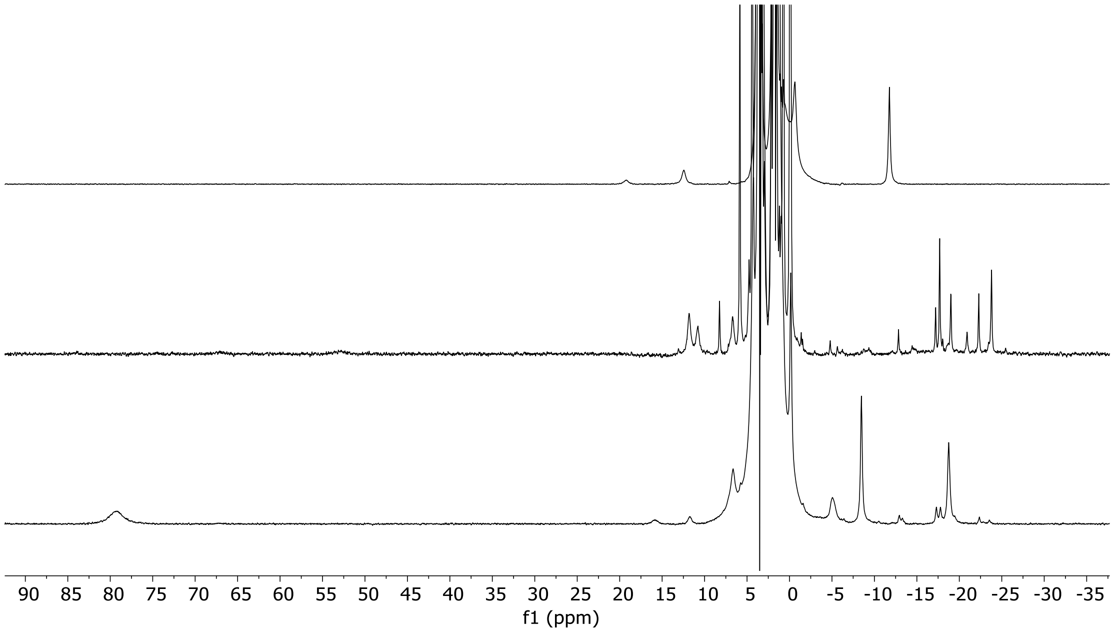

Figure S10: ^{1}H-NMR spectra of $[Et_4N][Tp^*WS_3Fe_3(CH_2SiMe_3)_3]$ (top), after reaction with 1 equivalent of AgOTf for 2 hours at -78 °C (middle), and with 2 equivalents of AgOTf for 2 hours at -78 °C (bottom).

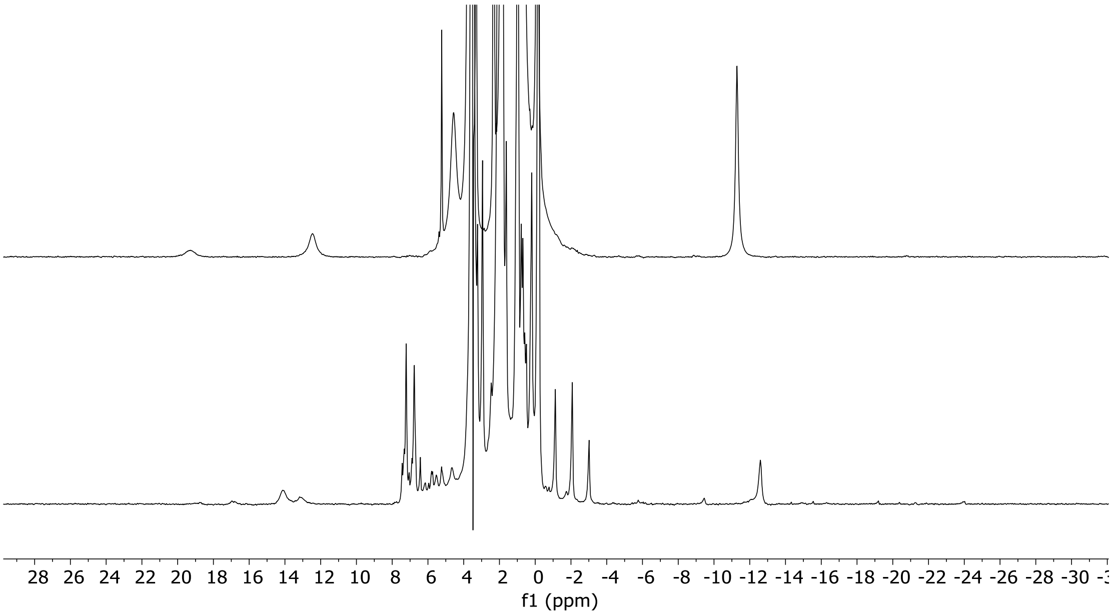

Figure S11: ^{1}H-NMR spectra of $[Et_4N][Tp^*WS_3Fe_3(CH_2SiMe_3)_3]$ (top) after reaction with 1 equivalent of $[N(4\text{-}BrPh)_3][OTf]$ for 2 h at -78 °C (bottom).

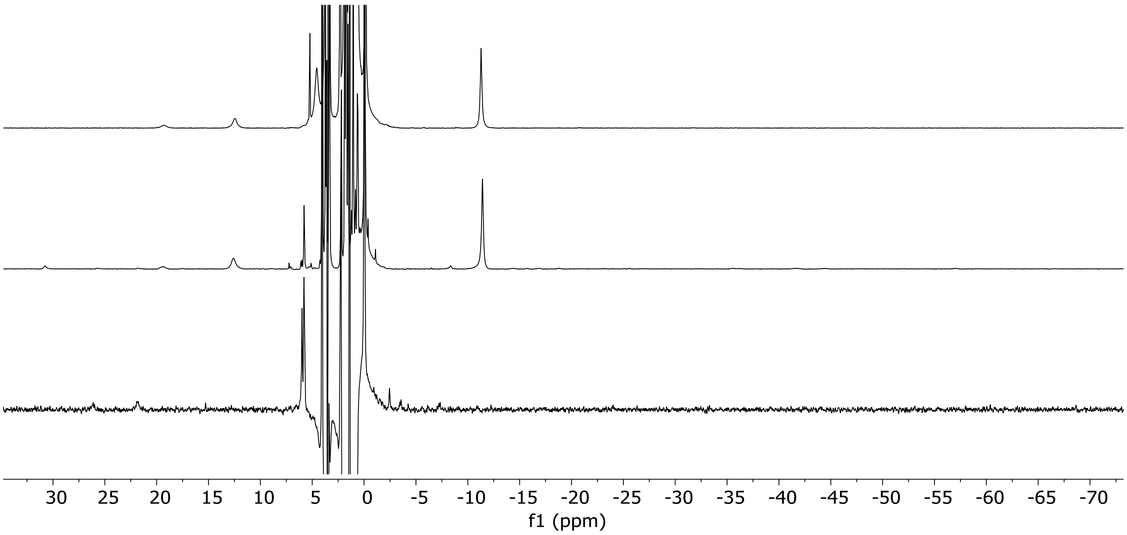

Figure S12: ^{1}H-NMR spectra of $[Et_4N][Tp^*WS_3Fe_3(CH_2SiMe_3)_3]$ (top), after reaction with 2 equivalents of $[FeCp_2][BPh_4]$ for 12 h at -40 ˚C (middle) and for 12 h at room temperature (bottom).

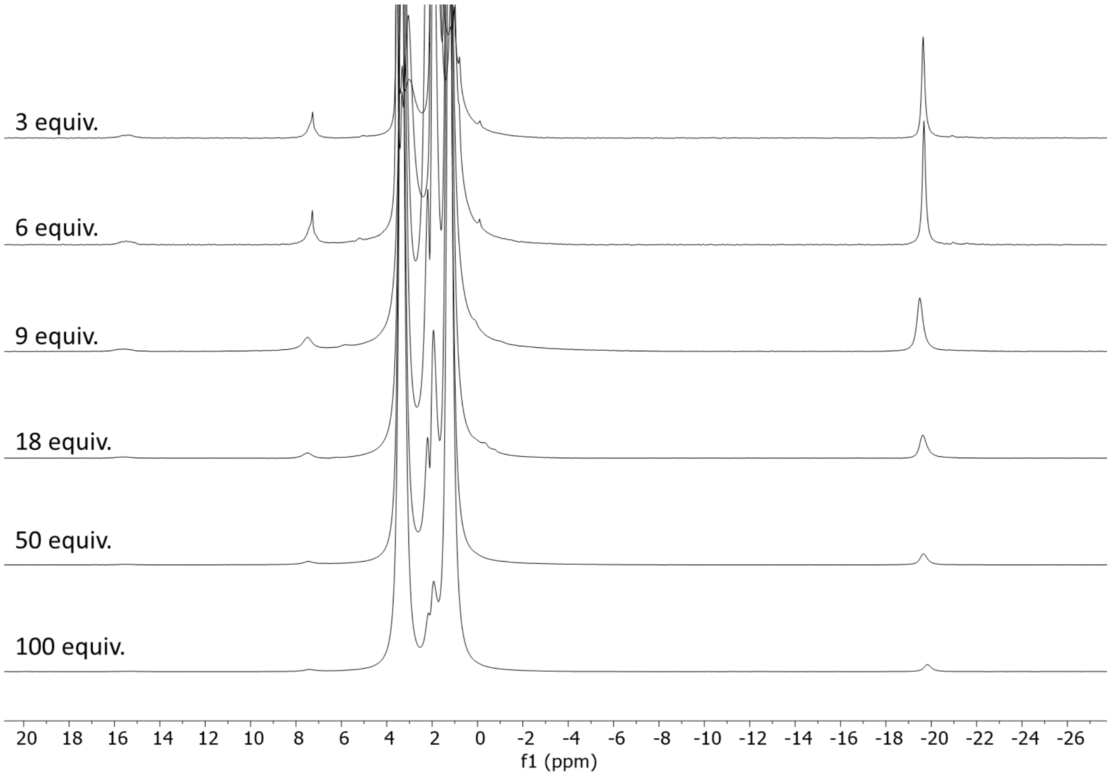

Figure S13: ^{1}H-NMR spectra of [Et_4N][$Tp^*WS_3Fe_3(CH_2SiMe_3)_3$] in THF with the addition of increasing equivalents of Et_4NCl. Increased broadening of the resonances indicates a dynamic process in solution.

Mössbauer Data

General

Zero applied field ^{57}Fe Mossbauer spectra were recorded at 80 K in constant acceleration mode on a spectrometer from See Co (Edina, MN) equipped with an SVT- S6 400 cryostat (Janis, Wilmington, WA). The isomer shifts are relative to the centroid of an α-Fe foil signal at room temperature. Samples were prepared by mixing polycrystalline material (20 mg) with boron nitride in a cup fitted with a screw cap. The data were fit to Lorentzian lineshapes using WMOSS (www.wmoss.org).

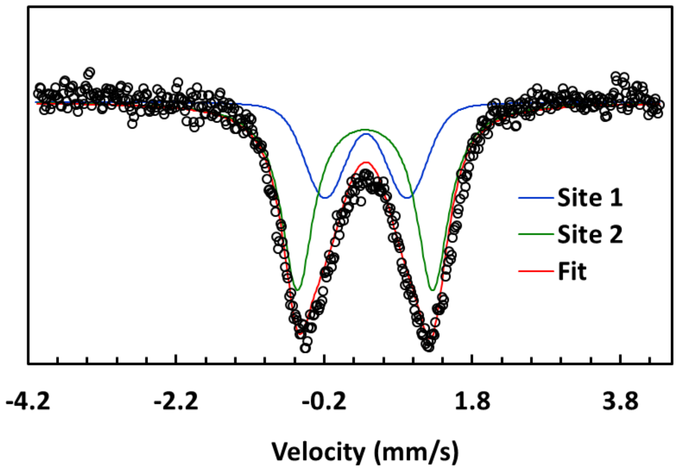

	δ (mm/s)	ΔE_q (mm/s)	χ^2	Relative Fraction
1 Site Fit	0.35	1.62	0.89	1
2 Site Fit, Site 1	0.36	1.11	0.61	1/3
2 Site Fit, Site 2	0.35	1.83		2/3

Figure S14: Mössbauer spectrum of $[Et_4N][Tp^*WFe_3S_3(CH_3SiMe_3)_3]$ (**2**) showing one and two site fits. Parameters are shown in table. Black circles are raw data.

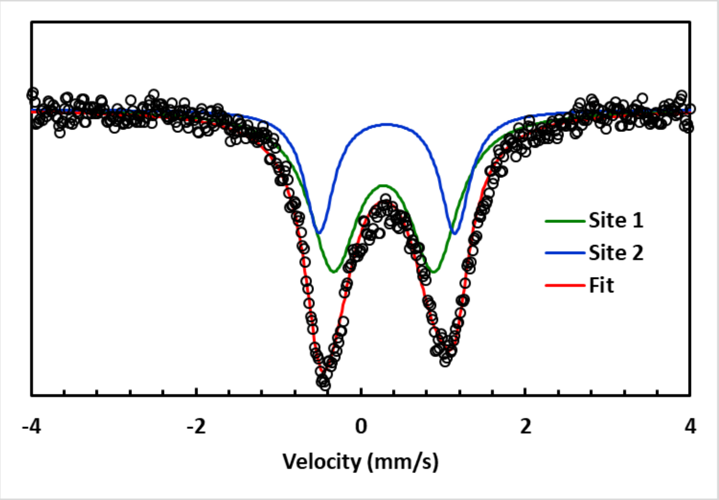

	δ (mm/s)	ΔE_q (mm/s)	χ^2	Relative Fraction
1 Site Fit	0.29	1.36	0.89	1
Site 1	0.28	1.22	0.70	2/3
Site 2	0.32	1.65		1/3
Average, 2 Site Fit	0.29	1.36		

Figure S15: Mössbauer spectrum of [Et_4N][$Tp^*MoFe_3S_3(CH_3SiMe_3)_3$] (**2-Mo**) showing one and two site fits. Parameters are shown in table. Black circles are raw data.

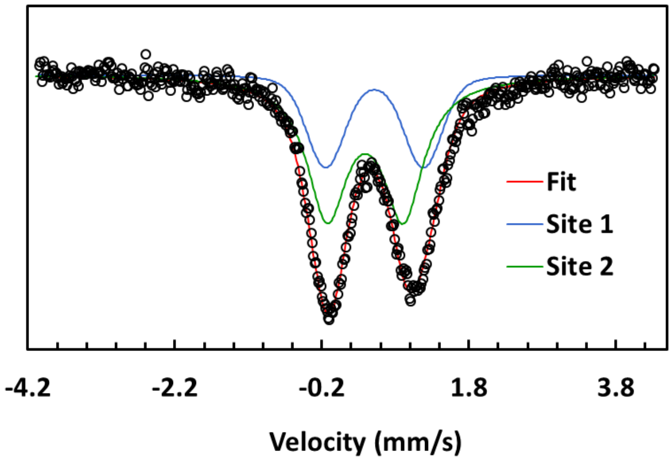

	δ (mm/s)	ΔE$_q$ (mm/s)	χ^2	Relative Fraction
Site 1	0.52	1.33	0.58	1/3
Site 2	0.42	1.04		2/3

Figure S16: Mössbauer spectrum of [Tp*WFe$_3$S$_3$(BAC)$_3$][PBh$_4$] (**3**) showing two site fit. Parameters are shown in table. Black circles are raw data.

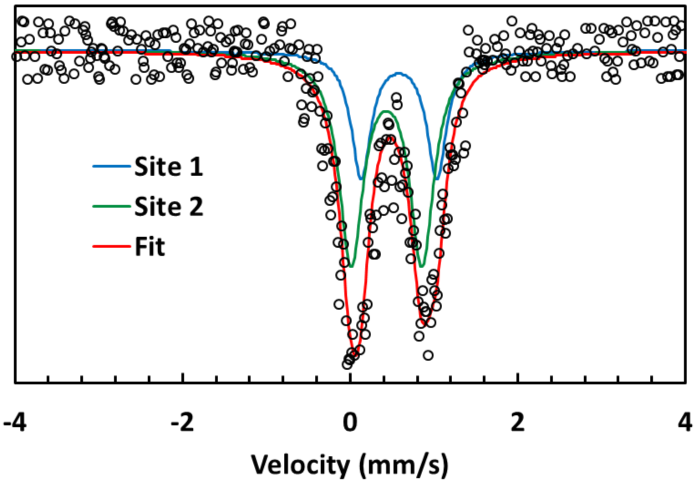

	δ (mm/s)	ΔE$_q$ (mm/s)	χ^2	Relative Fraction
Site 1	0.43	0.84	0.60	1/3
Site 2	0.58	0.90		2/3

Figure S17: Mössbauer spectrum of [Et$_4$N]$_2$[Tp*WFe$_3$S$_3$(μ$_3$-CSiMe$_3$)Cl$_3$] (**4**) showing two site fit. Parameters are shown in table. Black circles are raw data.

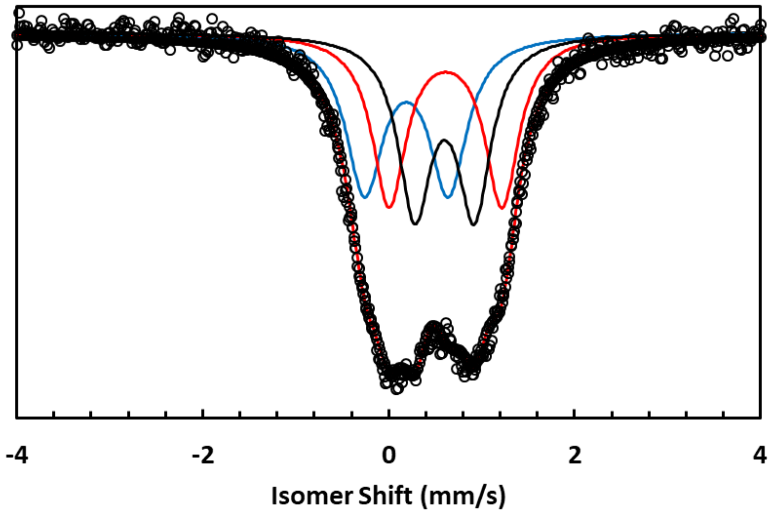

	δ (mm/s)	ΔE$_q$ (mm/s)	χ^2	Relative Fraction
Site 1	0.19	0.90	0.65	1/3
Site 2	0.61	1.21		1/3
Site 3	0.60	0.64		1/3
Average	0.47	0.92		

Figure S18: Mössbauer spectrum of [Et$_4$N]$_2$[Tp*MoFe$_3$S$_3$(μ$_3$-CSiMe$_3$)Cl$_3$] (**3-Mo**) showing fit. Parameters are shown in table. Black circles are raw data.

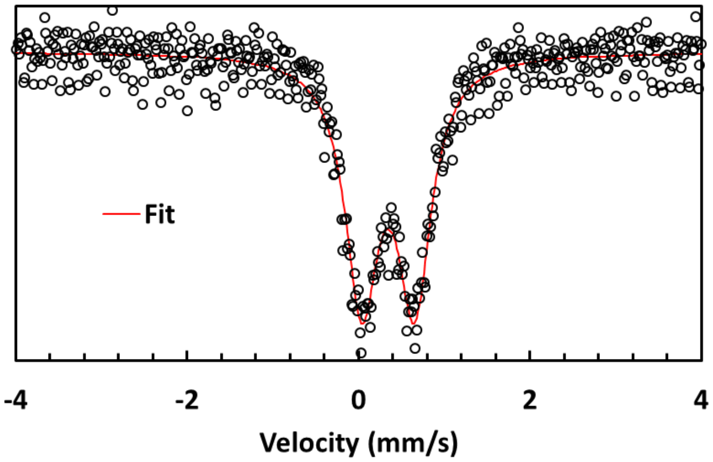

	δ (mm/s)	ΔE$_q$ (mm/s)	χ^2	Relative Fraction
1 Site Fit	0.34	0.62	0.50	1

Figure S19: Mössbauer spectrum of [Et$_4$N][Tp*WFe$_3$S$_3$(μ$_3$-CSiMe$_3$)Cl$_3$] (**6**) showing fit. Parameters are shown in table. Black circles are raw data.

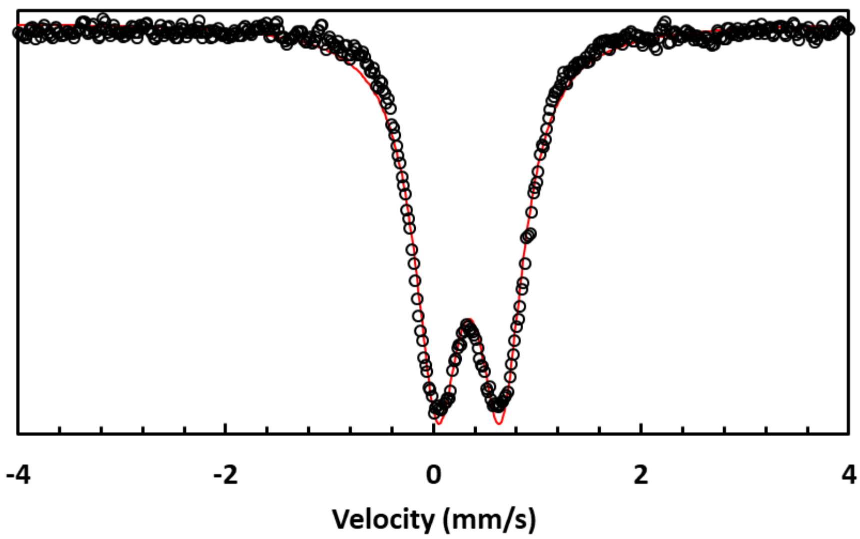

	δ (mm/s)	ΔE_q (mm/s)	χ^2	**Relative Fraction**
Fit	0.34	0.61	0.70	1

Figure S20: Mössbauer spectrum of $[Et_4N][Tp^*MoFe_3S_3(\mu_3\text{-}CSiMe_3)Cl_3]$ (**5-Mo**) showing fit. Parameters are shown in table. Black circles are raw data.

Electrochemistry Data

General

Cyclic voltammetry experiments were performed with a Pine Instrument Company AFCBP1 biopotentiostat with the AfterMathsoftware package. All measurements were performed in a three-electrode cell, which consisted of glassy carbon (working; ⌀= 3.0 mm), Ag wire (reference), and bare Pt wire (counter), in a N_2-filled MBraun glovebox at room temperature. Dry CH_3CN or DMF that contained ~0.2 M $[Bu_4N][PF_6]$ was used as the electrolyte solution. Redox potentials are reported relative to the ferrocene/ferrocenium redox wave (Fc/Fc^+;ferrocene added as an internal standard).The open circuit potential was measured prior to each voltammogram being collected. Voltammograms were scanned reductively in order to minimize the oxidative damage that was frequently observed on scanning more oxidatively.

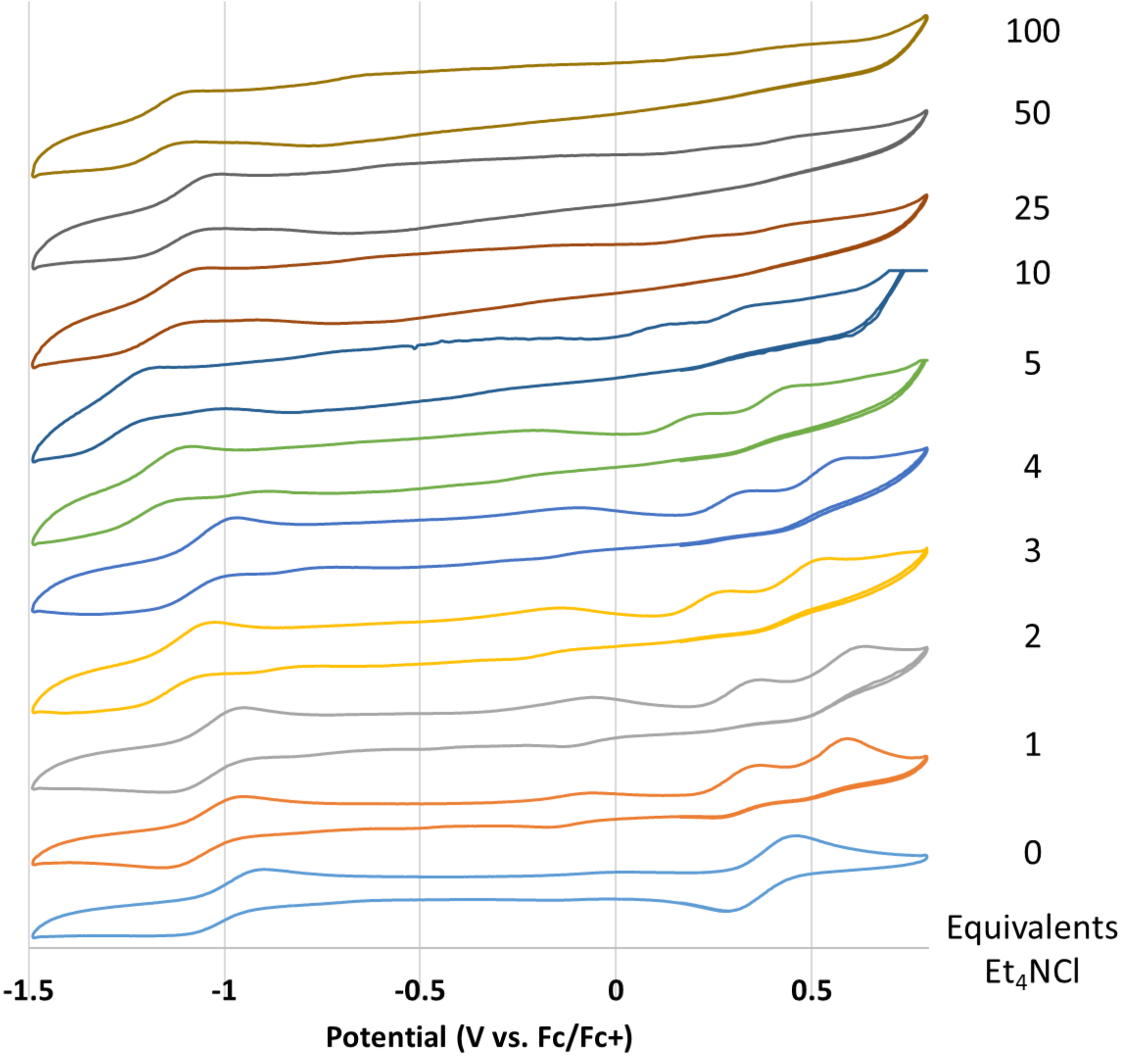

Figure S21: Cyclic voltammograms of [Et_4N][Tp*$WFe_3S_3(CH_2SiMe_3)_3$] (**2**) with increasing equivalents of Et_4NCl showing a potential shift of the oxidative redox feature to more negative potentials. Conditions: 250 mV/s, 2.5 mM cluster, CH_3CN, 0.1 M $TBAPF_6$.

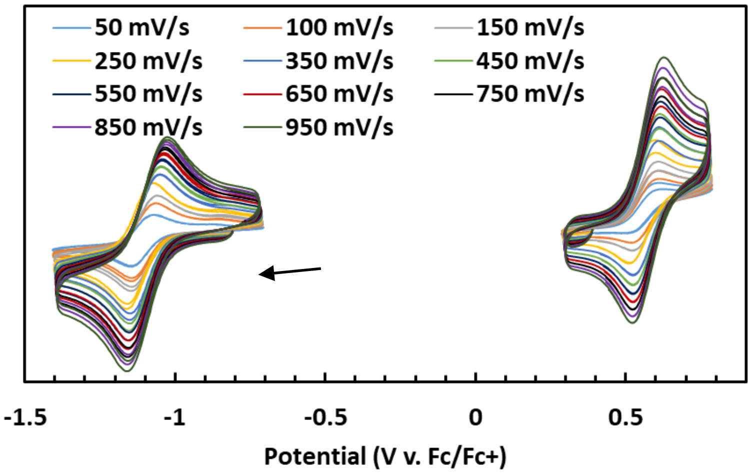

Figure S22: Cyclic voltammetry of [Et_4N][$Tp^*WFe_3S_3(CH_3SiMe_3)_3$] **(2)** at different scan rates. Conditions: 250 mV/s, 2.5 mM cluster, CH_3CN, 0.1 M $TBAPF_6$.

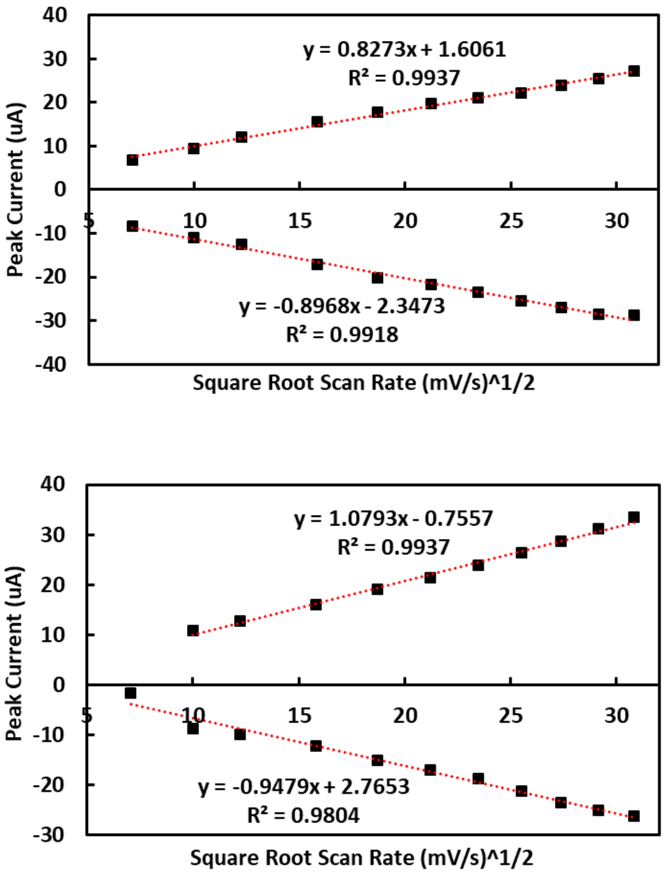

Figure S23: Peak current vs. square root of scan rate for -0.97 V (top) and 0.59 V (bottom) redox features of [Et_4N][$Tp^*WFe_3S_3(CH_3SiMe_3)_3$] **(2)**.

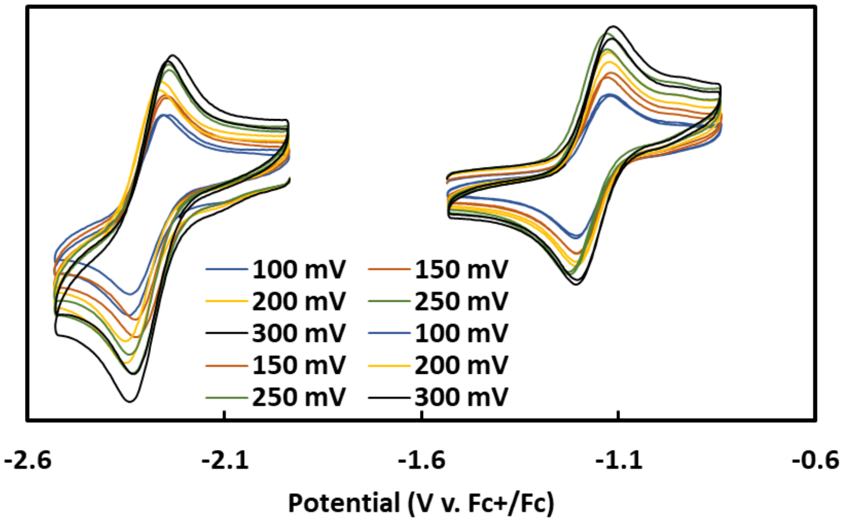

Figure S24: Cyclic voltammetry of [Et$_4$N][Tp*WFe$_3$S$_3$(BAC)$_3$] **(3)** at different scan rates. Conditions: 250 mV/s, 2.5 mM cluster, CH$_3$CN, 0.1 M TBAPF$_6$.

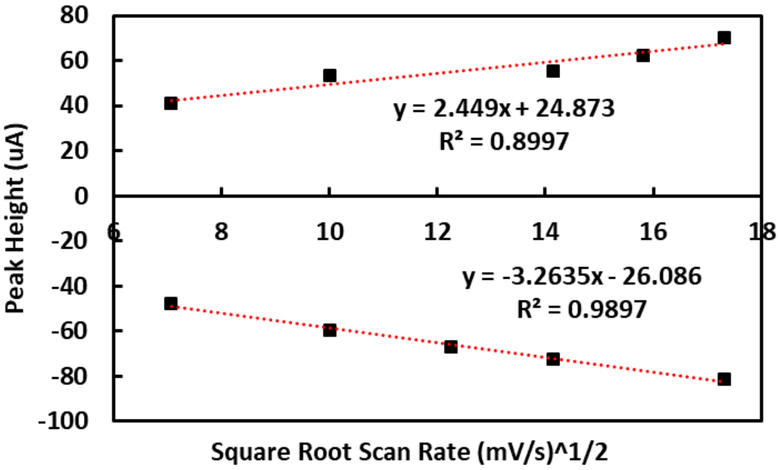

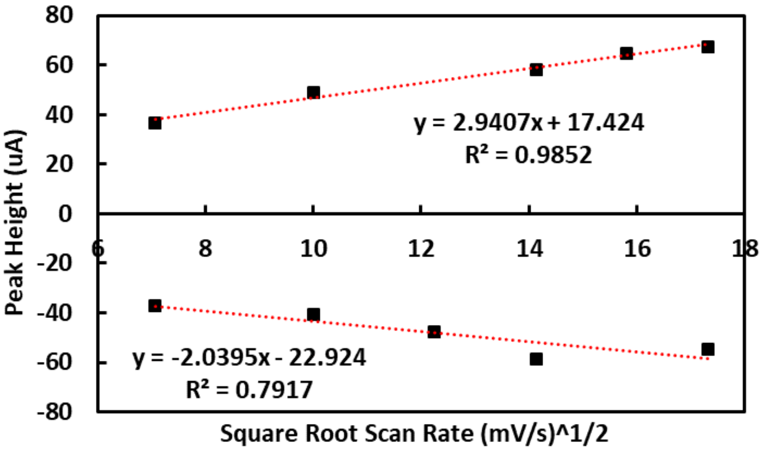

Figure S25: Peak current vs. square root of scan rate for the -2.25 V (top) and -1.10 V (bottom) redox features of [Et_4N][$Tp*WFe_3S_3(BAC)_3$] **(3)**.

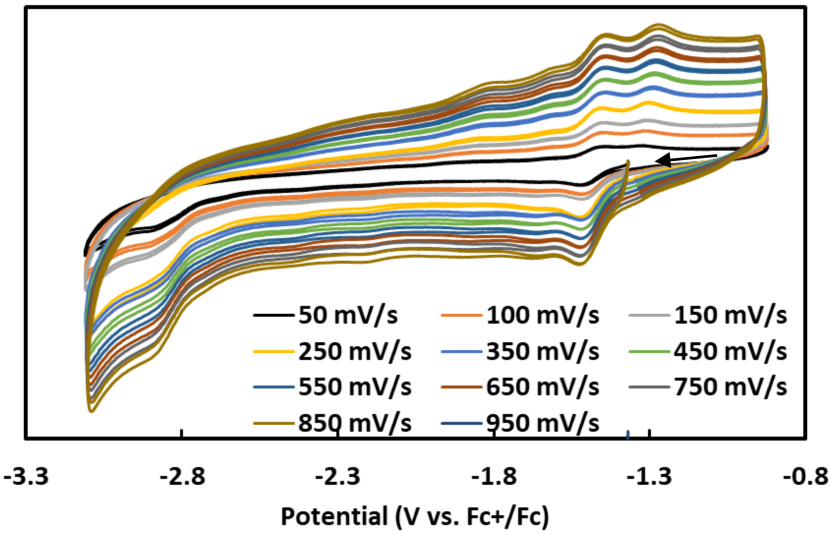

Figure S26: Cyclic voltammetry of $[Et_4N]_2[Tp^*WFe_3S_3(\mu_3\text{-}CSiMe_3)Cl_3]$ **(4)** at different scan rates. Conditions: 250 mV/s, 2.5 mM cluster, DMF, 0.1 M $TBAPF_6$.

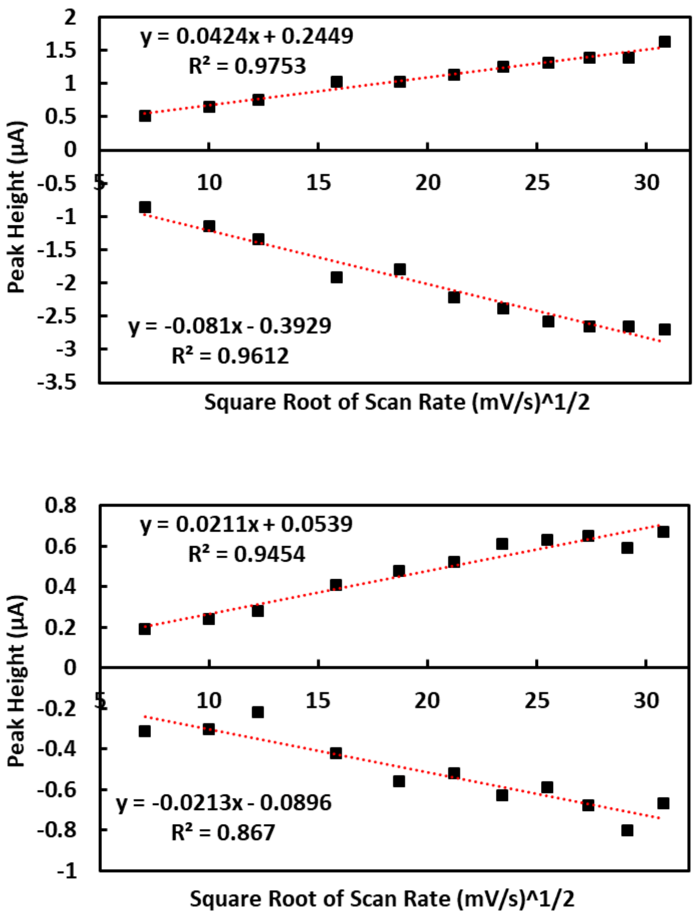

Figure S27: Peak current vs. square root of scan rate for the -1.48 V (top) and -2.82 V (bottom) redox features of $[Et_4N]_2[Tp^*WFe_3S_3(\mu_3\text{-}CSiMe_3)Cl_3]$ **(4)**.

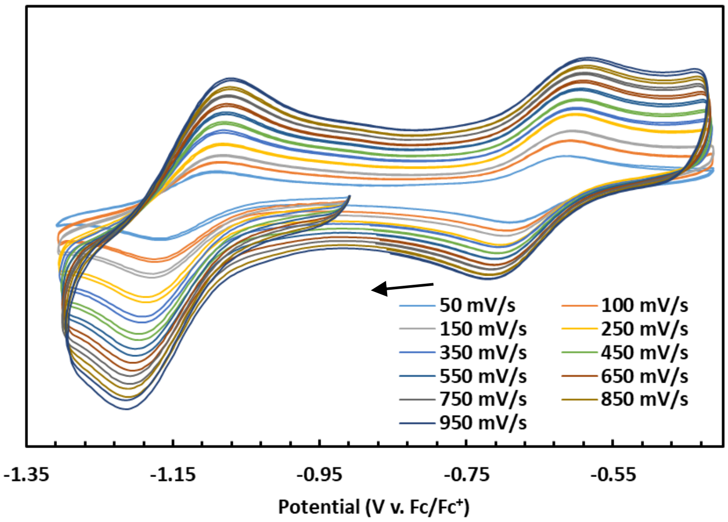

Figure S28: Cyclic voltammetry of $[Et_4N][Tp^*WFe_3S_3(\mu_3\text{-}S)Cl_3]$ **(5)** at different scan rates. Conditions: 250 mV/s, 2.5 mM cluster, CH_3CN, 0.1 M $TBAPF_6$.

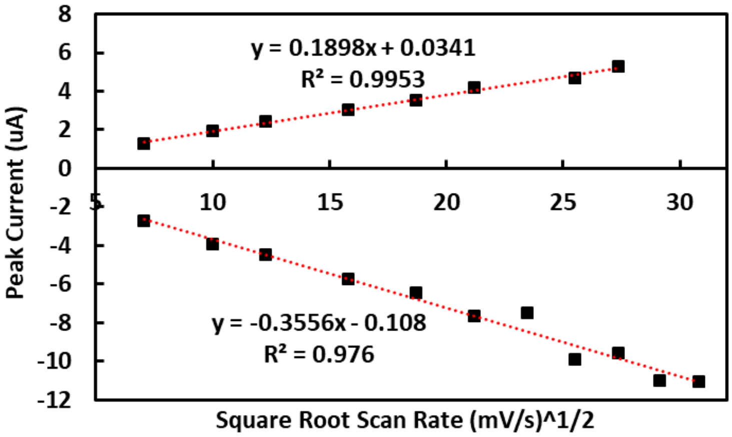

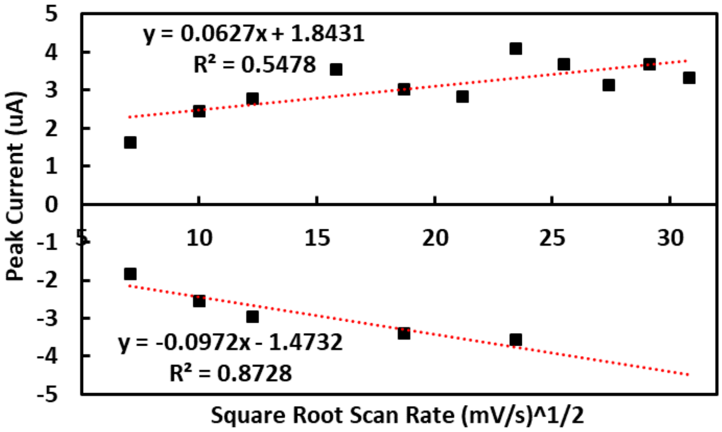

Figure S29: Peak current vs. square root of scan rate for the -1.16 and -0.66 V redox features of [Et$_4$N][Tp*WFe$_3$S$_3$(μ_3-S)Cl$_3$] **(5)**.

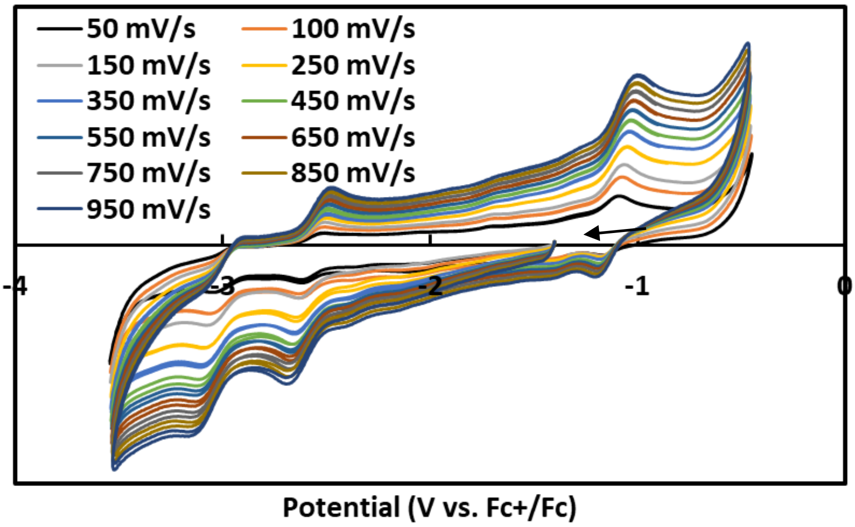

Figure S30: Cyclic voltammetry of $[Et_4N][Tp^*WFe_3S_3(\mu_3\text{-}S)Cl_3]$ **(5)** at different scan rates.

Conditions: 250 mV/s, 2.5 mM cluster, DMF, 0.1 M $TBAPF_6$.

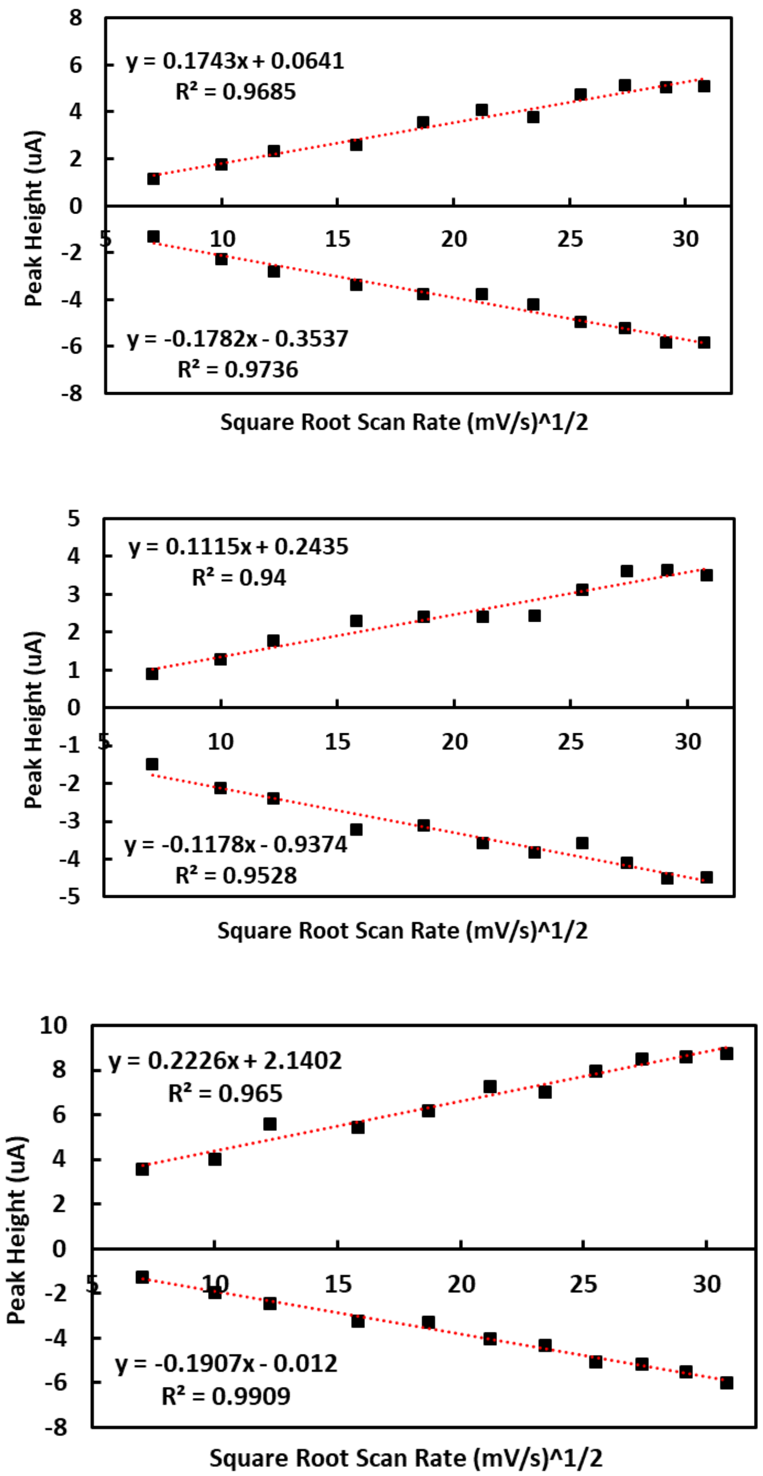

Figure S31: Peak current vs. square root of scan rate for the -1.10, -2.56 and -2.99 V redox features of [Et_4N][$Tp^*WFe_3S_3(\mu_3\text{-}S)Cl_3$] **(5)**.

Electron Paramagnetic Resonance (EPR) Data

General

Samples were prepared as solutions (c.a. 1 mM) and rapidly cooled in liquid nitrogen to form a frozen glass. All X-band CW-EPR experiments presented in this study were acquired at the Caltech EPR facility. X-band CW EPR spectra were acquired on a Bruker (Billerica, MA) EMX spectrometer using Bruker Win-EPR software (ver.3.0). Temperature control was achieved using liquid helium and an Oxford Instruments (Oxford, UK) ESR-900 cryogen flow cryostat and an ITC-503 temperature controller. Data were collected at T = 5 K. Spectra were simulated using EasySpin8(release 5.2.33) with Matlab R2020b.

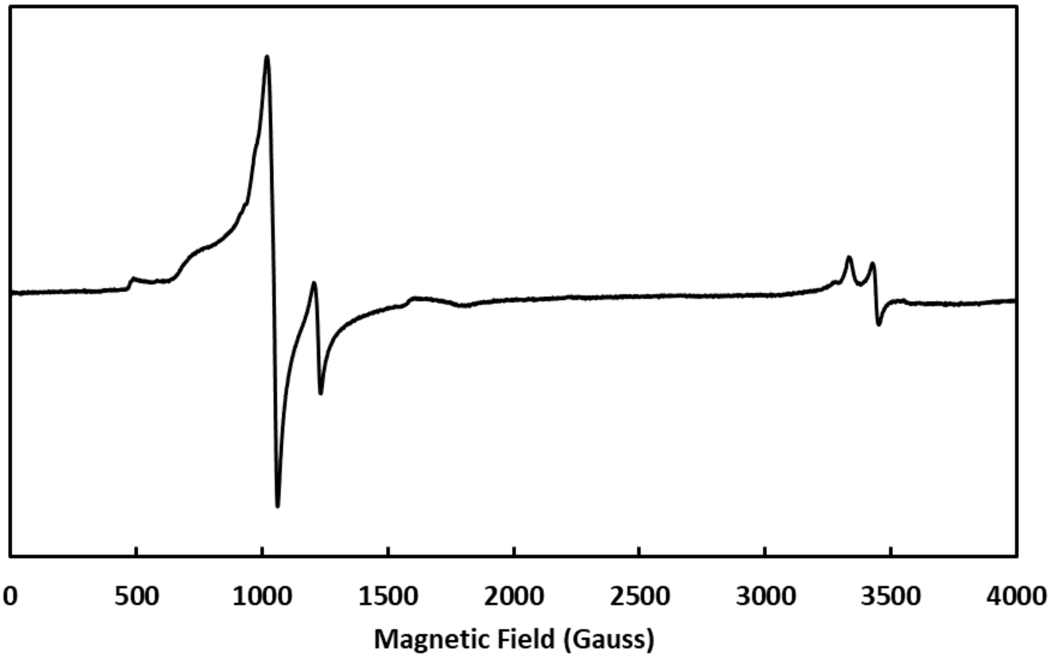

Figure S32: EPR spectrum of [Et_4N][$Tp^*WFe_3S_3(CH_3SiMe_3)_3$] (**2**) in 2-MeTHF. Data acquisition parameters: frequency = 9.6390 MHz, power = 2 mW, conversion time = 10.12 ms, and modulation amplitude = 8 G.

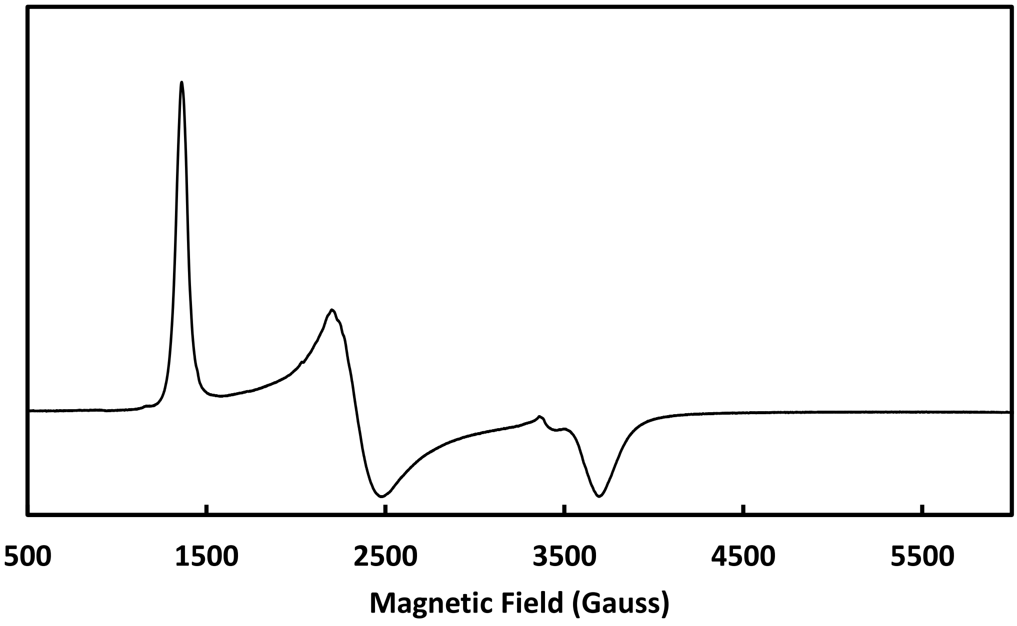

Figure S33: EPR spectrum of $[Et_4N]_2[Tp^*WFe_3S_3(\mu_3\text{-}CSiMe_3)Cl_3]$ **(4)** in DMF Data acquisition parameters: frequency = 9.6375 MHz, power = 2 mW, conversion time = 10.12 ms, and modulation amplitude = 8 G.

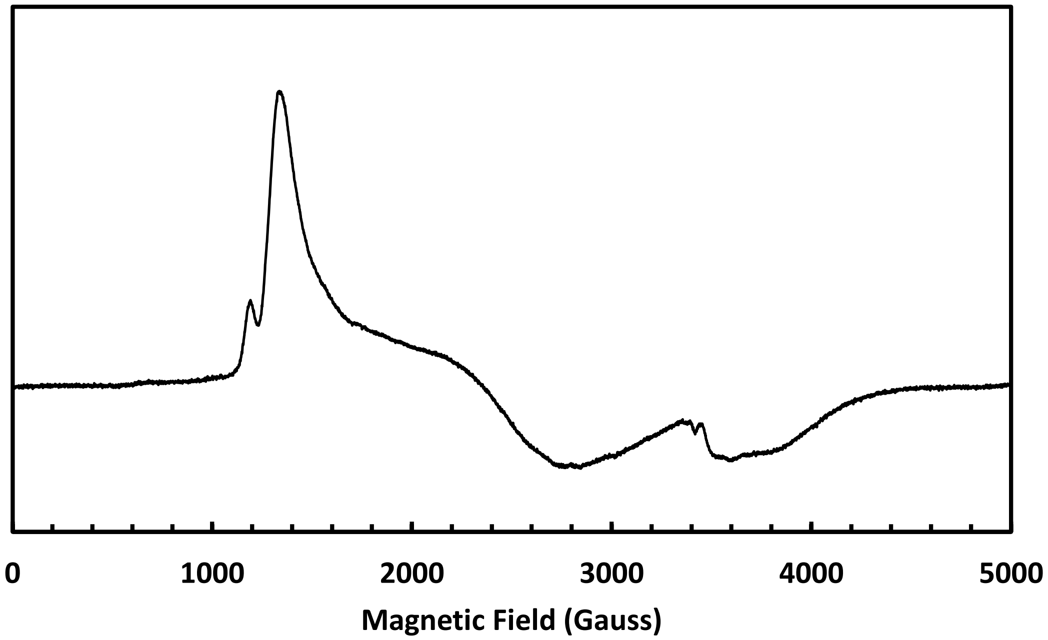

Figure S34: EPR spectra of $[Et_4N]_2[Tp^*MoFe_3S_3(\mu_3\text{-}CSiMe_3)Cl_3]$ **(3-Mo)** in DMF black. Data acquisition parameters, respectively: frequency = 9.6371 MHz, power = 2 mW, conversion time = 10.12 ms, and modulation amplitude = 8 G.

X-ray Crystallography Data

General

XRD data were collected at 100 K on a Bruker AXS D8 KAPPA or Bruker AXS D8 VENTURE diffractometer [microfocus sealed X-ray tube, λ(Mo Kα) = 0.71073 Å or λ(Cu Kα) = 1.54178 Å]. All manipulations, including data collection, integration, and scaling, were carried out using the Bruker APEX3 software.[101] Absorption corrections were applied using SADABS.[102] Structures were solved by direct methods using XS(incorporated into SHELXTL),[103] Sir92[104] or SUPERFLIP[105] and refined using full-matrix least-squares on Olex2[106] to convergence. All non-H atoms were refined using anisotropic displacement parameters. H atoms were placed in idealized positions and refined using a riding model.

Cluster	**2**	**4**	**6**
CCDC	2170937	2218658	2218656
Empirical formula	$C_{35}H_{75}BFe_3N_7S_3WSi3$	$C_{40}H_{82}BCl_3O_2Fe_3N_{10}S_3WSi$	$C_{27}H_{51}BCl_3Fe_3N_7S_3WSi$
Formula weight	1136.68	1316.68	1066.57
Temperature/K	100	100	100
Crystal system	Orthorhombic	Triclinic	Monoclinic
Space group	$P2_12_12_1$	P-1	$P2_1/c$
a/Å	10.5856(15)	10.7345(6)	10.7565(5)
b/Å	18.200(2)	15.6406(9)	19.0986(9)
c/Å	26.002(4)	17.7292(10)	19.3433(9)
α/°	90	84.975(3)	90
β/°	90	80.136(3)	90.878(2)
γ/°	90	80.913(3)	90
Volume/Å^3	5009.5(12)	2890.2(3)	3973.3(2)
Z	4	2	4
ρ_{calc}/g cm^{-3}	1.507	1.513	1.783
μ/mm^{-1}	3.369	12.300	17.679
F(000)	2324	1345	2128
Crystal size/mm^3	0.10 × 0.25 × 0.35	0.03 × 0.08 × 0.14	0.05 × 0.05 × 0.37
Radiation	Mo Kα	Cu Kα	Cu Kα
θ_{max}/°	37.42	72.72	72.40

Index ranges	$-17 \leq h \leq 18$ $-24 \leq k \leq 31$ $-38 \leq l \leq 44$	$-13 \leq h \leq 13$ $-19 \leq k \leq 19$ $-21 \leq l \leq 21$	$-13 \leq h \leq 13$ $-23 \leq k \leq 23$ $-23 \leq l \leq 23$
Reflections measured	26456	59466	41043
Independent reflections	9865	9901	9943
Restraints/Parameters	0/498	145/761	0/428
GOF on F^2	0.893	1.077	1.139
R-factor	0.0391	0.0355	0.0305
Weighted R-factor	0.0611	0.0880	0.0764
Largest diff. peak/hole/e Å^{-3}	2.144/-1.359	2.008/-1.377	1.159/-1.154

Cluster	**2-Mo**	**6-Mo**	**4-Mo**
CCDC			
Empirical formula	$C_{35}H_{75}BFe_3N_7S_3MoSi_3$	C27H51BFe3Cl$_3$N7 S3MoSi	$C_{35}H_{54}BO_4Fe_3N_6S_3MoCl_3Si$
Formula weight	1048.77	978.66	1134.75
Temperature/K	100	100	100
Crystal system	Orthorhombic	Monoclinic	Monoclinic
Space group	$P2_12_12_1$	P1 21/c 1	P1 21/c 1
a/Å	10.608(2)	10.7686(5)	10.5432(7)
b/Å	18.143(4)	19.1042(8)	19.0099(15)
c/Å	26.105(5)	19.3386(9)	24.6318(17)
α/°	90	90	90
β/°	90	90.852(2)	93.975(4)
γ/°	90	90	90
Volume/Å^3	5023.9(17)	3978.0(3)	4925.0(6)
Z	4	4	4
ρ_{calc}/g cm^{-3}	1.387	1.634	1.530
μ/mm^{-1}	10.897	14.974	12.238
F(000)	2196	2000	2316
Crystal size/mm^3	0.03 × 0.13 × 0.17	0.02 × 0.14 × 0.3	0.1 × 0.2 × 0.3
Radiation	Cu Kα	Cu Kα	Cu Kα
θ_{max}/°	72.287	72.441	72.399
Index ranges	$-13 \leq h \leq 13$ $-22 \leq k \leq 32$ $-32 \leq l \leq 32$	$-13 \leq h \leq 13$ $-23 \leq k \leq 23$ $-22 \leq l \leq 23$	$-12 \leq h \leq 13$ $-23 \leq k \leq 22$ $-30 \leq l \leq 20$
Reflections measured	75346	48732	65928
Independent reflections	9886	9239	9377
Restraints/Parameters	0/498	0/428	0/607
GOF on F^2	1.074	1.122	1.085
R-factor	0.0528	0.0326	0.0301
Weighted R-factor	0.1222	0.0794	0.0683

Largest diff. peak/hole/e Å^{-3}	2.989/-1.422	1.093/-0.891	0.511/-0.552

Cluster	**7-Mo**	**9-Mo**	**10-Mo**
CCDC			
Empirical formula	$C_{50}H_{77}BCl_{0.64}Fe_3N_7S_3MoSi_3$	$C_{44}H_{66}BFe_3Cl_3N6O_{0.25}S_3MoSi$	$C_{49.5}H_{65}BOFe_3N_7S_3MoCl_3Si$
Formula weight	1253.62	1187.94	1278.97
Temperature/K	100	100	100
Crystal system	Triclinic	Monoclinic	Triclinic
Space group	P-1	P1 21/c 1	P-1
a/Å	12.6473(5)	10.7242(5)	14.2551(6)
b/Å	14.5256(5)	23.3175(11)	14.8064(6)
c/Å	18.9101(6)	19.4691(9)	14.8327(6)
α/°	104.4540(10)	90	113.653(2)
β/°	92.014(2)	103.921(2)	101.507(2)
γ/°	115.4980(10)	90	92.616(2)
Volume/Å^3	2995.67(19)	4725.5(4)	2782.4(2)
Z	2	4	2
ρ_{calc}/g cm^{-3}	1.390	1.670	1.527
μ/mm^{-1}	9.494	12.727	10.872
F(000)	1304	2448	1314
Crystal size/mm^3	0.05 × 0.19 × 0.28	0.02 × 0.08 × 0.13	0.02 × 0.07 × 0.18
Radiation	Mo Kα	Cu Kα	Cu Kα
θ_{max}/°	67.679	72.703	72.48
Index ranges	$-15 \leq h \leq 15$ $-17 \leq k \leq 17$ $-23 \leq l \leq 23$	$-13 \leq h \leq 13$ $-28 \leq k \leq 28$ $-23 \leq l \leq 24$	$-17 \leq h \leq 17$ $-15 \leq k \leq 18$ $-18 \leq l \leq 18$
Reflections measured	50634	63821	53452
Independent reflections	9072	9767	9707
Restraints/Parameters	0/724	0/540	24/687
GOF on F^2	1.039	1.091	1.024
R-factor	0.0503	0.0623	0.0251
Weighted R-factor	0.1174	0.1489	0.0580
Largest diff. peak/hole/e Å^{-3}	2.265/-1.039	1.476/-2.068	0.636/-0.565

Cluster	**11**	**12-Mo**
CCDC		
Empirical formula	$C_{44}H_{66}BCl_3Fe_3N_8S_3WSi$	$C_{34.5}H_{52}B_{0.5}Fe_{1.5}Cl_{1.5}{}^{F}N_{5.5}O_{0.25}S_{1.5}Mo_{0.5}$
Formula weight	1304.25	801.08
Temperature/K	100	100
Crystal system	Monoclinic	Triclinic
Space group	C1 2/c 1	P-1
a/Å	23.991(9)	16.031(3)
b/Å	40.428(17)	19.711(3)
c/Å	15.477(6)	25.366(4)
α/°	90	93.289(10)
β/°	121.029(14)	99.654(9)
γ/°	90	91.004(14)
Volume/Å^3	12863(9)	7886(2)
Z	8	8
ρ_{calc}/g cm^{-3}	1.347	1.349
μ/mm^{-1}	2.720	7.682
F(000)	5265	3346
Crystal size/mm^3	0.05 × 0.1 × 0.25	0.2 × 0.2 × 0.1
Radiation	Mo Kα	Cu Kα
θ_{max}/°	35.641	72.52
Index ranges	$-32 \leq h \leq 39$ $-66 \leq k \leq 65$ $-25 \leq l \leq 25$	$-19 \leq h \leq 19$ $-24 \leq k \leq 24$ $-26 \leq l \leq 31$
Reflections measured	146453	81085
Independent reflections	9714	9508
Restraints/Parameters	3/544	0/1714
GOF on F^2	1.036	1.098
R-factor	0.0453	0.1091
Weighted R-factor	0.1136	0.2199
Largest diff. peak/hole/e Å^{-3}	2.298/-1.307	2.077/-1.443

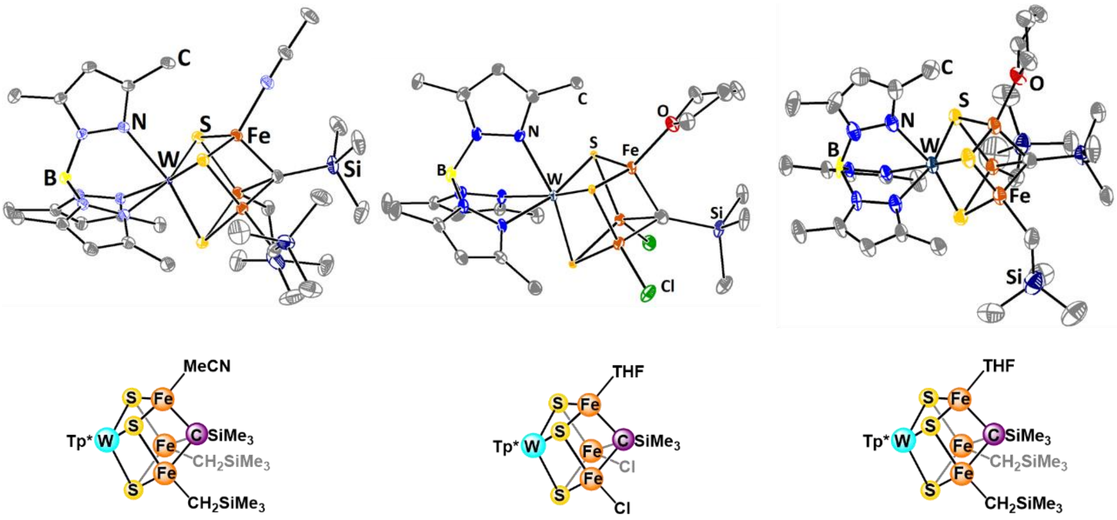

13 **14** **15**

Figure S35: Crystal structures (top) and ChemDraws (bottom) of isolated products from reactions of [Et$_4$N][Tp*WFe$_3$S$_3$(CH$_2$SiMe$_3$)$_3$] (**2**) with AgOTf (left and middle) or [N(4-BrPh)$_3$][OTf] (right): Tp*WFe$_3$S$_3$(μ$_3$-CSiMe$_3$)(CH$_2$SiMe$_3$)$_2$(CH$_3$CN) (**13**, left), Tp*WFe$_3$S$_3$(μ$_3$-CSiMe$_3$)Cl$_2$(THF) (**14**, middle), and Tp*WFe$_3$S$_3$(μ$_3$-CSiMe$_3$)(CH$_2$SiMe$_3$)$_2$(THF) (**15**, right). Ellipsoids plotted at the 50% probability level. Solvent and hydrogen atoms omitted for clarity.

References

(1) Wang, C.-H.; DeBeer, S. Structure, Reactivity, and Spectroscopy of Nitrogenase-Related Synthetic and Biological Clusters. *Chemical Society Reviews* **2021**, *50* (15), 8743–8761. https://doi.org/10.1039/D1CS00381J.

(2) Zhang, B.; Sun, L. Artificial Photosynthesis: Opportunities and Challenges of Molecular Catalysts. *Chemical Society Reviews* **2019**, *48* (7), 2216–2264. https://doi.org/10.1039/C8CS00897C.

(3) Schilter, D.; Camara, J. M.; Huynh, M. T.; Hammes-Schiffer, S.; Rauchfuss, T. B. Hydrogenase Enzymes and Their Synthetic Models: The Role of Metal Hydrides. *Chem. Rev.* **2016**, *116* (15), 8693–8749. https://doi.org/10.1021/acs.chemrev.6b00180.

(4) Spatzal, T.; Aksoyoglu, M.; Zhang, L.; Andrade, S. L. A.; Schleicher, E.; Weber, S.; Rees, D. C.; Einsle, O. Evidence for Interstitial Carbon in Nitrogenase FeMo Cofactor. *Science* **2011**, *334* (6058), 940–940. https://doi.org/10.1126/science.1214025.

(5) Jasniewski, A. J.; Lee, C. C.; Ribbe, M. W.; Hu, Y. Reactivity, Mechanism, and Assembly of the Alternative Nitrogenases. *Chem. Rev.* **2020**. https://doi.org/10.1021/acs.chemrev.9b00704.

(6) Eady, R. R. Structure-Function Relationships of Alternative Nitrogenases. *Chemical Reviews* **1996**, *96* (7), 3013–3030. https://doi.org/10.1021/cr950057h.

(7) Burén, S.; Jiménez-Vicente, E.; Echavarri-Erasun, C.; Rubio, L. M. Biosynthesis of Nitrogenase Cofactors. *Chem. Rev.* **2020**, *120* (12), 4921–4968. https://doi.org/10.1021/acs.chemrev.9b00489.

(8) Lee, S. C.; Lo, W.; Holm, R. Developments in the Biomimetic Chemistry of Cubane-Type and Higher Nuclearity Iron–Sulfur Clusters. *Chemical reviews* **2014**, *114* (7), 3579–3600.

(9) Coucouvanis, D.; Al-Ahmad, S. A.; Salifoglou, A.; Papaefthymiou, V.; Kostikas, A.; Simopoulos, A. Synthesis, Characterization, and Reactivity of New Clusters That Contain the [MFe3S4]0 Core, M = Molybdenum, Tungsten. A Weakly Perturbed [MFe3S4]0 Unit Structurally and Electronically Analogous to the Reduced Three-Ion Centers in Ferredoxins. *J. Am. Chem. Soc.* **1992**, *114* (7), 2472–2482. https://doi.org/10.1021/ja00033a023.

(10) Tanifuji, K.; Ohki, Y. Metal–Sulfur Compounds in N2 Reduction and Nitrogenase-Related Chemistry. *Chem. Rev.* **2020**, *120* (12), 5194–5251. https://doi.org/10.1021/acs.chemrev.9b00544.

(11) Stack, T. D. P.; Weigel, J. A.; Holm, R. H. The Cavitand Concept in the Synthesis of Subsite-Differentiated Analogs of Biological [4Fe-4S/Se]2+ Clusters: Cluster Capture Reactions, Ligand Conformational Analysis, and the Structure of a Trigonal [4Fe-4Se]2+ Analog. *Inorg. Chem.* **1990**, *29* (19), 3745–3760. https://doi.org/10.1021/ic00344a022.

(12) He, J.; Wei, J.; Xu, G.; Chen, X.-D. Stepwise Construction of Mo–Fe–S Clusters Using a LEGO Strategy. *Inorg. Chem.* **2022**, *61* (9), 4150–4158. https://doi.org/10.1021/acs.inorgchem.1c03998.

(13) Gibney, B. R.; Rabanal, F.; Dutton, P. L. Synthesis of Novel Proteins. *Current Opinion in Chemical Biology* **1997**, *1* (4), 537–542. https://doi.org/10.1016/S1367-5931(97)80050-6.

(14) Henderson, R. A. Mechanistic Studies on Synthetic Fe−S-Based Clusters and Their Relevance to the Action of Nitrogenases. *Chem. Rev.* **2005**, *105* (6), 2365–2438. https://doi.org/10.1021/cr030706m.

(15) Koay, M. S.; Antonkine, M. L.; Gärtner, W.; Lubitz, W. Modelling Low-Potential [Fe4S4] Clusters in Proteins. *Chemistry & Biodiversity* **2008**, *5* (8), 1571–1587. https://doi.org/10.1002/cbdv.200890145.

(16) Brown, A. C.; Suess, D. L. M. 8.08 - Synthetic Iron-Sulfur Clusters. In *Comprehensive Coordination Chemistry III*; Constable, E. C., Parkin, G., Que Jr, L., Eds.; Elsevier: Oxford, 2021; pp 134–156. https://doi.org/10.1016/B978-0-08-102688-5.00053-2.

(17) Ohta, S.; Ohki, Y.; Hashimoto, T.; Cramer, R. E.; Tatsumi, K. A Nitrogenase Cluster Model [Fe8S6O] with an Oxygen Unsymmetrically Bridging Two Proto-Fe4S3 Cubes: Relevancy to the Substrate Binding Mode of the FeMo Cofactor. *Inorg. Chem.* **2012**, *51* (21), 11217–11219. https://doi.org/10.1021/ic301348f.

(18) Ohki, Y.; Sunada, Y.; Honda, M.; Katada, M.; Tatsumi, K. Synthesis of the P-Cluster Inorganic Core of Nitrogenases. *J. Am. Chem. Soc.* **2003**, *125* (14), 4052–4053. https://doi.org/10.1021/ja029383m.

(19) Ohki, Y.; Ikagawa, Y.; Tatsumi, K. Synthesis of New [8Fe-7S] Clusters: A Topological Link between the Core Structures of P-Cluster, FeMo-Co, and FeFe-Co of Nitrogenases. *J. Am. Chem. Soc.* **2007**, *129* (34), 10457–10465. https://doi.org/10.1021/ja072256b.

(20) Ohki, Y.; Imada, M.; Murata, A.; Sunada, Y.; Ohta, S.; Honda, M.; Sasamori, T.; Tokitoh, N.; Katada, M.; Tatsumi, K. Synthesis, Structures, and Electronic Properties of [8Fe-7S] Cluster Complexes Modeling the Nitrogenase P-Cluster. *J. Am. Chem. Soc.* **2009**, *131* (36), 13168–13178. https://doi.org/10.1021/ja9055036.

(21) Liu, L.; Rauchfuss, T. B.; Woods, T. J. Iron Carbide–Sulfide Carbonyl Clusters. *Inorg. Chem.* **2019**, *58* (13), 8271–8274. https://doi.org/10.1021/acs.inorgchem.9b01231.

(22) Joseph, C.; Cobb, C. R.; Rose, M. J. Single-Step Sulfur Insertions into Iron Carbide Carbonyl Clusters: Unlocking the Synthetic Door to FeMoco Analogues. *Angewandte Chemie International Edition* **2021**, *60* (7), 3433–3437. https://doi.org/10.1002/anie.202011517.

(23) Reesbeck, M. E.; Grubel, K.; Kim, D.; Brennessel, W. W.; Mercado, B. Q.; Holland, P. L. Diazoalkanes in Low-Coordinate Iron Chemistry: Bimetallic Diazoalkyl and Alkylidene Complexes of Iron (II). *Inorganic chemistry* **2017**, *56* (3), 1019–1022.

(24) Arnett, C. H.; Agapie, T. Activation of an Open Shell, Carbyne-Bridged Diiron Complex Toward Binding of Dinitrogen. *J. Am. Chem. Soc.* **2020**, *142* (22), 10059–10068. https://doi.org/10.1021/jacs.0c01896.

(25) Arnett, C. H.; Bogacz, I.; Chatterjee, R.; Yano, J.; Oyala, P. H.; Agapie, T. Mixed-Valent Diiron μ-Carbyne, μ-Hydride Complexes: Implications for Nitrogenase. *J. Am. Chem. Soc.* **2020**, *142* (44), 18795–18813. https://doi.org/10.1021/jacs.0c05920.

(26) Kienast, A.; Galich, L.; Murray, K. S.; Moubaraki, B.; Lazarev, G.; Cashion, J. D.; Homborg, H. μ-Carbido Diporphyrinates and Diphthalocyaninates of Iron and Ruthenium. *J. Porphyrins Phthalocyanines* **1997**, *01* (02), 141–157. https://doi.org/10.1002/(SICI)1099-1409(199704)1:2<141::AID-JPP18>3.0.CO;2-M.

(27) Churchill, M. R.; Wormald, J.; Knight, J.; Mays, M. J. Synthesis and Crystallographic Characterization of Bis(Tetramethylammonium) Carbidohexadecacarbonylhexaferrate, a Hexanuclear Carbidocarbonyl Derivative of Iron. *J. Am. Chem. Soc.* **1971**, *93* (12), 3073–3074. https://doi.org/10.1021/ja00741a058.

(28) Braye, E. H.; Dahl, L. F.; Hubel, Walter.; Wampler, D. L. The Preparation, Properties and Structure of the Iron Carbonyl Carbide Fe5(CO)15C. *J. Am. Chem. Soc.* **1962**, *84* (24), 4633–4639. https://doi.org/10.1021/ja00883a004.

(29) Wiig, J. A.; Hu, Y.; Lee, C. C.; Ribbe, M. W. Radical SAM-Dependent Carbon Insertion into the Nitrogenase M-Cluster. *Science* **2012**, *337* (6102), 1672–1675. https://doi.org/10.1126/science.1224603.

(30) Wiig, J. A.; Hu, Y.; Ribbe, M. W. NifEN-B Complex of Azotobacter Vinelandii Is Fully Functional in Nitrogenase FeMo Cofactor Assembly. *PNAS* **2011**, *108* (21), 8623–8627. https://doi.org/10.1073/pnas.1102773108.

(31) Rettberg, L. A.; Wilcoxen, J.; Lee, C. C.; Stiebritz, M. T.; Tanifuji, K.; Britt, R. D.; Hu, Y. Probing the Coordination and Function of Fe4S4 Modules in Nitrogenase Assembly Protein NifB. *Nat Commun* **2018**, *9* (1), 2824. https://doi.org/10.1038/s41467-018-05272-8.

(32) Wiig, J. A.; Hu, Y.; Ribbe, M. W. Refining the Pathway of Carbide Insertion into the Nitrogenase M-Cluster. *Nat Commun* **2015**, *6* (1), 8034. https://doi.org/10.1038/ncomms9034.

(33) Fay, A. W.; Wiig, J. A.; Lee, C. C.; Hu, Y. Identification and Characterization of Functional Homologs of Nitrogenase Cofactor Biosynthesis Protein NifB from Methanogens. *PNAS* **2015**, *112* (48), 14829–14833. https://doi.org/10.1073/pnas.1510409112.

(34) Wilcoxen, J.; Arragain, S.; Scandurra, A. A.; Jimenez-Vicente, E.; Echavarri-Erasun, C.; Pollmann, S.; Britt, R. D.; Rubio, L. M. Electron Paramagnetic Resonance Characterization of Three Iron–Sulfur Clusters Present in the Nitrogenase Cofactor Maturase NifB from Methanocaldococcus Infernus. *J. Am. Chem. Soc.* **2016**, *138* (24), 7468–7471. https://doi.org/10.1021/jacs.6b03329.

(35) Le, L. N. V.; Bailey, G. A.; Scott, A. G.; Agapie, T. Partial Synthetic Models of FeMoco with Sulfide and Carbyne Ligands: Effect of Interstitial Atom in Nitrogenase Active Site. *PNAS* **2021**, *118* (49), e2109241118. https://doi.org/10.1073/pnas.2109241118.

(36) Mindiola, D. J.; Bailey, B. C.; Basuli, F. What a Difference One Electron Makes! Generating Low-Coordinate Ti–C and V–C Multiply Bonded Frameworks through One Electron Oxidatively Induced α-Hydrogen Abstractions. *European Journal of Inorganic Chemistry* **2006**, *2006* (16), 3135–3146. https://doi.org/10.1002/ejic.200600316.

(37) Mindiola, D. J. Oxidatively Induced Abstraction Reactions. A Synthetic Approach to Low-Coordinate and Reactive Early Transition Metal Complexes Containing Metal−Ligand Multiple Bonds. *Acc. Chem. Res.* **2006**, *39* (11), 813–821. https://doi.org/10.1021/ar0500113.

(38) Brown, A. C.; Suess, D. L. M. Reversible Formation of Alkyl Radicals at [Fe4S4] Clusters and Its Implications for Selectivity in Radical SAM Enzymes. *J. Am. Chem. Soc.* **2020**, *142* (33), 14240–14248. https://doi.org/10.1021/jacs.0c05590.

(39) Ye, M.; Thompson, N. B.; Brown, A. C.; Suess, D. L. M. A Synthetic Model of Enzymatic [Fe4S4]–Alkyl Intermediates. *J. Am. Chem. Soc.* **2019**, *141* (34), 13330–13335. https://doi.org/10.1021/jacs.9b06975.

(40) McSkimming, A.; Sridharan, A.; Thompson, N. B.; Müller, P.; Suess, D. L. M. An [Fe4S4]3+–Alkyl Cluster Stabilized by an Expanded Scorpionate Ligand. *J. Am. Chem. Soc.* **2020**, *142* (33), 14314–14323. https://doi.org/10.1021/jacs.0c06334.

(41) Muñoz, S. B.; Daifuku, S. L.; Brennessel, W. W.; Neidig, M. L. Isolation, Characterization, and Reactivity of Fe8Me12 –: Kochi's S = 1/2 Species in Iron-Catalyzed Cross-Couplings with MeMgBr and Ferric Salts. *J. Am. Chem. Soc.* **2016**, *138* (24), 7492–7495. https://doi.org/10.1021/jacs.6b03760.

(42) Ohki, Y.; Murata, A.; Imada, M.; Tatsumi, K. C−H Bond Activation of Decamethylcobaltocene Mediated by a Nitrogenase Fe8S7 P-Cluster Model. *Inorg. Chem.* **2009**, *48* (10), 4271–4273. https://doi.org/10.1021/ic900284f.

(43) Xu, G.; Wang, Z.; Ling, R.; Zhou, J.; Chen, X.-D.; Holm, R. H. Ligand Metathesis as Rational Strategy for the Synthesis of Cubane-Type Heteroleptic Iron–Sulfur Clusters Relevant to the FeMo Cofactor. *Proceedings of the National Academy of Sciences* **2018**, *115* (20), 5089–5092.

(44) Xu, G.; Zhou, J.; Wang, Z.; Holm, R. H.; Chen, X.-D. Controlled Incorporation of Nitrides into W-Fe-S Clusters. *Angewandte Chemie International Edition* **2019**, *58* (46), 16469–16473.

(45) Schrock, R. R. Alkylcarbene Complex of Tantalum by Intramolecular. Alpha.-Hydrogen Abstraction. *Journal of the American Chemical Society* **1974**, *96* (21), 6796–6797.

(46) Mowat, W.; Wilkinson, G. Elimination Stabilized Alkyls. Part III. Trimethylsilylmethyl and Neopentyl Alkyls of Transition Metals. *J. Chem. Soc., Dalton Trans.* **1973**, No. 10, 1120–1124. https://doi.org/10.1039/DT9730001120.

(47) Bjornsson, R.; A. Lima, F.; Spatzal, T.; Weyhermüller, T.; Glatzel, P.; Bill, E.; Einsle, O.; Neese, F.; DeBeer, S. Identification of a Spin-Coupled Mo(Iii) in the Nitrogenase Iron–Molybdenum Cofactor. *Chemical Science* **2014**, *5* (8), 3096–3103. https://doi.org/10.1039/C4SC00337C.

(48) *The redox features for the sulfide bridged analogue [Et4N][Tp*WFe3S3(μ3-S)Cl3] (5) are only separated by 500 mV, small compared to other WFeS clusters, where the separation is generally greater than 1 V.33 Only the reductive redox feature for [Et4N][Tp*WFe3S3(μ3-S)Cl3] (5) is reported in the original literature report (-1.17 V v. Fc/Fc+, MeCN).48 In dichloromethane the separation be-tween redox features increases to 760 mV (Fig. S14) sug-gesting a solvent effect potentially involving halide sol-vent coordination.*

(49) Hauser, C.; Bill, E.; Holm, R. H. Single- and Double-Cubane Clusters in the Multiple Oxidation States [VFe3S4]3+,2+,1+. *Inorg. Chem.* **2002**, *41* (6), 1615–1624. https://doi.org/10.1021/ic011011b.

(50) Solomon, E. I.; Ginsbach, J. W.; Kroll, T.; Liu, L. V.; Pierce, E. M.; Qayyum, M. F. 3.20 - Spectroscopic Methods for Understanding Metals in Proteins. In *Comprehensive Inorganic Chemistry II (Second Edition)*; Reedijk, J., Poeppelmeier, K., Eds.; Elsevier: Amsterdam, 2013; pp 595–622. https://doi.org/10.1016/B978-0-08-097774-4.00326-0.

(51) Meyer, J. Ferredoxins of the Third Kind. *FEBS Letters* **2001**, *509* (1), 1–5. https://doi.org/10.1016/S0014-5793(01)03049-6.

(52) Beinert, H.; Holm, R. H.; Münck, E. Iron-Sulfur Clusters: Nature's Modular, Multipurpose Structures. *Science* **1997**, *277* (5326), 653–659.

(53) Crouse, B. R.; Meyer, J.; Johnson, M. K. Spectroscopic Evidence for a Reduced Fe2S2 Cluster with a S = 9/2 Ground State in Mutant Forms of Clostridium

Pasteurianum 2Fe Ferredoxin. *J. Am. Chem. Soc.* **1995**, *117* (37), 9612–9613. https://doi.org/10.1021/ja00142a049.

(54) Achim, C.; Golinelli, M.-P.; Bominaar, E. L.; Meyer, J.; Münck, E. Mössbauer Study of Cys56Ser Mutant 2Fe Ferredoxin from Clostridium Pasteurianum: Evidence for Double Exchange in an [Fe2S2]+ Cluster. *J. Am. Chem. Soc.* **1996**, *118* (34), 8168–8169. https://doi.org/10.1021/ja9617698.

(55) Johnson, D. C.; Dean, D. R.; Smith, A. D.; Johnson, M. K. Structure, Function, and Formation of Biological Iron-Sulfur Clusters. *Annual Review of Biochemistry* **2005**, *74* (1), 247–281. https://doi.org/10.1146/annurev.biochem.74.082803.133518.

(56) Van Stappen, C.; Decamps, L.; Cutsail, G. E.; Bjornsson, R.; Henthorn, J. T.; Birrell, J. A.; DeBeer, S. The Spectroscopy of Nitrogenases. *Chem. Rev.* **2020**. https://doi.org/10.1021/acs.chemrev.9b00650.

(57) Gamelin, D. R.; Bominaar, E. L.; Kirk, M. L.; Wieghardt, K.; Solomon, E. I. Excited-State Contributions to Ground-State Properties of Mixed-Valence Dimers: Spectral and Electronic-Structural Studies of [Fe2(OH)3(Tmtacn)2]2+ Related to the [Fe2S2]+ Active Sites of Plant-Type Ferredoxins. *J. Am. Chem. Soc.* **1996**, *118* (34), 8085–8097. https://doi.org/10.1021/ja9536633.

(58) Ding, X.; Bominaar, E. L.; Bill, E.; Winkler, H.; Trautwein, A. X.; Drüeke, S.; Chaudhuri, P.; Wieghardt, K. Mössbauer and Electron Paramagnetic Resonance Study of the Double-exchange and Heisenberg-exchange Interactions in a Novel Binuclear Fe(II/III) Delocalized-valence Compound. *The Journal of Chemical Physics* **1990**, *92* (1), 178–186. https://doi.org/10.1063/1.458460.

(59) Hazra, S.; Sasmal, S.; Fleck, M.; Grandjean, F.; Sougrati, M. T.; Ghosh, M.; Harris, T. D.; Bonville, P.; Long, G. J.; Mohanta, S. Slow Magnetic Relaxation and Electron Delocalization in an S = 9/2 Iron(II/III) Complex with Two Crystallographically Inequivalent Iron Sites. *The Journal of Chemical Physics* **2011**, *134* (17), 174507. https://doi.org/10.1063/1.3581028.

(60) Henthorn, J. T.; Cutsail, G. E.; Weyhermüller, T.; DeBeer, S. Stabilization of Intermediate Spin States in Mixed-Valent Diiron Dichalcogenide Complexes. *Nat. Chem.* **2022**, *14* (3), 328–333. https://doi.org/10.1038/s41557-021-00853-5.

(61) Hagen, W. R. EPR Spectroscopy of Iron—Sulfur Proteins. In *Advances in Inorganic Chemistry*; Cammack, R., Ed.; Academic Press, 1992; Vol. 38, pp 165–222. https://doi.org/10.1016/S0898-8838(08)60064-1.

(62) Noodleman, L.; Peng, C. Y.; Case, D. A.; Mouesca, J.-M. Orbital Interactions, Electron Delocalization and Spin Coupling in Iron-Sulfur Clusters. *Coordination Chemistry Reviews* **1995**, *144*, 199–244. https://doi.org/10.1016/0010-8545(95)07011-L.

(63) Noodleman, L.; Case, D. A.; Mouesca, J.-M.; Lamotte, B. Valence Electron Delocalization in Polynuclear Iron-Sulfur Clusters. *JBIC* **1996**, *1* (2), 177–182. https://doi.org/10.1007/s007750050039.

(64) Hans, M.; Buckel, W.; Bill, E. The Iron–Sulfur Clusters in 2-Hydroxyglutaryl-CoA Dehydratase from Acidaminococcus Fermentans. *European Journal of Biochemistry* **2000**, *267* (24), 7082–7093. https://doi.org/10.1046/j.1432-1327.2000.01809.x.

(65) Angove, H. C.; Yoo, S. J.; Münck, E.; Burgess, B. K. An All-Ferrous State of the Fe Protein of Nitrogenase: INTERACTION WITH NUCLEOTIDES AND ELECTRON TRANSFER TO THE MoFe PROTEIN *. *Journal of Biological Chemistry* **1998**, *273* (41), 26330–26337. https://doi.org/10.1074/jbc.273.41.26330.

(66) Rupnik, K.; Lee, C. C.; Hu, Y.; Ribbe, M. W.; Hales, B. J. [4Fe4S]2+ Clusters Exhibit Ground-State Paramagnetism. *J Am Chem Soc* **2011**, *133* (18), 6871–6873. https://doi.org/10.1021/ja201384w.

(67) Watt, G. D.; Reddy, K. R. N. Formation of an All Ferrous Fe4S4 Cluster in the Iron Protein Component of Azotobacter Vinelandii Nitrogenase. *Journal of Inorganic Biochemistry* **1994**, *53* (4), 281–294. https://doi.org/10.1016/0162-0134(94)85115-8.

(68) Angove, H. C.; Yoo, S. J.; Burgess, B. K.; Münck, E. Mössbauer and EPR Evidence for an All-Ferrous Fe4S4 Cluster with S = 4 in the Fe Protein of Nitrogenase. *J. Am. Chem. Soc.* **1997**, *119* (37), 8730–8731. https://doi.org/10.1021/ja9712837.

(69) Hans, M.; Buckel, W.; Bill, E. Spectroscopic Evidence for an All-Ferrous [4Fe–4S]0 Cluster in the Superreduced Activator of 2-Hydroxyglutaryl-CoA Dehydratase from Acidaminococcus Fermentans. *J Biol Inorg Chem* **2008**, *13* (4), 563–574. https://doi.org/10.1007/s00775-008-0345-z.

(70) Münck, E.; Rhodes, H.; Orme-Johnson, W. H.; Davis, L. C.; Brill, W. J.; Shah, V. K. Nitrogenase. VIII. Mössbauer and EPR Spectroscopy. The MoFe Protein Component from Azotobacter Vinelandii OP. *Biochimica et Biophysica Acta (BBA) - Protein Structure* **1975**, *400* (1), 32–53. https://doi.org/10.1016/0005-2795(75)90124-5.

(71) Huynh, B. H.; Henzl, M. T.; Christner, J. A.; Zimmermann, R.; Orme-Johnson, W. H.; Münck, E. Nitrogenase XII. Mössbauer Studies of the MoFe Protein from Clostridium Pasteurianum W5. *Biochimica et Biophysica Acta (BBA) - Protein Structure* **1980**, *623* (1), 124–138. https://doi.org/10.1016/0005-2795(80)90015-X.

(72) Smith, J. P.; Emptage, M. H.; Orme-Johnson, W. H. Magnetic Susceptibility Studies of Native and Thionine-Oxidized Molybdenum-Iron Protein from Azotobacter Vinelandii Nitrogenase. *Journal of Biological Chemistry* **1982**, *257* (5), 2310–2313. https://doi.org/10.1016/S0021-9258(18)34923-8.

(73) Johnson, M. K.; Thomson, A. J.; Robinson, A. E.; Smith, B. E. Characterization of the Paramagnetic Centres of the Molybdenum-Iron Protein of Nitrogenase from Klebsiella Pneumoniae Using Low Temperature Magnetic Circular Dichroism Spectroscopy. *Biochimica et Biophysica Acta (BBA) - Protein Structure* **1981**, *671* (1), 61–70. https://doi.org/10.1016/0005-2795(81)90094-5.

(74) Yoo, S. J.; Angove, H. C.; Papaefthymiou, V.; Burgess, B. K.; Münck, E. Mössbauer Study of the MoFe Protein of Nitrogenase from Azotobacter Vinelandii Using Selective 57Fe Enrichment of the M-Centers. *J. Am. Chem. Soc.* **2000**, *122* (20), 4926–4936. https://doi.org/10.1021/ja000254k.

(75) Lovell, T.; Li, J.; Liu, T.; Case, D. A.; Noodleman, L. FeMo Cofactor of Nitrogenase: A Density Functional Study of States MN, MOX, MR, and MI. *J. Am. Chem. Soc.* **2001**, *123* (49), 12392–12410. https://doi.org/10.1021/ja011860y.

(76) Hoffman, B. M.; Lukoyanov, D.; Yang, Z.-Y.; Dean, D. R.; Seefeldt, L. C. Mechanism of Nitrogen Fixation by Nitrogenase: The next Stage. *Chemical reviews* **2014**, *114* (8), 4041–4062.

(77) Seefeldt, L. C.; Yang, Z.-Y.; Lukoyanov, D. A.; Harris, D. F.; Dean, D. R.; Raugei, S.; Hoffman, B. M. Reduction of Substrates by Nitrogenases. *Chem. Rev.* **2020**. https://doi.org/10.1021/acs.chemrev.9b00556.

(78) Dance, I. Computational Investigations of the Chemical Mechanism of the Enzyme Nitrogenase. *ChemBioChem* **2020**, *21* (12), 1671–1709. https://doi.org/10.1002/cbic.201900636.

(79) Burgess, B. K.; Lowe, D. J. Mechanism of Molybdenum Nitrogenase. *Chem. Rev.* **1996**, *96* (7), 2983–3012. https://doi.org/10.1021/cr950055x.

(80) Buscagan, T. M.; Rees, D. C. Rethinking the Nitrogenase Mechanism: Activating the Active Site. *Joule* **2019**, *3* (11), 2662–2678. https://doi.org/10.1016/j.joule.2019.09.004.

(81) Pérez-González, A.; Yang, Z.-Y.; Lukoyanov, D. A.; Dean, D. R.; Seefeldt, L. C.; Hoffman, B. M. Exploring the Role of the Central Carbide of the Nitrogenase Active-Site FeMo-Cofactor through Targeted 13C Labeling and ENDOR Spectroscopy. *J. Am. Chem. Soc.* **2021**, *143* (24), 9183–9190. https://doi.org/10.1021/jacs.1c04152.

(82) Rees, J. A.; Bjornsson, R.; Kowalska, J. K.; Lima, F. A.; Schlesier, J.; Sippel, D.; Weyhermüller, T.; Einsle, O.; Kovacs, J. A.; DeBeer, S. Comparative Electronic Structures of Nitrogenase FeMoco and FeVco. *Dalton Transactions* **2017**, *46* (8), 2445–2455.

(83) Carney, M. J.; Kovacs, J. A.; Zhang, Y. P.; Papaefthymiou, G. C.; Spartalian, K.; Frankel, R. B.; Holm, R. H. Comparative Electronic Properties of Vanadium-Iron-Sulfur and Molybdenum-Iron-Sulfur Clusters Containing Isoelectronic Cubane-Type [VFe3S4]2+ and [MoFe3S4]3+ Cores. *Inorg. Chem.* **1987**, *26* (5), 719–724. https://doi.org/10.1021/ic00252a016.

(84) Bjornsson, R.; Delgado-Jaime, M. U.; Lima, F. A.; Sippel, D.; Schlesier, J.; Weyhermüller, T.; Einsle, O.; Neese, F.; DeBeer, S. Molybdenum L-Edge XAS Spectra of MoFe Nitrogenase. *Zeitschrift für anorganische und allgemeine Chemie* **2015**, *641* (1), 65–71. https://doi.org/10.1002/zaac.201400446.

(85) Kowalska, J. K.; Henthorn, J. T.; Van Stappen, C.; Trncik, C.; Einsle, O.; Keavney, D.; DeBeer, S. X-Ray Magnetic Circular Dichroism Spectroscopy Applied to Nitrogenase and Related Models: Experimental Evidence for a Spin-Coupled Molybdenum(III) Center. *Angewandte Chemie International Edition* **2019**, *58* (28), 9373–9377. https://doi.org/10.1002/anie.201901899.

(86) Rawlings, J.; Shah, V. K.; Chisnell, J. R.; Brill, W. J.; Zimmermann, R.; Münck, E.; Orme-Johnson, W. H. Novel Metal Cluster in the Iron-Molybdenum Cofactor of Nitrogenase. Spectroscopic Evidence. *J Biol Chem* **1978**, *253* (4), 1001–1004.

(87) Bjornsson, R.; Neese, F.; DeBeer, S. Revisiting the Mössbauer Isomer Shifts of the FeMoco Cluster of Nitrogenase and the Cofactor Charge. *Inorg. Chem.* **2017**, *56* (3), 1470–1477. https://doi.org/10.1021/acs.inorgchem.6b02540.

(88) Benediktsson, B.; Bjornsson, R. QM/MM Study of the Nitrogenase MoFe Protein Resting State: Broken-Symmetry States, Protonation States, and QM Region Convergence in the FeMoco Active Site. *Inorg. Chem.* **2017**, *56* (21), 13417–13429. https://doi.org/10.1021/acs.inorgchem.7b02158.

(89) Spatzal, T.; Schlesier, J.; Burger, E.-M.; Sippel, D.; Zhang, L.; Andrade, S. L.; Rees, D. C.; Einsle, O. Nitrogenase FeMoco Investigated by Spatially Resolved Anomalous Dispersion Refinement. *Nature communications* **2016**, *7*, 10902.

(90) Bjornsson, R.; Neese, F.; Schrock, R. R.; Einsle, O.; DeBeer, S. The Discovery of Mo(III) in FeMoco: Reuniting Enzyme and Model Chemistry. *J Biol Inorg Chem* **2015**, *20* (2), 447–460. https://doi.org/10.1007/s00775-014-1230-6.

(91) Pesavento, R. P.; Berlinguette, C. P.; Holm, R. H. Stabilization of Reduced Molybdenum−Iron−Sulfur Single- and Double-Cubane Clusters by Cyanide

Ligation. *Inorg. Chem.* **2007**, *46* (2), 510–516. https://doi.org/10.1021/ic061704y.

(92) Fomitchev, D. V.; McLauchlan, C. C.; Holm, R. H. Heterometal Cubane-Type MFe3S4 Clusters (M = Mo, V) Trigonally Symmetrized with Hydrotris(Pyrazolyl)Borate(1−) and Tris(Pyrazolyl)Methanesulfonate(1−) Capping Ligands. *Inorg. Chem.* **2002**, *41* (4), 958–966. https://doi.org/10.1021/ic011106d.

(93) Hauser, C.; Bill, E.; Holm, R. H. Single- and Double-Cubane Clusters in the Multiple Oxidation States [VFe3S4]3+,2+,1+. *Inorg. Chem.* **2002**, *41* (6), 1615–1624. https://doi.org/10.1021/ic011011b.

(94) Sridharan, A.; Brown, A. C.; Suess, D. L. M. A Terminal Imido Complex of an Iron–Sulfur Cluster. *Angewandte Chemie International Edition* **2021**, *60* (23), 12802–12806. https://doi.org/10.1002/anie.202102603.

(95) Xu, G.; Wang, Z.; Ling, R.; Zhou, J.; Chen, X.-D.; Holm, R. H. Ligand Metathesis as Rational Strategy for the Synthesis of Cubane-Type Heteroleptic Iron–Sulfur Clusters Relevant to the FeMo Cofactor. *Proceedings of the National Academy of Sciences* **2018**, *115* (20), 5089–5092.

(96) Le, L.; Bailey, G.; Scott, A.; Agapie, T. Cluster Models of FeMoco with Sulfide and Carbyne Ligands: Effect of Interstitial Atom in Nitrogenase Active Site. **2021**. https://doi.org/10.26434/chemrxiv.14614152.v1.

(97) Piglosiewicz, I. M.; Beckhaus, R.; Wittstock, G.; Saak, W.; Haase, D. Selective Oxidation and Reduction of Trinuclear Titanium(II) Hexaazatrinaphthylene ComplexesSynthesis, Structure, and Electrochemical Investigations. *Inorg. Chem.* **2007**, *46* (18), 7610–7620. https://doi.org/10.1021/ic701009u.

(98) Sun, H.; DiMagno, S. G. Anhydrous Tetrabutylammonium Fluoride. *J. Am. Chem. Soc.* **2005**, *127* (7), 2050–2051. https://doi.org/10.1021/ja0440497.

(99) Barrett, A. N.; Woof, C. R.; Goult, C. A.; Gasperini, D.; Mahon, M. F.; Webster, R. L. Hydrogen/Halogen Exchange of Phosphines for the Rapid Formation of Cyclopolyphosphines. *Inorg. Chem.* **2021**, *60* (21), 16826–16833. https://doi.org/10.1021/acs.inorgchem.1c02734.

(100) Pangborn, A. B.; Giardello, M. A.; Grubbs, R. H.; Rosen, R. K.; Timmers, F. J. Safe and Convenient Procedure for Solvent Purification. *Organometallics* **1996**, *15* (5), 1518–1520. https://doi.org/10.1021/om9503712.

(101) Bruker, APEX3(Bruker AXS Inc., 2012).

(102) Bruker, SADABS(Bruker AXS Inc., 2001).

(103) Sheldrick, G. M. SHELXT – Integrated Space-Group and Crystal-Structure Determination. *Acta Cryst A* **2015**, *71* (1), 3–8. https://doi.org/10.1107/S2053273314026370.

(104) Altomare, A.; Cascarano, G.; Giacovazzo, C.; Guagliardi, A.; Burla, M. C.; Polidori, G.; Camalli, M. SIRPOW.92 – a Program for Automatic Solution of Crystal Structures by Direct Methods Optimized for Powder Data. *J Appl Cryst* **1994**, *27* (3), 435–436. https://doi.org/10.1107/S0021889894000221.

(105) Palatinus, L.; Chapuis, G. SUPERFLIP – a Computer Program for the Solution of Crystal Structures by Charge Flipping in Arbitrary Dimensions. *J Appl Cryst* **2007**, *40* (4), 786–790. https://doi.org/10.1107/S0021889807029238.

(106) Dolomanov, O. V.; Bourhis, L. J.; Gildea, R. J.; Howard, J. a. K.; Puschmann, H. OLEX2: A Complete Structure Solution, Refinement and Analysis Program. *J Appl Cryst* **2009**, *42* (2), 339–341. https://doi.org/10.1107/S0021889808042726.

Chapter III

SYNTHESIS AND REACTIVITY OF OCTANUCLEAR CH_n BRIDGED MOFES CLUSTERS

Abstract

Organometallic complexes of the type M(CH_n) have great relevance in industrial and biological catalysis. Enzymes have developed catalytic processes involving such species utilizing the earth abundant metal Fe, which is incorporated into FeS clusters that are ubiquitous in a large variety of catalytic processes. While many FeS(CH_n) species are implicated in these important biological processes, the study of such clusters is limited, perhaps due to their instability in enzymatic systems. Synthetic inorganic chemistry offers the opportunity to make model systems that will allow for important structural, benchmarking, and reactivity studies to better understand the chemistry of FeS(CH_n) species. Described herein is the synthesis of three novel $Mo_2Fe_6(\mu\text{-}CH_n)_m$ clusters. Characterization and reactivity studies provide insight into the nature of the bridging ligands as well as possible reaction pathways for these biologically relevant species.

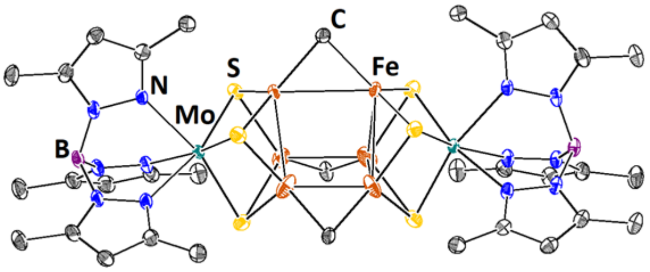

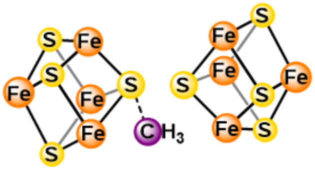

K Clusters

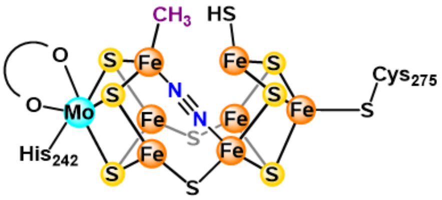

FeMoco

Introduction

Organometallic species involving CH_n ligands have been intensely studied due to their prevalence in industrial synthesis and catalysis[1,2] as well as in biological catalysis.[3–6] Development of earth abundant Fe catalysts have seen success in cross-coupling reactions, metathesis reactions, and ethylene and olefin oligomerization and polymerization.[7–10] In biology, Fe methyl species are implicated in radical SAM enzyme catalysis[3,4] as well as the biosynthesis of the carbide containing co-factor FeMco.[5] In some proposed mechanisms of N_2 reduction to NH_3 the central carbide of FeMco is thought to have fluxional binding modes and protonation states.[11–17] In synthetic organometallic chemistry, bridging CH_n ligands between Fe centers are relatively rare, and mainly consist of CO or NO containing systems, with CH_2 being the most common bridging ligand. Species without the strong-field ligands CO and CN are represented in Fig. 1. Only one synthetic system was found with a $(\mu\text{-}CH_n)Fe_2$ bridge (n = 0) in an FeS cluster (Fig. 1), although the clusters reported only contain one sulfide ligand and multiple strong-field CO ligands.[18] A $(\mu\text{-}CH_n)(\mu\text{-}Se)Fe_2$ system has also been reported, but again with strong-field ligands, NO in this case.[19] As such there are virtually no examples reported in the literature of FeS clusters with bridging CH_n ligands despite the implication of such species in various biological processes (Fig. 1). Synthetic species of this type will aid in benchmarking the spectroscopy of $(\mu\text{-}CH_n)Fe_2$ as well as understanding the reactivity of such systems.

Although bridging CH_n ligands are rare for synthetic FeS clusters, one method for incorporating bridging CR ligands is the oxidation of trialkyl clusters, such as $[Et_4N][Tp^*MFe_3S_3(CH_3SiMe_3)_3]$ (M = W or Mo), clusters to form μ_3-CR carbyne ligands, such as $[Et_4N][Tp^*MFe_3S_3(\mu_3\text{-}CSiMe_3)Cl_3]$ (Fig. 2), where the trialkyl cluster can be formed using $LiCH_3SiMe_3$.[20] Attempts to perform analogous chemistry

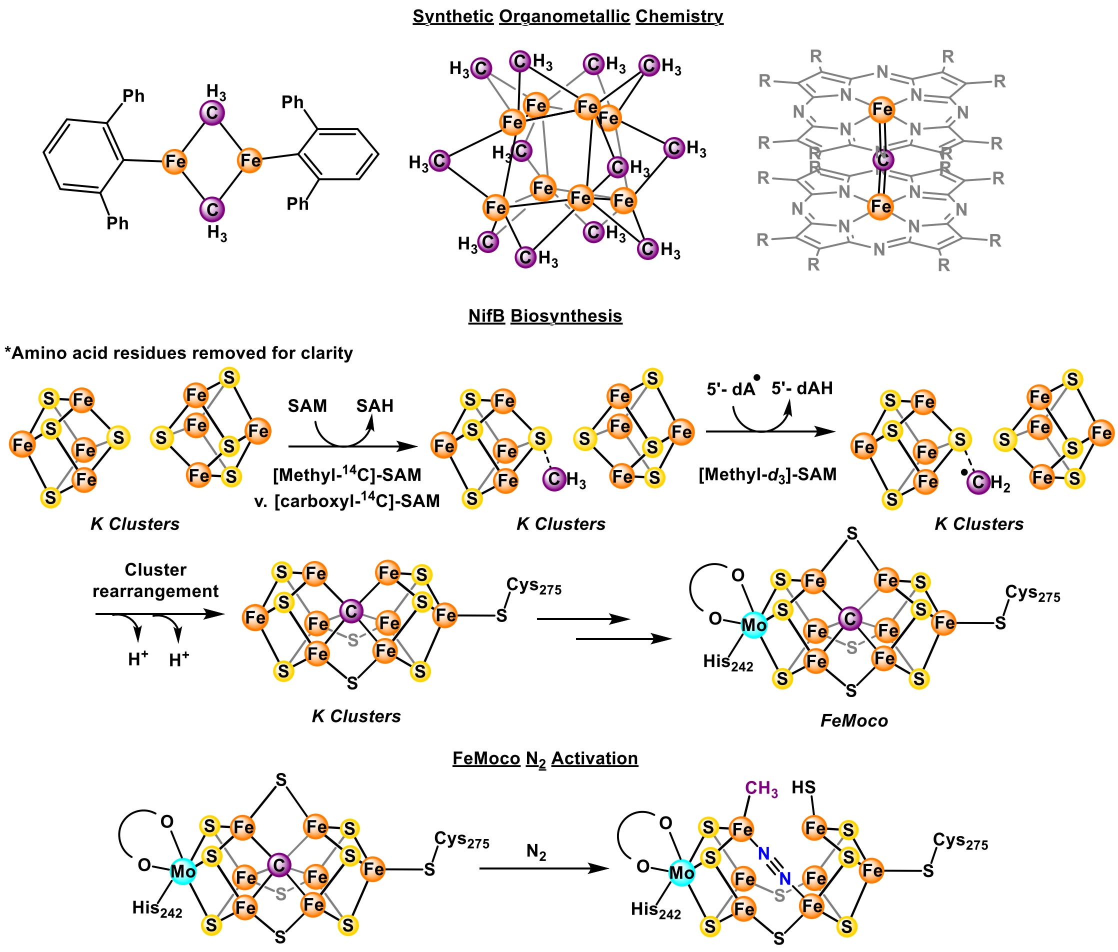

Figure 1: Examples of synthetic μ-CH_3 and μ-C Fe bridged complexes not containing CO or NO ligands (top).[8,21,22] Biosynthesis of FeMoco showing proposed mechanism for carbon ligand incorporation on NifB (middle).[5] One proposed mechanism for N_2 binding and activation by FeMoco.[17]

using $LiCH_3$ or CH_3MgCl (Fig. 2) resulted in low yields of the desired cluster [Et_4N][Tp*$MoFe_3S_3(CH_3)_3$] (**3**) based on ^{1}H-NMR spectroscopy (Fig. S1 and S2) and SC- XRD (Fig. 3), and pure material could not be isolated. Attempts to synthesize [Et_4N][Tp*$MoFe_3S_3$(μ_3-CH)Cl_3] from as isolated [Et_4N][Tp*$MoFe_3S_3(CH_3)_3$] were not successful.

In an attempt to improve the synthesis of **3**, excess CH_3MgCl and longer reaction times were used. A SC-XRD study of the precipitate that formed under these

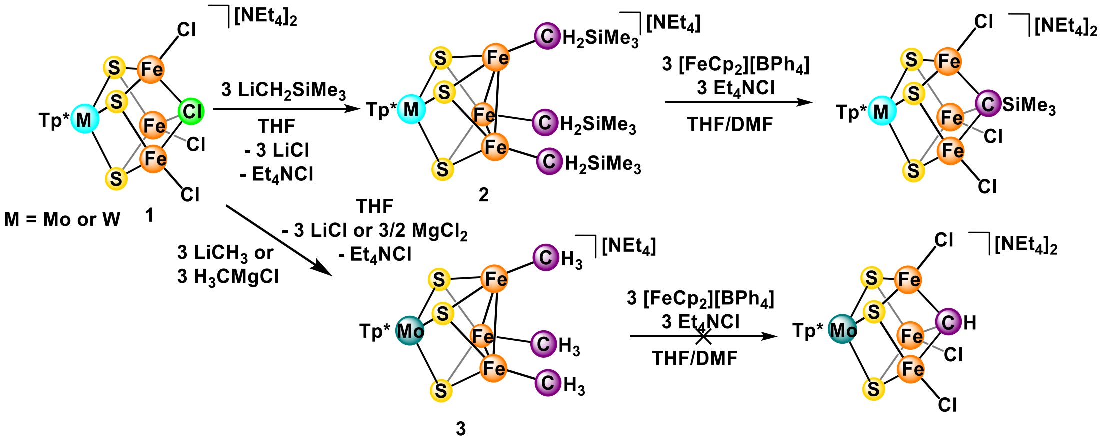

Figure 2: Synthesis of trialkyl MFeS clusters and carbyne synthesis conditions.

reaction conditions revealed a novel octanuclear FeS cluster with CH_n bridging ligands $[Et_4N][Tp_2^*Mo_2Fe_6S_6(\mu\text{-}CH_n)_3]$ (**4**) (Fig. 4, 5). Described herein is the synthesis of three octanuclear FeS clusters with bridging CH_n ligands. Attempts to determine the number of hydrogens on the carbon based bridging ligands is discussed based on the observed reactivities of the clusters. Characterization of the octanuclear CH_n bridged FeS clusters is also carried out to better understand the electronic structure of these biologically relevant species.

Results and Discussion

In an attempt to improve the synthesis of the trialkyl cluster **3**, excess CH_3MgCl was used (Fig. 4) and stirring the reaction for 48 hours in THF resulted in the formation of **3**, detected via

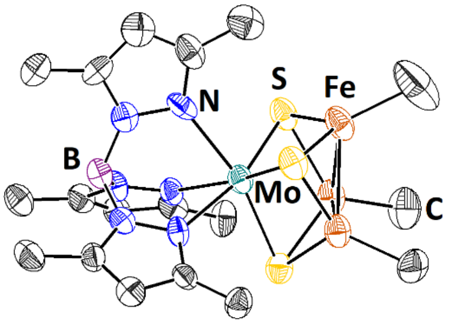

Figure 3: Crystal structure of **3** with ellipsoids plotted at the 50% probability level. Solvent and counter ions omitted for clarity.

^{1}H-NMR spectroscopy, and a precipitate that was only soluble in *N*,*N*-dimethylformamide (DMF). A SC-XRD study of the DMF soluble material that was recrystallized from DMF revealed the formation of $[Et_4N][Tp_2*Mo_2Fe_6S_6(\mu\text{-} CH_n)_3]$ (**4**), an octanuclear FeS cluster that does not contain a μ_6 bridging atom (Fig. 5). This cluster is notable due to the lack of synthetic alkyl FeS clusters in the literature,[20,23–26] especially those containing bridging carbon based ligands.[20,27,28] Although the number of hydrogen atoms on the bridging carbon ligands cannot be definitively determined using SC-XRD, the formation of the monocation cluster **4** with loss of chloride implies reductive chemistry must occur to form the cluster.

4 recrystallized from DMF is initially only slightly soluble in DMF and MeCN, but in the solid state slowly becomes insoluble in DMF and more soluble in MeCN, indicating decomposition and/or disproportionation of **4** over time. To determine the identity of the new species formed, **4** was stirred in MeCN overnight (Fig. 4) and the reaction mixture was diffused with Et_2O resulting in the formation of a mixture of dark block like crystals. A SC-XRD study of these crystals revealed **4** and a dicationic $[Et_4N]_2[Tp_2*Mo_2Fe_6S_6(\mu\text{-}CH_n)_3]$ cluster (**5**) (Fig. 4 and 6).

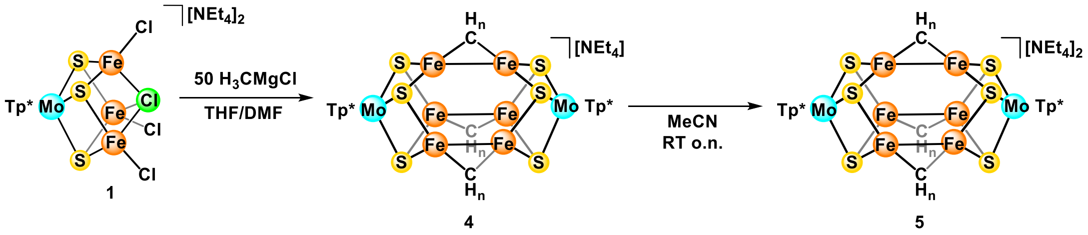

Figure 4: Synthesis of **4** and **5**.

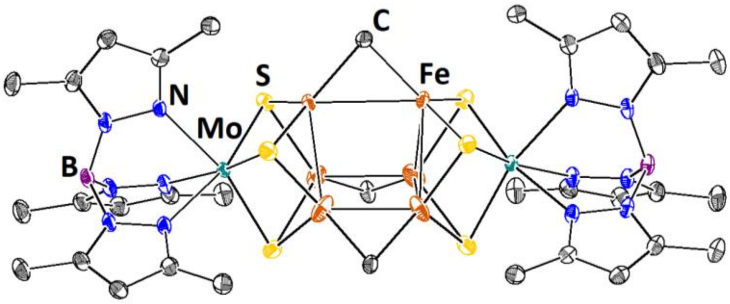

Figure 5: Crystal structure of **4** with ellipsoids plotted at the 50% probability level. Solvent and counter ions omitted for clarity.

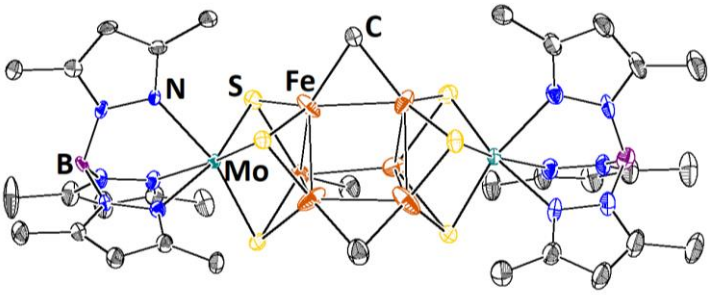

Figure 6: Crystal structure of **5** with ellipsoids plotted at the 50% probability level. Solvent and counter ions omitted for clarity.

Starting from **4**, ligand substitution reactions of two of the CH_n bridges with sulfides or thiolates were attempted, but isolation of the desired products was unsuccessful (Fig.7). Instead formation of another CH_n bridged cluster with a μ_6-S atom was observed via SC-XRD (Fig. 8). The stoichiometry of these reactions are not balanced and the source of the μ_6-S atom is undetermined; however, this product can also be made in higher yields starting from **1**, using an excess of MeMgCl, and with the addition of potassium phenylthiolate (KPh) (Fig. 7). In the case of this reaction, a precipitate forms from the THF reaction mixture that is soluble in MeCN from which **6** is recrystallized using Et_2O vapor diffusion.

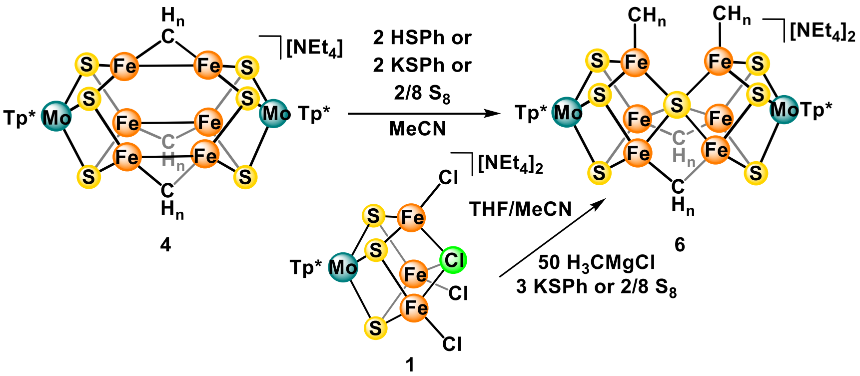

Figure 7: Synthesis of **6** from **1** or **4**.

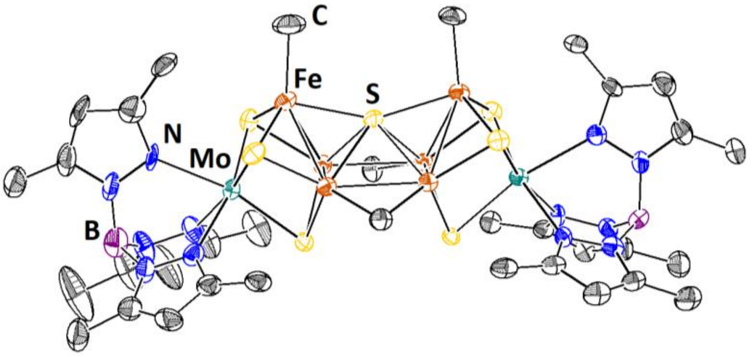

Figure 8: Crystal structure of **6** with ellipsoids plotted at the 50% probability level. Solvent and counter ions omitted for clarity.

Searching the Cambridge Crystallographic Database for (μ-CH_n)Fe_2 motifs, there are a very limited number of complexes found of which the majority contain μ-CH_2, or methylidene bridges (7 hits),[19,29–34] followed by μ-CH_3, or methyl bridges (3 hits)[8,21,35] and μ-C, or carbide bridges (3 hits),[22,22,36] No hits were found for μ-CH, or methylidyne bridges, or for μ-CH_4 bridges. The ranges of bond lengths for each of these types of complexes are listed in Table 1.

Table 1: Ranges of bond lengths for (μ-CH$_n$)Fe$_2$ motifs.

(μ-CH$_n$)Fe$_2$ Bridge Type	μ-C	μ-CH$_2$	μ-CH$_3$
Range of C-Fe Bond Lengths (Å)	1.683 - 1.692	1.916 – 2.041	2.008 – 2.366

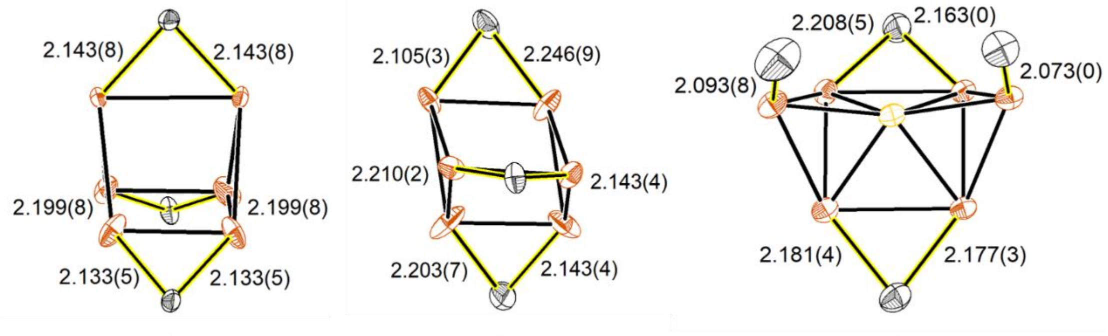

4
Average: 2.159 Å

5
Average: 2.175 Å

6
Average: 2.183 Å

Figure 9: Fe-CH$_n$ bond lengths in Å for clusters **4-6** where the crystal structures of the Fe$_6$(μ-CH$_n$)$_m$ core are shown. Ellipsoids are plotted at the 50% probability level.

Bond lengths of the Fe-CH$_n$ bonds in clusters **4-6** are summarized in Fig. 9, all of which are in the range of the Fe-C bond lengths for (μ-CH$_3$)Fe$_2$ literature compounds. Comparing the similar clusters **4** and **5**, cluster **4** has symmetric Fe-(CH$_n$)-Fe bonds, whereas **5** has asymmetric bonds that are on average slightly longer than those of **4**. In the case of **6**, one set of Fe-(CH$_n$)-Fe bonds are nearly symmetric whereas the other set are asymmetric, although less so when compared to those of **5**. The distances between the two cubane halves of clusters **4-6** are summarized in Fig. 10 based on the Fe-Fe distances in the clusters. Cluster **5** is the most compact, despite having longer Fe-CH$_n$ bonds than **4**.

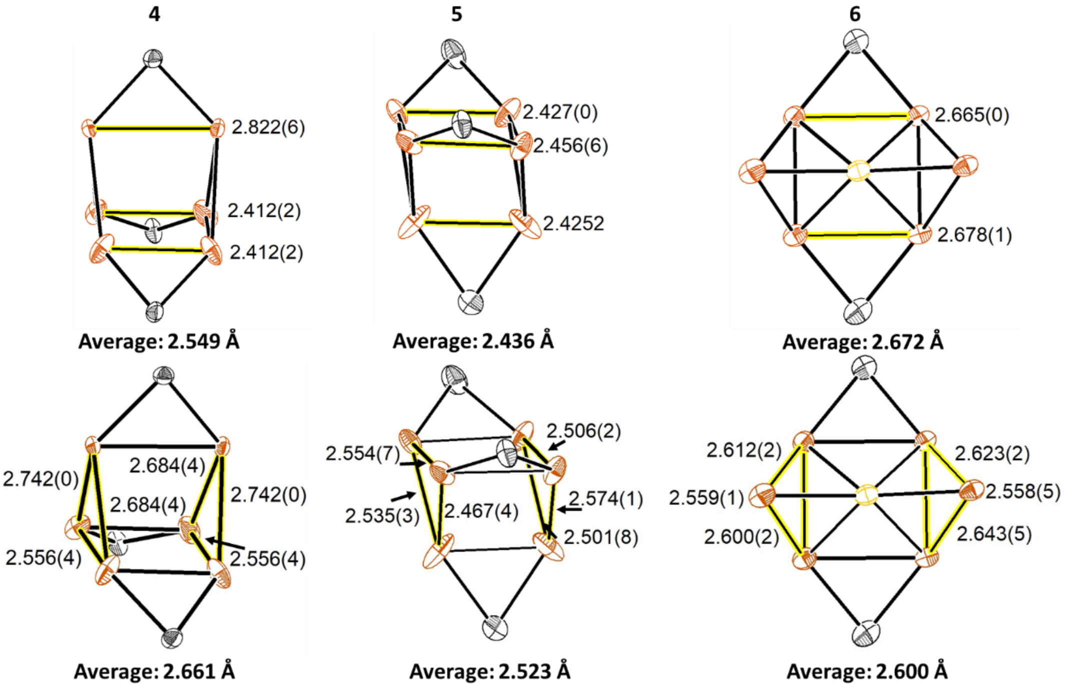

Figure 10: Fe-Fe distances in Å for clusters **4-6** where the crystal structures of the $Fe_6(\mu\text{-}CH_n)_m$ core are shown. Ellipsoids are plotted at the 50% probability level.

Unsurprisingly, **6** has the longest Fe-Fe distances, likely due to the presence of the additional sulfide ligand in the center of the cluster. Compared to open faced trialkyl MoFeS clusters **2** and **3**, the Fe-C bond lengths of the bridging atoms in clusters **4-6** are longer, consistent with the shorter bond lengths of the terminal CH_n ligands of **6** compared to the bridging CH_n ligands as well as the crystal structure of Al_2Me_6 (Table 2).[37]

Table 2: Fe-CH_n bond lengths of terminal and bridging Fe-CH_n clusters.

Cluster	**2**	**3**	**4**	**5**	**6**
Average Fe-CH_n Bond Length (Å)	2.006	2.01	2.159	2.175	2.183
Range of Fe-CH_n Bond Lengths (Å)	1.991(2) – 2.022(2)	2.00(7) – 2.01(9)	2.133(5) – 2.199(8)	2.105(3) – 2.246(9)	2.163(0) – 2.208(5)

Definitive determination of the number of H atoms on the carbon bridges is not possible using SC-XRD, but refinement of the structures of **4-6** without hydrogen atoms modelled on the bridging and terminal CH_n ligands indicate between 2 and 4 hydrogen atoms (Fig. S7). Reflux of **4** for 24 hours was performed to detect the generation of any organic products that may be released upon reactions of the clusters at higher temperatures that could give insight into the identity of the CH_n ligands. The ^1H-NMR spectrum of this reaction (Fig. S5 and 6) indicates the formation of methane. Using an internal standard, the amount of **4** was reduced by 77% after refluxing in CD_3CN and the presence of new paramagnetic species are evident in the ^1H-NMR spectrum (Fig. S5).

To further elucidate the number of hydrogen atoms on the CH_n ligands, deuterated analogues of clusters **4** and **6** (**4-D** and **6-D**) were synthesized using $Mg(CD_3)_2$ instead of CH_3MgCl (see experimental section). Then an excess of Brookhart's acid ($HBAr^F$) was added to the clusters that were suspended (**4**) or dissolved (**5**) in CD_3CN and the formation of organic products was tracked via ^1H-NMR (Fig. 11-13). Formation of CD_3H was detected in both cases suggesting the presence of μ-CH_3 bridges in clusters **4** and **6**. Additionally, the generation of H_2 and HD were detected suggesting the presence and/or formation of metal hydrides during the protonation reactions.

Addition of excess $DBAr^F$ (66% deuterium incorporation) to proteo **4** and **6** was also performed as a complementary experiment to those described above (Fig. 11-13). Similar results were obtained, where CDH_3 and CH_4, likely due to incomplete labelling of the $DBAr^F$, were detected as well as H_2 and HD.

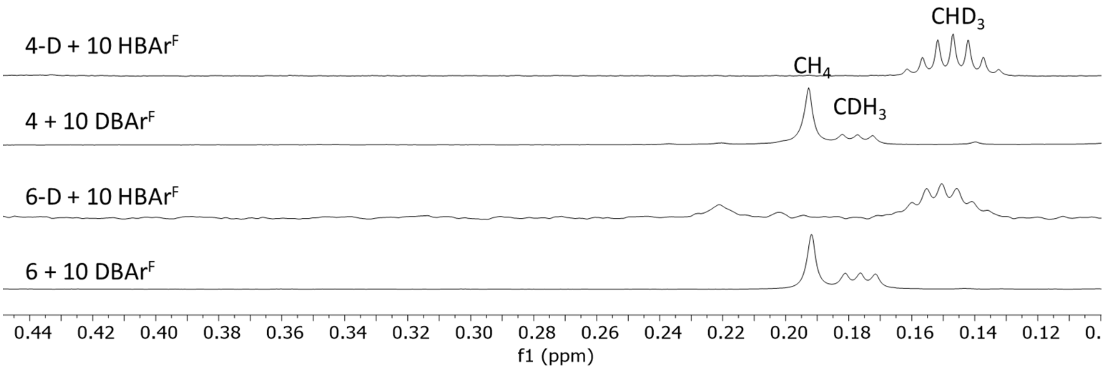

Figure 11: ^{1}H-NMR spectra (CD_3CN) of **4, 4-D, 6, and 6-D** after reaction with $HBAr^F$ or $DBAr^F$ indicating formation of methane.

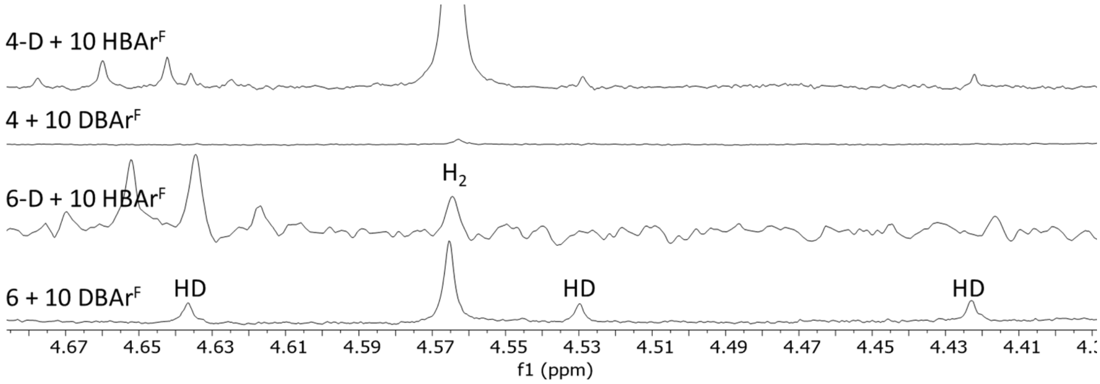

Figure 12: ^{1}H-NMR spectra (CD_3CN) of **4, 4-D, 6,** and **6-D** after reaction with $HBAr^F$ or $DBAr^F$ indicating formation of H_2.

The electronic structures of clusters **4** and **6** were investigated using electron paramagnetic resonance (EPR) and Mössbauer spectroscopy. **6** is EPR silent indicating an integer spin state. Assuming the terminal CH_n ligands to be methyl ligands based on the bond lengths and the labelling experiments described above, the only possible assignments of the $(CH_n)_2(\mu\text{-}CH_n)_2$ ligands are $(CH_3)_2(\mu\text{-}CH_3)_2$, $(CH_3)_2(\mu\text{-}CH_2)_2$, or $(CH_3)_2(\mu\text{-}CH)_2$ indicating $[Mo_2Fe_6]^{18+}$, $[Mo_2Fe_6]^{20+}$, or $[Mo_2Fe_6]^{22+}$ oxidations states, respectively. Thus, the $(CH_3)_2(\mu\text{-}CH_3)_2$ assignment is consistent with the presented data. However, based on the observation of H_2 and HD in the labelling experiments described above, further characterization is necessary to confirm the proposed structural assignment of **6**. Although the ligands of the Fe centers in clusters **4** and **6** differ significantly, the Mössbauer data of each cluster (Fig. 13 and 14) suggest that the Fe centers of **6** are more reduced compared to those of **4**.

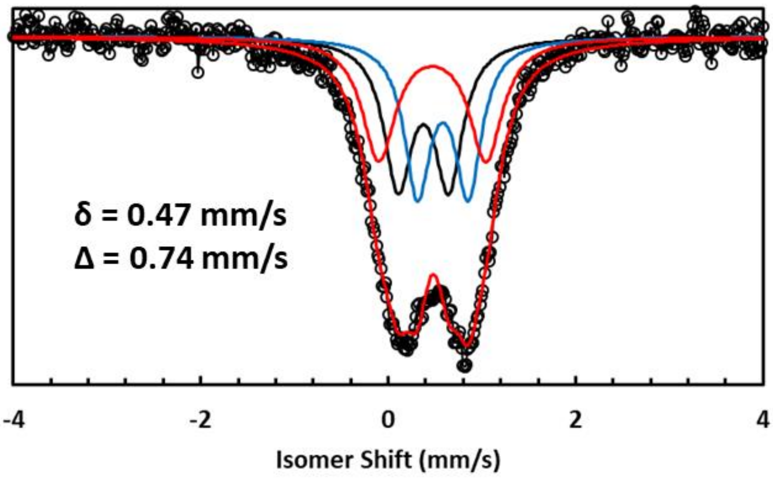

Figure 13: Mössbauer spectrum of **4**. For fitting details see experimental section.

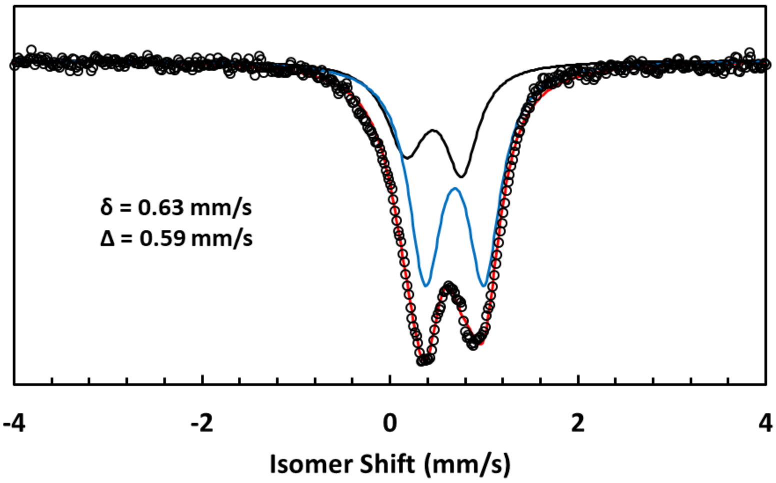

Figure 14: Mössbauer spectrum of **6**. For fitting details see experimental section.

Conclusion

The synthesis of three novel octanuclear FeS clusters containing bridging CH_n ligands has been accomplished. This cluster motif is unprecedented in the literature and the release of organic products from the clusters at high temperatures and in the presence of acid provides insight into the reactivity of such systems that have relevance in biology as well as industrial processes. The reactivity studies and structural and electronic characterization of the clusters provide evidence for (μ-CH_3)Fe_2 ligands and provide support for mechanistic proposals of N_2 turnover by FeMco where the central carbide ligand has a flexible binding mode and can participate in proton transfers. Further studies are necessary to definitively determine the identity of the carbon based bridging ligands and the overall cluster compositions.

Experimental

General Considerations

All reactions were performed at room temperature in an N_2-filled M. Braun glovebox or using standard Schlenk techniques unless otherwise specified. Glassware was oven dried at 140 °C for at least 2 h prior to use, and allowed to cool under vacuum. Sodium tetrafluoroborate ($NaBPh_4$) was purchased in an anhydrous form and dissolved in acetonitrile (CH_3CN) and dried over 3 Å molecular sieves for 2 days before being filtered over Celite and dried in vacuo. $[Et_4N]_2[Tp^*WFe_3S_3(\mu_3\text{-}Cl)Cl_3]$[38] **(1)** (Tp* = tris(3,5-dimethyl-1-pyrazolyl)borate) and $[Et_4N]_2[Tp^*MoFe_3S_3(\mu_3\text{-}Cl)Cl_3]$ (**1-Mo**)[28] were prepared according to literature procedures. Tetrahydrofuran (THF), diethyl ether (Et_2O), benzene (C_6H_6), toluene, CH_3CN, hexanes, and pentane were dried by sparging with nitrogen for at least 15 minutes, then passing through a column of activated A2 alumina under positive N_2 pressure and then degassed via several consecutive cycles of active vacuum and agitation on the Schlenk line before use.[39] Dimethylformamide was purchased in an anhydrous form from MiliporeSigma@, cannula-transferred to an oven dried Schlenk under N_2, degassed via several consecutive cycles of active vacuum and agitation on the Schlenk line, and then brought into the glovebox and dried over 3 Å molecular sieves for 2 days before use. ^1H and ^{31}P NMR spectra were recorded on a Varian 400 MHz spectrometer. ^1H-NMR spectra in proteo solvents were recorded on a Varian 400 MHz spectrometer using solvent suppression protocols. *d8*-THF,

CD_3CN, and C_6D_6, were purchased from Cambridge Isotope Laboratories, dried over calcium hydride, degassed by three freeze-pump-thaw cycles, and vacuum transferred prior to use. All other reagents were purchased from commercial sources in their anhydrous forms and used without further purification.

Synthetic Procedures

Synthesis of $[Et_4N][Tp^*WFe_3S_3(CH_3)_3]$ (3-W). $[Et_4N]_2[Tp^*WFe_3S_3(\mu_3\text{-}Cl)Cl_3]$ (100 mg, 0.087 mmol) was measured into a scintillation vial and suspended in THF (6 mL). CH_3MgCl (0.09 ml of 3 M THF solution, 0.26 mmol) was added to the stirring suspension dropwise at room temperature. The reaction suspension was allowed to stir at room temperature for 48 h. The suspension was filtered over a Celite pad and then dried *in-vacuo*. After trituration three times with Et_2O, the solids were washed with Et_2O and then C_6H_6 until the filtrate was colorless. The desired product was extracted into a minimum of THF and crystallization was set up with vapor diffusion of 2x volume of Et_2O to yield dark block like crystals and colorless block light crystals.

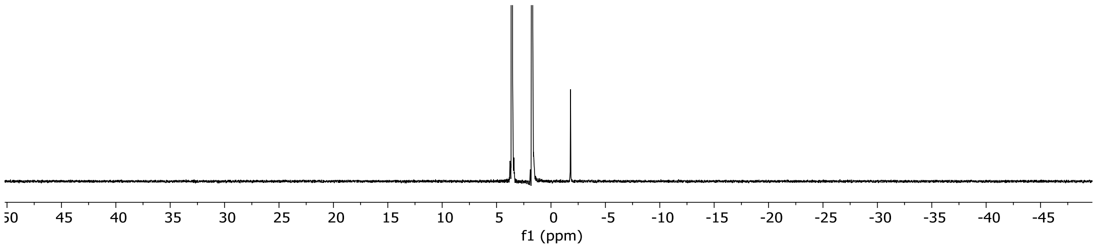

Figure S1: ^{1}H-NMR spectrum of crystallization mixture containing $[Et_4N][Tp^*WFe_3S_3(CH_3)_3]$ (**3-W**).

Synthesis of $[Et_4N][Tp^*MoFe_3S_3(CH_3)_3]$ (3). 4-Mo was prepared in an analogous manner to **4**. $[Et_4N]_2[Tp^*MoFe_3S_3(\mu_3\text{-}Cl)Cl_3]$ (100 mg, 0.095 mmol) was measured into a scintillation vial and suspended in THF (6 mL). CH_3MgCl (0.1 ml of 3 M pentane solution, 0.29 mmol) was added to the stirring suspension dropwise at room temperature.

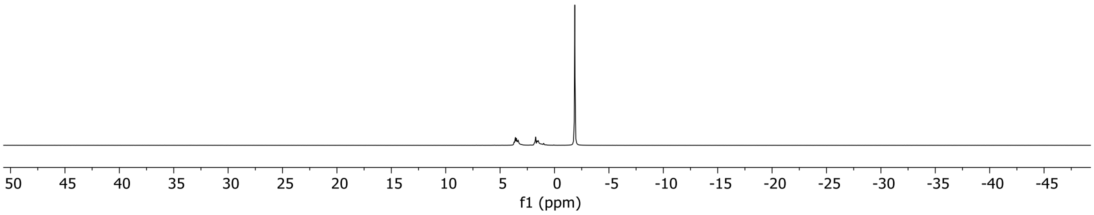

Figure S2: ^{1}H-NMR spectrum of crystallization mixture containing $[Et_4N][Tp^*MoFe_3S_3(CH_3)_3]$ (**3**).

Synthesis of $[Et_4N][Tp^*{}_2Mo_2Fe_6S_6(\mu\text{-}CH_n)_3]$ (4). $[Et_4N]_2[Tp^*MoFe_3S_3(\mu_3\text{-}Cl)Cl_3]$ (100 mg, 0.095 mmol) was measured into a scintillation vial and suspended in THF (6 mL). CH_3MgCl (1.60 ml of 3 M pentane solution, 4.8 mmol) was added to the stirring suspension dropwise at room temperature. The reaction suspension was allowed to stir at room temperature for 48 h. The precipitate was collected on a frit and washed with THF and then MeCN until the filtrate was colorless. The desired product was extracted into a minimum of DMF and crystallization was set up with vapor diffusion of 2x volume of Et_2O to yield 30 mg of dark needle like crystals (10% yield). NMR (400 MHz, DMF): δ -15.7 (br s) and -59 (s) ppm.

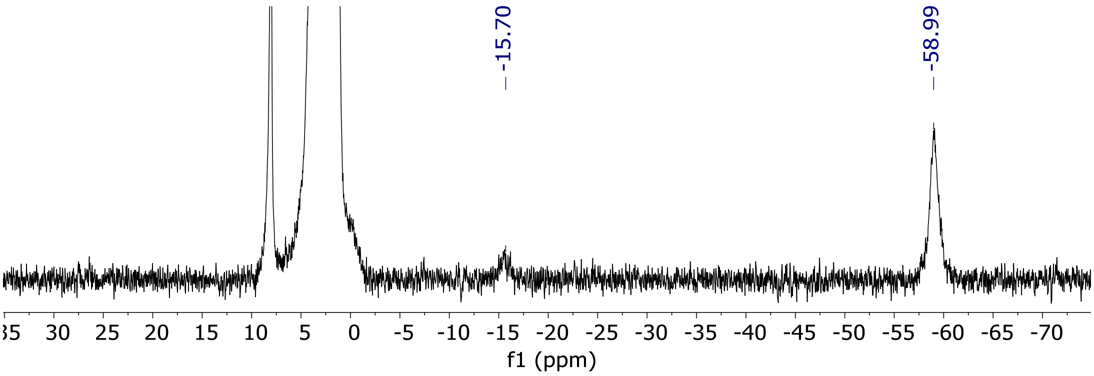

Figure S3: ^{1}H-NMR spectrum of $[Et_4N][Tp^*{}_2Mo_2Fe_6S_6(\mu\text{-}CH_n)_3]$ in DMF.

Synthesis of $[Et_4N]_2[Tp^*{}_2Mo_2Fe_6S_6(\mu\text{-}CH_n)_3]$ (5). Crystals of **4** (20 mg, 0.013 mmol) were suspended in MeCN (2 mL) and stirred at room temperature for 24 h.

The reaction was filtered and crystallization was set up with vapor diffusion of 2x volume of Et_2O to yield dark block like crystals. The crystals were a mixture of **4** and **5**.

Synthesis of $[Et_4N]_2[Tp^*{}_2Mo_2Fe_6S_6(\mu_6\text{-}S)(\mu\text{-}CH_n)_2(CH_n)_2]$ (6).

$[Et_4N]_2[Tp^*MoFe_3S_3(\mu_3\text{-}Cl)Cl_3]$ (100 mg, 0.095 mmol) was measured into a scintillation vial and suspended in THF (6 mL). CH_3MgCl (1.60 ml of 3 M pentane solution, 4.8 mmol) and KSPh (43.3 mg, 0.29 mmol) were added to the stirring suspension at room temperature. The reaction suspension was allowed to stir at room temperature for 48 h. The precipitate was collected on a frit and washed with THF until the filtrate was colorless. The desired product was extracted into a minimum of MeCN and crystallization was set up with vapor diffusion of 2x volume of Et_2O to yield 10 mg of dark needle like crystals (3% yield). NMR (400 MHz, MeCN): δ 7.4 (s), -13.6 (br s) and -22.6 (s) ppm.

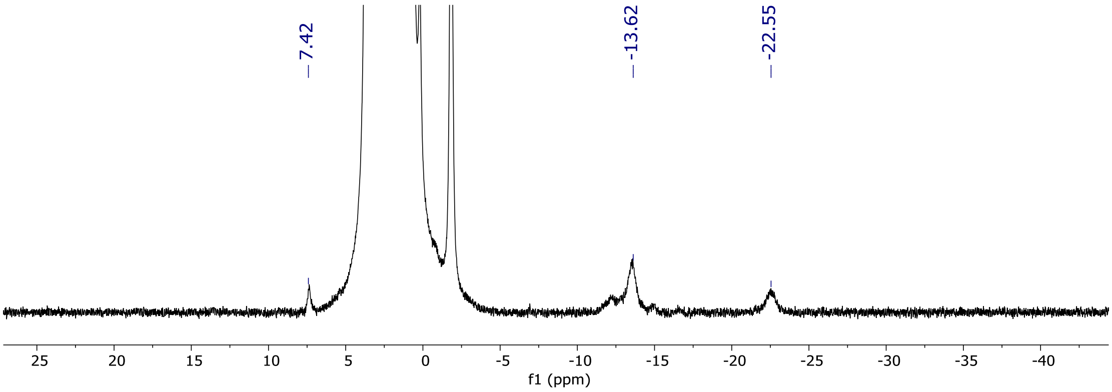

Figure S4: ^{1}H-NMR spectrum of $[Et_4N]_2[Tp^*{}_2Mo_2Fe_6S_6(\mu_6\text{-}S)(\mu\text{-}CH_n)_2(CH_n)_2]$ in MeCN.

NMR Experiments

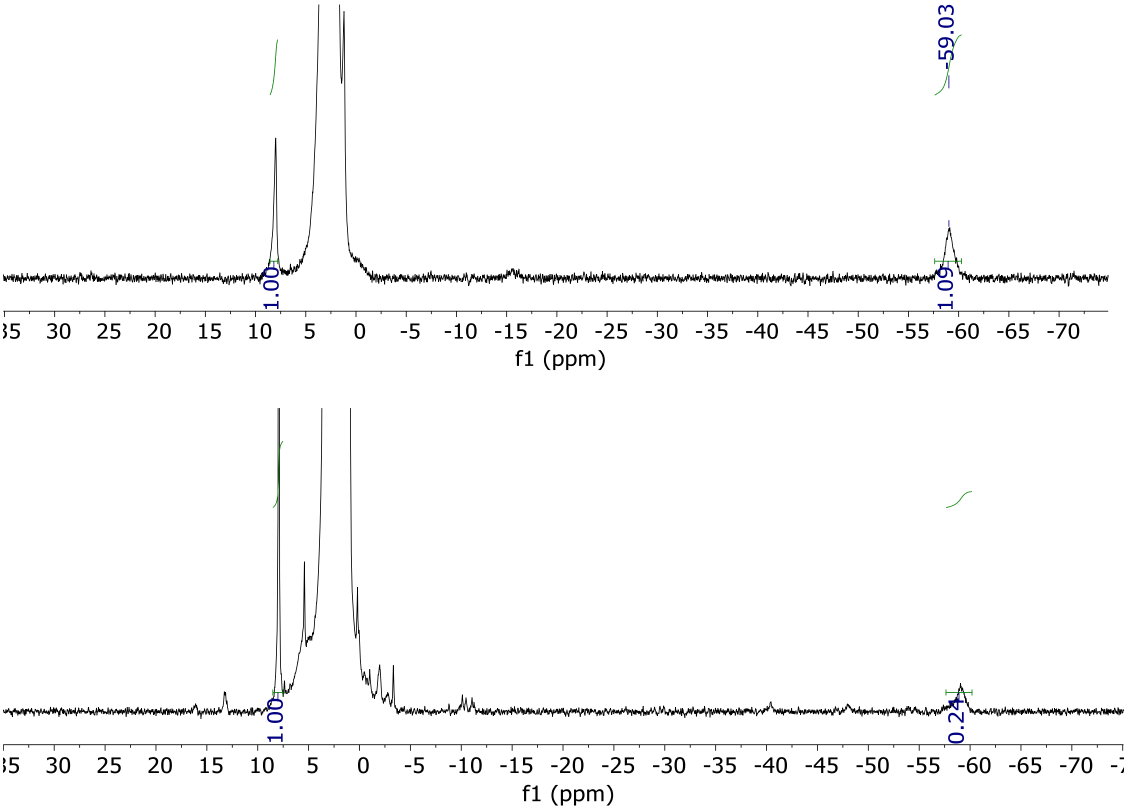

Figure S5: ^{1}H-NMR spectra of **4** before (top) and after (bottom) refluxing for 24 hours in CD_3CN with DMF used as an internal standard.

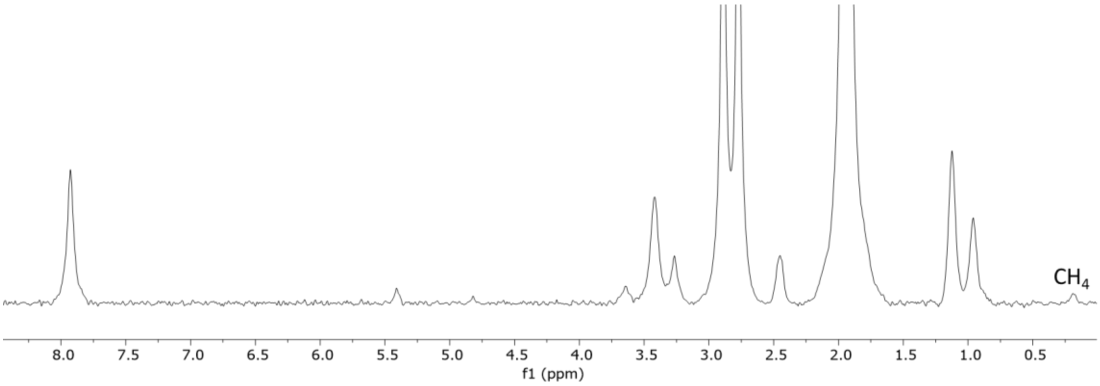

Figure S6: ^{1}H-NMR spectrum of **4** after refluxing for 24 hours in CD_3CN.

Magnetometry

General

Magnetic measurements were conducted with a Quantum Design MPMS3 SQUID Magnetometer at the University of California, Los Angeles. A polycrystalline sample of 3 was wrapped in plastic film and placed in a gelatin capsule. The capsule was then inserted into a plastic straw. Magnetization data at 100 K from 0 to 4 T were collected to confirm the absence of ferromagnetic impurities. Direct current variable temperature magnetic susceptibility measurements were collected between 1.8 and 300 K. Reduced magnetization data was collected between 1.8 and 9 K at fields between 1 and 7 T. Magnetic susceptibility data was corrected for diamagnetism of the sample, estimated using Pascal's constants. Magnetic susceptibility data was simulated with julX (Prof. Eckhard Bill) and reduced magnetization data was simulated with PHI.

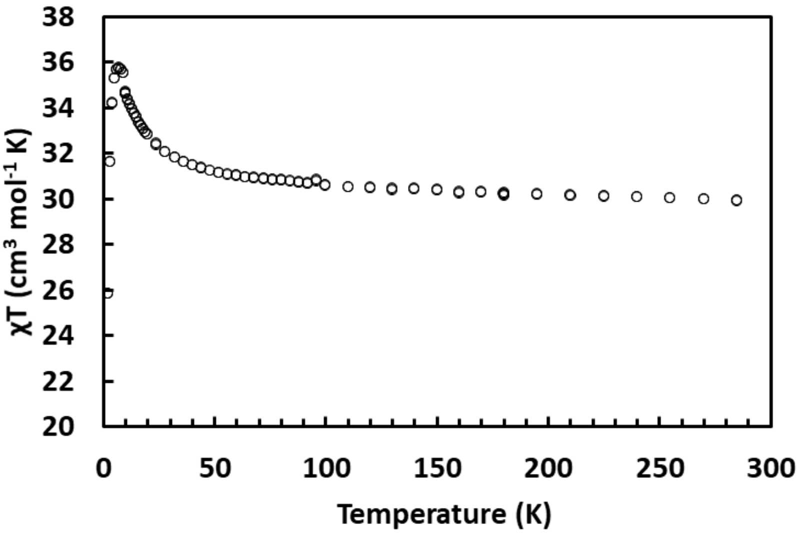

Figure S9: Magnetic susceptibility of **4**.

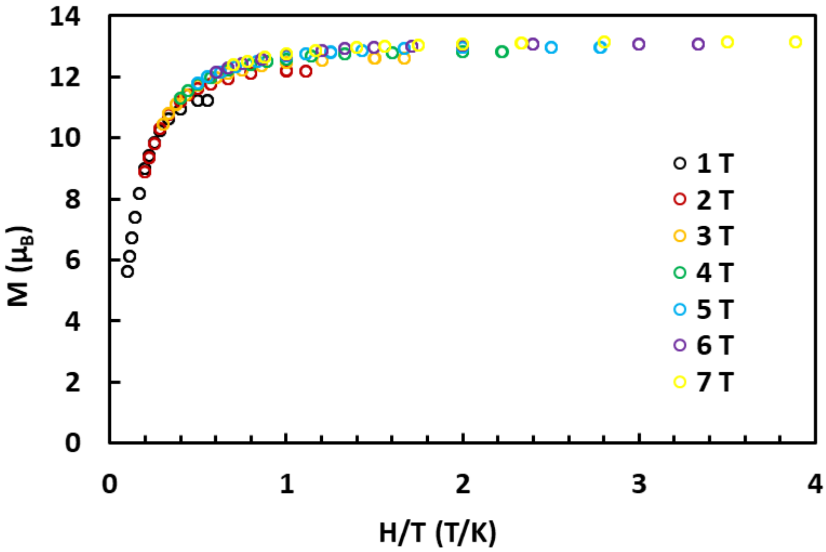

Figure 10: Reduced magnetism of **4** at different fields.

Mössbauer Measurements

General

Zero applied field ^{57}Fe Mossbauer spectra were recorded at 80 K in constant acceleration mode on a spectrometer from See Co (Edina, MN) equipped with an SVT- S6 400 cryostat (Janis, Wilmington, WA). The isomer shifts are relative to the centroid of an α-Fe foil signal at room temperature. Samples were prepared by mixing polycrystalline material (20 mg) with boron nitride in a cup fitted with a screw cap. The data were fit to Lorentzian lineshapes using WMOSS (www.wmoss.org).

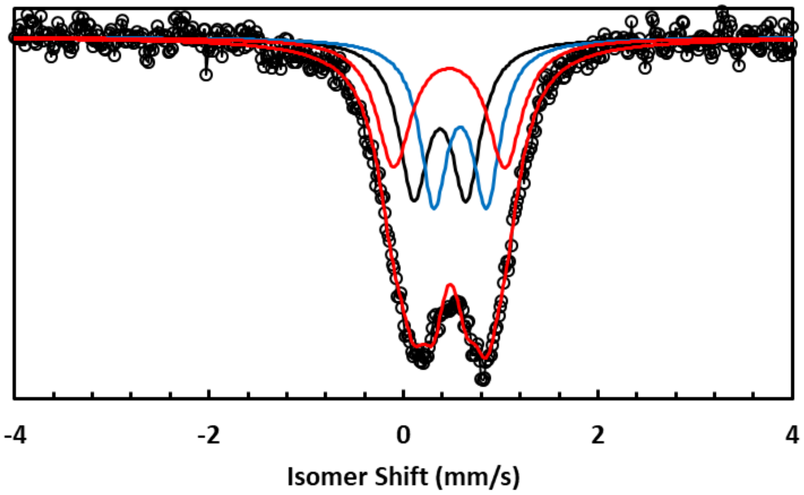

χ^2 = 0.57	δ (mm/s)	ΔE_q (mm/s)
Site 1	0.37	0.54
Site 2	0.58	0.54
Site 3	0.47	1.14
Average	0.47	0.74

Figure S7: Mössbauer spectrum of **4** using a 3 site fit.

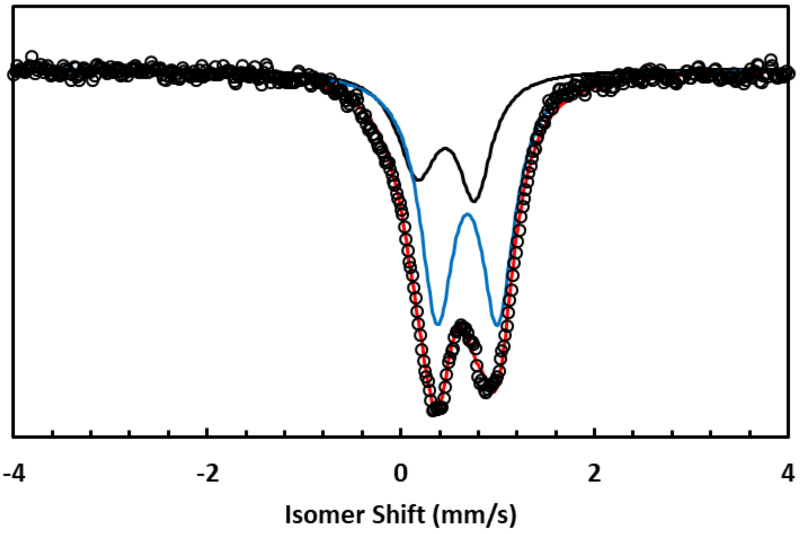

χ^2 = 0.57	δ (mm/s)	ΔE_q (mm/s)
Site 1 (2/3)	0.63	0.47
Site 2 (1/3)	0.63	0.88
Average	0.63	0.59

Figure S8: Figure SX: Mössbauer spectrum of **6** using a 2 site fit.

X-ray Crystallography Data

General

XRD data were collected at 100 K on a Bruker AXS D8 KAPPA or Bruker AXS D8 VENTURE diffractometer [microfocus sealed X-ray tube, λ(Mo Kα) = 0.71073 Å or λ(Cu Kα) = 1.54178 Å]. All manipulations, including data collection, integration, and scaling, were carried out using the Bruker APEX3 software.[71] Absorption corrections were applied using SADABS.[72] Structures were solved by direct methods using XS(incorporated into SHELXTL),[73] Sir92[74] or SUPERFLIP[75] and refined using full-matrix least-squares on Olex2[76] to convergence. All non-H atoms were refined using anisotropic displacement parameters. H atoms were placed in idealized positions and refined using a riding model.

Crystal Structure Refinement Details

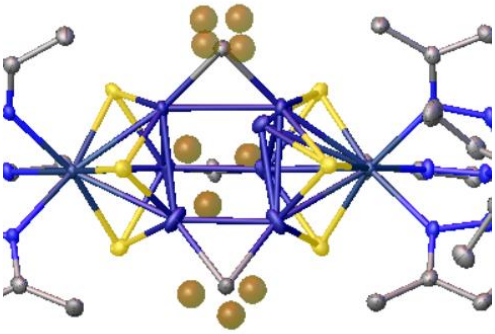

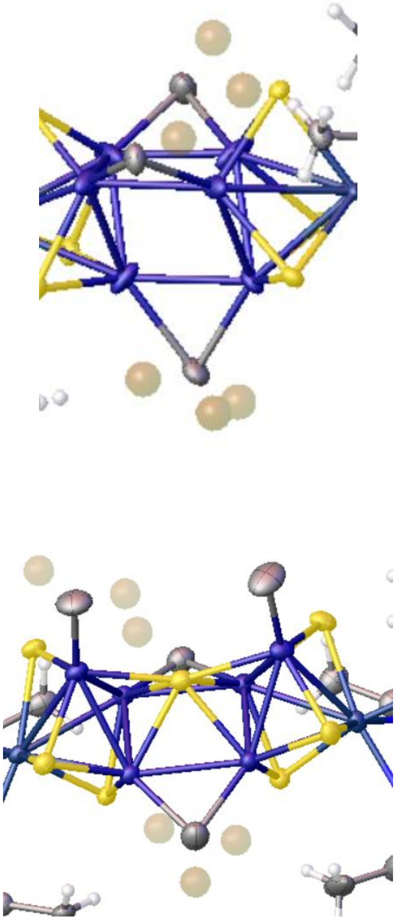

Figure S7: Refinement of **4** (top), **5** (middle), and **6** (bottom) without hydrogen atoms modelled showing electron density possibly corresponding to hydrogen atoms near the carbon atoms. For the structures of **5** and **6**, symmetry operations must be applied to the top two sets of electron density peaks such that they are doubled.

Cluster	**4**	**5**	**6**
CCDC			
Empirical formula	$C_{44}H_{66}BFe_3N_6S_3MoO$	$C_{37}H_{57}BO_1Fe_4N_{10}S_5Mo$	$C_{28}H_{47}BFe_3N_9S_3Mo$
Formula weight	1065.50	1158.77	872.49
Temperature/K	100	100	100
Crystal system	Monoclinic	Monoclinic	Orthorhombic
Space group	C 1 2/c 1	P 1 21/n 1	P c a 21
a/Å	20.5251(14)	10.6400(4)	19.7769(5)
b/Å	17.8552(13)	39.9480(16)	20.2774(5)
c/Å	22.0096(15)	17.9085(7)	19.0102(5)
α/°	90	90	90
β/°	113.776(3)	97.291(2)	90
γ/°	90	90	90
Volume/Å^3	7381.5(9)	7550.4(5)	7623.5(3)
Z	8	6	8
ρ_{calc}/g cm^{-3}	1.918	1.529	1.520

μ/mm^{-1}	13.969	13.762	13.387
F(000)	4424	3546	3575
Crystal size/mm^3	0.04 × 0.04 × 0.16	0.03 × 0.06 × 0.07	0.02 × 0.05 × 0.11
Radiation	Cu Kα	Cu Kα	Cu Kα
θ_{max}/°	72.588	72.310	72.475
Index ranges	$-25 \leq h \leq 25$ $-22 \leq k \leq 22$ $-26 \leq l \leq 27$	$-13 \leq h \leq 13$ $-49 \leq k \leq 49$ $-19 \leq l \leq 21$	$-24 \leq h \leq 24$ $-24 \leq k \leq 25$ $-23 \leq l \leq 23$
Reflections measured	53417	106755	106570
Independent reflections	9913	9907	9359
Restraints/Parameters	0/423	0/847	1/1255
GOF on F^2	1.049	1.138	1.023
R-factor	0.0302	0.0962	0.0511
Weighted R-factor	0.0684	0.2001	0.1188
Largest diff. peak/hole/e Å^{-3}	0.622/-0.696	3.302/-1.558	1.438/-1.493

References

(1) Campos, J.; López-Serrano, J.; Peloso, R.; Carmona, E. Methyl Complexes of the Transition Metals. *Chemistry – A European Journal* **2016**, *22* (19), 6432–6457. https://doi.org/10.1002/chem.201504483.

(2) Cui, M.; Jia, G. Organometallic Chemistry of Transition Metal Alkylidyne Complexes Centered at Metathesis Reactions. *J. Am. Chem. Soc.* **2022**, *144* (28), 12546–12566. https://doi.org/10.1021/jacs.2c01192.

(3) Byer, A. S.; Yang, H.; McDaniel, E. C.; Kathiresan, V.; Impano, S.; Pagnier, A.; Watts, H.; Denler, C.; Vagstad, A. L.; Piel, J.; Duschene, K. S.; Shepard, E. M.; Shields, T. P.; Scott, L. G.; Lilla, E. A.; Yokoyama, K.; Broderick, W. E.; Hoffman, B. M.; Broderick, J. B. Paradigm Shift for Radical S-Adenosyl-l-Methionine Reactions: The Organometallic Intermediate Ω Is Central to Catalysis. *J. Am. Chem. Soc.* **2018**, *140* (28), 8634–8638. https://doi.org/10.1021/jacs.8b04061.

(4) Yang, H.; Impano, S.; Shepard, E. M.; James, C. D.; Broderick, W. E.; Broderick, J. B.; Hoffman, B. M. Photoinduced Electron Transfer in a Radical SAM Enzyme Generates an S-Adenosylmethionine Derived Methyl Radical. *J. Am. Chem. Soc.* **2019**, *141* (40), 16117–16124. https://doi.org/10.1021/jacs.9b08541.

(5) Burén, S.; Jiménez-Vicente, E.; Echavarri-Erasun, C.; Rubio, L. M. Biosynthesis of Nitrogenase Cofactors. *Chem. Rev.* **2020**, *120* (12), 4921–4968. https://doi.org/10.1021/acs.chemrev.9b00489.

(6) Hoffman, B. M.; Lukoyanov, D.; Yang, Z.-Y.; Dean, D. R.; Seefeldt, L. C. Mechanism of Nitrogen Fixation by Nitrogenase: The next Stage. *Chemical reviews* **2014**, *114* (8), 4041–4062.

(7) Tondreau, A. M.; Milsmann, C.; Patrick, A. D.; Hoyt, H. M.; Lobkovsky, E.; Wieghardt, K.; Chirik, P. J. Synthesis and Electronic Structure of Cationic, Neutral, and Anionic Bis(Imino)Pyridine Iron Alkyl Complexes: Evaluation of Redox Activity in Single-Component Ethylene Polymerization Catalysts. *J. Am. Chem. Soc.* **2010**, *132* (42), 15046–15059. https://doi.org/10.1021/ja106575b.

(8) Muñoz, S. B.; Daifuku, S. L.; Brennessel, W. W.; Neidig, M. L. Isolation, Characterization, and Reactivity of Fe8Me12 –: Kochi's S = 1/2 Species in Iron-Catalyzed Cross-Couplings with MeMgBr and Ferric Salts. *J. Am. Chem. Soc.* **2016**, *138* (24), 7492–7495. https://doi.org/10.1021/jacs.6b03760.

(9) Hashimoto, T.; Urban, S.; Hoshino, R.; Ohki, Y.; Tatsumi, K.; Glorius, F. Synthesis of Bis(N-Heterocyclic Carbene) Complexes of Iron(II) and Their Application in Hydrosilylation and Transfer Hydrogenation. *Organometallics* **2012**, *31* (12), 4474–4479. https://doi.org/10.1021/om300298q.

(10) Bolm, C.; Legros, J.; Le Paih, J.; Zani, L. Iron-Catalyzed Reactions in Organic Synthesis. *Chemical reviews* **2004**, *104* (12), 6217–6254.

(11) George, S. J.; Barney, B. M.; Mitra, D.; Igarashi, R. Y.; Guo, Y.; Dean, D. R.; Cramer, S. P.; Seefeldt, L. C. EXAFS and NRVS Reveal a Conformational Distortion of the FeMo-Cofactor in the MoFe Nitrogenase Propargyl Alcohol Complex. *Journal of Inorganic Biochemistry* **2012**, *112*, 85–92. https://doi.org/10.1016/j.jinorgbio.2012.02.004.

(12) Jiang, H.; Ryde, U. Thermodynamically Favourable States in the Reaction of Nitrogenase without Dissociation of Any Sulfide Ligand. *Chemistry – A European Journal* **2022**, *28* (14), e202103933. https://doi.org/10.1002/chem.202103933.

(13) McKee, M. L. A New Nitrogenase Mechanism Using a CFe8S9 Model: Does H2 Elimination Activate the Complex to N2 Addition to the Central Carbon Atom? *J. Phys. Chem. A* **2016**, *120* (5), 754–764. https://doi.org/10.1021/acs.jpca.5b10384.

(14) Dance, I. Computational Investigations of the Chemical Mechanism of the Enzyme Nitrogenase. *ChemBioChem* **2020**, *21* (12), 1671–1709. https://doi.org/10.1002/cbic.201900636.

(15) Dance, I. The Stereochemistry and Dynamics of the Introduction of Hydrogen Atoms onto FeMo-Co, the Active Site of Nitrogenase. *Inorg. Chem.* **2013**, *52* (22), 13068–13077. https://doi.org/10.1021/ic401818k.

(16) Rao, L.; Xu, X.; Adamo, C. Theoretical Investigation on the Role of the Central Carbon Atom and Close Protein Environment on the Nitrogen Reduction in Mo Nitrogenase. *ACS Catal.* **2016**, *6* (3), 1567–1577. https://doi.org/10.1021/acscatal.5b02577.

(17) M. Siegbahn, P. E. The Mechanism for Nitrogenase Including All Steps. *Physical Chemistry Chemical Physics* **2019**, *21* (28), 15747–15759. https://doi.org/10.1039/C9CP02073J.

(18) Liu, L.; Rauchfuss, T. B.; Woods, T. J. Iron Carbide–Sulfide Carbonyl Clusters. *Inorganic chemistry* **2019**.

(19) Mathur, P.; Manimaran, B.; Hossain, Md. M.; Rheingold, A. L.; Liable-Sands, L. M.; Yap, G. P. A. Synthesis and Structural Characterisation of a Novel Tris-Methylene Bridged Compound (NO) 4Fe2 Se(μ-CH2)3. *Journal of Organometallic Chemistry* **1997**, *540* (1), 165–168. https://doi.org/10.1016/S0022-328X(97)00134-4.

(20) Scott, A. G.; Agapie, T. Synthesis of a Fe3–Carbyne Motif by Oxidation of an Alkyl Ligated Iron–Sulfur (WFe3S3) Cluster. *J. Am. Chem. Soc.* **2023**, *145* (1), 2–6. https://doi.org/10.1021/jacs.2c04826.

(21) Ni, C.; Power, P. P. Methyl-Bridged Transition Metal Complexes (M = Cr−Fe) Supported by Bulky Terphenyl Ligands. *Organometallics* **2009**, *28* (22), 6541–6545. https://doi.org/10.1021/om900724p.

(22) Kienast, A.; Galich, L.; Murray, K. S.; Moubaraki, B.; Lazarev, G.; Cashion, J. D.; Homborg, H. μ-Carbido Diporphyrinates and Diphthalocyaninates of Iron and Ruthenium. *J. Porphyrins Phthalocyanines* **1997**, *01* (02), 141–157. https://doi.org/10.1002/(SICI)1099-1409(199704)1:2<141::AID-JPP18>3.0.CO;2-M.

(23) Brown, A. C.; Suess, D. L. M. Reversible Formation of Alkyl Radicals at [Fe4S4] Clusters and Its Implications for Selectivity in Radical SAM Enzymes. *J. Am. Chem. Soc.* **2020**, *142* (33), 14240–14248. https://doi.org/10.1021/jacs.0c05590.

(24) Ye, M.; Thompson, N. B.; Brown, A. C.; Suess, D. L. M. A Synthetic Model of Enzymatic [Fe4S4]–Alkyl Intermediates. *J. Am. Chem. Soc.* **2019**, *141* (34), 13330–13335. https://doi.org/10.1021/jacs.9b06975.

(25) McSkimming, A.; Sridharan, A.; Thompson, N. B.; Müller, P.; Suess, D. L. M. An [Fe4S4]3+–Alkyl Cluster Stabilized by an Expanded Scorpionate Ligand. *J. Am. Chem. Soc.* **2020**, *142* (33), 14314–14323. https://doi.org/10.1021/jacs.0c06334.

(26) Ohki, Y.; Murata, A.; Imada, M.; Tatsumi, K. C−H Bond Activation of Decamethylcobaltocene Mediated by a Nitrogenase Fe8S7 P-Cluster Model. *Inorg. Chem.* **2009**, *48* (10), 4271–4273. https://doi.org/10.1021/ic900284f.

(27) Joseph, C.; Cobb, C. R.; Rose, M. J. Single-Step Sulfur Insertions into Iron Carbide Carbonyl Clusters: Unlocking the Synthetic Door to FeMoco Analogues. *Angewandte Chemie International Edition* **2021**, *60* (7), 3433–3437. https://doi.org/10.1002/anie.202011517.

(28) Le, L.; Bailey, G.; Scott, A.; Agapie, T. Cluster Models of FeMoco with Sulfide and Carbyne Ligands: Effect of Interstitial Atom in Nitrogenase Active Site. **2021**. https://doi.org/10.26434/chemrxiv.14614152.v1.

(29) Böttcher, H.-C.; Merzweiler, K.; Wagner, C. Koordinativ ungesättigte Dieisenkomplexe: Synthese und Kristallstrukturen von [Fe2(CO)4(μ-H)(μ-PtBu2)(μ-Ph2PCH2PPh2)] und [Fe2(CO)4(μ-CH2)(μ-H)(μ-PtBu2)(μ-Ph2PCH2PPh2)]. *Zeitschrift für anorganische und allgemeine Chemie* **1999**, *625* (6), 857–865. https://doi.org/10.1002/(SICI)1521-3749(199906)625:6<857::AID-ZAAC857>3.0.CO;2-3.

(30) Chau, C. N.; Yu, Y. F.; Wojcicki, A.; Calligaris, M.; Nardin, G.; Balducci, G. Synthesis and Characterization of Isomeric Binuclear Double-Bridged Alkylidene-Tetraphenyldiphosphine and Diphenylphosphido-Methylenediphenylphosphine Iron Nitrosyl Complexes. *Organometallics* **1987**, *6* (2), 308–316. https://doi.org/10.1021/om00145a012.

(31) Yu, Y. F.; Chau, C. N.; Wojcicki, A.; Calligaris, M.; Nardin, G.; Balducci, G. Reduction Chemistry of Fe2(NO)4(.Mu.-PPh2)2 and Selective Synthesis of Isomeric Doubly Bridged Methylenetetraphenylbiphosphine and (Diphenylphosphido)Methylenediphenylphosphine Complexes. *J. Am. Chem. Soc.* **1984**, *106* (12), 3704–3705. https://doi.org/10.1021/ja00324a069.

(32) Korswagen, R.; Alt, R.; Speth, D.; Ziegler, M. L. Novel Reactions of Phosphorus Ylides with Carbonyl(Cyclopentadienyl)Metal Complexes: Preparative Access to μ-Alkylidene Complexes and Unexpected Acylations. *Angewandte Chemie International Edition in English* **1981**, *20* (12), 1049–1051. https://doi.org/10.1002/anie.198110491.

(33) Altbach, M. I.; Fronczek, F. R.; Butler, L. G. Structure of a New Polymorph of Cis-[(μ-CH2)(μ-CO){Fe(H5-C5H5)CO}2]. *Acta Cryst C* **1992**, *48* (4), 644–650. https://doi.org/10.1107/S010827019101123X.

(34) Fong, R. H.; Hersh, W. H. Synthesis and X-Ray Crystal Structure of (.Mu.3-COCH3)(.Mu.2-CH2)(Cp)(MeCp)Fe2Mn(CO)5, the First Carbyne-Methylene Cluster. Carbon-Carbon Coupling to Give a Methoxyvinyl Cluster. *J. Am. Chem. Soc.* **1987**, *109* (9), 2843–2845. https://doi.org/10.1021/ja00243a058.

(35) Dawkins, G. M.; Green, M.; Orpen, A. G.; Stone, F. G. A. Synthesis and X-Ray Crystal Structure of [Fe2(μ-CH3)(μ-CO)(μ-Ph2PCH2PPh2)(η-C5H5)2][PF6]: A Salt with a Bridging Methyl Group Having a C---H---Fe Interaction. *J. Chem. Soc., Chem. Commun.* **1982**, No. 1, 41–43. https://doi.org/10.1039/C39820000041.

(36) Rossi, G.; L. Goedken, V.; Ercolani, C. M-Carbido-Bridged Iron Phthalocyanine Dimers: Synthesis and Characterization. *Journal of the Chemical Society, Chemical Communications* **1988**, *0* (1), 46–47. https://doi.org/10.1039/C39880000046.

(37) McGrady, G. S.; Turner, J. F. C.; Ibberson, R. M.; Prager, M. Structure of the Trimethylaluminum Dimer As Determined by Powder Neutron Diffraction at Low Temperature. *Organometallics* **2000**, *19* (21), 4398–4401. https://doi.org/10.1021/om0004794.

(38) Xu, G.; Wang, Z.; Ling, R.; Zhou, J.; Chen, X.-D.; Holm, R. H. Ligand Metathesis as Rational Strategy for the Synthesis of Cubane-Type Heteroleptic

Iron–Sulfur Clusters Relevant to the FeMo Cofactor. *Proceedings of the National Academy of Sciences* **2018**, *115* (20), 5089–5092.

(39) Pangborn, A. B.; Giardello, M. A.; Grubbs, R. H.; Rosen, R. K.; Timmers, F. J. Safe and Convenient Procedure for Solvent Purification. *Organometallics* **1996**, *15* (5), 1518–1520. https://doi.org/10.1021/om9503712.

Chapter IV

CHARACTERIZATION OF A FAMILY OF MFES CLUSTERS FOR SPECTROSCOPIC BENCHMARKING OF MFES CLUSTERS

Abstract

FeS clusters are ubiquitous in biology and are central to a variety of enzymatic processes. While much work has been done on the synthetic chemistry of FeS clusters to model enzymatic systems, detailed characterization of such clusters to determine electronic structures are lacking. Further, the ability to perform single point modifications on a variety of components of synthetic FeS clusters has continued to increase, thus providing additional clusters for spectroscopic benchmarking studies. Described herein is the detailed characterization of an extensive set of MFeS cubane clusters that provide information on the electronic structure and properties of this cluster motif and how these are affected by alterations in M identity, ligand identity, and oxidation state of the cluster.

Introduction

FeS clusters are ubiquitous in biology serving a wide variety of roles in catalysis, electron transfer, Fe storage and transport, oxygen binding, and protein structural stabilization.[1,2] Enzymatic FeS clusters vary in cluster topology, terminal ligands, and heterometal incorporation, which all affect electronic and therefore functional properties of the clusters.[3,4] Synthetic inorganic chemists have long sought to model such clusters in order to create more easily tunable systems that can be systematically studied using molecular characterization techniques and provide benchmarking for spectroscopy of complex enzymatic systems.[5–8] An impressive number of synthetic FeS clusters have been developed in the literature with methods for substituting terminal ligands and incorporating heterometals.[5–7] More recently, Holm and Chen and others have developed routes for systematically incorporating bridging atoms into MFeS (M = Mo and W) clusters using various terminal ligands.[9–13] The ability to vary the M atom, the (μ_3-L)Fe_3 bridging atom, the terminal atoms, and the oxidation states of the clusters presents an opportunity to systematically develop a family of MFeS clusters for ideal structure property studies. These clusters are directly relevant to the co-factors of nitrogense enzymes, FeMco, and carbon monoxide dehyrogenases (CODH) (Fig. 1) that contain heterometals and bridging ligands other than sulfides.[14,15] During turnover the nitrogenase and CODH clusters adopt different redox states and bind non-sulfurous substrates. Thus, an understanding of how heterometals, bridging ligands, and terminal ligands affect cluster structural and electronic properties is important for answering outstanding mechanistic questions and analyzing current spectroscopic characterization data.

Herein, electrochemical, Mössbauer, EPR, and magnetism data is presented for a family of MFeS clusters to gain insight into the effects of various structural components on the structural and electronic properties of the clusters. This study provides important benchmarking data for synthetic and biological FeS clusters using a system of tunable MFeS clusters.

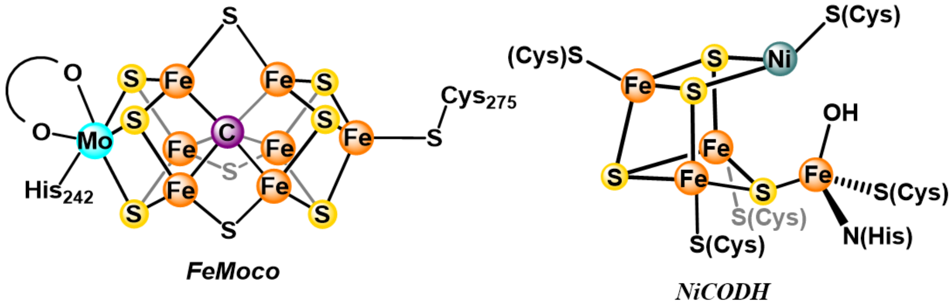

Figure 1: Structures of the FeMoco and NiCODH co-factors.

Results and Discussion

Holm and others have done an impressive amount of synthetic work to synthesize a large variety of $[TpMFe_3S_3(\mu_3\text{-}S)L_3]^n$ cubane clusters[5,9–13] (Fig. 2, Y = S) as well as to characterize these clusters using Mössbauer and electrochemical techniques.[10–13,16–23] EPR and magnetism data has also been collected on some of these clusters, although these types of characterization are more limited.[13,16–19] Provided in Tables 5 and 7 are Mössbauer parameters, spin states, and reduction potentials of literature MFeS cubane clusters.

In the simplest form, ^{57}Fe Mössbauer spectra consist of quadrupole doublets and are described by the isomer shift (δ; mm/s), the center value of the quadrupole doublet, and the quadrupole splitting (ΔE_q; mm/s), the difference between the values of the two components of the quadrupole doublet.[24] The isomer shift is indicative of the *s*-electron density at the Fe center and is sensitive to the covalency of the Fe-ligand bonds, the type and number of ligands of the Fe center, and the oxidation and spin state of the Fe center. Generally speaking, the isomer shift increases with more reduced and higher spin Fe centers and decreased covalency of the Fe-L bond resulting from the presence of hard versus soft ligands and/or increased coordination number around Fe. The quadrupole splitting reflects the electric field around an ^{57}Fe center or, more generally, the population of the d-orbitals and the symmetry of the ligand charges around the Fe center. The sensitivity of δ and ΔE_q to a number of factors indicate the importance of limiting the number of differences between complexes in comparative studies of Mössbauer parameters. The study of Fe centers in multi-metallic complexes is further complicated by coupling interactions between the Fe atoms, which affect the overall spin state of the cluster.[25,26] Complementary use of EPR and magnetism are thus helpful in understanding Mössbauer parameters. The Mössbauer parameters of FeS clusters are well understood and can provide diagnostic information about the oxidation state and ligand coordination of the Fe centers based on isomer shift and thus overall cluster electronic structure.[25]

MFeS clusters with alternate bridging ligands are not as well understood in terms of how alterations in structure affect Mössbauer parameters. However, tunability of synthetic $[TpMFe_3S_3(\mu_3\text{-}Y)L_3]^n$ clusters has been demonstrated and an increasing number of synthetic compounds provide the opportunity to understand the effects of single components of the cluster on cluster properties, which are described below. In discussions below average isomer shifts are used because of difficulties in resolving Mössbauer parameters for single Fe centers in MFeS clusters. Isomer shifts could certainly be affected by changes in the oxidation states of the M center, but this has not been demonstrated in the literature and so other proposals are discussed. Further characterization of the described clusters, including XAS, are needed to determine the relative oxidation states of the metal centers in the clusters discussed. Increased oxidation state of the M center is expected to cause decreases in the observed isomer shifts of the clusters.

One Electron Redox Events

In $[4Fe\text{-}4S]^n$ clusters the average change in isomer shift resulting from a one electron redox event is 0.09 mm/s, where there are four Fe centers that can participate in electron delocalization.[27] It should be mentioned, though, that addition of one electron to $[4Fe\text{-}4S]^n$ clusters can result in changes of isomer shifts from 0.07 mm/s to 0.14 mm/s.[7,25] In $[TpMFe_3S_3(\mu_3\text{-}Y)L_3]^n$ cubane clusters it can be seen that one electron redox events result in a 0.12 mm/s average change in the isomer shift, with a 0.08 – 0.14 mm/s range in reported values. This is true in clusters where L = Cl across different metals (M = Mo, V, or W) and S or $CSiMe_3$ bridging ligands. One exception is in $[TpMFe_3S_3(\mu_3\text{-}S)(CN)_3]^n$ clusters, where the change in isomer shift is 0.08 mm/s upon a one electron redox event, perhaps due to the pi accepting nature of the CN ligands.[24] Comparing the bond lengths of MoFeS clusters with terminal CN versus Cl ligands, the Fe-L bond lengths are considerably shorter while the other bond metrics are similar (Table 1).[18,19] Compared to the cluster with Y = S and L = Cl, the redox features of the L = CN cluster are positively shifted by about 500 mV. Both the bond metrics and the redox behavior of the L = CN cluster indicate a stronger interaction with the terminal ligands compared to the Cl case and thus greater possible electron delocalization onto the terminal ligands that could be responsible for the lower change in isomer shift upon a one electron redox event.[24] Studies on clusters with alternate terminal and bridging ligands are required to determine the possible ranges of changes in isomer shift per one electron redox event in various MFeS clusters.

Table 1: Bond Lengths and Distances (Å)			
	M = Mo **Y = S** **L = Cl** **n = 2-**	**M = Mo** **Y = S** **L = CN** **n = 2-**	**M = Mo** **Y = $CSiMe_3$** **L = Cl** **n = 2-**
M-S	2.368	2.36	2.370
Fe-S	2.282	2.26	2.273
Fe-Y	N/A	N/A	1.918
Fe-L	2.54	2.02	2.255
Fe-Fe distance	2.719	2.64	2.510

Identity of Heterometal M

Nitrogenase enzymes implement three different metals in the different FeMco clusters (M = V, Mo, or Fe), which impart different substrate reactivities and product distributions.[28,29] In $[TpMFe_3S_3(\mu_3\text{-}Y)L_3]^n$ clusters substitution of V to Mo to W causes the isomer shift to change by about 0.04 mm/s across clusters with different terminal ligands, different bridging ligands, and different overall cluster charges. In the case of Y = S, L = F, and n = 2^- the difference between W and Mo clusters is 0.09 mm/s, indicating a greater influence of the heterometal on the electronic structure of the Fe centers. Another interesting case is comparing clusters with Y = $CSiMe_3$, where the change in isomer shift between Mo and W is nearly 0 mm/s indicating a similar influence of Mo and W on the electronic structure of the Fe centers. Comparing the changes in bond metrics of the L = F and Y = $CSiMe_3$ clusters as a result of changing M to those of other clusters (Tables 2a-2c)[19,20,27,30,31] indicate no significant differences. Comparisons of redox potentials do not provide any insights either and further characterization of these clusters is necessary to explain the differences in Mössbauer properties.

Table 2a: Bond Lengths and Distances (Å)

	M = Mo Y = S L = Cl n = 2-	M = V Y = S L = Cl n = 2-	M = Mo Y = S L = F n = 2-	M = V Y = S L = F n = 2-	M = Mo Y = $CSiMe_3$ L = Cl n = 1-	M = W Y = $CSiMe_3$ L = Cl n = 1-
M-S	2.355	2.302	2.367	2.354	2.363	2.351
Fe-S	2.263	2.251	2.310	2.287	2.228	2.238
Fe-Y	N/A	N/A	N/A	N/A	1.905	1.910
Fe-L	2.232	2.232	1.862	1.853	2.209	2.213
Fe-Fe distance	2.688	2.670	2.706	2.727	2.524	2.545

Table 2b: Bond Lengths and Distances (Å)

	M = Mo Y = S L = Cl n = 1-	M = W Y = S L = Cl n = 1-	M = Mo Y = S L = BAC n = 1+	M = W Y = S L = BAC n = 1+	M = Mo Y = Cl L = Cl n = 2-	M = W Y = Cl L = Cl n = 2-
M-S	2.343	2.345	2.369	2.355	2.389	2.378
Fe-S	2.264	2.272	2.265	2.272	2.336	2.270
Fe-Y	N/A	N/A	N/A	N/A	2.443	2.495
Fe-L	2.189	2.216	2.025	2.039	2.273	2.284
Fe-Fe distance	2.719	2.692	2.657	2.642	2.641	2.618

Table 2c: Bond Lengths and Distances (Å)

	M = Mo Y = Carbyne L = BAC n = 0	M = W Y = Carbyne L = BAC n = 0	M = Mo Y = S L = CN n = 2-	M = V Y = S L = CN n = 2-	M = Mo Y = S L = PEt_3 n = 1+	M = V Y = S L = PEt_3 n = 1+
M-S	2.378	2.365	2.356	2.335	2.369	2.346
Fe-S	2.257	2.270	2.259	2.261	2.224	2.240
Fe-Y	1.949	1.949	N/A	N/A	N/A	N/A
Fe-L	2.009	1.994	2.016	2.035	2.309	2.377
Fe-Fe distance	2.507	2.506	2.637	2.646	2.585	2.607

Identities of Terminal Ligands

Changes in the terminal ligands can result in significant alterations of the isomer shift in $[TpMFe_3S_3(\mu_3\text{-}Y)L_3]^n$ clusters. In clusters with bridging sulfides, the isomer shift can range from 0.52 – 0.63 mm/s in clusters with the same overall cluster and metal core (MFe_3) charge, with stronger field ligands expectedly resulting in lower isomer shifts.[24] The range is even larger if one considers clusters with the same metal core charge, but different overall complex charge (0.34 – 0.63 mm/s), where ligand charge and overall complex charge likely play a role. Comparing bond lengths between clusters with lower versus higher isomer shifts, the only clear trend seems to be that decreased isomer shifts resulting from terminal ligand substitution seems to correlate with shorter Fe-Fe bonds (Table 3a and 3b). Generally, decreases in isomer shifts are accompanied by negative shifts in redox potentials, except for in the case of N_3 versus CN where the trend is opposite. This perhaps seems counter intuitive considering that decreased isomer shifts would indicate more oxidized Fe centers, which should be easier to reduce.

Table 3a: Bond Lengths and Distances (Å)

	M = Mo Y = S L = Cl n = 1-	**M = Mo Y = S L = SEt n = 1-**	**M = Mo Y = S L = Cl n = 2-**	**M = Mo Y = S L = F n = 2-**	**M = Mo Y = S L = CN n = 2-**	**M = Mo Y = S L = SPh n = 2-**	**M = Mo Y = S L = PEt_3 n = 1+**
M-S	2.343	2.354	2.368	2.367	2.356	2.367	2.369
Fe-S	2.264	2.263	2.282	2.310	2.259	2.280	2.224
Fe-L	2.189	2.231	2.254	1.862	2.016	2.276	2.309
Fe-Fe distance	2.719	2.688	2.719	2.706	2.637	2.693	2.585

Table 3b: Bond Lengths and Distances (Å)					
	M = V **Y = S** **L = Cl** **n = 2-**	**M = V** **Y = S** **L = F** **n = 2-**	**M = V** **Y = S** **L = CN** **n = 2-**	**M = V** **Y = S** **L = N_3** **n = 2-**	**M = V** **Y = S** **L = PEt_3** **n = 1+**
M-S	2.302	2.354	2.335	2.349	2.346
Fe-S	2.251	2.287	2.261	2.278	2.240
Fe-L	2.232	1.853	2.035	1.970	2.377
Fe-Fe distance	2.670	2.727	2.646	2.695	2.607

Identity of Bridging Ligand

Comparison of isomer shifts between $[TpMFe_3S_3(\mu_3\text{-}Y)L_3]^n$ clusters with varying bridging ligands Y, but with $[MFe_3]^m$ cores of the same oxidation state show a range of values. Within W clusters that contain terminal BAC ligands, the values range from 0.30 mm/s (μ_3-N) to 0.49 and 0.50 mm/s for the isoelectronic μ_3-$NSiMe_3$ and μ_3-S ligands, respectively. In W and Mo clusters with terminal Cl ligands, clusters with $[MFe_3]^{11+}$ cores show only a 0.02 mm/s difference between μ_3-S and μ_3-$CSiMe_3$ bridging ligands. Comparing the bond metrics and the redox potentials between the clusters, there is no clear trend to account for the differences in isomer shifts.

Table 4a: Bond Lengths and Distances (Å)				
	M = Mo **Y = S** **L = Cl** **n = 1-**	**M = Mo** **Y = $CSiMe_3$** **L = Cl** **n = 2-**	**M = W** **Y = S** **L = Cl** **n = 1-**	**M = W** **Y = $CSiMe_3$** **L = Cl** **n = 2-**
M-S	2.343	2.363	2.345	2.351
Fe-S	2.264	2.228	2.272	2.238
Fe-Y	N/A	1.905	N/A	1.910
Fe-L	2.189	2.209	2.216	2.213
Fe-Fe distance	2.719	2.524	2.692	2.545

Table 4b: Bond Lengths and Distances (Å)

	M = W **Y = N** **L = BAC** **n = 0**	**M = W** **Y = S** **L = BAC** **n = 1+**	**M = W** **Y = $NSiMe_3$** **L = BAC** **n = 1+**	**M = W** **Y = Carbyne** **L = BAC** **n = 0**
M-S	2.359	2.355	2.356	2.365
Fe-S	2.244	2.272	2.281	2.270
Fe-Y	1.849	2.275	1.949	1.949
Fe-L	1.989	2.039	2.047	1.994
Fe-Fe distance	2.503	2.642	2.574	2.506

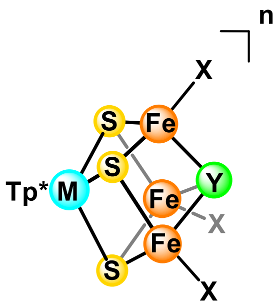

Figure 2: Cubane cluster of the type $[TpMFe_3S_3(\mu_3\text{-}Y)X_3]^n$.

Table 5: Average Mössbauer parameters and spin states of literature $[TpMFe_3S_3(\mu_3\text{-}S)L_3]^n$ cubane clusters

Cluster	**$[MFe_3]^{m+}$**	**δ (mm/s)**	**Δ (mm/s)**	**Spin State**	**References**
$[TpMoFe_3S_4(PEt_3)_2(N_3)]$	10+	0.44	1.33	2	[17]
$[TpMoFe_3S_4Cl_3]^{1-}$	11+	0.49	0.77	3/2	[18] [19]
$[TpMoFe_3S_4Cl_3]^{2-}$	10+	0.61	0.91		
$[TpMoFe_3S_4(SEt)_3]^{1-}$	11+	0.39	1.02		
$[TpMoFe_3S_4F_3]^{2-}$	10+	0.63	1.28		
$[TpMoFe_3S_4(SPh)_3]^{2-}$	10+	0.52	1.28		
$[TpMoFe_3S_4(CN)_3]^{2-}$	10+	0.47	1.46		
$[TpMoFe_3S_4(PEt_3)_3]^{1+}$	10+	0.34	1.69		

$[TpMoFe_3S_4(CN)_3]^{3-}$	9+	0.55	2.31		
$[TpVFe_3S_4Cl_3]^{1-}$	11+	0.43	1.19	3/2 g = 2, D =2.3 cm^{-1}, E/D = 0.33	19 16
$[TpVFe_3S_4Cl_3]^{2-}$	10+	0.55	1.12	0	16
$[TpVFe_3S_4F_3]^{2-}$	10+	0.54	1.10		20
$[TpVFe_3S_4(N_3)_3]^{2-}$	10+	0.56	1.28		
$[TpVFe_3S_4(CN)_3]^{2-}$	10+	0.42	1.10		
$[TpVFe_3S_4(PEt)_3]^{1+}$	10+	0.38	1.02	3/2 (g = 2, D =1.11 cm^{-1}, E/D = 0.24)	16
$[TpMoFe_3SeS_3(PEt_3)_3]^{1+}$	10+	0.51			21
$[TpMoFe_3SeS_3Cl_3]^{1-}$	11+	0.52	0.96		
$[TpMoFe_3SeS_3(SEt)_3]^{1-}$	11+	0.44	1.27		

Table 6: Average Mössbauer parameters and spin states of $[TpMFe_3S_3(\mu_3\text{-}X)L_3]^n$ cubane clusters. NHC = 1,3-diisopropyl-4,5-dimethylimidazol-2-ylidene ($^iPr_2Me_2$NHC)

Cluster	$[MFe_3]^{m+}$	δ (mm/s)	Δ (mm/s)	Spin State
$[Tp^*WFe_3S_3(\mu_3\text{-}CSiMe_3)(Cl)_3]^{1-}$	12+	0.34	0.62	0
$[Tp^*WFe_3S_3(\mu_3\text{-}CSiMe_3)(Cl)_3]^{2-}$	11+	0.48	0.86	3/2
$[Tp^*MoFe_3S_3(\mu_3\text{-}CSiMe_3)(Cl)_3]^{1-}$	12+	0.34	0.61	0
$[Tp^*MoFe_3S_3(\mu_3\text{-}CSiMe_3)(Cl)_3]^{2-}$	11+	0.47	0.92	3/2

$[\mathrm{Tp^*WFe_3S_3(\mu_3\text{-}NPPh_3)(Cl)_3}]^{1-}$	10+	0.52	1.10	
$[\mathrm{Tp^*WFe_3S_3(\mu_3\text{-}S)(BAC)_3}]^{1+}$	10+	0.50	1.22	
$[\mathrm{Tp^*WFe_3S_3(\mu_3\text{-}N)(BAC)_3}]$	10+	0.30	1.82	
$[\mathrm{Tp^*WFe_3S_3(\mu_3\text{-}NSiMe_3)(BAC)_3}]^{1+}$	10+	0.49	1.37	2
$[\mathrm{Tp^*WFe_3S_3(\mu_3\text{-}NSiMe_3)(NHC)_3}]^{1+}$	10+	0.39	1.02	
$[\mathrm{Tp^*WFe_3S_3(\mu_3\text{-}carbyne)(BAC)_2}]$	11+	0.38	1.26	
$[\mathrm{Tp^*MoFe_3S_3(\mu_3\text{-}carbyne)(BAC)_2}]$	11+	0.34	1.14	
$[\mathrm{Tp^*MoFe_3S_3(\mu_3\text{-}S)(BAC)_3}]^{1+}$	10+	0.45	1.22	
$[\mathrm{Tp^*MoFe_3S_3(\mu_3\text{-}CO)(BAC)_3}]^{1+}$	8+	0.35	1.48	
$[\mathrm{Tp^*WFe_3S_3(\mu_3\text{-}Cl)Cl_3}]^{2-}$	9+	0.63	1.15	9/2
$[\mathrm{Tp^*MoFe_3S_3(\mu_3\text{-}Cl)Cl_3}]^{2-}$	9+	0.59	1.28	9/2
$[\mathrm{Tp^*WFe_3S_3(CH_2SiMe_3)_3}]^{1-}$	9+	0.35	1.83	9/2
$[\mathrm{Tp^*MoFe_3S_3(CH_2SiMe_3)_3}]^{1-}$	9+	0.29	1.36	9/2
$[\mathrm{Tp^*WFe_3S_3(BAC)_3}]^{1+}$	8+	0.42	1.04	

Table 7: Reduction potentials vs. SCE of literature $[TpMFe_3S_3(\mu_3\text{-}S)L_3]^n$ cubane clusters in MeCN

Cluster	10+/9+ (V)	11+/10+ (V)	12+/11+	Difference	Reference
$[TpVFe_3S_4(SPh)_3]^{2-}$	-1.50	-0.41		1.09	[22]
$[TpVFe_3S_4(SH)_3]^{2-}$	-1.56	-0.37		1.19	
$[TpVFe_3S_4Cl_3]^{2-}$	-1.40	-0.11		1.29	[19]
$[TpVFe_3S_4F_3]^{2-}$	-1.57	-0.25		1.32	
$[TpVFe_3S_4(N_3)_3]^{2-}$	-1.29	-0.11		1.18	[20]
$[TpVFe_3S_4(CN)_3]^{2-}$	-1.18	-0.04		1.14	
$[TpMoFe_3S_4Cl_3]^{1-}$	-1.64	-0.57		1.08	[18]
$[TpMoFe_3S_4(SEt)_3]^{1-}$		-0.96			
$[TpMoFe_3S_4F_3]^{2-}$	-1.87	-0.73		1.14	
$[TpMoFe_3S_4(SPh)_3]^{2-}$	-1.76	-0.69		1.18	
$[TpMoFe_3S_4(CN)_3]^{2-}$	-1.49	-0.23		1.26	
$[TpMoFe_3S_4(PEt_3)_3]^{1+}$	-0.79				
$[TpMoFe_3SeS_3(PEt_3)_3]^{1+}$	-0.89				[21]
$[TpMoFe_3SeS_3Cl_3]^{1-}$	-1.64	-0.69		0.95	
$[TpMoFe_3SeS_3(SEt)_3]^{1-}$	-1.92	-1.10		0.82	
$[Tp^*WFe_3S_3(\mu_3\text{-}NSiMe_3)(Cl)_3]^{1-}$		-1.88	-2.42	0.54	[23]
$[Tp^*WFe_3S_3(\mu_3\text{-}NSiMe_3)(SEt)_3]^{1-}$	-0.95	-2.12		1.16	

[Tp*WFe$_3$S$_3$(μ$_3$-NSiMe$_3$)(SMe)$_3$]$^{1-}$	-0.93	-2.09		1.15	
[Tp*WFe$_3$S$_3$(μ$_3$-NSiMe$_3$)(S^{p}Tol)$_3$]$^{1-}$	-0.73	-1.85		1.12	
[Tp*WFe$_3$S$_3$(μ$_3$-NSiMe$_3$)(SPh)$_3$]$^{1-}$	-0.75	-1.87		1.12	
[Tp*WFe$_3$S$_3$(μ$_3$-NSiMe$_3$)(N$_3$)$_3$]$^{1-}$	-0.85	-1.77		0.92	
[Tp*WFe$_3$S$_3$(μ$_3$-NSiMe$_3$)(NHC^{Me})$_3$]$^{1+}$		-1.28	-2.42	1.15	

Table 8: Reduction potentials vs. Fc/Fc$^+$ of [TpMFe$_3$S$_3$(μ$_3$-X)L$_3$]^n clusters in MeCN

Cluster	**9+/8+**	**10+/9+**	**11+/10+**	**12+/11+**	**13+/12+**	**Difference**
[Tp*WFe$_3$S$_3$(μ$_3$-carbyne)(BAC)$_2$]			-2.82	-1.75		1.70
[Tp*MoFe$_3$S$_3$(μ$_3$-carbyne)(BAC)$_2$]			-2.75	-1.69		1.60
[Tp*WFe$_3$S$_3$(μ$_3$-NSiMe$_3$)(BAC)$_3$]$^{1+}$		-2.30	-1.10			1.20
[Tp*WFe$_3$S$_3$(μ$_3$-NSiMe$_3$)(NHC)$_3$]$^{1+}$		-2.13	-1.35			0.78

[Tp*WFe$_3$S$_3$(μ$_3$-N)(BAC)$_3$]		-2.10	-0.90			1.20
[Tp*WFe$_3$S$_3$(μ$_3$-S)(Cl)$_3$]$^{1-}$			-1.13	-0.65		0.48
[Tp*MoFe$_3$S$_3$(μ$_3$-S)(Cl)$_3$]$^{1-}$				-0.55		
[Tp*WFe$_3$S$_3$(μ$_3$-S)(BAC)$_3$]$^{1+}$		-1.83	-0.62			1.21
[Tp*MoFe$_3$S$_3$(μ$_3$-S)(BAC)$_3$]$^{1+}$		-1.81	-0.71			
[Tp*WFe$_3$S$_3$(μ$_3$-S)(NHC)$_3$]$^{1+}$		-1.82	-0.62			1.20
[Tp*W(μ$_3$-NPPh$_3$)(NHC)$_3$]$^{2+}$		-1.23	-0.22			1.01
[Tp*WFe$_3$S$_3$(CH$_2$SiMe$_3$)$_3$]$^{1-}$	-0.97	0.59				1.56
[Tp*WFe$_3$S$_3$(BAC)$_3$]$^{1+}$	-1.10 (-2.25)					1.15
[Tp*WFe$_3$S$_3$(μ$_3$-CSiMe$_3$)(Cl)$_3$]$^{1-}$				-2.82	-1.59	0.90

Spin States

Spin states of [TpMFe$_3$S$_3$(μ$_3$-S)L$_3$]^n are generally lacking in the literature, but electronic configurations of clusters with known values can be proposed (Fig. 3; see Chapter II). Clusters

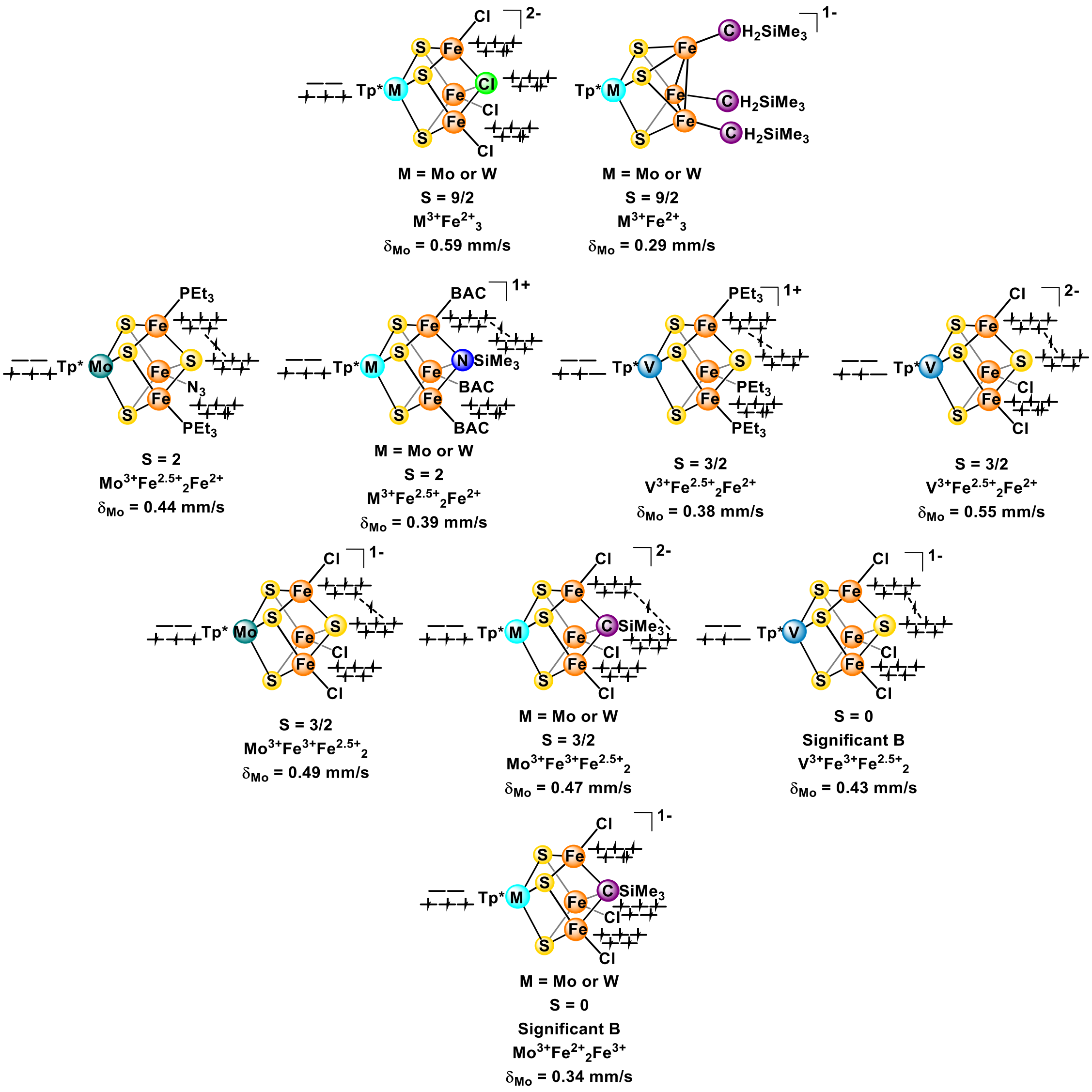

Figure 3: Proposed electronic structures of cubane clusters.

with $[MFe_3]^{11+}$ cores, terminal chloride ligands, and M = Mo or W exhibit S = 3/2 spin states with either μ_3-S and μ_3-$CSiMe_3$ bridging ligands. This can be explained based on a similar electronic structure to that proposed in FeMoco where two $Fe^{2.5+}$ centers with a delocalized electron are antiferromagnetically coupled to the Fe^{3+} center and W^{3+} center that is in a non-Hund electron configuration.[26] Clusters with $[MFe_3]^{10+}$ cores (M = Mo or W) can have the same spin states of S = 2 with differing terminal and bridging ligands and with M in a non-Hund electron configuration, which is an electronic configuration proposed for the E_1 state of FeMoco.[26] Clusters with $[MFe_3]^{9+}$ cores (M = Mo or W) exhibit spin states of 9/2 whether there is a bridging ligand or not. In these cases, the M atom would need to be in a Hund electron configuration and antiferromagnetically coupled to each of the ferrous Fe centers. This type of coupling has also been observed in all ferrous [4Fe-4S] clusters, where three Fe centers are antiferromagnetically coupled to the final Fe center.[32–35] In all cases, the same spin states are exhibited for clusters with fairly different isomer shifts, up to 0.30 mm/s in one case, which could be a consequence of different relative Fe oxidation states and/or different ligands.

In the case of V containing clusters, different spin states are achieved for the same core VFe_3 oxidation states because V is a d_5 metal. With $[VFe_3]^{10+}$ cores, a spin state of $S = 3/2$ is observed with clusters containing bridging sulfide ligands and chloride or phosphine terminal ligands. The electronic coupling to describe this spin state is similar to that for clusters containing $[MFe_3]^{11+}$ cores (M = Mo or W) and has been proposed for one state of VFeco.[29] The isomer shifts are 0.38 mm/s and 0.55 mm/s, likely due to differences in terminal ligands, but still exhibit the same spin state. In the case of a $[VFe_3]^{11+}$ core, an interesting spin state of $S = 0$ is observed, which cannot be explained by the simplistic coupling scheme shown in Fig. 3, even if the V is reduced to V^{2+} and the Fe^{2+} center is oxidized to Fe^{3+}. An alternate explanation is that the Fe centers are in an intermediate spin state due to a non-tetrahedral d-splitting. However, there is not precedence for this in the FeS cluster literature for clusters with bridging sulfide ligands (see Chapter II).[36] A final explanation is that there is significant double exchange interactions between the metal centers that results in intermediate spin states.[37] Similar explanations are proposed for the carbyne bridged clusters with a $[MFe_3]^{12+}$ core (M = Mo or W).

Redox Properties

Substitutions of anionic terminal ligands or the M atom seem to have minimal effects on the reduction potentials of the $[TpMFe_3S_3(\mu_3\text{-}S)L_3]^n$ clusters. However, substituting anionic terminal ligands for neutral ligands has much larger effects, as can be seen from the 850 mV negative shift of the $10^+/9^+$ redox couple of $[TpMoFe_3S_3(\mu_3\text{-}S)Cl_3]^{1-}$ compared to $[TpMoFe_3S_3(\mu_3\text{-}S)(PEt)_3]^{1+}$. The separation of the redox features of the $[TpMFe_3S_3(\mu_3\text{-}S)L_3]^n$ clusters is generally similar across different M atoms and terminal ligands. In the case of $[TpMFe_3S_3(\mu_3\text{-}Se)L_3]^n$ clusters, this separation decreases indicating a different electron delocalization in the case of S versus Se bridging ligands. Listed in Table 7 are a number of reduction potentials for $[TpMFe_3S_3(\mu_3\text{-}Y)L_3]^n$ clusters. Some have been reported previously, while others represent new compounds. These clusters represent a new class of compounds where the effects of the bridging atom can be probed. Indeed, it can be seen that Y can have a large impact on redox potentials.

Conclusion

Presented here are new electrochemical and Mössbauer data for $TpMFe_3S_3(\mu_3\text{-}Y)X_3$ clusters that present new information into how different cluster components affect electronic properties of clusters. This data indicates that caution should be taken in assigning the oxidation states of Fe centers in such clusters using Mössbauer data because large variations in parameters can result from changes in M, Y, and X identity. More detailed studies, such as XANES, SQUID, and EPR will be necessary to rigorously determine the electronic structures and oxidation states of the metal centers in these clusters.

Experimental

General Considerations

All reactions were performed at room temperature in an N_2-filled M. Braun glovebox or using standard Schlenk techniques unless otherwise specified. Glassware was oven dried at 140 ºC for at least 2 h prior to use, and allowed to cool under vacuum. Sodium tetrafluoroborate ($NaBPh_4$) was purchased in an anhydrous form and dissolved in acetonitrile (CH_3CN) and dried over 3 Å molecular sieves for 2 days before being filtered over Celite and dried in vacuo. $[Et_4N]_2[Tp^*WFe_3S_3(\mu_3\text{-}Cl)Cl_3]$[9] (Tp* = tris(3,5-dimethyl-1-pyrazolyl)borate), $[Et_4N]_2[Tp^*MoFe_3S_3(\mu_3\text{-}Cl)Cl_3]$,[12] $[Et_4N][Tp^*WFe_3S_3(\mu_3\text{-}CSiMe_3)(Cl)_3]$, $[Et_4N][Tp^*MoFe_3S_3(\mu_3\text{-}CSiMe_3)(Cl)_3]$, $[Et_4N]_2[Tp^*WFe_3S_3(\mu_3\text{-}CSiMe_3)(Cl)_3]$, $[Et_4N]_2[Tp^*MoFe_3S_3(\mu_3\text{-}CSiMe_3)(Cl)_3]$, $[Tp^*WFe_3S_3(u_3\text{-}S)(BAC)_3][BPh_4]$, $[Tp^*MoFe_3S_3(u_3\text{-}S)(BAC)_3][BPh_4]$, $Tp^*WFe_3S_3(u_3\text{-}N)(BAC)_3$, $[Tp^*WFe_3S_3(u_3\text{-}NSiMe_3)(BAC)_3][BPh_4]$, $Tp^*WFe_3S_3(u_3\text{-}carbyne)(BAC)_2$, $Tp^*MoFe_3S_3(u_3\text{-}carbyne)(BAC)_2$ $[Et_4N][Tp^*WFe_3S_3(CH_2SiMe_3)_3]$, $[Et_4N][Tp^*MoFe_3S_3(CH_2SiMe_3)_3]$, and $[Tp^*WFe_3S_3(BAC)_3][BPh_4]$ were prepared according to literature procedures.[12,13] Tetrahydrofuran (THF), diethyl ether (Et_2O), benzene (C_6H_6), toluene, CH_3CN, hexanes, and pentane were dried by sparging with nitrogen for at least 15 minutes, then passing through a column of activated A2 alumina under positive N_2 pressure and then degassed via several consecutive cycles of active vacuum and agitation on the Schlenk line before use.[38] Dimethylformamide was purchased in an anhydrous form from MiliporeSigma@, cannula-transferred to an oven dried Schlenk under N_2, degassed via several consecutive cycles of active vacuum and agitation on the Schlenk line, and then brought into the glovebox and dried over 3 Å molecular sieves for 2 days before use. ^1H and ^{31}P NMR spectra were recorded on a Varian 400 MHz spectrometer. ^1H-NMR spectra in proteo solvents were recorded on a Varian 400 MHz spectrometer using solvent suppression protocols. *d8*-THF, CD_3CN, and C_6D_6, were purchased from Cambridge Isotope Laboratories, dried over calcium hydride, degassed by three freeze-pump-thaw cycles, and vacuum transferred prior to use. All other reagents were purchased from commercial sources in their anhydrous forms and used without further purification.

Synthetic Procedures

Synthesis of [Tp*WFe$_3$S$_3$(^{i}Pr$_2$Me$_2$NHC)$_3$][BPh$_4$].

[Tp*WFe$_3$S$_3$(^{i}Pr$_2$Me$_2$NHC)$_3$][BPh$_4$] was synthesized following the synthetic procedure to synthesize [Tp*WFe$_3$S$_3$(BAC)$_3$][BPh$_4$].[12] Crystallization yielded dark block like crystals.

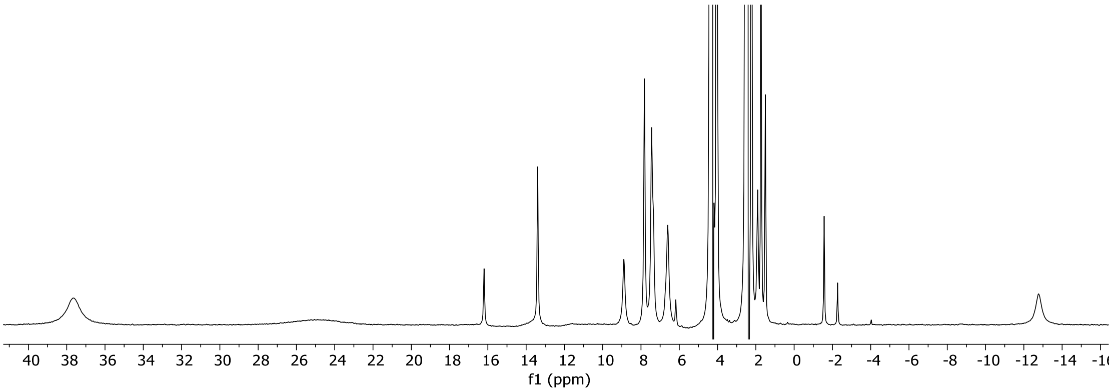

Figure S1: ^{1}H-NMR spectrum of **[Tp*WFe$_3$S$_3$(^{i}Pr$_2$Me$_2$NHC)$_3$][BPh$_4$]** in THF.

Synthesis of [Tp*WFe$_3$S$_3$(u$_3$-NSiMe$_3$)(^{i}Pr$_2$Me$_2$NHC)$_3$][BPh$_4$]. [Tp*WFe$_3$S$_3$(u$_3$-NSiMe$_3$)(^{i}Pr$_2$Me$_2$NHC)$_3$][BPh$_4$] was synthesized following the synthetic procedure to synthesize [Tp*WFe$_3$S$_3$(u$_3$-NSiMe$_3$)(BAC)$_3$][BPh$_4$].[12] Crystallization yielded dark block like crystals.

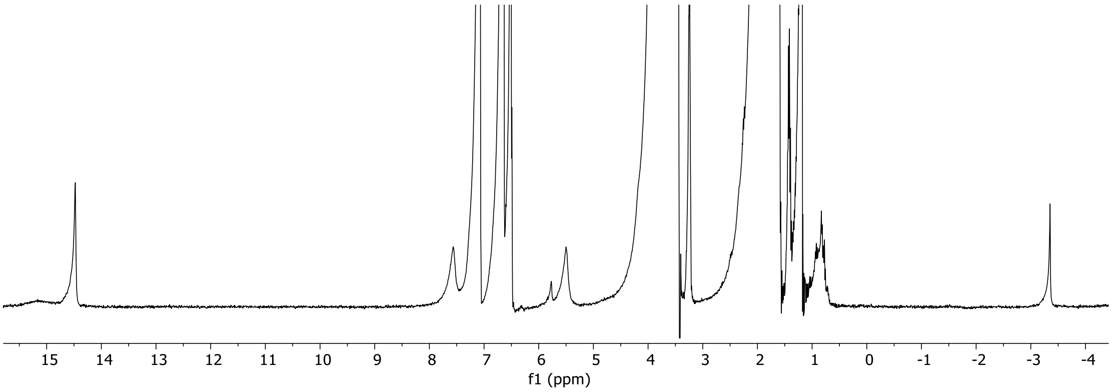

Figure S2: ^{1}H-NMR spectrum of **[Tp*WFe$_3$S$_3$(u$_3$-NSiMe$_3$)(^{i}Pr$_2$Me$_2$NHC)$_3$][BPh$_4$]** in THF.

Synthesis of [Tp*WFe$_3$S$_3$(u$_3$-S)(^{i}Pr$_2$Me$_2$NHC)$_3$][BPh$_4$]. [Tp*WFe$_3$S$_3$(u$_3$-S)(^{i}Pr$_2$Me$_2$NHC)$_3$][BPh$_4$] was synthesized following the synthetic procedure to synthesize [Tp*WFe$_3$S$_3$(u$_3$-S)(BAC)$_3$][BPh$_4$].[12] Crystallization yielded dark needle like crystals.

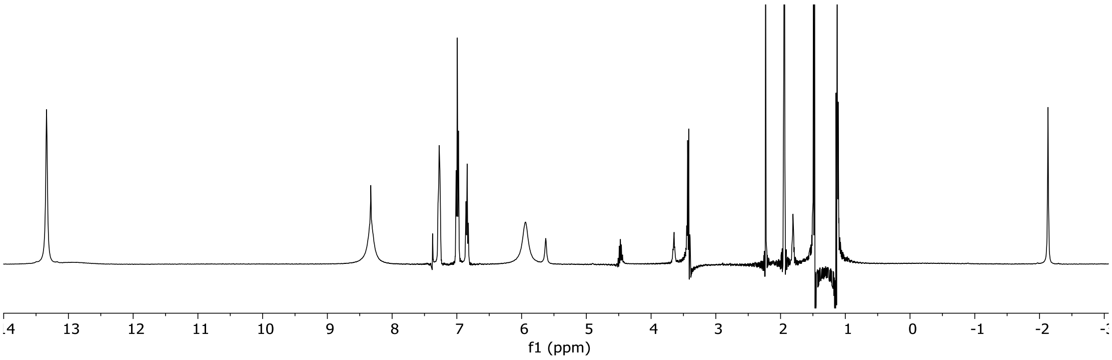

Figure S3: ^{1}H-NMR spectrum of **[Tp*WFe$_3$S$_3$(u$_3$-S)(^{i}Pr$_2$Me$_2$NHC)$_3$][BPh$_4$]** in CD$_3$CN.

Synthesis of [Et$_4$N][Tp*W(u$_3$-NPPh$_3$)Cl$_3$]. [Et$_4$N]$_2$[Tp*WFe$_3$S$_3$(μ$_3$-Cl)Cl$_3$] was dissolved in MeCN and the solution was frozen. An MeCN solution of HNPPh3 was added dropwise to a thawing solution of [Et$_4$N]$_2$[Tp*WFe$_3$S$_3$(μ$_3$-Cl)Cl$_3$] and the reaction was stirred at -78 ˚C 1 h and then at room temperature for 24 h. The reaction mixture was filtered and the solvent was then evaporated under vacuum. The solid was washed with pentane, Et$_2$O, and C$_6$H$_6$ until the filtrates were colorless. The product was extracted into THF and crystallizations were set up with vapor diffusion of a 1:1 mixture of pentane:Et$_2$O.

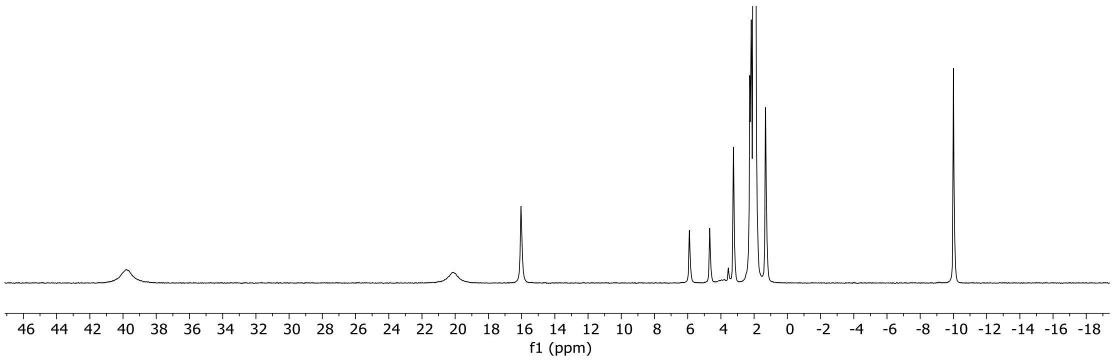

Figure S4: ^{1}H-NMR spectrum of **[Et$_4$N][Tp*W(u$_3$-NPPh$_3$)Cl$_3$]** in CD$_3$CN.

Synthesis of [Tp*W(u$_3$-NPPh$_3$)(^{i}Pr$_2$Me$_2$NHC)$_3$][PF$_6$]$_2$. [Et$_4$N][Tp*W(u$_3$-NPPh$_3$)Cl$_3$] was dissolved in THF and frozen. NaPF$_6$ was added to the thawing reaction solution until the reaction was completely thawed and then the reaction suspension was refrozen. A THF solution of ^{i}Pr$_2$Me$_2$NHC was added dropwise to the thawing reaction suspension. The reaction was then allowed to stir at -78 ˚C for 5 h. The reaction suspension was filtered and the solvent evaporated under vacuum. The solid was washed with pentane, Et$_2$O, and C$_6$H$_6$ until the filtrates were colorless. The product was extracted into THF and crystallizations were set up with vapor diffusion of Et$_2$O.

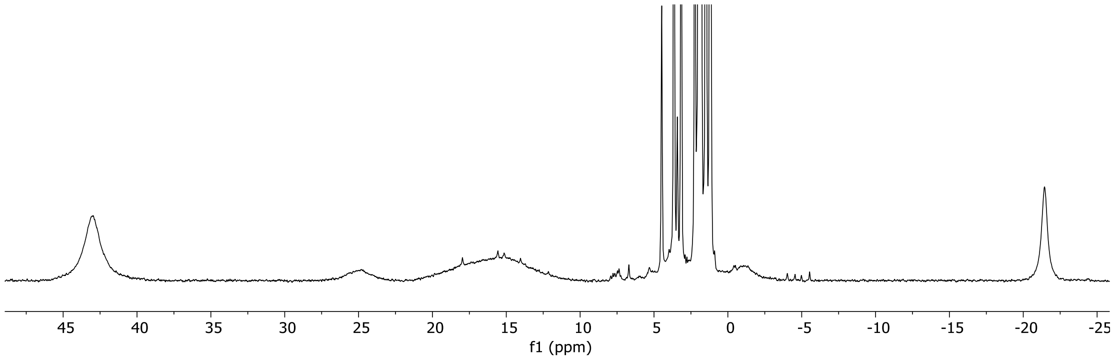

Figure S5: ^{1}H-NMR spectrum of **[Tp*W(u$_3$-NPPh$_3$)(^{i}Pr$_2$Me$_2$NHC)$_3$][PF$_6$]$_2$** in THF.

Electrochemistry Data

General

Cyclic voltammetry experiments were performed with a Pine Instrument Company AFCBP1 biopotentiostat with the AfterMathsoftware package. All measurements were performed in a three-electrode cell, which consisted of glassy carbon (working; ⌀= 3.0

mm), Ag wire (reference), and bare Pt wire (counter), in a N_2-filled MBraun glovebox at room temperature. Dry CH_3CN or DMF that contained ~0.2 M $[Bu_4N][PF_6]$ was used as the electrolyte solution. Redox potentials are reported relative to the ferrocene/ferrocenium redox wave (Fc/Fc^+;ferrocene added as an internal standard).The open circuit potential was measured prior to each voltammogram being collected. Voltammograms were scanned reductively in order to minimize the oxidative damage that was frequently observed on scanning more oxidatively.

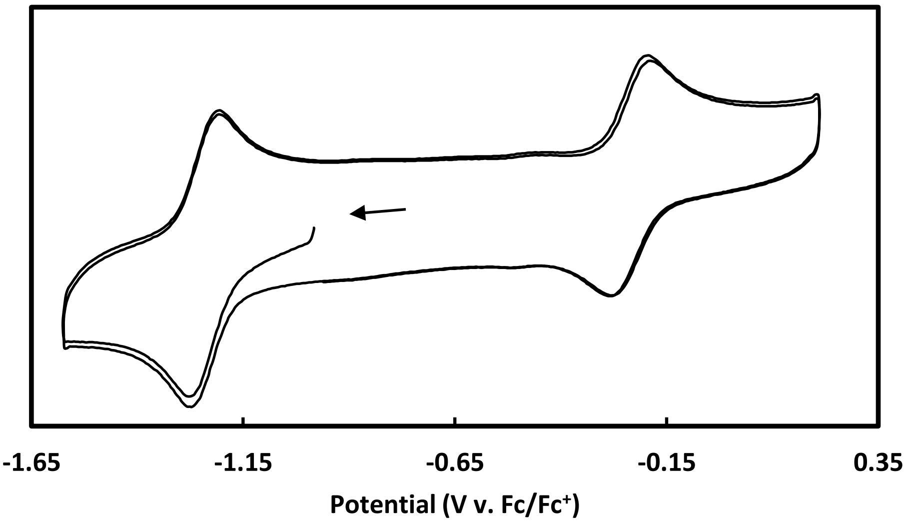

Figure S6: Cyclic voltammogram of **$[Tp^*W(u_3\text{-}NPPh_3)(^iPr_2Me_2NHC)_3][PF_6]_2$**.

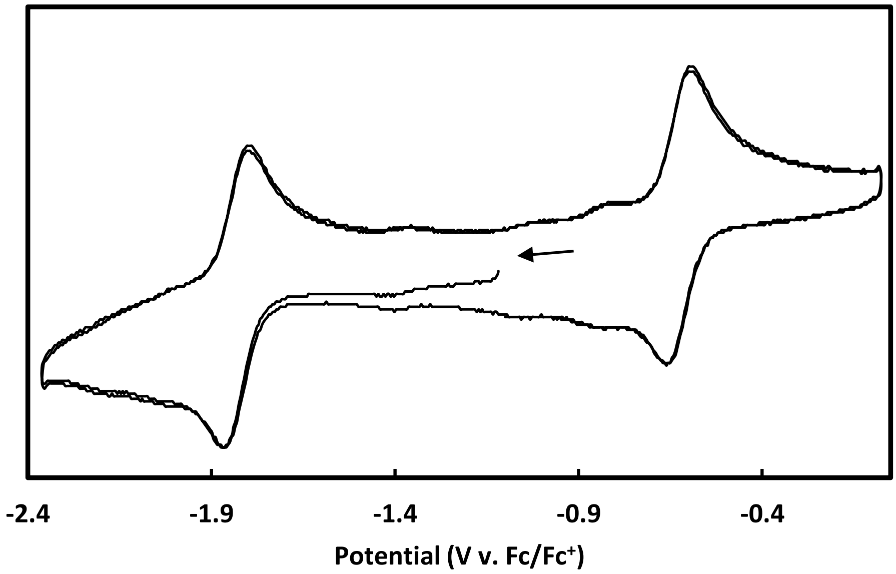

Figure S7: Cyclic voltammogram of **[Tp*WFe$_3$S$_3$(u$_3$-S)(^{i}Pr$_2$Me$_2$NHC)$_3$][BPh$_4$]**.

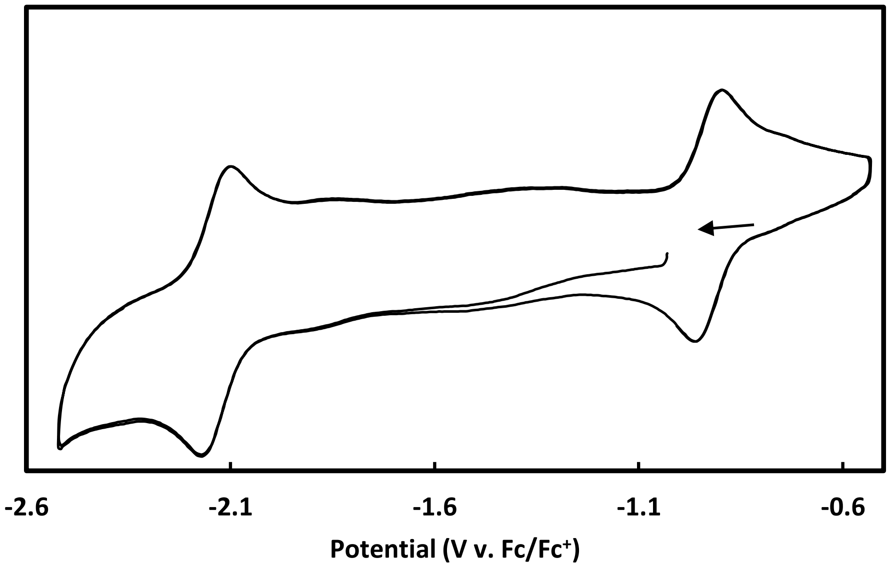

Figure S8: Cyclic voltammogram of **[Tp*WFe$_3$S$_3$(u$_3$-NSiMe$_3$)(^{i}Pr$_2$Me$_2$NHC)$_3$][BPh$_4$]**.

Mössbauer Measurements

General

Zero applied field ^{57}Fe Mossbauer spectra were recorded at 80 K in constant acceleration mode on a spectrometer from See Co (Edina, MN) equipped with an SVT- S6 400 cryostat (Janis, Wilmington, WA). The isomer shifts are relative to the centroid of an α-Fe foil signal at room temperature. Samples were prepared by mixing polycrystalline material (20 mg) with boron nitride in a cup fitted with a screw cap. The data were fit to Lorentzian lineshapes using WMOSS (www.wmoss.org).

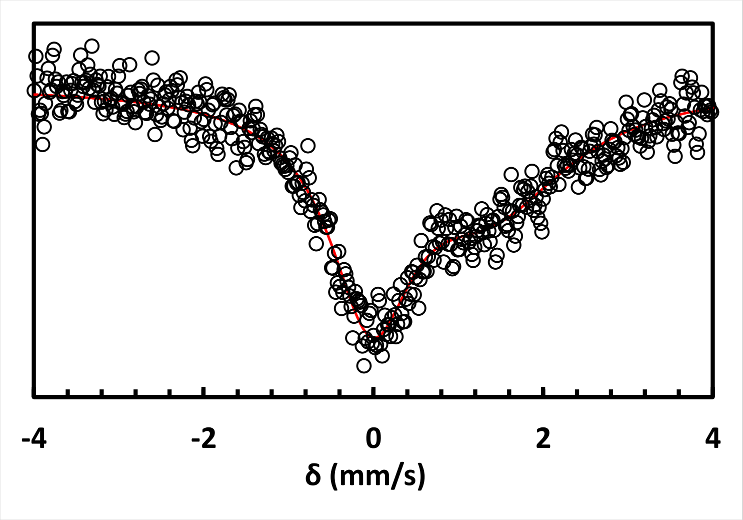

	δ (mm/s)	**ΔE_q (mm/s)**	**χ^2**	**Relative Fraction**
Site 1	0.50	0.85	0.9	1/3
Site 2	0.53	1.31		2/3
Average	0.52	1.10		

Figure S9: Mössbauer spectrum of **$[Et_4N]$ $[Tp^*W(u_3\text{-}NPPh_3)Cl_3]$** showing fit. Parameters are shown in table. Black circles are raw data.

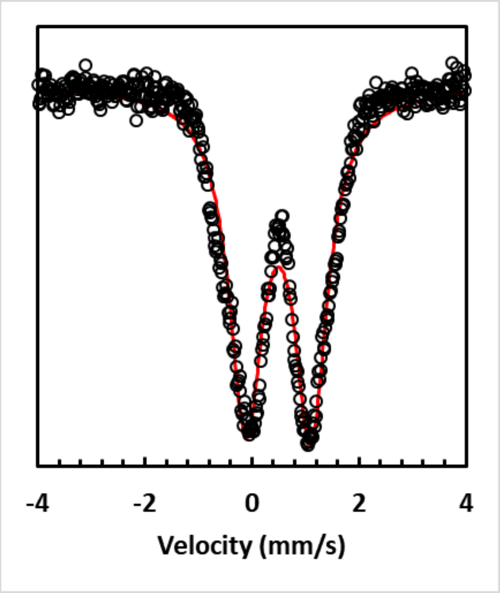

	δ (mm/s)	**ΔE_q (mm/s)**	**χ^2**
Fit	0.50	1.22	0.58

Figure S10: Mössbauer spectrum of **[Tp*W(u$_3$-S)(BAC)$_3$][PF$_6$]** showing fit. Parameters are shown in table. Black circles are raw data.

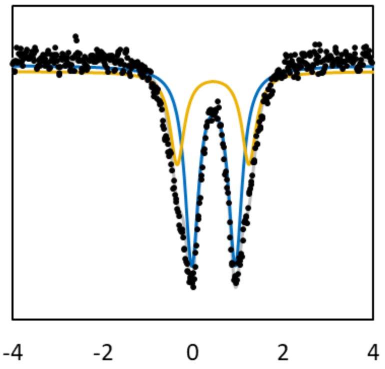

	δ (mm/s)	**ΔE_q (mm/s)**	**χ^2**	**Relative Fraction**
Site 1	0.46	0.97	0.44	2/3
Site 2	0.45	1.60		1/3
Average	0.46	1.18		

Figure S11: Mössbauer spectrum of **[Tp*Mo(u$_3$-S)(BAC)$_3$][PF$_6$]** showing fit. Parameters are shown in table. Black circles are raw data.

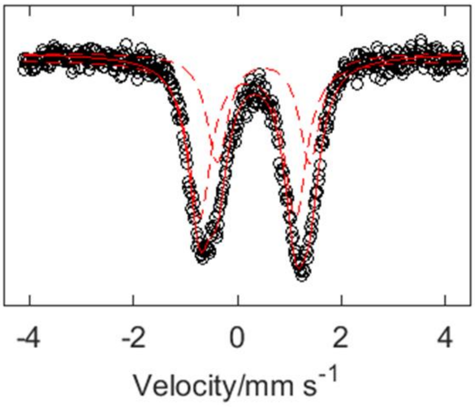

	δ (mm/s)	**ΔE_q (mm/s)**	**χ^2**	**Relative Fraction**
Site 1	0.20	1.85	0.58	2/3
Site 2	0.5	1.78		1/3
Average	0.30	1.82		

Figure S12: Mössbauer spectrum of **Tp*W(u$_3$-N)(BAC)$_3$** showing fit. Parameters are shown in table. Black circles are raw data.

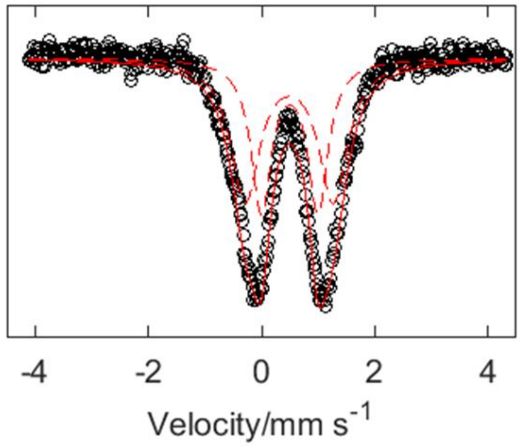

	δ (mm/s)	**ΔE_q (mm/s)**	**χ^2**	**Relative Fraction**
Site 1	0.49	1.56	0.58	2/3
Site 2	0.50	1.00		1/3
Average	0.49	1.37		

Figure S13: Mössbauer spectrum of **[Tp*W(u$_3$-NSiMe$_3$)(BAC)$_3$][PF$_6$]** showing fit. Parameters are shown in table. Black circles are raw data.

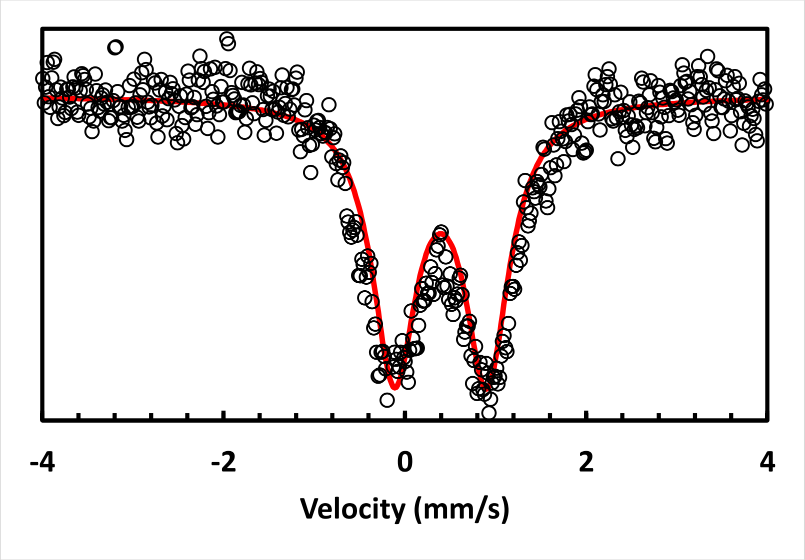

	δ (mm/s)	**ΔE$_q$ (mm/s)**	χ^2
Fit	0.39	1.02	0.6

Figure S14: Mössbauer spectrum of **[Tp*W(u$_3$-NSiMe$_3$)(^{i}Pr$_2$Me$_2$NHC)$_3$][PF$_6$]** showing fit. Parameters are shown in table. Black circles are raw data.

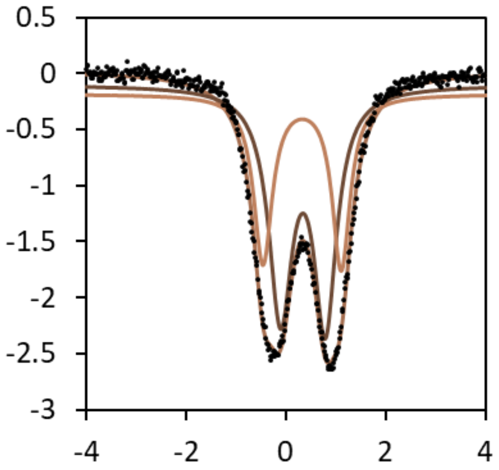

	δ (mm/s)	ΔE$_q$ (mm/s)	χ^2	Relative Fraction
Site 1	0.34	0.90	0.62	2/3
Site 2	0.33	1.57		1/3
Average	0.34			

Figure S15: Mössbauer spectrum of **Tp*Mo(u$_3$-carbyne)(BAC)$_3$** showing fit. Parameters are shown in table. Black circles are raw data.

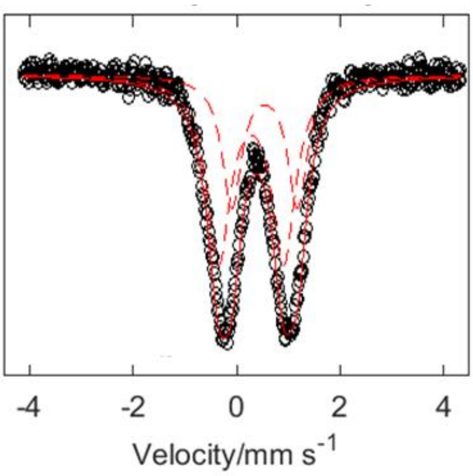

	δ (mm/s)	ΔE$_q$ (mm/s)	χ^2	Relative Fraction
Site 1	0.28	1.26	0.73	2/3
Site 2	0.33	1.27		1/3
Average	0.30	1.26		

Figure S16: Mössbauer spectrum of **Tp*W(u$_3$-carbyne)(BAC)$_3$** showing fit. Parameters are shown in table. Black circles are raw data.

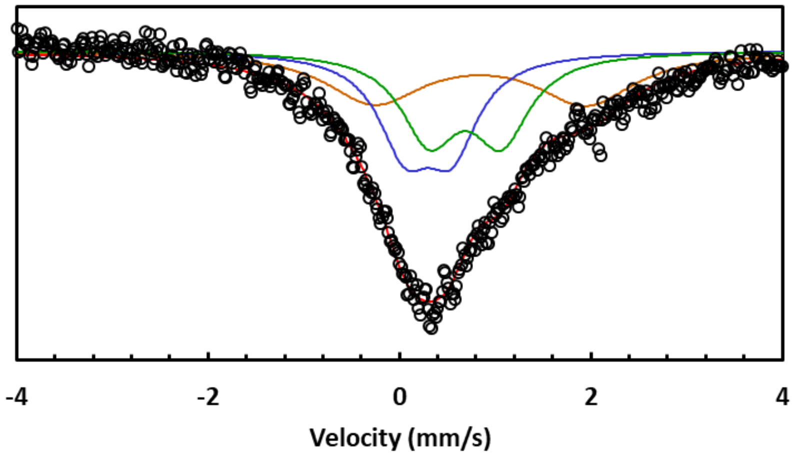

	δ (mm/s)	ΔE_q (mm/s)	χ^2	Relative Fraction
Site 1	0.86	2.21	0.66	1/3
Site 2	0.32	0.49		1/3
Site 3	0.70	0.75		1/3
Average	0.63	1.15		

Figure S17: Mössbauer spectrum of **$[Et_4N]_2[Tp^*W(u_3\text{-}Cl)Cl_3]$** showing fit. Parameters are shown in table. Black circles are raw data.

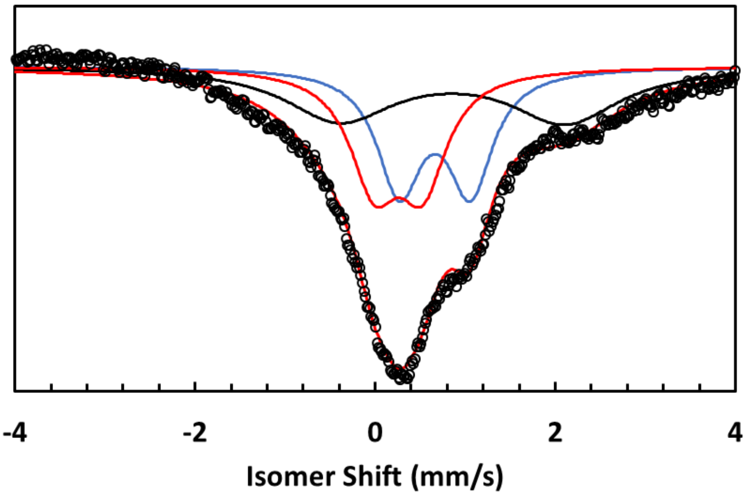

	δ (mm/s)	ΔE_q (mm/s)	χ^2	**Relative Fraction**
Site 1	0.26	0.54	0.89	1/3
Site 2	0.66	0.79		1/3
Site 3	0.86	2.5		1/3
Average	0.59	1.28		

Figure S18: Mössbauer spectrum of **$[Et_4N]_2[Tp^*Mo(u_3\text{-}Cl)Cl_3]$** showing fit. Parameters are shown in table. Black circles are raw data.

Magnetometry

General

Magnetic measurements were conducted with a Quantum Design MPMS3 SQUID Magnetometer at the University of California, Los Angeles. A polycrystalline sample of 3 was wrapped in plastic film and placed in a gelatin capsule. The capsule was then inserted into a plastic straw. Magnetization data at 100 K from 0 to 4 T were collected to confirm the absence of ferromagnetic impurities. Direct current variable temperature magnetic susceptibility measurements were collected between 1.8 and 300 K. Reduced magnetization data was collected between 1.8 and 9 K at fields between 1 and 7 T.

Magnetic susceptibility data was corrected for diamagnetism of the sample, estimated using Pascal's constants. Magnetic susceptibility data and reduced magnetization data were simulated with PHI.

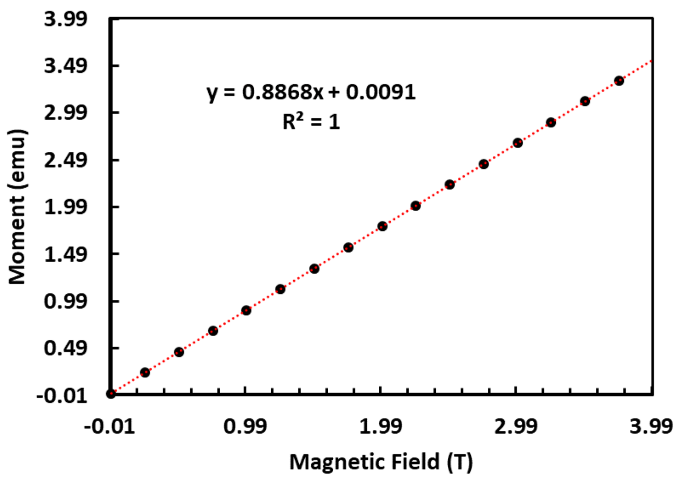

Figure S19: Magnetization data collected at 100 K from 0 to 4 T for **[Et$_4$N]$_2$[Tp*Mo(u$_3$-Cl)Cl$_3$]** to confirm the absence of ferromagnetic impurities.

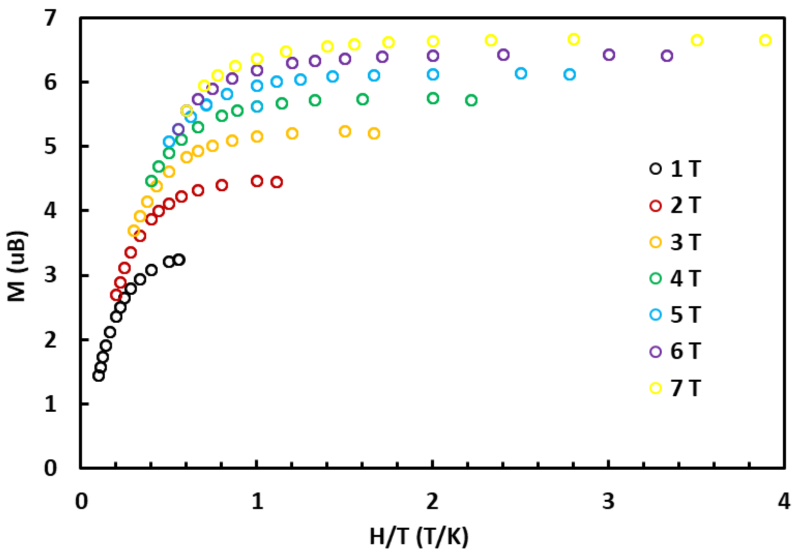

Figure S20: Reduced magnetism plot for **[Et$_4$N]$_2$[Tp*Mo(u$_3$-Cl)Cl$_3$]**.

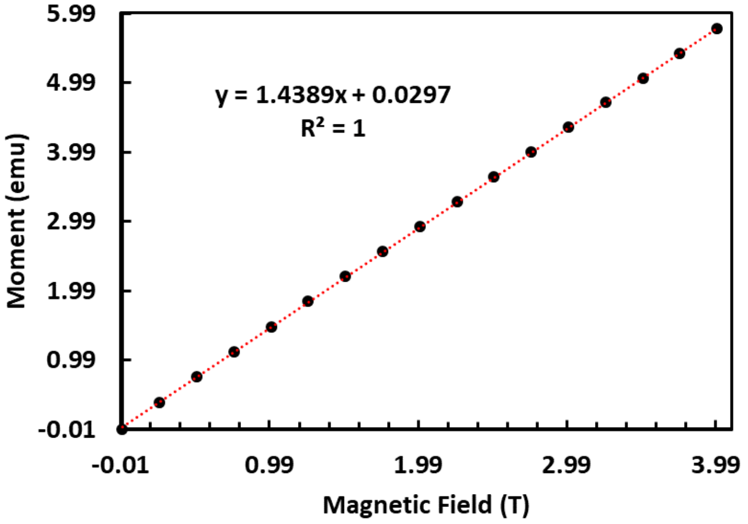

Figure S. Magnetization data collected at 100 K from 0 to 4 T for **$[Et_4N]_2[Tp^*W(u_3\text{-}Cl)Cl_3]$** to confirm the absence of ferromagnetic impurities.

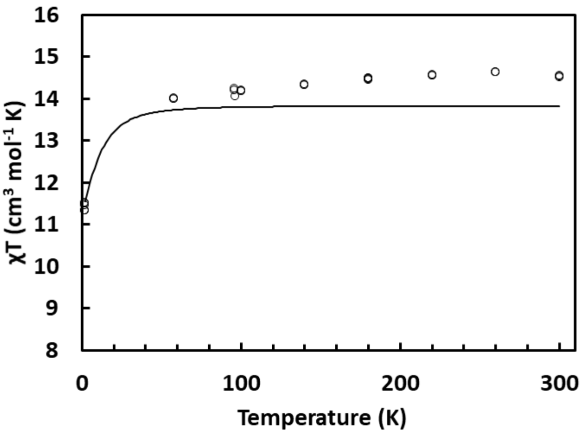

Figure S. Magnetic susceptibility plot for **$[Et_4N]_2[Tp^*W(u_3\text{-}Cl)Cl_3]$** with fit shown with black line for S = 9/2, *g* = 2.11, and D = -1.07 cm^{-1}.

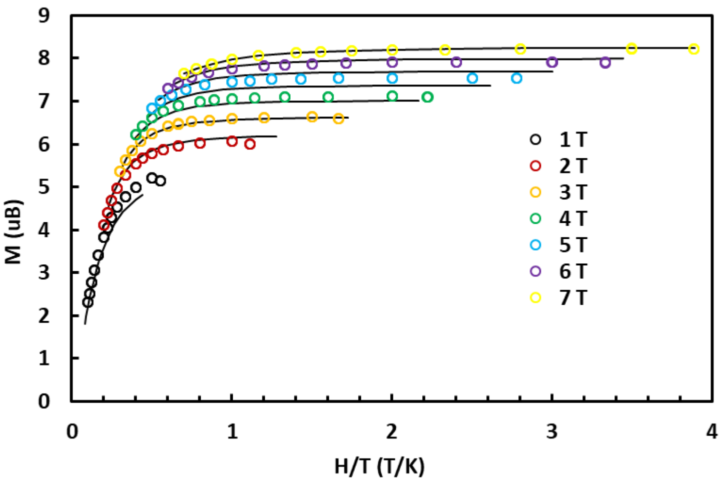

Figure S. Reduced magnetism plot for **[Et4N]2[Tp*W(u3-Cl)Cl3]** with fits shown with black lines for S = 9/2, *g* = 2.11, and D = -1.07 cm^{-1}.

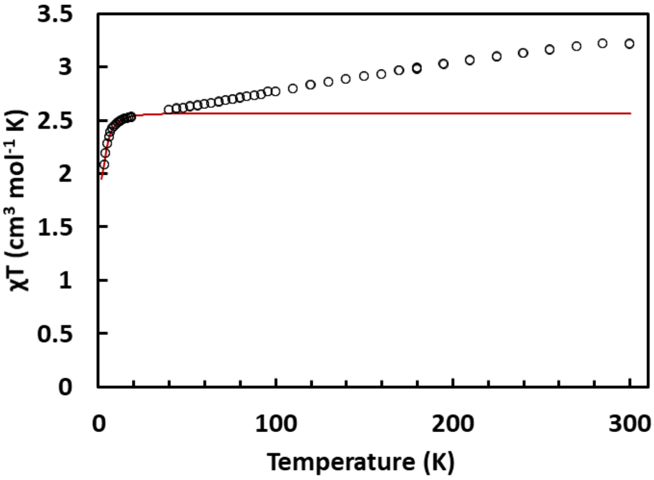

Figure S. Magnetic susceptibility plot for **[Tp*W(u3-NSiMe3)(BAC)3][PF6]** with fit shown with black line for S = 2, *g* = 1.85, and D = -1.00 cm^{-1}.

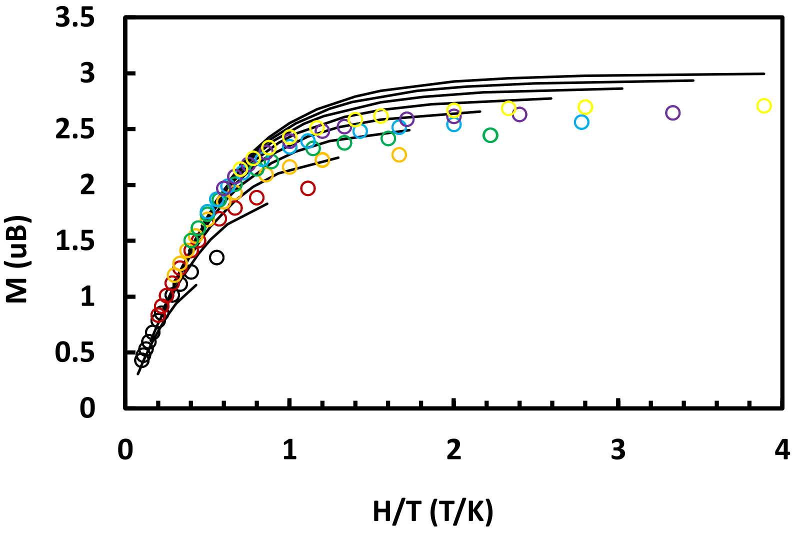

Figure S. Reduced magnetism plot for **[Tp*W(μ_3-NSiMe$_3$)(BAC)$_3$][PF$_6$]** with fits shown with black lines for S = 2, *g* = 1.85, and D = -1.00 cm^{-1}.

Single Crystal X-ray Diffraction Data

General

XRD data were collected at 100 K on a Bruker AXS D8 KAPPA or Bruker AXS D8 VENTURE diffractometer [microfocus sealed X-ray tube, λ(Mo Kα) = 0.71073 Å or λ(Cu Kα) = 1.54178 Å]. All manipulations, including data collection, integration, and scaling, were carried out using the Bruker APEX3 software.[39] Absorption corrections were applied using SADABS.[40] Structures were solved by direct methods using XS(incorporated into SHELXTL),[41] Sir92[42] or SUPERFLIP[43] and refined using full-matrix least-squares on Olex2[44] to convergence. All non-H atoms were refined using anisotropic displacement parameters. H atoms were placed in idealized positions and refined using a riding model.

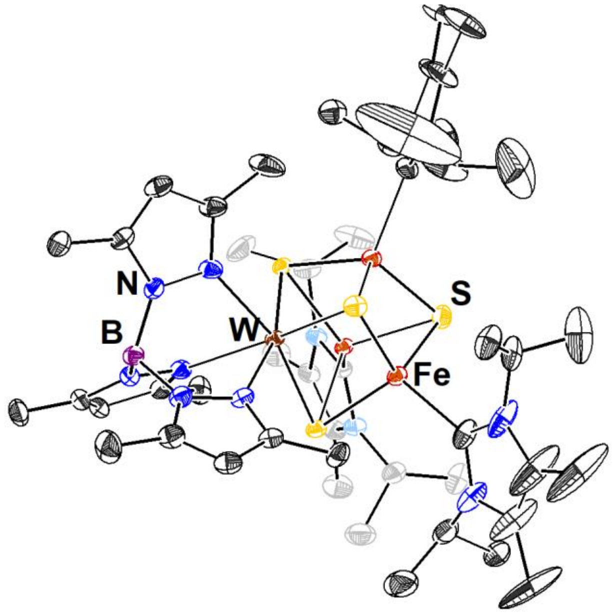

$[\mathrm{Tp^{*}MoFe_3S_3(\mu_3\text{-}S)(^{i}Pr_2Me_2NHC)_3}][\mathrm{BPh_4}]$ (**1**)

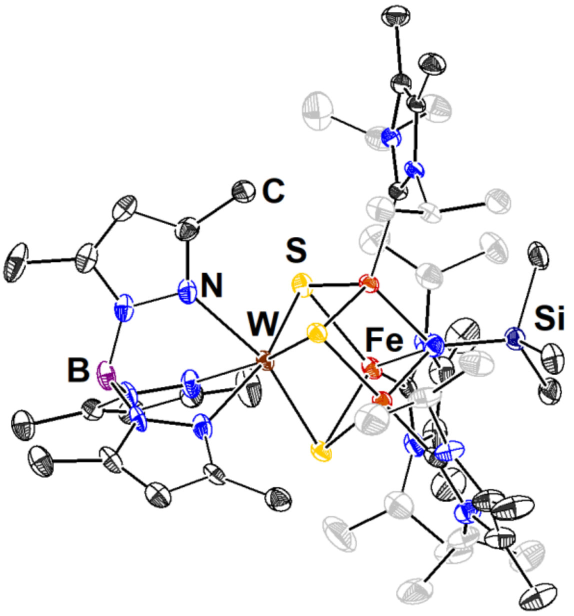

$[\mathrm{Tp^{*}MoFe_3S_3(\mu_3\text{-}NSiMe_3)(^{i}Pr_2Me_2NHC)_3}][\mathrm{BPh_4}]$ (**2**)

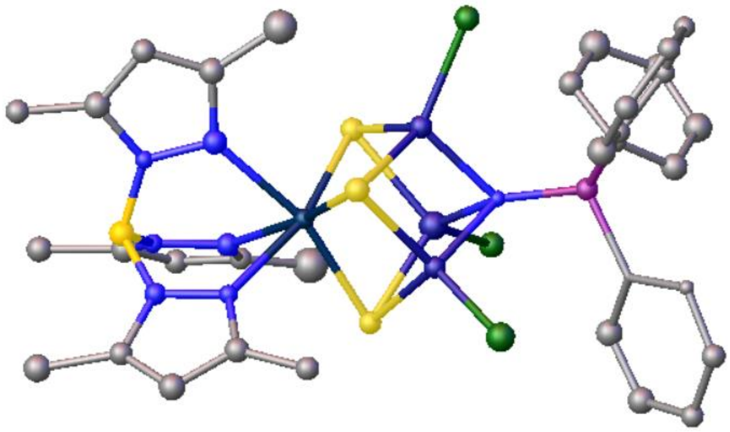

Tp*$\mathrm{WFe_3S_3(\mu_3\text{-}NPPh_3)Cl_3}$ (**3**)

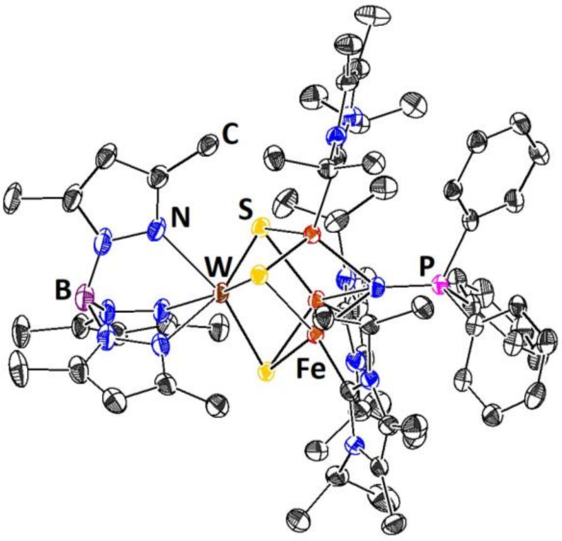

[Tp*$\mathrm{MoFe_3S_3(\mu_3\text{-}NPPh_3)(^{i}Pr_2Me_2NHC)_3][PF_6]_2}$ (**4**)

References:

(1) Johnson, M. K. Iron—Sulfur Proteins: New Roles for Old Clusters. *Current opinion in chemical biology* **1998**, *2* (2), 173–181.

(2) Peters, J. W.; Broderick, J. B. Emerging Paradigms for Complex Iron-Sulfur Cofactor Assembly and Insertion. *Annual review of biochemistry* **2012**, *81*, 429–450.

(3) Holm, R. H.; Kennepohl, P.; Solomon, E. I. Structural and Functional Aspects of Metal Sites in Biology. *Chemical reviews* **1996**, *96* (7), 2239–2314.

(4) Bak, D. W.; Elliott, S. J. Alternative FeS Cluster Ligands: Tuning Redox Potentials and Chemistry. *Current opinion in chemical biology* **2014**, *19*, 50–58.

(5) Lee, S. C.; Lo, W.; Holm, R. Developments in the Biomimetic Chemistry of Cubane-Type and Higher Nuclearity Iron–Sulfur Clusters. *Chemical reviews* **2014**, *114* (7), 3579–3600.

(6) Tanifuji, K.; Ohki, Y. Metal–Sulfur Compounds in N2 Reduction and Nitrogenase-Related Chemistry. *Chem. Rev.* **2020**, *120* (12), 5194–5251. https://doi.org/10.1021/acs.chemrev.9b00544.

(7) Brown, A. C.; Suess, D. L. M. 8.08 - Synthetic Iron-Sulfur Clusters. In *Comprehensive Coordination Chemistry III*; Constable, E. C., Parkin, G., Que Jr, L., Eds.; Elsevier: Oxford, 2021; pp 134–156. https://doi.org/10.1016/B978-0-08-102688-5.00053-2.

(8) Lubitz, W.; Ogata, H.; Rüdiger, O.; Reijerse, E. Hydrogenases. *Chem. Rev.* **2014**, *114* (8), 4081–4148. https://doi.org/10.1021/cr4005814.

(9) Xu, G.; Wang, Z.; Ling, R.; Zhou, J.; Chen, X.-D.; Holm, R. H. Ligand Metathesis as Rational Strategy for the Synthesis of Cubane-Type Heteroleptic Iron–Sulfur Clusters Relevant to the FeMo Cofactor. *Proceedings of the National Academy of Sciences* **2018**, *115* (20), 5089–5092.

(10) He, J.; Wei, J.; Xu, G.; Chen, X.-D. Stepwise Construction of Mo–Fe–S Clusters Using a LEGO Strategy. *Inorg. Chem.* **2022**, *61* (9), 4150–4158. https://doi.org/10.1021/acs.inorgchem.1c03998.

(11) Xu, G.; Zhou, J.; Wang, Z.; Holm, R. H.; Chen, X.-D. Controlled Incorporation of Nitrides into W-Fe-S Clusters. *Angewandte Chemie International Edition* **2019**, *58* (46), 16469–16473.

(12) Le, L.; Bailey, G.; Scott, A.; Agapie, T. Cluster Models of FeMoco with Sulfide and Carbyne Ligands: Effect of Interstitial Atom in Nitrogenase Active Site. **2021**. https://doi.org/10.26434/chemrxiv.14614152.v1.

(13) Scott, A. G.; Agapie, T. Synthesis of a Fe3–Carbyne Motif by Oxidation of an Alkyl Ligated Iron–Sulfur (WFe3S3) Cluster. *J. Am. Chem. Soc.* **2023**, *145* (1), 2–6. https://doi.org/10.1021/jacs.2c04826.

(14) Hoffman, B. M.; Lukoyanov, D.; Yang, Z.-Y.; Dean, D. R.; Seefeldt, L. C. Mechanism of Nitrogen Fixation by Nitrogenase: The next Stage. *Chemical reviews* **2014**, *114* (8), 4041–4062.

(15) Can, M.; Armstrong, F. A.; Ragsdale, S. W. Structure, Function, and Mechanism of the Nickel Metalloenzymes, CO Dehydrogenase, and Acetyl-CoA Synthase. *Chem. Rev.* **2014**, *114* (8), 4149–4174. https://doi.org/10.1021/cr400461p.

(16) Hauser, C.; Bill, E.; Holm, R. H. Single- and Double-Cubane Clusters in the Multiple Oxidation States [VFe3S4]3+,2+,1+. *Inorg. Chem.* **2002**, *41* (6), 1615–1624. https://doi.org/10.1021/ic011011b.

(17) Xi, B.; Holm, R. H. The [MoFe3S4]2+ Oxidation State: Synthesis, Substitution Reactions, and Structures of Phosphine-Ligated Cubane-Type Clusters with the

S = 2 Ground State. *Inorg. Chem.* **2011**, *50* (13), 6280–6288. https://doi.org/10.1021/ic200641k.

(18) Pesavento, R. P.; Berlinguette, C. P.; Holm, R. H. Stabilization of Reduced Molybdenum−Iron−Sulfur Single- and Double-Cubane Clusters by Cyanide Ligation. *Inorg. Chem.* **2007**, *46* (2), 510–516. https://doi.org/10.1021/ic061704y.

(19) Fomitchev, D. V.; McLauchlan, C. C.; Holm, R. H. Heterometal Cubane-Type MFe3S4 Clusters (M = Mo, V) Trigonally Symmetrized with Hydrotris(Pyrazolyl)Borate(1−) and Tris(Pyrazolyl)Methanesulfonate(1−) Capping Ligands. *Inorg. Chem.* **2002**, *41* (4), 958–966. https://doi.org/10.1021/ic011106d.

(20) Scott, T. A.; Holm, R. H. VFe3S4 Single and Double Cubane Clusters: Synthesis, Structures, and Dependence of Redox Potentials and Electron Distribution on Ligation and Heterometal. *Inorg. Chem.* **2008**, *47* (8), 3426–3432. https://doi.org/10.1021/ic702372f.

(21) Zheng, B.; Chen, X.-D.; Zheng, S.-L.; Holm, R. H. Selenium as a Structural Surrogate of Sulfur: Template-Assisted Assembly of Five Types of Tungsten–Iron–Sulfur/Selenium Clusters and the Structural Fate of Chalcogenide Reactants. *J. Am. Chem. Soc.* **2012**, *134* (14), 6479–6490. https://doi.org/10.1021/ja3010539.

(22) Zuo, J.-L.; Zhou, H.-C.; Holm, R. H. Vanadium−Iron−Sulfur Clusters Containing the Cubane-Type [VFe3S4] Core Unit: Synthesis of a Cluster with the Topology of the PN Cluster of Nitrogenase. *Inorg. Chem.* **2003**, *42* (15), 4624–4631. https://doi.org/10.1021/ic0301369.

(23) Zhang, H.-Y.; Qiu, S.-J.; Yang, H.-H.; Wang, M.-T.; Yang, J.; Wang, H.-B.; Liu, N.-H.; Chen, X.-D. Cubane-Type Tungsten–Iron–Sulfur Clusters with a Nitrogen Atom in the Core: Terminal Ligand Substitutions and Redox Behaviors. *Dalton Transactions* **2023**, *52* (21), 7166–7174. https://doi.org/10.1039/D3DT00865G.

(24) Gütlich, P.; Bill, E.; Trautwein, A. X. *Mössbauer Spectroscopy and Transition Metal Chemistry: Fundamentals and Applications*; Springer Science & Business Media, 2010.

(25) Pandelia, M.-E.; Lanz, N. D.; Booker, S. J.; Krebs, C. Mössbauer Spectroscopy of Fe/S Proteins. *Biochimica et Biophysica Acta (BBA) - Molecular Cell Research* **2015**, *1853* (6), 1395–1405. https://doi.org/10.1016/j.bbamcr.2014.12.005.

(26) Van Stappen, C.; Decamps, L.; Cutsail, G. E.; Bjornsson, R.; Henthorn, J. T.; Birrell, J. A.; DeBeer, S. The Spectroscopy of Nitrogenases. *Chem. Rev.* **2020**, *120* (12), 5005–5081. https://doi.org/10.1021/acs.chemrev.9b00650.

(27) Hauser, C.; Bill, E.; Holm, R. H. Single- and Double-Cubane Clusters in the Multiple Oxidation States [VFe3S4]3+,2+,1+. *Inorg. Chem.* **2002**, *41* (6), 1615–1624. https://doi.org/10.1021/ic011011b.

(28) Eady, R. R. Structure-Function Relationships of Alternative Nitrogenases. *Chemical Reviews* **1996**, *96* (7), 3013–3030. https://doi.org/10.1021/cr950057h.

(29) Rees, J. A.; Bjornsson, R.; Kowalska, J. K.; Lima, F. A.; Schlesier, J.; Sippel, D.; Weyhermüller, T.; Einsle, O.; Kovacs, J. A.; DeBeer, S. Comparative Electronic Structures of Nitrogenase FeMoco and FeVco. *Dalton Transactions* **2017**, *46* (8), 2445–2455.

(30) Berlinguette, C. P.; Miyaji, T.; Zhang, Y.; Holm, R. H. Precursors to Clusters with the Topology of the PN Cluster of Nitrogenase: Edge-Bridged Double

Cubane Clusters [(Tp)2Mo2Fe6S8L4]z: Synthesis, Structures, and Electron Transfer Series. *Inorg. Chem.* **2006**, *45* (5), 1997–2007. https://doi.org/10.1021/ic051770k.

(31) Zhang, Y.; Zuo, J.-L.; Zhou, H.-C.; Holm, R. H. Rearrangement of Symmetrical Dicubane Clusters into Topological Analogues of the P Cluster of Nitrogenase: Nature’s Choice? *J. Am. Chem. Soc.* **2002**, *124* (48), 14292–14293. https://doi.org/10.1021/ja0279702.

(32) Watt, G. D.; Reddy, K. R. N. Formation of an All Ferrous Fe4S4 Cluster in the Iron Protein Component of Azotobacter Vinelandii Nitrogenase. *Journal of Inorganic Biochemistry* **1994**, *53* (4), 281–294. https://doi.org/10.1016/0162-0134(94)85115-8.

(33) Angove, H. C.; Yoo, S. J.; Münck, E.; Burgess, B. K. An All-Ferrous State of the Fe Protein of Nitrogenase: INTERACTION WITH NUCLEOTIDES AND ELECTRON TRANSFER TO THE MoFe PROTEIN *. *Journal of Biological Chemistry* **1998**, *273* (41), 26330–26337. https://doi.org/10.1074/jbc.273.41.26330.

(34) Angove, H. C.; Yoo, S. J.; Burgess, B. K.; Münck, E. Mössbauer and EPR Evidence for an All-Ferrous Fe4S4 Cluster with S = 4 in the Fe Protein of Nitrogenase. *J. Am. Chem. Soc.* **1997**, *119* (37), 8730–8731. https://doi.org/10.1021/ja9712837.

(35) Hans, M.; Buckel, W.; Bill, E. Spectroscopic Evidence for an All-Ferrous [4Fe–4S]0 Cluster in the Superreduced Activator of 2-Hydroxyglutaryl-CoA Dehydratase from Acidaminococcus Fermentans. *J Biol Inorg Chem* **2008**, *13* (4), 563–574. https://doi.org/10.1007/s00775-008-0345-z.

(36) Sridharan, A.; Brown, A. C.; Suess, D. L. M. A Terminal Imido Complex of an Iron–Sulfur Cluster. *Angewandte Chemie International Edition* **2021**, *60* (23), 12802–12806. https://doi.org/10.1002/anie.202102603.

(37) Henthorn, J. T.; Cutsail, G. E.; Weyhermüller, T.; DeBeer, S. Stabilization of Intermediate Spin States in Mixed-Valent Diiron Dichalcogenide Complexes. *Nat. Chem.* **2022**, *14* (3), 328–333. https://doi.org/10.1038/s41557-021-00853-5.

(38) Pangborn, A. B.; Giardello, M. A.; Grubbs, R. H.; Rosen, R. K.; Timmers, F. J. Safe and Convenient Procedure for Solvent Purification. *Organometallics* **1996**, *15* (5), 1518–1520. https://doi.org/10.1021/om9503712.

(39) Bruker, APEX3(Bruker AXS Inc., 2012).

(40) Bruker, SADABS(Bruker AXS Inc., 2001).

(41) Sheldrick, G. M. SHELXT – Integrated Space-Group and Crystal-Structure Determination. *Acta Cryst A* **2015**, *71* (1), 3–8. https://doi.org/10.1107/S2053273314026370.

(42) Altomare, A.; Cascarano, G.; Giacovazzo, C.; Guagliardi, A.; Burla, M. C.; Polidori, G.; Camalli, M. SIRPOW.92 – a Program for Automatic Solution of Crystal Structures by Direct Methods Optimized for Powder Data. *J Appl Cryst* **1994**, *27* (3), 435–436. https://doi.org/10.1107/S0021889894000221.

(43) Palatinus, L.; Chapuis, G. SUPERFLIP – a Computer Program for the Solution of Crystal Structures by Charge Flipping in Arbitrary Dimensions. *J Appl Cryst* **2007**, *40* (4), 786–790. https://doi.org/10.1107/S0021889807029238.

(44) Dolomanov, O. V.; Bourhis, L. J.; Gildea, R. J.; Howard, J. a. K.; Puschmann, H. OLEX2: A Complete Structure Solution, Refinement and Analysis Program. *J Appl Cryst* **2009**, *42* (2), 339–341. https://doi.org/10.1107/S0021889808042726.

Chapter V

HIGH-SPIN AND REACTIVE Fe_{13} CLUSTER WITH EXPOSED METAL SITES

Abstract

Atomically defined large metal clusters have applications in new reaction development and preparation of materials with tailored properties. Expanding the synthetic toolbox for reactive high nuclearity metal complexes, we report a new class of Fe clusters, **Tp*$_4$W$_4$Fe$_{13}$S$_{12}$**, displaying a Fe$_{13}$ core with M-M bonds that has precedent only in main group and late metal chemistry. M$_{13}$ clusters with closed shell electron configurations can show significant stability and have been classified as superatoms. In contrast, **Tp*$_4$W$_4$Fe$_{13}$S$_{12}$** displays a large spin ground state of $S = 13$. This compound performs small molecule activations involving the transfer of up to 12 electrons resulting in significant cluster rearrangements.

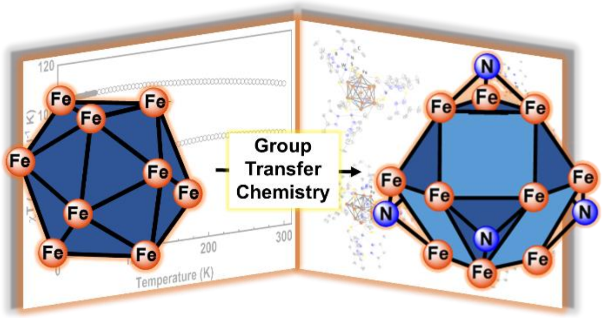

Introduction

Isolable transition metal-only high nuclearity clusters of well-defined atomic composition and structure are of interest for understanding nanoparticle growth processes and electronic structures, new optical and magnetic properties, designing new materials with tailored properties, tuning reactivity, and modeling heterogeneous catalysts.[1–8] Towards such applications, larger transition metal-only clusters displaying M-M interactions, without supporting interstitial bridging anionic ligands have been prepared for late transition metals, most commonly noble metals, although examples are known for first row transition metals such as Cu and Ni.[5,9–21] Isolation of some of these clusters is proposed to be facilitated by a closed shell electronic configuration that imparts particular stability within the superatom model.[22,23] However, while the structure of numerous large clusters has been determined using single-crystal X-ray diffraction (SC-XRD), use of such clusters to gain atomic level insight into reactivity on the surface of clusters has typically been hindered by the saturated coordination sphere and the propensity of complex clusters to fragment into smaller species.[23,24]

Toward developing new reactivity, synthetic protocols for larger clusters with open coordination sites for reaction chemistry and a greater number of metal-metal interactions are desirable.[25,26] Synthetic procedures for clusters of transition metals typically use metal salt precursors in combination with reducing agents and organic ligands.[1,7,9,27–29] Modification of known clusters has been demonstrated as a complementary route to new complexes.[10,12,30] Assembly of tetranuclear iron sulfur clusters into oligomers upon halide abstraction or reduction provides precedent for employing small clusters to generate higher complexity structures, though typically containing interstitial bridges.[31,32] Herein, we employ a tetranuclear precursor **$[Et_4N]_2[Tp^*WFe_3S_3(u_3\text{-}Cl)Cl_3]$**[33] as a building unit to a more complex cluster, **$Tp^*_4W_4Fe_{13}S_{12}$**, with an unprecedented Fe_{13} core. **$Tp^*_4W_4Fe_{13}S_{12}$**, a cluster with large spin ground state, displays open coordination sites and is reactive, yet sufficiently stabilized to allow the isolation of small molecule activation products including complexes with surface nitride, imide, and sulfide groups.

Results and Discussion

Toward lower oxidation state high nuclearity clusters for reductive reactivity, we employed precursors anchored by the robust Tp*WS_3 unit (Tp* = tris(3,5-dimethyl-1-pyrazolyl)borate).[34] Taking advantage of the lability of the chloride ligands in the presence of a halide abstracting reagent in comparison to the thiolate, phosphine, carbene, sulfide, or nitride ligands of previously reported clusters,[31,33] we previously developed reduction chemistry starting from **$[Et_4N]_2[Tp^*WFe_3S_3(\mu_3\text{-}Cl)Cl_3]$**[33] (Fig. 1A, Et_4N = tetraethylammonium) to access Tp*WFe_3S_3 complexes supported by carbene ligands (L) with Fe_3 open faces.[35] To generate higher nuclearity clusters, reduction was performed in the absence of additional supporting ligands L that could trap small metal clusters.

Treatment of **$[Et_4N]_2[Tp^*WFe_3S_3(\mu_3\text{-}Cl)Cl_3]$** with reductant and halogen abstracting reagent results in a cluster with the overall chemical formula **$Tp^*_4W_4Fe_{13}S_{12}$** as determined by SC-XRD (Fig. 1A). **$Tp^*_4W_4Fe_{13}S_{12}$** consists of four Tp*WS_3 units tetrahedrally arranged (Fig. 1D) around a pseudo-icosahedral Fe_{12} core with an additional Fe atom bound in the center.[36] The Fe-Fe distances are between 2.395(2) and 2.771(2) Å (Table S1), within the range of metal-metal bonds for molecular Fe complexes.[37,38] The W-S distances match the parameters observed for reduced Tp*WFe_3S_3 clusters supported by NHC ligands at Fe.[35] The Fe-S bonds show a significant lengthening relative to the precursor, consistent with reduction at Fe.[39] Overall, the 17 metal centers carry a 28+ charge, M_{17}^{28+}. There are four open Fe_3 faces, each with three surrounding bridging sulfides that create a cavity around these potential binding sites (Fig. 1C, S2).

The icosahedral metal cluster motif is known for transition metals past group 8.[10,40,41] Lower symmetry reduced clusters of group 8 metals, Ru_{10} and Os_{20},[42,43] have been reported,

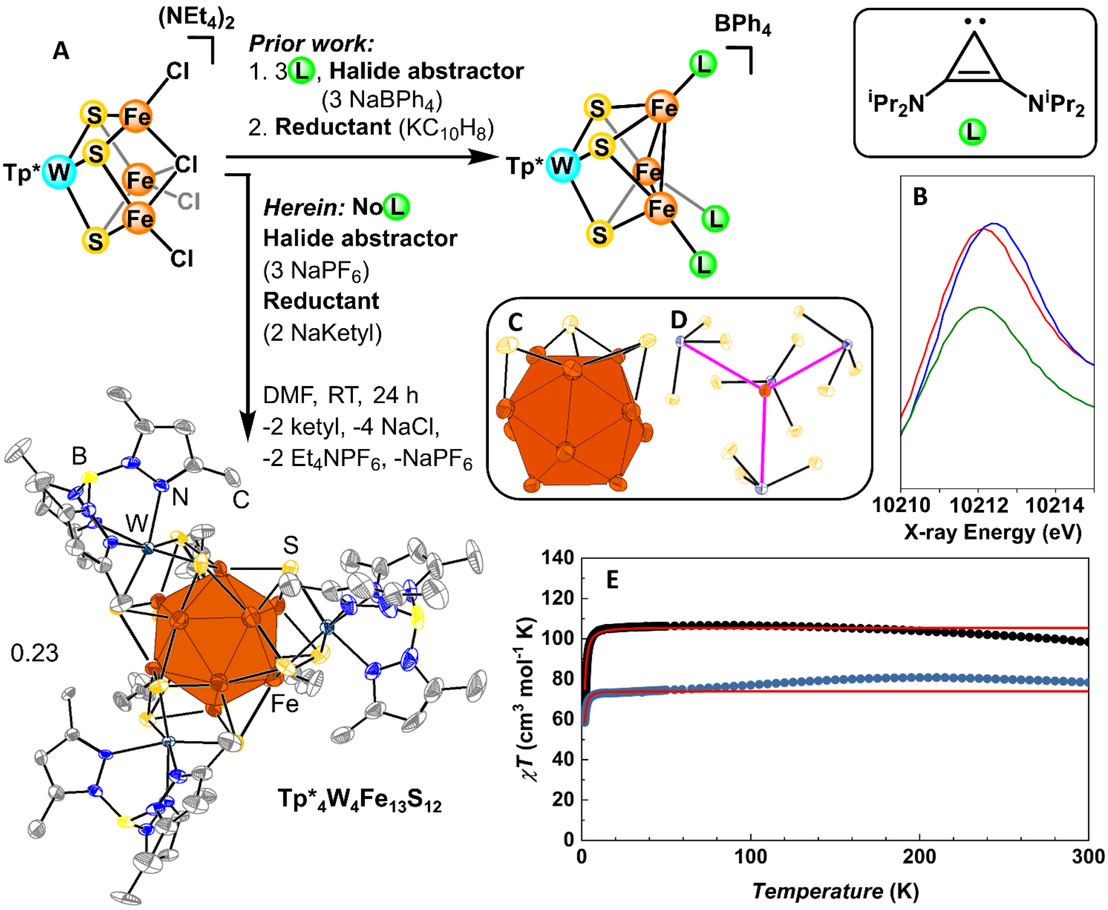

Figure 1. (A) Synthesis of **$Tp^*_4W_4Fe_{13}S_{12}$**. Solvent and hydrogen atoms omitted for clarity and ellipsoids plotted at the 50% probability level. (B) W L_3 XANES data for **$[Et_4N]_2[Tp^*WFe_3S_3(\mu_3\text{-}Cl)Cl_3]$** (green), **$Tp^*_4W_4Fe_{13}S_{12}$** (red)**,** and **$Tp^*_4W_4Fe_{13}S_{12}N_4$** (blue). (C) Fe_{13} core highlighting one Fe_3S_3 cavity motif. (D) Tetrahedral arrangement of 4 WS_3 units around the central Fe atom of the Fe_{13} core. (E) Direct current variable temperature magnetic susceptibility measurements for **$Tp^*_4W_4Fe_{13}S_{12}$** (black circles) and **$Tp^*_4W_4Fe_{13}S_{14}$** (blue circles) collected from 1.8 to 300 K, after diamagnetic correction. Red lines correspond to the best fitting using PHI software.[44] For **$Tp^*_4W_4Fe_{13}S_{12}$**, $S = 13$, $D = -0.6$ cm^{-1}, and $g = 2.15$. For **$Tp^*_4W_4Fe_{13}S_{14}$**, $S = 13$, $D = -0.16$ cm^{-1}, and $g = 1.80$.

but are coordinately saturated with CO ligands. Icosahedral M_{13} clusters of main group and later transition metals, including $[Al_{13}]^-$, $[Au_{13}]^{5+}$, $[Cu_{13}]^{5+}$, have been reported to be particularly robust and are described as metallic superatoms due to their closed shell electronic structure in the Jellium model and full shell of 12 atoms around the central metal.[1,10,45] To probe the open shell nature of **$Tp^*_4W_4Fe_{13}S_{12}$** direct current (dc) susceptibility measurements were performed on a polycrystalline sample restrained in grease to prevent torquing (see SI). At room temperature, a χT value of 98.39 cm^3 K mol^{-1} is observed (Figure 1E), which suggests the presence of S = 13 ground state open shell system. It is reasonable to assume all the spins within the clusters are strongly coupled even at room temperature, given the metal-metal bonded core within the cluster. Upon reducing the temperature, the χT product slightly increases to 106.67 cm^3 K mol^{-1} at 80 K. Such behavior was also previously seen for the hexanuclear metal-metal bonded Fe clusters.[46–48] The χT product remains relatively constant down to 10 K; thereafter it decreases rapidly to reach a minimum value of 58.89 cm^3 K mol^{-1} at 1.8 K. The low temperature behavior is likely due to zero-field splitting. To probe further, magnetization measurements at variable fields (0-7 T) in the temperature range of 2-9 K were performed on **$Tp^*_4W_4Fe_{13}S_{12}$**. Fitting of the data using PHI software[44] afforded a ground spin state of S = 13 (g = 2.15 and D = -0.6 cm^{-1}, Fig. 1E and S4). These results clearly set this system apart from the previously reported closed shell metallic superatoms.

To address electron distribution within the cluster, X-ray absorption near edge spectroscopy (XANES) experiments were performed on **$[Et_4N]_2[Tp^*WFe_3S_3(\mu_3\text{-}Cl)Cl_3]$** and **$Tp^*_4W_4Fe_{13}S_{12}$** to probe the W L_2 and L_3 edge, considering that the coordination sphere of W is maintained across these clusters (Fig. 1B, S5). Peak centers remain at

10214.2 eV for both clusters, while there is a less than 0.1 eV white line shift for L_2 and no shift for L_3. Assuming an oxidation state for **$[Et_4N]_2[Tp^*WFe_3S_3(\mu_3\text{-}Cl)Cl_3]$** as W(III),[49,50] a similar effective charge is maintained for **$Tp^*_4W_4Fe_{13}S_{12}$** according to the XANES data, although further studies are needed to conclusively assign the oxidation state.[51,52] Given this tentative W(III) assignment, the formal charge distribution on Fe is $[Fe_{13}]^{16+}$, placing 88 electrons in Fe d-based molecular orbitals. With only three weak field ligands coordinated to each outer Fe center, low d-d splitting is expected. Within the d-based molecular orbital manifold for the Fe-Fe and Fe-S interactions, the highest spin state corresponds to 42 unpaired electrons for $[Fe_{13}]^{16+}$. A sufficiently large orbital splitting resulting in an intermediate spin orbital population in combination with antiferromagnetic interactions with the four W centers[53,54] could bring the spin value of **$Tp^*_4W_4Fe_{13}S_{12}$** in the range estimated from the magnetization data. However, with the complexity given by the presence of three types of metal centers, two for Fe (the central atom and the twelve peripheral atoms) and one for W, additional studies will be necessary to interpret the electronic structure and magnetism of this compound. Clusters with notably high spin values are typically generated from higher nuclearity clusters with bridging ligands, such as oxides, that facilitate superexchange pathways for spin coupling.[55–58] However, these weak interactions are overcome at high temperatures. Stronger coupling can be achieved through a molecular orbital manifold in complexes with intermediate strength metal-metal interactions resulting in moderate splitting of the d-based orbitals, where the cluster is conceptually analogous to a high spin single metal complex.[46,48,59,60] Overall, **$Tp^*_4W_4Fe_{13}S_{12}$** demonstrates a strategy to achieve high spin states through high nuclearity metallic cores terminated with weak field bridging sulfide ligands.

Several aspects of **$Tp^*{}_4W_4Fe_{13}S_{12}$** suggest potential for reactivity, including a relatively reduced redox state, open coordination sites, a high spin, and metal-metal bonds. The open, coordinately unsaturated Fe_3 faces are reminiscent of triangular motifs known to undergo small molecule activations for M_3 clusters,[37,61,62] including nitrogen atom and nitrene transfer chemistry in up to four electron redox processes.[37,63–66] Such studies have shown that metal-metal interactions can allow for multi-electron redox chemistry without metal centers in particularly low oxidation states. **$Tp^*{}_4W_4Fe_{13}S_{12}$** has four of these surface Fe_3 structural motifs as well as the additional redox active central Fe atom and distal W centers. Considering that heterogeneous iron catalysts are employed in the Haber Bosch process and insight into the bonding of proposed intermediates of N_2 reduction to multimetallic sites is limited,[67,68] we targeted reactions with nitrogeneous ligands. Reaction of **$Tp^*{}_4W_4Fe_{13}S_{12}$** with four equivalents of trimethylsilylazide (N_3SiMe_3) results in the transfer of four nitride atoms (Fig. 2) to generate **$Tp^*{}_4W_4Fe_{13}S_{12}N_4$** in an overall 12 electron process, a remarkable number for a single molecule. The Fe_{13} core has been converted from a centered icosahedron to a centered cuboctahedron (Fig. 2, 3).[10,45] Despite the substantial reorganization of the Fe_{13} core and the formal transfer of 12 electrons, the Fe-Fe distances (2.568(2)-2.737(2) Å, Table S1) remain within the range of the starting material suggesting a propensity to maintain metal-metal interactions. The W-S bond lengths shorten slightly, to an average length of 2.331(9) Å,

suggesting partial oxidation at W. DFT studies of the relative stability of gas phase metal clusters without supporting ligands[69] indicate that the metal oxidation states impact the energies of various cluster geometries, of potential consequence here given the redox changes between M_{17}^{28+} and M_{17}^{40+}. Comparison of **$Tp^*{}_4W_4Fe_{13}S_{12}$** and **$Tp^*{}_4W_4Fe_{13}S_{12}N_4$**

demonstrates that cluster reorganization remains possible in the presence of surface ligands, where the energetics of metal-ligand interactions on geometry must be taken into account. For example, whereas the sulfides of the Tp*WS_3 fragments each bind trigonal Fe_3 faces in **Tp*$_4$W$_4$Fe$_{13}$S$_{12}$**, they coordinate to Fe-Fe edges of Fe_4 squares in **Tp*$_4$W$_4$Fe$_{13}$S$_{12}$N$_4$** (Fig. S6). Compared to **Tp*$_4$W$_4$Fe$_{13}$S$_{12}$**, **Tp*$_4$W$_4$Fe$_{13}$S$_{12}$N$_4$** exhibits a white line shift of 1.5 eV for the W L_2 edge and 1.0 eV for the W L_3 edge (Fig. 1B, S5). While this indicates a change in charge density at W, which is remote from the site of reaction chemistry at Fe, further studies are needed to assign formal oxidation state changes.

To gain access to an imide analog of **Tp*$_4$W$_4$Fe$_{13}$S$_{12}$N$_4$** for comparison, reactions with phenyl azide (PhN_3) were performed. Treatment of **Tp*$_4$W$_4$Fe$_{13}$S$_{12}$** with three

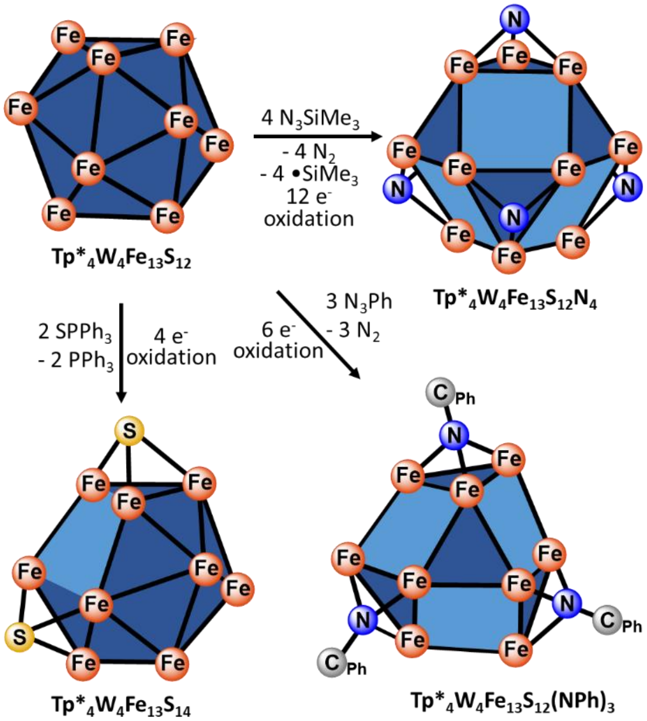

Figure 2. Reactions of Tp*$_4$W$_4$Fe$_{13}$S$_{12}$. Tp*WS$_3$ fragments are not shown for clarity. Triangular and square faces are shown in dark and light blue, respectively.

equivalents of PhN_3 resulted in the isolation of the tris-imide species **$Tp^*_4W_4Fe_{13}S_{12}(NPh)_3$**. Again, all of the atoms of the cluster precursor are maintained, and the geometry is altered toward a centered cuboctahedral geometry, but with substantial distortions (Fig. 2, 3).

Despite the redox state and Fe_{13} structure being between those of **$Tp^*_4W_4Fe_{13}S_{12}$** and **$Tp^*_4W_4Fe_{13}S_{12}N_4$**, **$Tp^*_4W_4Fe_{13}S_{12}(NPh)_3$** displays Fe-Fe distances that are longer than both (up to 2.941(5) Å compared to 2.737(2) and 2.771(2) Å, respectively). This observation indicates that the M-M distances are not directly predicated by the redox state of the metal. In fact, the cluster of intermediate oxidation state has the longest M-M distance.

To further explore the impact of the group transferred on the cluster structure, installation of sulfide was targeted, as a ligand isolobal to both nitride and imide. **$Tp^*_4W_4Fe_{13}S_{12}$** reacts with two equivalents of triphenylphosphine sulfide ($SPPh_3$) to form **$Tp^*_4W_4Fe_{13}S_{14}$** (Fig. 2), as observed by SC-XRD and the byproduct PPh_3 (^{31}P NMR

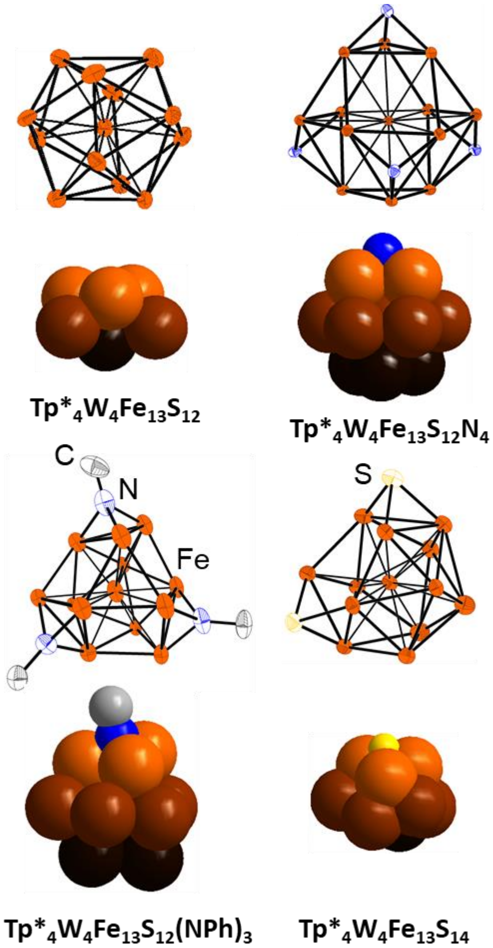

Tp*$_4$W$_4$Fe$_{13}$S$_{12}$ **Tp*$_4$W$_4$Fe$_{13}$S$_{12}$N$_4$**

Tp*$_4$W$_4$Fe$_{13}$S$_{12}$(NPh)$_3$ **Tp*$_4$W$_4$Fe$_{13}$S$_{14}$**

Figure 3. Thermal ellipsoid plots of Fe$_{13}$ cores with substrate molecules bound for Tp*$_4$W$_4$Fe$_{13}$S$_{12}$, Tp*$_4$W$_4$Fe$_{13}$S$_{12}$N$_4$, Tp*$_4$W$_4$Fe$_{13}$S$_{12}$(NPh)$_3$, and Tp*$_4$W$_4$Fe$_{13}$S$_{14}$ and space filling models for one Fe$_3$ face of each cluster with one of bound substrate molecules and adjacent Fe atoms shown in different shades of orange based on layer. Ellipsoids are plotted at the 50% probability level.

spectroscopy, Fig. S8). Two sulfur atoms have been transferred, in contrast to three and four for the reactions with PhN$_3$ and Me$_3$SiN$_3$, respectively, in a four electron redox process. The Fe$_{13}$ core of the product has lower symmetry and becomes distorted from an icosahedron such that two of the Fe-Fe distances increase to greater than 3 Å (Fig. 2 and 3). Magnetic data were also measured for **Tp*$_4$W$_4$Fe$_{13}$S$_{14}$** with the goal to understanding the impact of the sulfide addition on the overall magnetic properties. At room temperature, a lowering of the χT value to 78.28 cm^3 K mol^{-1} is observed (Figure 1E). However, fitting of the data also suggests the presence of $S = 13$ ground state open shell system ($g = 1.8$ and $D = -0.16$ cm^{-1}, Fig. 1E, and S11). Despite the fact that **$Tp*_4W_4Fe_{13}S_{14}$** and **$Tp*_4W_4Fe_{13}S_{12}$** differ by four electrons, their spin states are estimated to be the same. This could be a consequence of changes in electronic structure induced by the two additional sulfide ligands for example by altering the population of the d-orbital manifold of the Fe_{13} core, which highlights a strategy to tune the magnetism of these compounds with the surface ligands.

Analysis of the multiiron layers below an open triangular Fe_3 face in the precursor (**$Tp*_4W_4Fe_{13}S_{12}$**) versus a ligand coordinated Fe_3 face in each of the group transfer cluster products shows substantial Fe atom shifts (Fig. 3). Notably, the most pronounced variation of Fe-Fe distances within one cluster were observed in the cases where fewer groups and electrons were transferred.

Conclusion

In summary, we report a synthetic strategy for the synthesis of metallic Fe_{13} clusters upon reduction of a tetranuclear precursor, **$[Et_4N]_2[Tp*WFe_3S_3(\mu_3\text{-}Cl)Cl_3]$**. The atomically precise characterization of **$Tp*_4W_4Fe_{13}S_{12}$**, **$Tp*_4W_4Fe_{13}S_{12}N_4$**, **$Tp*_4W_4Fe_{13}S_{12}(NPh)_3$**, and **$Tp*_4W_4Fe_{13}S_{14}$** demonstrates that large clusters can maintain the metallic core while performing well-defined multi-electron multiple group transfer chemistry with overall redox changes of 4 to 12 electrons. **$Tp*_4W_4Fe_{13}S_{12}$** shows notably high spin values at room temperature for metallic clusters, highlighting the potential of this type of coordination compound for magnetic materials applications. The structural variation observed with the present clusters shows the ability of multimetallic systems to accommodate the bonding requirements of large redox and ligand changes. The propensity for surface rearrangement demonstrated with the transfer of nitrogen, nitrene, and sulfur ligands can serve as a tool for new reactive cluster design. The availability of clusters displaying the $Tp^*WM_3S_3$ motif for other transition metals[70] provides a starting point to a broader range of large metallic clusters related to those reported here.

Experimental

General Considerations

All reactions were performed at room temperature in an N_2-filled M. Braun glovebox or using

standard Schlenk techniques unless otherwise specified. Glassware was oven dried at 140 ºC for at least 2 h prior to use, and allowed to cool under vacuum. Trimethylsilylazide (N_3SiMe_3), sodium hexafluorophosphine ($NaPF_6$), and triphenylphosphinesulfide ($SPPh_3$) were purchased in an anhydrous form. N_3SiMe_3 was used without further purification. $NaPF_6$ and $SPPh_3$ were dissolved in acetonitrile (CH_3CN) and tetrahydrofuran (THF), respectively, and dried over 3 Å molecular sieves for 2 days before being filtered over Celite and dried *in vacuo*. $[Et_4N]_2[Tp^*WFe_3S_3(\mu_3\text{-}Cl)Cl_3]$[33] and N_3Ph[71] were prepared according to literature procedures. THF, diethyl ether (Et_2O), benzene, toluene, MeCN, hexanes, and pentane were dried by sparging with nitrogen for at least 15 minutes, then passing through a column of activated A2 alumina under positive N_2 pressure and then degassed via several consecutive cycles of active vacuum and agitation on the Schlenk line before use.[72] Dimethylformamide (DMF) was purchased in an anhydrous form from MiliporeSigma@, cannula-transferred to an oven dried Schlenk under N_2, degassed via several consecutive cycles of active vacuum and agitation on the Schlenk line, and then brought into the glovebox and dried over 3 Å molecular sieves for 2 days before use. ^{1}H and ^{31}P NMR spectra were recorded on a Varian 400 MHz spectrometer. ^{1}H-NMR spectra and ^{31}P-NMR in DMF were recorded on a Varian 400 MHz spectrometer using solvent suppression protocols. ^{1}H-NMR spectra of **$Tp^*_4W_4Fe_{13}S_{12}$, $Tp^*_4W_4Fe_{13}S_{12}N_4$, $Tp^*_4W_4Fe_{13}S_{12}(NPh)_3$, and $Tp^*_4W_4Fe_{13}S_{14}$** were NMR silent except for solvent peaks and so ^{1}H-NMRs are not shown. All other reagents were purchased from commercial sources in their anhydrous forms and used without further purification.

Physical Methods

Magnetic Measurements. Magnetic measurements were conducted with a Quantum Design MPMS3 Magnetometer running MPMS Multivu software. Polycrystalline samples were restrained in a matrix of vacuum grease and wrapped and sealed in a polyethylene membrane under an inert atmosphere. The magnetization data were collected at 100 K to check for ferromagnetic impurities, which were absent. Multiple batches of material were tested to confirm homogeneity between samples. Diamagnetic corrections were applied for the sample holder, and the inherent diamagnetism of the prepared sample was estimated with the use of Pascal's constants. χT and reduced magnetization data were fitted using PHI software.[44]

X-ray crystallography. XRD data were collected at 100 K on a Bruker AXS D8 KAPPA or Bruker AXS D8 VENTURE diffractometer [microfocus sealed X-ray tube, λ(Mo Kα) = 0.71073 Å or λ(Cu Kα) = 1.54178 Å]. All manipulations, including data collection, integration, and scaling, were carried out using the Bruker APEX3 software.[73]

Absorption corrections were applied using SADABS.[74] Structures were solved by direct methods using XS(incorporated into SHELXTL),[75] Sir92[76] or SUPERFLIP[77] and refined using full-matrix least-squares on Olex2[78] to convergence. All non-H atoms were refined using anisotropic displacement parameters. H atoms were placed in idealized positions and refined using a riding model.

X-ray absorption spectroscopy. W L-edge X-ray absorption data were collected using beamline 9-3 at the Stanford Synchrotron Radiation Lightsource (SSRL) operating with standard ring conditions of 3.0 GeV energy and 500 mA current. A Si (220) double crystal monochromator at W L_{II} and L_{III}-edge was used. The intensities of incident and transmitted X-rays were monitored with N_2-filled ion chambers before the sample (I_0) and after the sample (I_1 and I_2), respectively. XAS data of samples were collected as fluorescence excitation spectra using a 100-element Ge solid-state detector (Canberra). The monochromator energy was calibrated with the rising edge energy of Ge foil (K-edge of 11.103 keV.). The data were collected at 10 K using a liquid He flow cryostat (Oxford Instruments).

Synthetic Procedures and Characterization

Synthesis of [$Tp^*_4W_4Fe_{13}S_{12}$]. [Et_4N]$_2$[$Tp^*WFe_3S_3(\mu_3\text{-}Cl)Cl_3$] (100 mg, 0.0870 mmol) was measured into a scintillation vial and dissolved in DMF (3 mL). Sodium benzophenone (1.75 mL, 0.1 mM THF solution, 0.175 mmol) was added to the stirring DMF solution. Finally, $NaPF_6$ (44.0 mg, 0.262 mmol) was added portionwise. The reaction solution was allowed to stir at room temperature for 48 h. The solution was filtered over a Celite pad and then crystallization via vapor diffusion of 1.5 x volume of Et_2O was performed to obtain black diamond shaped crystals after 3 days. The mother liquor was decanted from the crystals and the crystals were washed with DMF until washes were colorless and then washed with 3 x 2 mL of Et_2O. Finally, the crystals were dried under vacuum to yield 27.7 mg of the final product (45%). The cluster is NMR silent and ^{1}H-NMR indicates no diamagnetic or NMR active paramagnetic impurities. Magnetism data indicates no ferromagnetic impurities. Anal. calcd. (%) for $C_{60}H_{88}B_4Fe_{13}N_{24}S_{12}W_4$•$(DMF)_3(THF)_2$: C, 27.93; H, 3.84; N, 10.99. Found: C, 27.91; H, 3.54; N, 10.68.

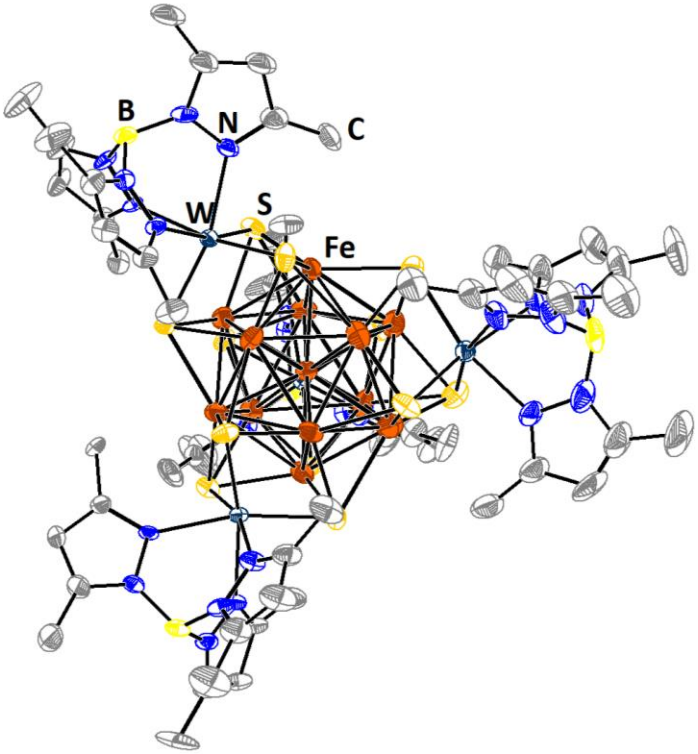

Figure S1. Crystal structure of **$Tp^*_4W_4Fe_{13}S_{12}$**. Ellipsoids are shown at the 50% probability level. Hydrogen atoms and co-crystallized solvent molecules are not shown for clarity.

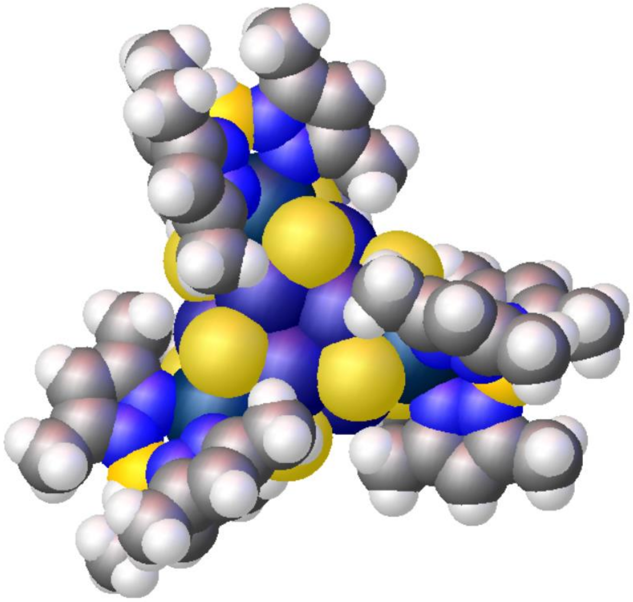

Figure S2. Space filling model of **$Tp^*_4W_4Fe_{13}S_{12}$** (Fe = orange, S = yellow).

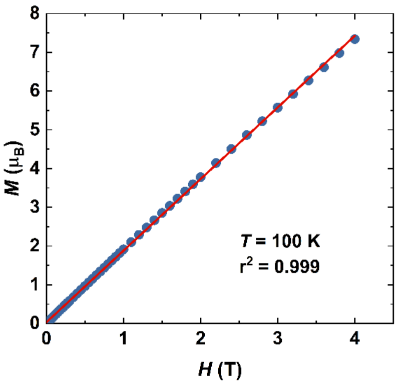

Figure S3. Magnetization data collected at 100 K from 0 to 4 T for **$Tp^*_4W_4Fe_{13}S_{12}$** to confirm the absence of ferromagnetic impurities.

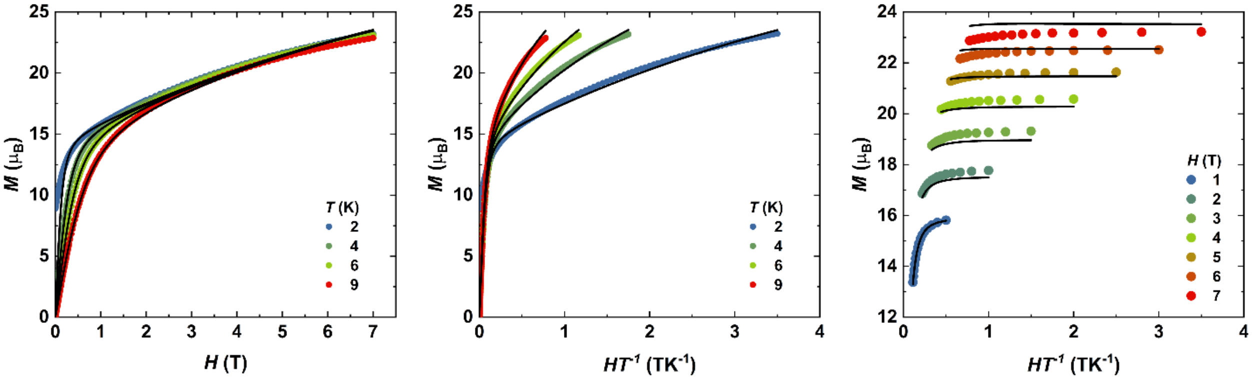

Figure S4. Magnetization and reduced magnetization plots for **Tp*$_4$W$_4$Fe$_{13}$S$_{12}$**. Black lines represent the best fits obtained with PHI software. Fit parameters obtained were $g = 2.15$, $S = 13$, and $D = -0.6\ \text{cm}^{-1}$.

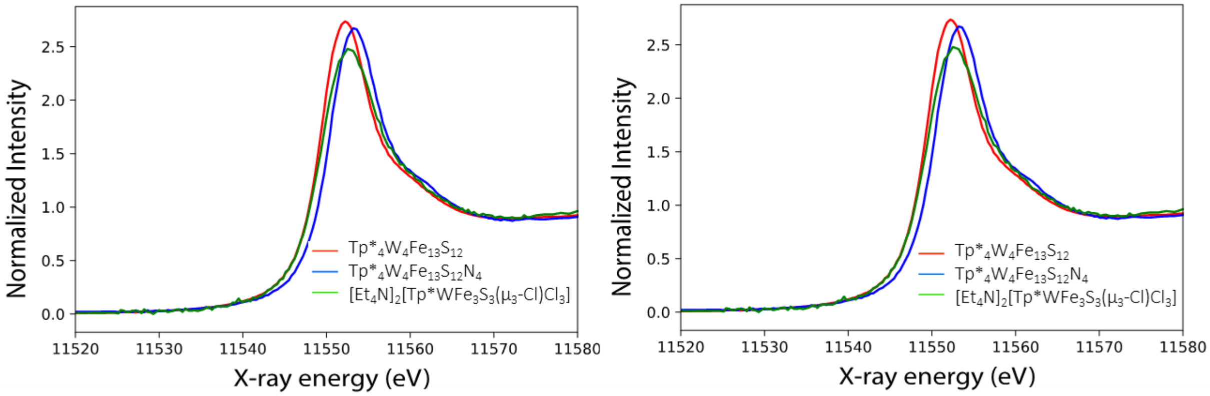

Figure S5. W L$_2$ (left) and L$_3$-edge (right) X-ray absorption near edge structure (XANES) data for **[Et$_4$N]$_2$[Tp*WFe$_3$S$_3$(μ$_3$-Cl)Cl$_3$]**, **Tp*$_4$W$_4$Fe$_{13}$S$_{12}$**, and **Tp*$_4$W$_4$Fe$_{13}$S$_{12}$N$_4$**.

Synthesis of Tp*$_4$W$_4$Fe$_{13}$S$_{12}$N$_4$. Tp*$_4$W$_4$Fe$_{13}$S$_{12}$ (66.0 mg, 0.022 mmol) was measured into a scintillation vial and suspended in DMF (2 mL). 2 mL of a 0.1 M Et$_2$O solution of N$_3$SiPh$_3$ (0.88 mL, 0.10 M Et$_2$O solution, 0.088 mmol) was added and the mixture was allowed to stir at room temperature for 14 h. The solution was filtered over a Celite pad and then crystallization via vapor diffusion of 2 x volume of Et_2O was performed to obtain black rod shaped crystals after 4 days. The mother liquor was decanted from the crystals and the crystals were washed with DMF until washes were colorless and then washed with 3 x 2 mL of Et_2O. Finally, the crystals were dried under vacuum to yield 18.7 mg of the final product (26% yield). The cluster is NMR silent and ^{1}H-NMR indicates no diamagnetic or NMR active paramagnetic impurities. Magnetism data indicates no ferromagnetic impurities. Anal. calcd. (%) for $C_{60}H_{88}B_4Fe_{13}N_{28}S_{12}W_4 \bullet (DMF)_4$: C, 25.61; H, 3.25; N, 13.28. Found: C, 25.69; H, 3.09; N, 13.36.

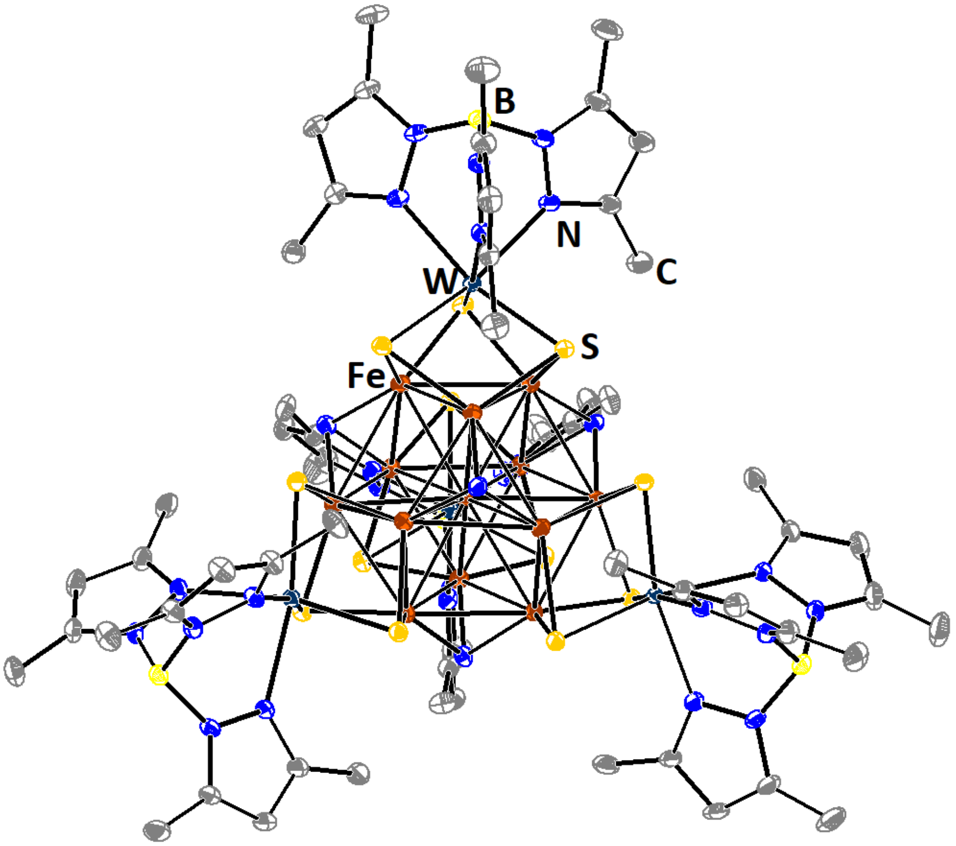

Figure S6. Crystal structure of **$Tp^*_4W_4Fe_{13}S_{12}N_4$**. Ellipsoids are shown at the 50% probability level. Hydrogen atoms and co-crystallized solvent molecules are not shown for clarity.

Synthesis of $Tp^*_4W_4Fe_{13}S_{12}(NPh)_3$. **$Tp^*_4W_4Fe_{13}S_{12}$** (34.1 mg, 0.0110 mmol) was measured into a scintillation vial and suspended in DMF (1 mL). N_3Ph (0.33 mL, 0.10 M Et_2O, 0.0330 mmol) was added and the mixture was allowed to stir at room temperature for 14 h. The solution was filtered over a Celite pad and then crystallization via vapor diffusion of 2 x volume of Et_2O was performed to obtain black rod shaped crystals after 4 days. The mother liquor was decanted from the crystals and the crystals were washed with DMF until washes were colorless and then washed with 3 x 2 mL of Et_2O. Finally, the crystals were dried under vacuum to yield 7.8 mg of the final product (21% yield). The cluster is NMR silent and ^{1}H-NMR indicates no diamagnetic or NMR active paramagnetic impurities. Magnetism data indicates no ferromagnetic impurities. Anal. calcd. (%) for $C_{78}H_{103}B_4Fe_{13}N_{27}S_{12}W_4(DMF)_3$: C, 30.28; H, 3.67; N, 11.77. Found: C, 30.30; H, 3.75; N, 11.85.

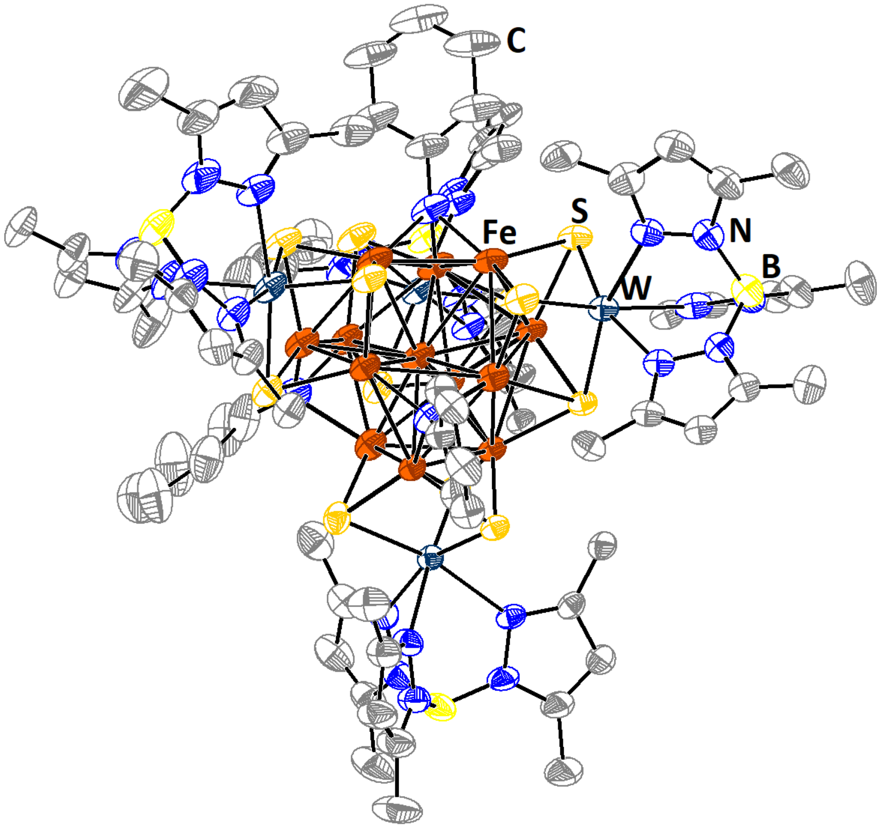

Figure S7. Crystal structure of **Tp*$_4$W$_4$Fe$_{13}$S$_{12}$(NPh)$_3$**. Ellipsoids are shown at the 50% probability level. Hydrogen atoms and co-crystallized solvent molecules are not shown for clarity.

Synthesis of Tp*$_4$W$_4$Fe$_{13}$S$_{14}$. Tp*$_4$W$_4$Fe$_{13}$S$_{12}$ (23.2 mg, 0.00800 mmol) was measured into a scintillation vial and suspended in DMF (2 mL). SPPh$_3$ (2.0 mg, 0.016 mmol) was added portionwise and the mixture was allowed to stir at room temperature for 14 h. Et$_2$O (2 mL) was added to the solution and then it was filtered over a Celite pad and crystallized via vapor diffusion of 1 x volume of Et$_2$O to obtain black triangle shaped crystals after 2 days. The mother liquor was decanted from the crystals and the crystals were washed with DMF until washes were colorless and then washed with 3 x 2 mL of Et$_2$O. Finally, the crystals were dried under vacuum to yield 9.4 mg of the desired product (39.7% yield). The cluster is NMR silent and ^{1}H-NMR indicates no diamagnetic or NMR active paramagnetic impurities. Magnetism data indicates no ferromagnetic impurities. Anal. calcd. (%) for $C_{60}H_{88}B_4Fe_{13}N_{24}S_{14}W_4(DMF)_6$: C, 27.68; H, 3.95; N, 11.60. Found: C, 27.68; H, 3.75; N, 11.82.

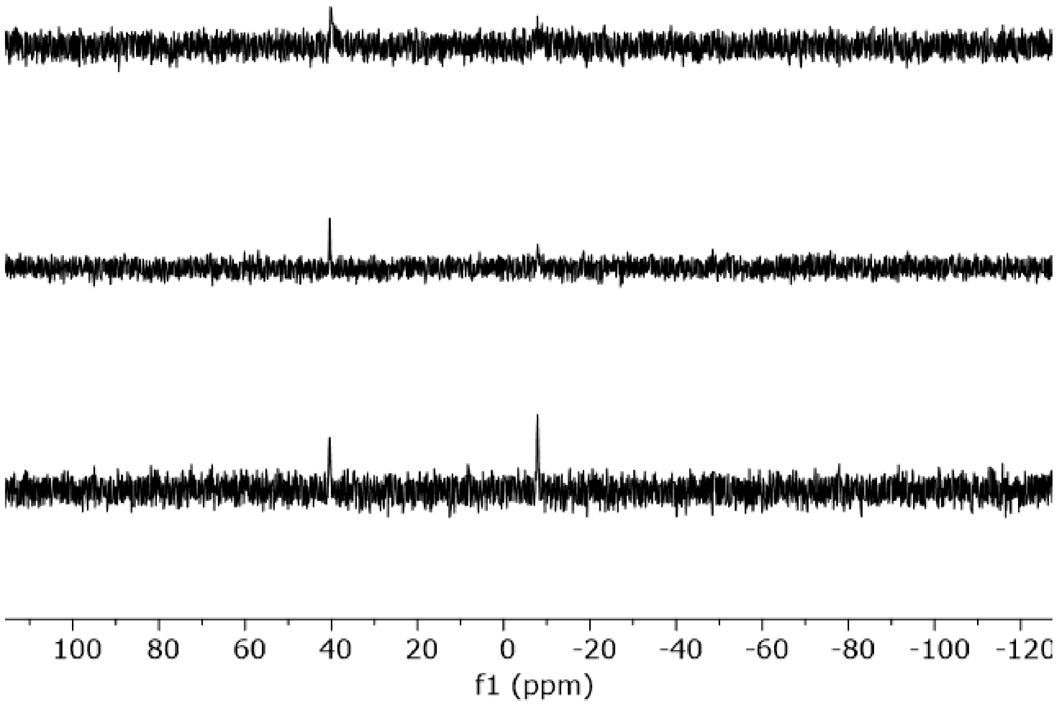

Figure S8. ^{31}P NMR of synthesis of **$Tp^*_4W_4Fe_{13}S_{14}$** after addition of 3 equivalents $SPPh_3$ (40 ppm) and formation of PPh_3 (-10 ppm): top (1 hour RT), middle (3 hours RT), bottom (16 hours RT).

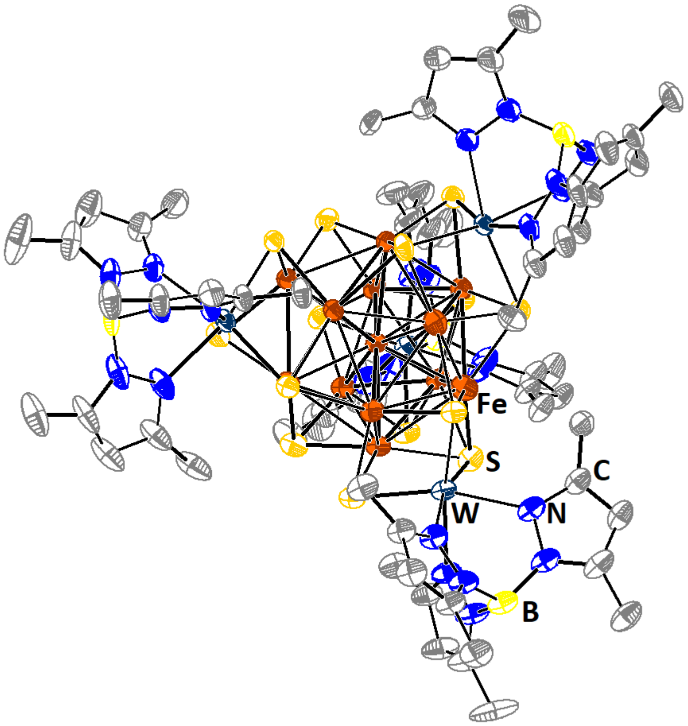

Figure S9. Crystal structure of **Tp*$_4$W$_4$Fe$_{13}$S$_{14}$**. Ellipsoids are shown at the 50% probability level. Hydrogen atoms and co-crystallized solvent molecules are not shown for clarity.

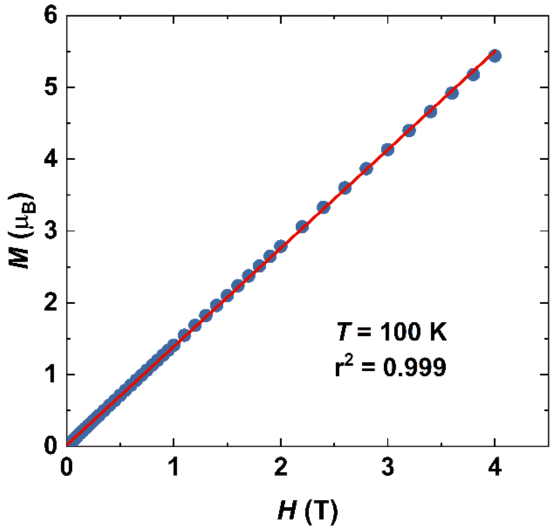

Figure S10. Magnetization data collected at 100 K from 0 to 4 T for **Tp*$_4$W$_4$Fe$_{13}$S$_{14}$** to confirm the absence of ferromagnetic impurities.

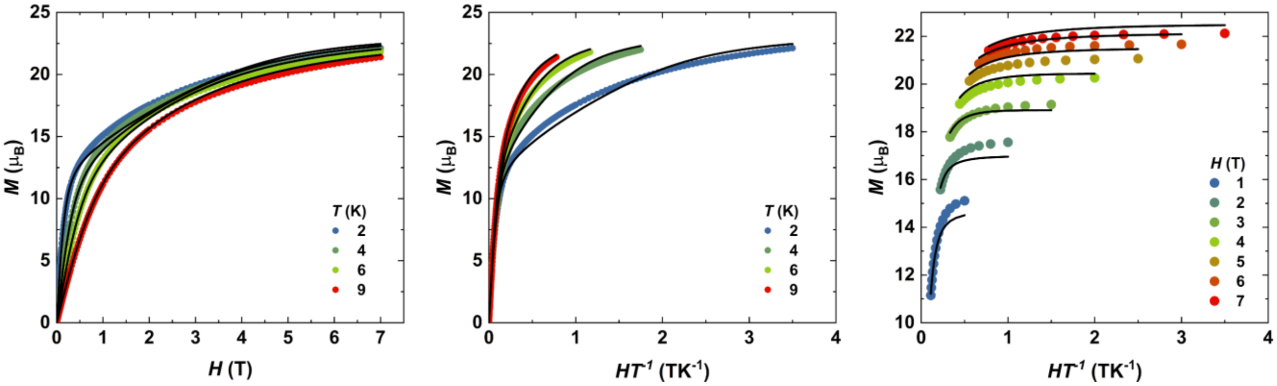

Figure S11. Magnetization and reduced magnetization plots for **$Tp*_4W_4Fe_{13}S_{14}$**. Black lines represent the best fits obtained with PHI software. Fit parameters obtained were $g = 1.80$, $S = 13$, and $D = -0.16$ cm^{-1}.

Additional Crystallographic Information

Additional refinement details:

$Tp*_4W_4Fe_{13}S_{12}$: The asymmetric unit of the structure contains diffuse solvent peaks, which could not be modelled satisfactorily. Therefore, the electron density for co-crystallized solvent molecules were accounted for using the *SQUEEZE* procedure in *PLATON*,[79] whereby 2220 electrons were found in a volume of 6995 Å^3, consistent with the presence of 13 [C_3H_7ON] in the asymmetric unit.

$Tp*_4W_4Fe_{13}S_{12}(NPh)_3$: The asymmetric unit of the structure contains diffuse solvent peaks, which could not be modelled satisfactorily. Therefore, the electron density for co-crystallized solvent molecules were accounted for using the *SQUEEZE* procedure in *PLATON*,[79] whereby 575 electrons were found in a volume of 2099 Å^3, consistent with the presence of 2 [C_3H_7ON] in the asymmetric unit.

This structure had a minor twin component. The twin was attempted to be resolved, but the intensities and frequency of reflections were not sufficient for integration. While the reciprocal lattice plot shows predominantly single crystal order, there are groups of reflections that overlap. Reflections were omitted if Fobs was significantly greater than Fcalc, which were calculated after integrating all of the reflections together. The number of reflections omitted was one-half of one percent or less of the total number of reflections collected and the structure remained at > 99% completion after these reflections were omitted.

$Tp^*_4W_4Fe_{13}S_{14}$: The asymmetric unit of the structure contains diffuse solvent peaks, which could not be modelled satisfactorily. Therefore, the electron density for co-crystallized solvent molecules were accounted for using the *SQUEEZE* procedure in *PLATON,*[79] whereby 1508 electrons were found in a volume of 3877 $Å^3$, consistent with the presence of 2.5 [C_3H_7ON] in the asymmetric unit.

This structure had a minor twin component. The twin was attempted to be resolved, but the intensities and frequency of reflections were not sufficient for integration. While the reciprocal lattice plot shows predominantly single crystal order, there are groups of reflections that overlap. Reflections were omitted if Fobs was significantly greater than Fcalc, which were calculated after integrating all of the reflections together. The number of reflections omitted was one-half of one percent or less of the total number of reflections collected and the structure remained at > 99% completion after these reflections were omitted.

Table S1: Comparison of cluster bond lengths (Å) and angles. Average bond lengths and angles given as the average ± the standard deviation.

	$\text{Tp*}_4\text{W}_4\text{Fe}_{13}\text{S}_{12}$	$\text{Tp*}_4\text{W}_4\text{Fe}_{13}\text{S}_{12}\text{N}_4$	$\text{Tp*}_4\text{W}_4\text{Fe}_{13}\text{S}_{12}(\text{NPh})_3$	$\text{Tp*}_4\text{W}_4\text{Fe}_{13}\text{S}_{14}$
$\text{Fe-Fe}_{\text{outer}}$	2.395(2) -2.771(2)	2.568(2) -2.737(2)	2.437(3) -2.941(5)	2.255(2) -2.845(8)
$\text{Fe-Fe}_{\text{inner}}$	2.486(2) -2.523(9)	2.602(2) -2.646(2)	2.462(9) -2.856(1)	2.452(3) -2.754(1)
Average S-W	2.397 ± 0.009	2.331 ± 0.004	2.347 ± 0.022	2.362 ± 0.029
Average Fe-S	2.358 ± 0.156	2.239 ± 0.015	2.277 ± 0.064	2.310 ± 0.077
Average $\text{Fe-X}_{\text{terminal}}$	N/A	1.909 ± 0.010	1.958 ± 0.053	2.259 ± 0.057
S-W-S Average	102.62° ± 0.31	102.21° ± 0.26	102.06° ± 0.88	102.96° ± 0.92

Table S2: Summary of statistics for diffraction data relevant for complexes.

Cluster	**$Tp^*_4W_4Fe_{13}S_{12}$**	**$Tp^*_4W_4Fe_{13}S_{12}N_4$**	**$Tp^*_4W_4Fe_{13}S_{12}(NPh)_3$**
CCDC	2128366	2128364	2128365
Empirical formula	$C_{73}\ H_{179}\ B_4\ Fe_{13}$ $N_{37}\ O_{13}\ S_{12}\ W_4$	$C_{72}\ H_{109}\ B_4\ Fe_{13}$ $N_{32}\ O_4\ S_{12}\ W_4$	$C_{45}\ H_{65.5}\ B_2\ Fe_{6.50}$ $N_{15.5}\ O_2\ S_6\ W_2$
Formula weight	3835.93	3376.35	1768.29
Temperature/K	100	100	100
Crystal system	Trigonal	Cubic	Triclinic
Space group	R-3	$P2_13$	P-1
a/Å	18.635(2)	22.167(17)	18.130 (6)
b/Å	18.635(2)	22.167(17)	18.381 (3)
c/Å	61.227(19)	22.167(17)	21.755 (8)
α/°	90	90	92.901 (14)
β/°	90	90	108.941 (12)
γ/°	120	90	104.906 (15)
Volume/Å^3	18414(7)	10892(25)	6555 (4)
Z	6	4	4
ρ_{calc}/g cm^{-3}	1.835	2.059	1.676
μ/mm^{-1}	20.955	6.164	5.116
F(000)	9934	6572	3212
Crystal size/mm^3	0.06 × 0.11 × 0.25	0.24 × 0.24 × 0.26	0.08 × 0.12 × 0.26
Radiation	Cu Kα	Mo Kα	Mo Kα
θ_{max}/°	79.31	37.257	32.033
Index ranges	$-23 \leq h \leq 18$ $-16 \leq k \leq 23$ $-77 \leq l \leq 74$	$-36 \leq h \leq 36$ $-31 \leq k \leq 37$ $-37 \leq l \leq 37$	$-26 \leq h \leq 26$ $-26 \leq k \leq 26$ $-32 \leq l \leq 32$
Reflections measured	36569	389217	306171
Independent reflections	8711	18318	39093
Restraints/Parameters	82/452	0/449	37/1267
GOF on F^2	1.034	1.060	1.038
R-factor	0.0828	0.0382	0.0756
Weighted R-factor	0.1641	0.0537	0.1152
Largest diff. peak/hole/e Å^{-3}	2.203/-2.957	1.380/-1.122	3.475/-1.806

Cluster	**$Tp^*_4W_4Fe_{13}S_{14}$**
CCDC	2128367
Empirical formula	$C_{37.5}$ $H_{59.5}$ B_2 $Fe_{6.50}$ $N_{14.5}$ $O_{2.5}$ S_7 W_2
Formula weight	1730.22
Temperature/K	100
Crystal system	Monoclinic
Space group	C2/c
a/Å	34.544(11)
b/Å	20.361(6)
c/Å	21.599(5)
α/°	90
β/°	123.092(9)
γ/°	90
Volume/Å^3	12728(6)
Z	8
ρ_{calc}/g cm^{-3}	1.691
μ/mm^{-1}	5.300
F(000)	6280
Crystal size/mm^3	0.10 × 0.13 × 0.20
Radiation	Mo Kα
θ_{max}/°	40.492
Index ranges	$-61 \le h \le 57$ $-36 \le k \le 33$ $-35 \le l \le 37$
Reflections measured	260392
Independent reflections	34625
Restraints/Parameters	18/584
GOF on F^2	1.018
R-factor	0.1229
Weighted R-factor	0.1503
Largest diff. peak/hole/e Å^{-3}	4.174/-3.440

References

(1) Doud, E. A.; Voevodin, A.; Hochuli, T. J.; Champsaur, A. M.; Nuckolls, C.; Roy, X. Superatoms in Materials Science. *Nat Rev Mater* **2020**, *5* (5), 371–387. https://doi.org/10.1038/s41578-019-0175-3.

(2) Claridge, S. A.; Castleman, A. W.; Khanna, S. N.; Murray, C. B.; Sen, A.; Weiss, P. S. Cluster-Assembled Materials. *ACS Nano* **2009**, *3* (2), 244–255. https://doi.org/10.1021/nn800820e.

(3) Yan, N.; Yuan, Y.; Dyson, P. J. Nanometallic Chemistry: Deciphering Nanoparticle Catalysis from the Perspective of Organometallic Chemistry and Homogeneous Catalysis. *Dalton Trans.* **2013**, *42* (37), 13294–13304. https://doi.org/10.1039/C3DT51180D.

(4) Reiss, G.; Hütten, A. Applications beyond Data Storage. *Nature Mater* **2005**, *4* (10), 725–726. https://doi.org/10.1038/nmat1494.

(5) Du, Y.; Sheng, H.; Astruc, D.; Zhu, M. Atomically Precise Noble Metal Nanoclusters as Efficient Catalysts: A Bridge between Structure and Properties. *Chemical reviews* **2019**, *120* (2), 526–622.

(6) Robertson, D. D.; Personick, M. L. Growing Nanoscale Model Surfaces to Enable Correlation of Catalytic Behavior Across Dissimilar Reaction Environments. *Chem. Mater.* **2019**, *31* (4), 1121–1141. https://doi.org/10.1021/acs.chemmater.8b04595.

(7) Jin, R.; Li, G.; Sharma, S.; Li, Y.; Du, X. Toward Active-Site Tailoring in Heterogeneous Catalysis by Atomically Precise Metal Nanoclusters with Crystallographic Structures. *Chem. Rev.* **2021**, *121* (2), 567–648. https://doi.org/10.1021/acs.chemrev.0c00495.

(8) Liu, L.; Corma, A. Metal Catalysts for Heterogeneous Catalysis: From Single Atoms to Nanoclusters and Nanoparticles. *Chemical reviews* **2018**, *118* (10), 4981–5079.

(9) Nguyen, T.-A. D.; Jones, Z. R.; Goldsmith, B. R.; Buratto, W. R.; Wu, G.; Scott, S. L.; Hayton, T. W. A Cu25 Nanocluster with Partial Cu(0) Character. *J. Am. Chem. Soc.* **2015**, *137* (41), 13319–13324. https://doi.org/10.1021/jacs.5b07574.

(10) Chakrahari, K. K.; Liao, J.-H.; Kahlal, S.; Liu, Y.-C.; Chiang, M.-H.; Saillard, J.-Y.; Liu, C. W. [Cu13 {S2CNnBu2} 6 (Acetylide) 4]+: A Two-Electron Superatom. *Angewandte Chemie International Edition* **2016**, *55* (47), 14704–14708.

(11) Dhayal, R. S.; Liao, J.-H.; Wang, X.; Liu, Y.-C.; Chiang, M.-H.; Kahlal, S.; Saillard, J.-Y.; Liu, C. W. Diselenophosphate-Induced Conversion of an Achiral [Cu20H11S2P(OiPr)29] into a Chiral [Cu20H11Se2P(OiPr)29] Polyhydrido Nanocluster. *Angewandte Chemie International Edition* **2015**, *54* (46), 13604–13608. https://doi.org/10.1002/anie.201506736.

(12) Nguyen, T.-A. D.; Jones, Z. R.; Leto, D. F.; Wu, G.; Scott, S. L.; Hayton, T. W. Ligand-Exchange-Induced Growth of an Atomically Precise Cu29 Nanocluster from a Smaller Cluster. *Chem. Mater.* **2016**, *28* (22), 8385–8390. https://doi.org/10.1021/acs.chemmater.6b03879.

(13) Sugiuchi, M.; Shichibu, Y.; Nakanishi, T.; Hasegawa, Y.; Konishi, K. Cluster–π Electronic Interaction in a Superatomic Au13 Cluster Bearing σ-Bonded Acetylide

Ligands. *Chem. Commun.* **2015**, *51* (70), 13519–13522. https://doi.org/10.1039/C5CC04312C.

(14) Touchton, A. J.; Wu, G.; Hayton, T. W. [Ni23Se12(PEt3)13] Revisited: Isolation and Characterization of [Ni23Se12Cl3(PEt3)10]. *Inorg. Chem.* **2021**, *60* (23), 17586–17592. https://doi.org/10.1021/acs.inorgchem.1c02184.

(15) Brennan, J. G.; Siegrist, T.; Kwon, Y. U.; Stuczynski, S. M.; Steigerwald, M. L. Nickel-Selenium-Triethylphosphine (Ni23Se12(PEt3)13), an Intramolecular Intergrowth of Nickel Selenide (NiSe) and Nickel. *J. Am. Chem. Soc.* **1992**, *114* (26), 10334–10338. https://doi.org/10.1021/ja00052a034.

(16) Fenske, D.; Krautscheid, H.; Müller, M. New Intermediate Steps in the Synthesis of Larger Nickel Clusters. *Angewandte Chemie International Edition in English* **1992**, *31* (3), 321–323. https://doi.org/10.1002/anie.199203211.

(17) Qian, H.; Zhu, M.; Wu, Z.; Jin, R. Quantum Sized Gold Nanoclusters with Atomic Precision. *Acc. Chem. Res.* **2012**, *45* (9), 1470–1479. https://doi.org/10.1021/ar200331z.

(18) Yang, H.; Wang, Y.; Zheng, N. Stabilizing Subnanometer Ag(0) Nanoclusters by Thiolate and Diphosphine Ligands and Their Crystal Structures. *Nanoscale* **2013**, *5* (7), 2674–2677. https://doi.org/10.1039/C3NR34328F.

(19) Desireddy, A.; Conn, B. E.; Guo, J.; Yoon, B.; Barnett, R. N.; Monahan, B. M.; Kirschbaum, K.; Griffith, W. P.; Whetten, R. L.; Landman, U.; Bigioni, T. P. Ultrastable Silver Nanoparticles. *Nature* **2013**, *501* (7467), 399–402. https://doi.org/10.1038/nature12523.

(20) Erickson, J. D.; Mednikov, E. G.; Ivanov, S. A.; Dahl, L. F. Isolation and Structural Characterization of a Mackay 55-Metal-Atom Two-Shell Icosahedron of Pseudo-Ih Symmetry, Pd55L12(M3-CO)20 (L = PR3, R = Isopropyl): Comparative Analysis with Interior Two-Shell Icosahedral Geometries in Capped Three-Shell Pd145, Pt-Centered Four-Shell Pd–Pt M165, and Four-Shell Au133 Nanoclusters. *J. Am. Chem. Soc.* **2016**, *138* (5), 1502–1505. https://doi.org/10.1021/jacs.5b13076.

(21) Chini, P. Large Metal Carbonyl Clusters (LMCC). *Journal of Organometallic Chemistry* **1980**, *200* (1), 37–61. https://doi.org/10.1016/S0022-328X(00)88636-2.

(22) Reber, A. C.; Khanna, S. N. Superatoms: Electronic and Geometric Effects on Reactivity. *Acc. Chem. Res.* **2017**, *50* (2), 255–263. https://doi.org/10.1021/acs.accounts.6b00464.

(23) Walter, M.; Akola, J.; Lopez-Acevedo, O.; Jadzinsky, P. D.; Calero, G.; Ackerson, C. J.; Whetten, R. L.; Grönbeck, H.; Häkkinen, H. A Unified View of Ligand-Protected Gold Clusters as Superatom Complexes. *PNAS* **2008**, *105* (27), 9157–9162. https://doi.org/10.1073/pnas.0801001105.

(24) Eremin, D. B.; Ananikov, V. P. Understanding Active Species in Catalytic Transformations: From Molecular Catalysis to Nanoparticles, Leaching, “Cocktails” of Catalysts and Dynamic Systems. *Coordination Chemistry Reviews* **2017**, *346*, 2–19. https://doi.org/10.1016/j.ccr.2016.12.021.

(25) Takano, S.; Tsukuda, T. Chemically Modified Gold/Silver Superatoms as Artificial Elements at Nanoscale: Design Principles and Synthesis Challenges. *J. Am. Chem. Soc.* **2021**, *143* (4), 1683–1698. https://doi.org/10.1021/jacs.0c11465.

(26) Yang, H.; Wang, Y.; Lei, J.; Shi, L.; Wu, X.; Mäkinen, V.; Lin, S.; Tang, Z.; He, J.; Häkkinen, H.; Zheng, L.; Zheng, N. Ligand-Stabilized Au13Cux (x = 2, 4, 8) Bimetallic Nanoclusters: Ligand Engineering to Control the Exposure of Metal Sites. *J. Am. Chem. Soc.* **2013**, *135* (26), 9568–9571. https://doi.org/10.1021/ja402249s.

(27) Si, W.-D.; Li, Y.-Z.; Zhang, S.-S.; Wang, S.; Feng, L.; Gao, Z.-Y.; Tung, C.-H.; Sun, D. Toward Controlled Syntheses of Diphosphine-Protected Homochiral Gold Nanoclusters through Precursor Engineering. *ACS Nano* **2021**, *15* (10), 16019–16029. https://doi.org/10.1021/acsnano.1c04421.

(28) Sun, C.; Mammen, N.; Kaappa, S.; Yuan, P.; Deng, G.; Zhao, C.; Yan, J.; Malola, S.; Honkala, K.; Häkkinen, H.; Teo, B. K.; Zheng, N. Atomically Precise, Thiolated Copper–Hydride Nanoclusters as Single-Site Hydrogenation Catalysts for Ketones in Mild Conditions. *ACS Nano* **2019**, *13* (5), 5975–5986. https://doi.org/10.1021/acsnano.9b02052.

(29) Zhu, M.; Lanni, E.; Garg, N.; Bier, M. E.; Jin, R. Kinetically Controlled, High-Yield Synthesis of Au25 Clusters. *J. Am. Chem. Soc.* **2008**, *130* (4), 1138–1139. https://doi.org/10.1021/ja0782448.

(30) Ito, E.; Takano, S.; Nakamura, T.; Tsukuda, T. Controlled Dimerization and Bonding Scheme of Icosahedral M@Au12 (M=Pd, Pt) Superatoms. *Angewandte Chemie International Edition* **2021**, *60* (2), 645–649. https://doi.org/10.1002/anie.202010342.

(31) Lee, S. C.; Lo, W.; Holm, R. Developments in the Biomimetic Chemistry of Cubane-Type and Higher Nuclearity Iron–Sulfur Clusters. *Chemical reviews* **2014**, *114* (7), 3579–3600.

(32) Xu, G.; Zhou, J.; Wang, Z.; Holm, R. H.; Chen, X.-D. Controlled Incorporation of Nitrides into W-Fe-S Clusters. *Angewandte Chemie International Edition* **2019**, *58* (46), 16469–16473.

(33) Xu, G.; Wang, Z.; Ling, R.; Zhou, J.; Chen, X.-D.; Holm, R. H. Ligand Metathesis as Rational Strategy for the Synthesis of Cubane-Type Heteroleptic Iron–Sulfur Clusters Relevant to the FeMo Cofactor. *Proceedings of the National Academy of Sciences* **2018**, *115* (20), 5089–5092.

(34) Zheng, B.; Chen, X.-D.; Zheng, S.-L.; Holm, R. H. Selenium as a Structural Surrogate of Sulfur: Template-Assisted Assembly of Five Types of Tungsten–Iron–Sulfur/Selenium Clusters and the Structural Fate of Chalcogenide Reactants. *J. Am. Chem. Soc.* **2012**, *134* (14), 6479–6490. https://doi.org/10.1021/ja3010539.

(35) Le, L. N. V.; Bailey, G. A.; Scott, A. G.; Agapie, T. Partial Synthetic Models of FeMoco with Sulfide and Carbyne Ligands: Effect of Interstitial Atom in Nitrogenase Active Site. *PNAS* **2021**, *118* (49), e2109241118. https://doi.org/10.1073/pnas.2109241118.

(36) *Partial decomposition is proposed to deliver the central Fe, corresponding to ~8% of the iron.*

(37) Powers, T. M.; Betley, T. A. Testing the Polynuclear Hypothesis: Multielectron Reduction of Small Molecules by Triiron Reaction Sites. *J. Am. Chem. Soc.* **2013**, *135* (33), 12289–12296. https://doi.org/10.1021/ja405057n.

(38) Pushkarevsky, N. A.; Konchenko, S. N.; Zabel, M.; Bodensteiner, M.; Scheer, M. Dimerization of Pentanuclear Clusters [Fe 3 Q (AsMe)(CO) 9](Q= Se, Te) as a Conversion Pathway to Novel Cubane-like Aggregates. *Dalton Transactions* **2011**, *40* (9), 2067–2074.

(39) Majumdar, A.; Holm, R. Specific Incorporation of Chalcogenide Bridge Atoms in Molybdenum/Tungsten-Iron-Sulfur Single Cubane Clusters. *Inorganic chemistry* **2011**, *50* (21), 11242–11251.

(40) Laupp, M.; Strähle, J. [(Ph3PAu)6(DppeAu2)(AuCl)4Pd], an Icosahedral Au12 Cluster with a Central Pd Atom. *Angewandte Chemie International Edition in English* **1994**, *33* (2), 207–209. https://doi.org/10.1002/anie.199402071.

(41) Dhayal, R. S.; Liao, J.-H.; Liu, Y.-C.; Chiang, M.-H.; Kahlal, S.; Saillard, J.-Y.; Liu, C. W. [Ag21S2P(OiPr)212]+: An Eight-Electron Superatom. *Angewandte Chemie International Edition* **2015**, *54* (12), 3702–3706. https://doi.org/10.1002/anie.201410332.

(42) J. Bailey, P.; A. Beswick, M.; G. Johnson, B. F.; Lewis, J.; R. Raithby, P.; Arellano, M. C. R. de. Dalton Communications. The First Undecaruthenium Hydrido Carbonyl Anion; Synthesis and Structural Characterisation of [Ru 11 H(CO) 27] 3– . *Journal of the Chemical Society, Dalton Transactions* **1992**, *0* (21), 3159–3160. https://doi.org/10.1039/DT9920003159.

(43) Gade, L. H.; Johnson, B. F. G.; Lewis, J.; McPartlin, M.; Powell, H. R.; Raithby, P. R.; Wong, W.-T. Synthesis and Structural Characterisation of the Osmium Cluster Dianions [Os17(CO)36]2– and [Os20(CO)40]2–. *J. Chem. Soc., Dalton Trans.* **1994**, No. 4, 521–532. https://doi.org/10.1039/DT9940000521.

(44) Chilton, N. F.; Anderson, R. P.; Turner, L. D.; Soncini, A.; Murray, K. S. PHI: A Powerful New Program for the Analysis of Anisotropic Monomeric and Exchange-Coupled Polynuclear d- and f-Block Complexes. *Journal of Computational Chemistry* **2013**, *34* (13), 1164–1175. https://doi.org/10.1002/jcc.23234.

(45) Roduner, E. Superatom Chemistry: Promising Properties of near-Spherical Noble Metal Clusters. *Physical Chemistry Chemical Physics* **2018**, *20* (37), 23812–23826.

(46) Sánchez, R. H.; Betley, T. A. Thermally Persistent High-Spin Ground States in Octahedral Iron Clusters. *J. Am. Chem. Soc.* **2018**, *140* (48), 16792–16806. https://doi.org/10.1021/jacs.8b10181.

(47) Nehrkorn, J.; Greer, S. M.; Malbrecht, B. J.; Anderton, K. J.; Aliabadi, A.; Krzystek, J.; Schnegg, A.; Holldack, K.; Herrmann, C.; Betley, T. A.; Stoll, S.; Hill, S. Spectroscopic Investigation of a Metal–Metal-Bonded Fe6 Single-Molecule Magnet with an Isolated S = 19/2 Giant-Spin Ground State. *Inorg. Chem.* **2021**, *60* (7), 4610–4622. https://doi.org/10.1021/acs.inorgchem.0c03595.

(48) Hernández Sánchez, R.; Betley, T. A. Meta-Atom Behavior in Clusters Revealing Large Spin Ground States. *J. Am. Chem. Soc.* **2015**, *137* (43), 13949–13956. https://doi.org/10.1021/jacs.5b08962.

(49) Hong, D.; Zhang, Y.; Holm, R. H. Heterometal Cubane-Type WFe3S4 and Related Clusters Trigonally Symmetrized with Hydrotris (3, 5-Dimethylpyrazolyl) Borate. *Inorganica chimica acta* **2005**, *358* (7), 2303–2311.

(50) Hauser, C.; Bill, E.; Holm, R. H. Single- and Double-Cubane Clusters in the Multiple Oxidation States [VFe3S4]3+,2+,1+. *Inorg. Chem.* **2002**, *41* (6), 1615–1624. https://doi.org/10.1021/ic011011b.

(51) Kowalska, J. K.; Hahn, A. W.; Albers, A.; Schiewer, C. E.; Bjornsson, R.; Lima, F. A.; Meyer, F.; DeBeer, S. X-Ray Absorption and Emission Spectroscopic Studies of [L2Fe2S2]n Model Complexes: Implications for the Experimental Evaluation of Redox States in Iron–Sulfur Clusters. *Inorg. Chem.* **2016**, *55* (9), 4485–4497. https://doi.org/10.1021/acs.inorgchem.6b00295.

(52) Jayarathne, U.; Chandrasekaran, P.; Greene, A. F.; Mague, J. T.; DeBeer, S.; Lancaster, K. M.; Sproules, S.; Donahue, J. P. X-Ray Absorption Spectroscopy Systematics at the Tungsten L-Edge. *Inorg. Chem.* **2014**, *53* (16), 8230–8241. https://doi.org/10.1021/ic500256a.

(53) Bjornsson, R.; A. Lima, F.; Spatzal, T.; Weyhermüller, T.; Glatzel, P.; Bill, E.; Einsle, O.; Neese, F.; DeBeer, S. Identification of a Spin-Coupled Mo(Iii) in the Nitrogenase Iron–Molybdenum Cofactor. *Chemical Science* **2014**, *5* (8), 3096–3103. https://doi.org/10.1039/C4SC00337C.

(54) Bigness, A.; Vaddypally, S.; Zdilla, M. J.; Mendoza-Cortes, J. L. Ubiquity of Cubanes in Bioinorganic Relevant Compounds. *Coordination Chemistry Reviews* **2022**, *450*, 214168. https://doi.org/10.1016/j.ccr.2021.214168.

(55) Ako, A. M.; Hewitt, I. J.; Mereacre, V.; Clérac, R.; Wernsdorfer, W.; Anson, C. E.; Powell, A. K. A Ferromagnetically Coupled Mn19 Aggregate with a Record S=83/2 Ground Spin State. *Angewandte Chemie International Edition* **2006**, *45* (30), 4926–4929. https://doi.org/10.1002/anie.200601467.

(56) Qin, L.; Zhang, H.-L.; Zhai, Y.-Q.; Nojiri, H.; Schröder, C.; Zheng, Y.-Z. A Giant Spin Molecule with Ninety-Six Parallel Unpaired Electrons. *iScience* **2021**, *24* (4), 102350. https://doi.org/10.1016/j.isci.2021.102350.

(57) Manoli, M.; Alexandrou, S.; Pham, L.; Lorusso, G.; Wernsdorfer, W.; Evangelisti, M.; Christou, G.; Tasiopoulos, A. J. Magnetic “Molecular Oligomers” Based on Decametallic Supertetrahedra: A Giant Mn49 Cuboctahedron and Its Mn25Na4 Fragment. *Angewandte Chemie International Edition* **2016**, *55* (2), 679–684. https://doi.org/10.1002/anie.201509461.

(58) Kang, S.; Zheng, H.; Liu, T.; Hamachi, K.; Kanegawa, S.; Sugimoto, K.; Shiota, Y.; Hayami, S.; Mito, M.; Nakamura, T.; Nakano, M.; Baker, M. L.; Nojiri, H.; Yoshizawa, K.; Duan, C.; Sato, O. A Ferromagnetically Coupled Fe42 Cyanide-Bridged Nanocage. *Nat Commun* **2015**, *6* (1), 5955. https://doi.org/10.1038/ncomms6955.

(59) Greer, S. M.; Gramigna, K. M.; Thomas, C. M.; Stoian, S. A.; Hill, S. Insights into Molecular Magnetism in Metal–Metal Bonded Systems as Revealed by a Spectroscopic and Computational Analysis of Diiron Complexes. *Inorg. Chem.* **2020**, *59* (24), 18141–18155. https://doi.org/10.1021/acs.inorgchem.0c02605.

(60) Chipman, J. A.; Berry, J. F. Paramagnetic Metal–Metal Bonded Heterometallic Complexes. *Chem. Rev.* **2020**, *120* (5), 2409–2447. https://doi.org/10.1021/acs.chemrev.9b00540.

(61) Ermert, D. M.; Gordon, J. B.; Abboud, K. A.; Murray, L. J. Nitride-Bridged Triiron Complex and Its Relevance to Dinitrogen Activation. *Inorg. Chem.* **2015**, *54* (19), 9282–9289. https://doi.org/10.1021/acs.inorgchem.5b00825.

(62) Wucherer, E. J.; Tasi, M.; Hansert, B.; Powell, A. K.; Garland, M. T.; Halet, J. F.; Saillard, J. Y.; Vahrenkamp, H. Intramolecular Conversion of an Azoalkane Ligand to Two Nitrene Ligands on a Triiron Cluster. *Inorganic Chemistry* **1989**, *28* (18), 3564–3572.

(63) Bartholomew, A. K.; Juda, C. E.; Nessralla, J. N.; Lin, B.; Wang, S. G.; Chen, Y.-S.; Betley, T. A. Ligand-Based Control of Single-Site vs. Multi-Site Reactivity by a Trichromium Cluster. *Angewandte Chemie* **2019**, *131* (17), 5743–5747.

(64) Dunn, P. L.; Chatterjee, S.; MacMillan, S. N.; Pearce, A. J.; Lancaster, K. M.; Tonks, I. A. The 4-Electron Cleavage of a N═N Double Bond by a Trimetallic TiNi2 Complex. *Inorg. Chem.* **2019**, *58* (17), 11762–11772. https://doi.org/10.1021/acs.inorgchem.9b01805.

(65) Li, Y.; Wong, W.-T. Low Valent Transition Metal Clusters Containing Nitrene/Imido Ligands. *Coordination Chemistry Reviews* **2003**, *243* (1), 191–212. https://doi.org/10.1016/S0010-8545(03)00082-1.

(66) Sappa, E.; Milone, L. Reactions of Ru3(CO)12 with Nitrobenzene and Aniline. *Journal of Organometallic Chemistry* **1973**, *61*, 383–388. https://doi.org/10.1016/S0022-328X(00)86569-9.

(67) Fuller, J.; Fortunelli, A.; Iii, W. A. G.; An, Q. Reaction Mechanism and Kinetics for Ammonia Synthesis on the Fe(211) Reconstructed Surface. *Phys. Chem. Chem. Phys.* **2019**, *21* (21), 11444–11454. https://doi.org/10.1039/C9CP01611B.

(68) Qian, J.; An, Q.; Fortunelli, A.; Nielsen, R. J.; Goddard, W. A. Reaction Mechanism and Kinetics for Ammonia Synthesis on the Fe(111) Surface. *J. Am. Chem. Soc.* **2018**, *140* (20), 6288–6297. https://doi.org/10.1021/jacs.7b13409.

(69) Piotrowski, M. J.; Piquini, P.; Da Silva, J. L. F. Density Functional Theory Investigation of $3d$, $4d$, and $5d$ 13-Atom Metal Clusters. *Phys. Rev. B* **2010**, *81* (15), 155446. https://doi.org/10.1103/PhysRevB.81.155446.

(70) Wang, J.; Sun, Z.-R.; Deng, L.; Wei, Z.-H.; Zhang, W.-H.; Zhang, Y.; Lang, J.-P. Reactions of a Tungsten Trisulfido Complex of Hydridotris(3,5-Dimethylpyrazol-1-Yl)Borate (Tp*) [Et4N][Tp*WS3] with CuX (X = Cl, NCS, or CN): Isolation, Structures, and Third-Order NLO Properties. *Inorg. Chem.* **2007**, *46* (26), 11381–11389. https://doi.org/10.1021/ic701641h.

(71) Zanato, C.; Cascio, M. G.; Lazzari, P.; Pertwee, R.; Testa, A.; Zanda, M. Tricyclic Fused Pyrazoles with a ‘Click’ 1,2,3-Triazole Substituent in Position 3 Are Nanomolar CB1 Receptor Ligands. *Synthesis* **2015**, *47* (06), 817–826. https://doi.org/10.1055/s-0034-1379887.

(72) Pangborn, A. B.; Giardello, M. A.; Grubbs, R. H.; Rosen, R. K.; Timmers, F. J. Safe and Convenient Procedure for Solvent Purification. *Organometallics* **1996**, *15* (5), 1518–1520. https://doi.org/10.1021/om9503712.

(73) Bruker, APEX3(Bruker AXS Inc., 2012).

(74) Bruker, SADABS(Bruker AXS Inc., 2001).

(75) Sheldrick, G. M. SHELXT – Integrated Space-Group and Crystal-Structure Determination. *Acta Cryst A* **2015**, *71* (1), 3–8. https://doi.org/10.1107/S2053273314026370.

(76) Altomare, A.; Cascarano, G.; Giacovazzo, C.; Guagliardi, A.; Burla, M. C.; Polidori, G.; Camalli, M. SIRPOW.92 – a Program for Automatic Solution of Crystal Structures by Direct Methods Optimized for Powder Data. *J Appl Cryst* **1994**, *27* (3), 435–436. https://doi.org/10.1107/S0021889894000221.

(77) Palatinus, L.; Chapuis, G. SUPERFLIP – a Computer Program for the Solution of Crystal Structures by Charge Flipping in Arbitrary Dimensions. *J Appl Cryst* **2007**, *40* (4), 786–790. https://doi.org/10.1107/S0021889807029238.

(78) Dolomanov, O. V.; Bourhis, L. J.; Gildea, R. J.; Howard, J. a. K.; Puschmann, H. OLEX2: A Complete Structure Solution, Refinement and Analysis Program. *J Appl Cryst* **2009**, *42* (2), 339–341. https://doi.org/10.1107/S0021889808042726.

(79) Spek, A. L. PLATON SQUEEZE: A Tool for the Calculation of the Disordered Solvent Contribution to the Calculated Structure Factors. *Acta Cryst C* **2015**, *71* (1), 9–18. https://doi.org/10.1107/S2053229614024929.

Appendix A

ISOLATION AND CHARACTERIZATION OF AN INTERMEDIATE IN THE SYNTHESIS OF MFE$_3$S$_3$(μ$_3$-CARBYNE) CLUSTERS

Abstract

Metal hydrides are implicated in the life sustaining transformation of N_2 to NH_3, which is performed by the nitrogenase enzymes at a complex octanuclear MFe_7S_9C co-factor called FeMco. Hydrides are proposed to play multiple roles in this reaction including imparting the ability of FeMco to accumulate multiple reducing equivalents under biological redox conditions and, through the release of H_2, act as a driving force for N_2 binding and activation at the co-factor. While detailed studies of these proposed metal hydrides have been conducted using spectroscopic techniques, structural confirmation and benchmarking studies are lacking. Current synthetic model systems of the proposed hydride intermediates consist of bi-nuclear Fe systems with sulfur based ligands, but complexes containing FeS clusters with carbon based bridging ligands, as in FeMco, are lacking. Described herein is the synthesis of an intermediate formed in the synthesis of $MFe_3S_3(\mu_3$-carbnye) clusters. Characterization of this cluster intermediate has led to the proposal that a metal hydride is present on the cluster, but further characterization is needed to confirm this hypothesis.

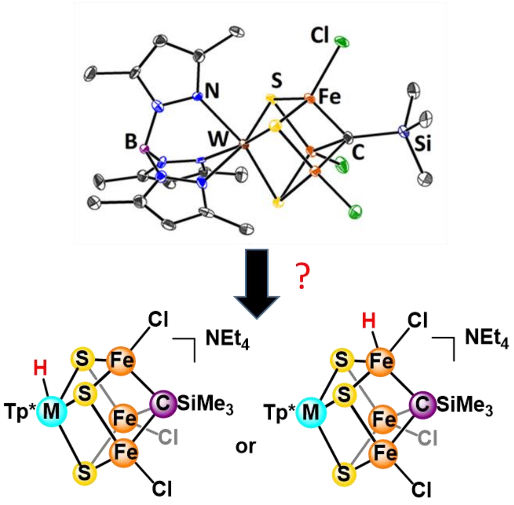

Introduction

The nitrogenase enzymes are involved in N_2 fixation to produce NH_3 and contain a complex metal active site termed FeMco that consists of a [M-7Fe-9S-C] cluster, where M = Mo, Fe, or V (Fig. 1).[1–3] Nitrogenase enzymes utilize protons and electrons to reduce N_2 based on the ideal reaction stoichiometry shown in Fig. 1, where H_2 is a byproduct.[4–6] The transfer of an impressive 8 protons and electrons to FeMco has been described using the Lowe-Thorneley mechanism for N_2 reduction, which involves the transfer of one proton and one electron in discrete steps to form intermediates E_1-E_8, where E_0 is the resting state of FeMco (Fig. 2).[4,7–9] N_2 binds to the enzymatic cluster in the E_4 state with concomitant loss of H_2.[4,10,11]

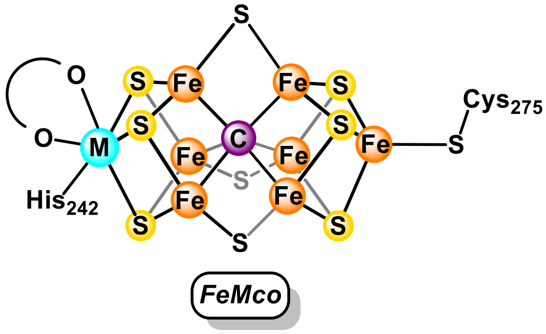

$$N_2 + 8H^+ + 16MgATP + 8\,e^- \longrightarrow 2NH_3 + H_2 + 16MgADP + 16P_i$$

Figure 1: Structure of FeMco and N_2 fixation reaction stoichiometry.

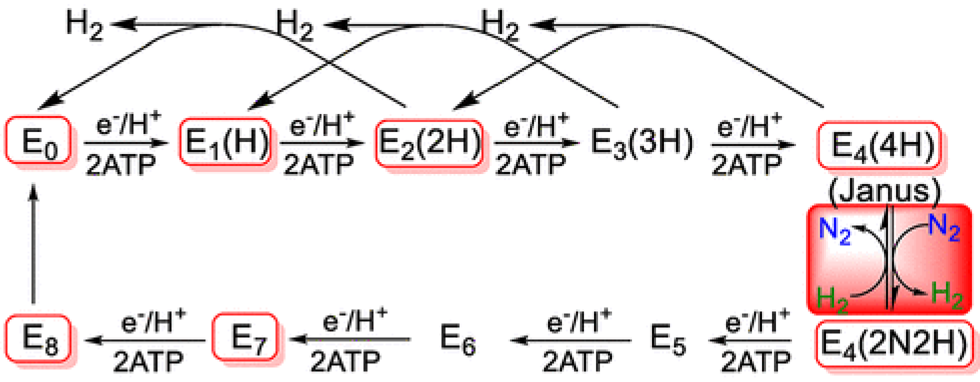

Figure 2: Lowe-Thorneley mechanism of N_2 reduction showing formation of E_1-E_8 states.

Generation of the different E states of FeMco is proposed to occur via formation of protonated sulfides and metal hydrides, which are implicated for strategically storing reducing equivalents at the cluster, as opposed to reduction of metal centers to biologically inaccessible and unstable redox states.[4,5,12,13] The presence of these species are hypothesized based on tracking the decomposition of the E_4 state of FeMco under photochemical conditions using electron paramagnetic resonance (EPR) spectroscopy with cryoannealing procedures[14,15] and the detection of H_2 loss.[16,17] Additionally, characterization of the freeze trapped E_1, E_2 and E_4 states using $^1H/^2H$ electron-nuclear double resonance spectroscopy (ENDOR) confirms the presence of metal hydride species.[14,15] For example, ENDOR and DFT have been used to propose the structure of the important E_4 state to which N_2 binds and suggest the presence of two protonated sulfides and two bridging hydrides (Fig. 3), where the presence of the bridging hydrides is proposed to be important for N_2 binding and activation due to facile reductive elimination of H_2.[4,18] Structural confirmation of these crucial hydride species using, for example, neutron diffraction has not been accomplished due to the difficulty of such studies on protein FeS clusters.

In metal hydride chemistry, paramagnetic metal hydrides are difficult to detect compared to their diamagnetic counterparts. A primary characterization method of diamagnetic metal hydrides involves using ^1H-NMR where the presence of an upfield resonance is diagnostic. However, a metal hydride in a paramagnetic species has not been observed via ^1H-NMR yet, due to the broadening of paramagnetic ^1H-NMR features and fast relaxation times.[19] IR and Raman spectroscopies have been used to detect metal hydrides, but the corresponding stretches are generally weak and difficult to observe.

Aside from neutron diffraction, which requires access to a beamline, another method for their detection is pulsed EPR, where synthesis of proteo and deutero species can provide confirmation of the presence of a metal hydride based on expected diagnostic parameters.

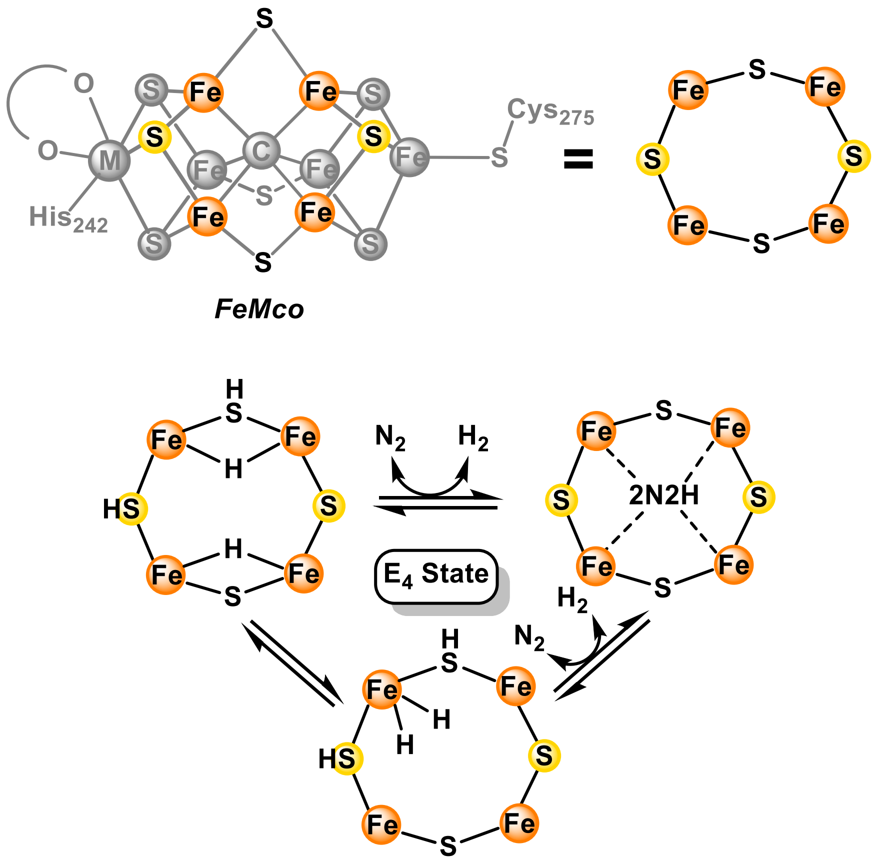

Figure 3: Reductive elimination mechanism of N_2 binding to the E_4 state of nitrogenase with loss of H_2 (bottom).

These parameters have been determined with the help of neutron diffraction studies to confirm the presence of a metal hydride in paramagnetic species. There are a limited number of synthetic Fe-hydrides containing bridging sulfides or thiolate ligands,[13,19–27] and even fewer containing carbon based ligands,[28,29] as are present in FeMco. In synthetic inorganic chemistry of FeS clusters, metal hydrides and/or protonated sulfide ligands have been proposed based on indirect evidence using protonated/unprotonated thiolate ligand exchange studies.[30] However, the direct identification of a metal hydride species on a synthetic FeS cluster that contains more than two Fe centers has not been confirmed and, further, one containing a bridging carbon based ligand.

We have previously reported the synthesis of $[Et_4N]_2[Tp^*WS_3Fe_3(\mu_3\text{-}CSiMe_3)Cl_3]$ (**3**) and $[Et_4N][Tp^*WS_3Fe_3(\mu_3\text{-}CSiMe_3)Cl_3]$ (**5**) carbyne clusters via oxidation and chloride addition to $[Et_4N][Tp^*WS_3Fe_3(CH_2SiMe_3)_3]$ (**2**) with crystallization in N,N-dimethylformamide (DMF) and oxidation using $[(Br\text{-}C_6H_4)_3N][BPh_4]$, respectively (Fig. 4).[31] Recrystallization of this cluster directly from acetonitrile (MeCN) results in formation of $[Et_4N][Tp^*WS_3Fe_3(\mu_3\text{-}CSiMe_3)Cl_3]$ (**4**) based on a single crystal X-ray diffraction (SC-XRD) study suggesting the formation of **5** and an even number of d-electrons (Fig. 4). However, a perpendicular mode electron paramagnetic resonance (EPR) study indicated a half-integer spin state of $S = 3/2$, implying the presence of an additional ligand on the cluster that is not detectable via SC-XRD, such as a hydrogen atom. Described herein is characterization data of **4** that lead to the proposal of a hydride ligand on **4**.

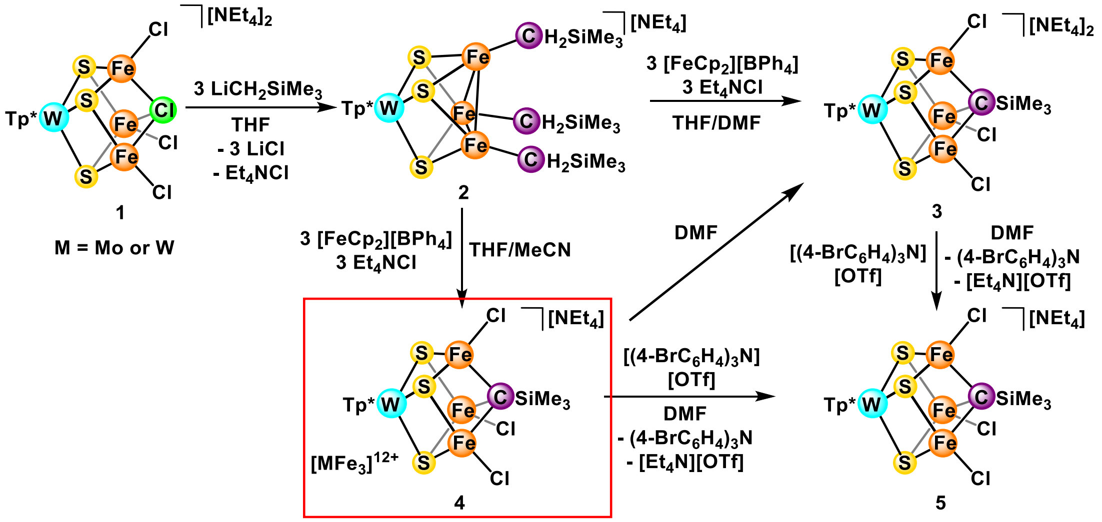

Figure 4: Synthesis of carbyne bridged WFeS clusters.

Results and Discussion

The synthesis of **4** with recrystallization from MeCN exhibits a S=3/2 EPR spectrum (Fig. 5) that is inconsistent with the SC-XRD structure and suggests either a miss-assignment of the atoms in the crystal structure or the presence of a hydrogen atom in the structure that cannot be resolved using SC-XRD. To determine if the presence of a half-integer spin species is due to solution state disproportionation, EPR was also taken of crystals of **4** diluted in boron nitride (Fig. 6) and also indicates an integer spin species. In terms of mis-assignment in the crystal structure, the resolution of the crystal structure does not allow for confirmation of the identity of the bridging non-metallic atoms in the cluster as sulfide as opposed to chloride atoms, whereas all other atoms can be assigned confidently. To determine the possibility of halide exchange within the cluster, the bromide analogue of **1**, $[Et_4N][Tp^*WS_3Fe_3(\mu_3\text{-}Br)Br_3]$,[32] was used to synthesize $[Et_4N][Tp^*WS_3Fe_3(\mu_3\text{-}CSiMe_3)Br_3]$ **4-Br** and using Et_4NBr instead of Et_4NCl in the second step of the synthesis (Fig. 4 and 7). Due to the large difference in electron

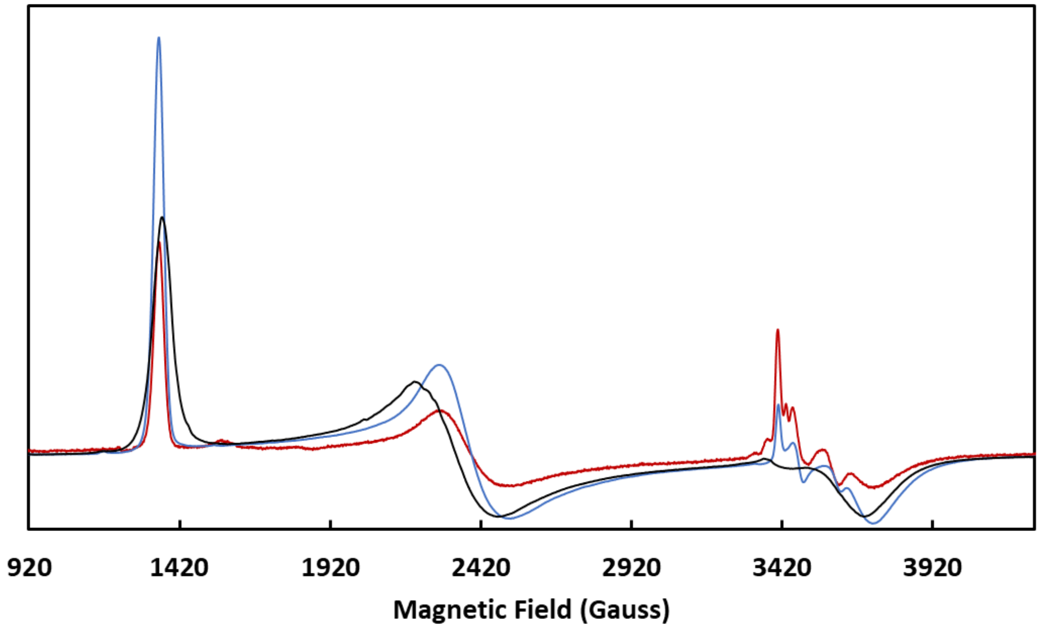

Figure 5: CW-EPR spectra of **5** in a 3:1 mixture of butyronitrile to propionitrile (blue) and **4** in a 3:1 mixture of butyronitrile to propionitrile (red) and DMF (black). Data acquisition parameters, respectively: frequency = 9.6375 MHz, 9.6385 MHz, and 9.6370 MHz; power = 2 mW, conversion time = 10.12 ms, and modulation amplitude = 8 G.

density of sulfur versus bromide, the synthesis of this analogue clearly identifies the bridging atoms in the cluster to be sulfides and the terminal atoms of the Fe centers to be bromides based on SC-XRD (Fig. 7, S30). An EPR study of **4-Br** is consistent with that of **4** (Fig. S10), both corresponding to half-integer spin species, suggesting the presence of either a metal hydride or a protonated sulfide.

Based on the proposal of a metal hydride or protonated sulfide, **4** was reacted with one equivalent of the phosphazene P_2Et and a ^{1}H-NMR study showed complete consumption of the base (Fig. S3). Recrystallization of the product clusters from DMF showed formation of $[Tp^*WS_3Fe_3(\mu_3\text{-}CSiMe_3)Cl_3]^{n-}$ based on SC-XRD, but with P_2Et co-

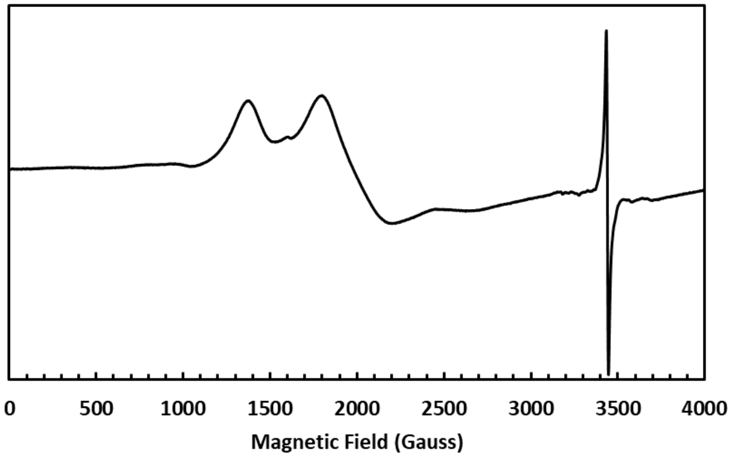

Figure 6: EPR spectrum of crystals of **4** diluted in boron nitride. Data acquisition parameters: frequency = 9.6389 MHz, conversion time = 10.12 ms, and modulation amplitude = 8 G.

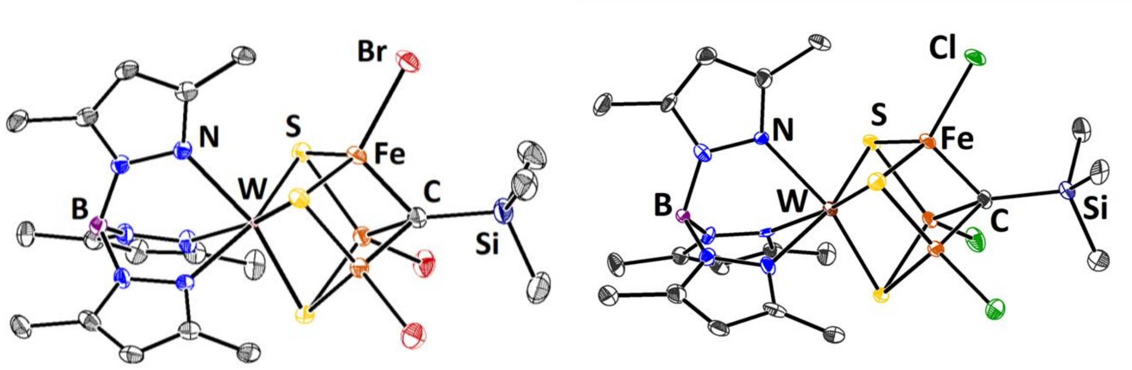

Figure 7: Crystal structures of [Et_4N][$Tp^*WS_3Fe_3(\mu_3\text{-}CSiMe_3)Br_3$] (**4-Br**) and [$Et_4N$][$Tp^*WS_3Fe_3(\mu_3\text{-}CSiMe_3)Cl_3$] (**4**). Ellipsoids plotted at the 50% probability level. Hydrogen, solvent, and counterion atoms not shown for clarity.

crystallized making it difficult to determine the oxidation state of the cluster due to the inability to resolve possible protons on P_2Et. Alternatively, simply dissolving **4** in DMF results in crystallization of **5** in 40% yield and adding one equivalent of Et_4NCl results in

90% yield of **5**, suggesting that DMF acts as a base in the transformation of the monoanionic cluster to the dianionic cluster. The EPR spectrum of **5** in both DMF and nitrile shows EPR features distinct, but similar to **4** suggesting a similar cluster spin state despite a difference in the cluster oxidation states (Fig. 5). One electron oxidation of **5** results in formation of the monoanionic cluster **6**, as described previously, which is EPR silent.

3, **4**, and **5** can be analyzed using SC-XRD to compare the bond metrics of the clusters (Table 1) and indicate similar W-S bond lengths. **4** has shortened Fe-S, Fe-Cl, and Fe-C bond lengths compared to **3**, which is consistent with a reduction at the Fe centers upon generation of **3** from **4**, as would occur with loss of a proton from a metal hydride rather than deprotonation of a bridging thiolate ligand to form a sulfide.

Table 1: Average Bond Lengths ± St. Dev. (Å)

Bond	**4**	**3**	**5**
W-S	2.352 ± 0.006	2.360 ± 0.001	2.351 ± 0.005
Fe-S	2.240 ± 0.006	2.282 ± 0.010	2.238 ± 0.005
Fe-Cl	2.214 ± 0.003	2.258 ± 0.004	2.213 ± 0.002
C-Si	1.859	1.845	1.858
Fe-C	1.910 ± 0.007	1.921 ± 0.015	1.910 ± 0.005

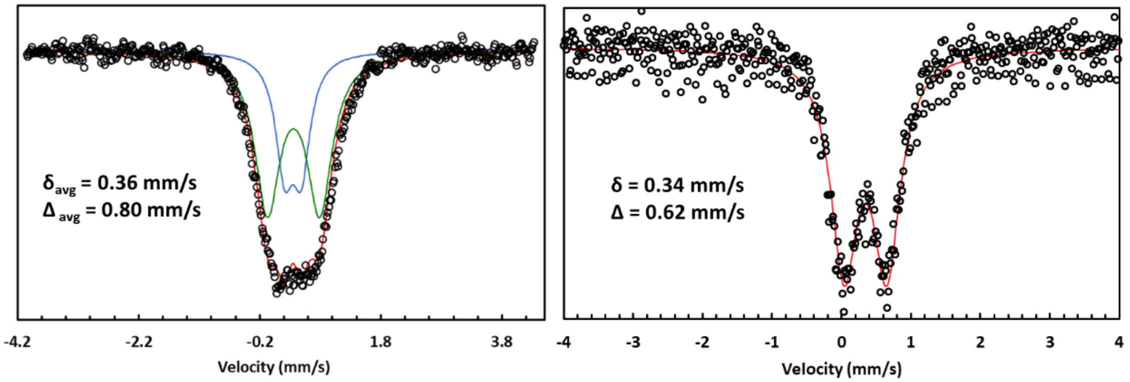

Figure 8: Mössbauer spectra and parameters for **4** (left) and **5** (right). Fitting details can be found in the experimental section.

To further confirm that **4** and **5** are different clusters, Mössbauer spectroscopy was performed. The Mössbauer spectra are clearly distinct (Fig. 8), although the Mössbauer parameters are similar. The Mo analogues of clusters **1-5** can be synthesized, as described in the experimental section, and show the same evidence for a metal hydride being present in terms of SC-XRD, CW-EPR, and Mössbauer data (see experimental section). Based on the presented data, two structures are proposed for the metal hydride

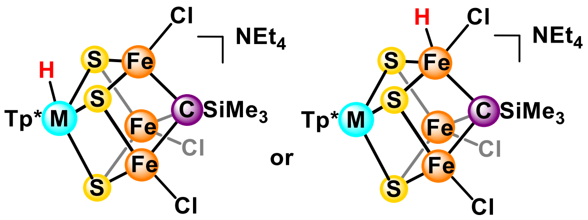

Figure 9: Proposed structures of metal hydrides of cluster **4**.

species where the hydride could be bound to one of the Fe centers or to the W/Mo center (Fig. 9).

Attempts to regenerate **4** from **3** and **5**, as summarized in Fig. 10, were unsuccessful. Reactions were analyzed using SC-XRD to determine the number of counterions present in the crystallized material. However, EPR spectra of the crystallized material were not consistent with the generation of **4**. This could imply that the deprotonation of the metal hydride is irreversible, at least under the conditions tried.

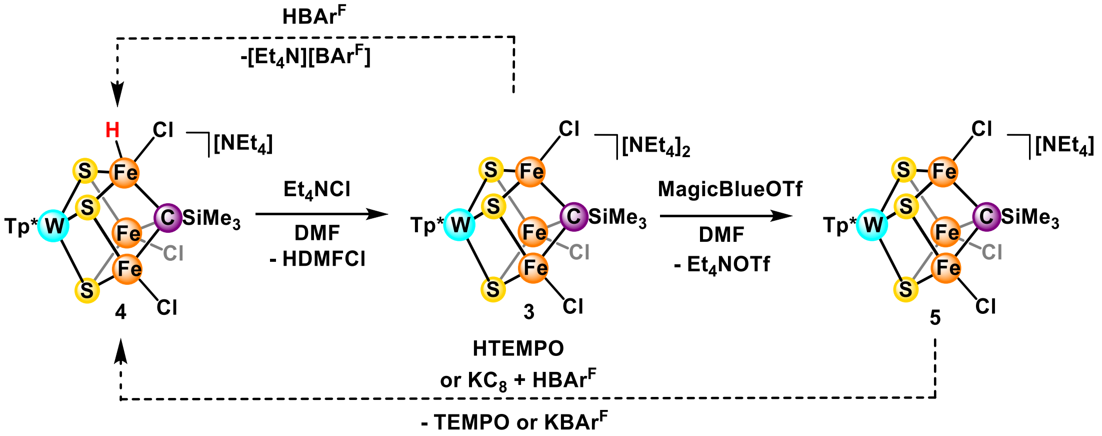

Figure 10: Synthetic routes in attempts to regenerate **4** from **5** or **6**.

Despite the one electron difference in the overall metal oxidation states of **4** and **5**, $[MFe_3]^{13+}$ and $[MFe_3]^{12+}$, respectively, the clusters exhibit similar structural and Mössbauer parameters, indicating similar oxidation states of the Fe centers. This suggests that the redox transformation between **4** and **5** is primarily centered at W.

Conclusion

The SC-XRD and EPR data of the carbyne cluster **4** indicate the presence of an additional ligand on the cluster that is not detectable using SC-XRD. Based on the structural and electronic data of **4** and comparisons of the characterization of **5** and **6**, a metal hydride is proposed. This would be the first metal hydride reported on a MFeS cluster and in multi-metallic FeS system with a bridging carbon based ligand. The proposed metal hydride imparts interesting electronic and structural properties on **4**, making the bond metrics and oxidation states of the Fe centers similar to **5**, despite different spin states of the two clusters.

To confirm the presence of a metal hydride species, labelling studies are underway to create the proposed deuterated metal hydride species. Pulsed EPR will be performed on the clusters to further understand if a metal hydride species is present based on published literature paramagnetic metal hydride parameters.

Experimental

General Considerations

All reactions were performed at room temperature in an N_2-filled M. Braun glovebox or using standard Schlenk techniques unless otherwise specified. Glassware was oven dried at 140 ºC for at least 2 h prior to use, and allowed to cool under vacuum. Sodium tetrafluoroborate ($NaBPh_4$) was purchased in an anhydrous form and dissolved in acetonitrile (CH_3CN) and dried over 3 Å molecular sieves for 2 days before being filtered over Celite and dried in vacuo. $[Et_4N]_2[Tp^*WFe_3S_3(\mu_3\text{-}Cl)Cl_3]$[32] **(1)** (Tp* = tris(3,5-dimethyl-1-pyrazolyl)borate), $[Et_4N]_2[Tp^*MoFe_3S_3(\mu_3\text{-}Cl)Cl_3]$ (**1-Mo**),[33] $[(4\text{-}BrC_6H_4)_3N][OTf]$, and ferrocenium tetrafluoroborate $[FeCp_2][BPh_4]$ were prepared according to literature procedures. Tetrahydrofuran (THF), diethyl ether (Et_2O), benzene (C_6H_6), toluene, CH_3CN, hexanes, and pentane were dried by sparging with nitrogen for at least 15 minutes, then passing through a column of activated A2 alumina under positive N_2 pressure and then degassed via several consecutive cycles of active vacuum and agitation on the Schlenk line before use.[34] Dimethylformamide was purchased in an anhydrous form from MiliporeSigma@, cannula-transferred to an oven dried Schlenk under N_2, degassed via several consecutive cycles of active vacuum and agitation on the Schlenk line, and then brought into the glovebox and dried over 3 Å molecular sieves for 2 days before use. ^{1}H and ^{31}P NMR spectra were recorded on a Varian 400 MHz spectrometer. ^{1}H-NMR spectra in proteo solvents were recorded on a Varian 400 MHz spectrometer using solvent suppression protocols. *d8*-THF, CD_3CN, and C_6D_6, were purchased from Cambridge Isotope Laboratories, dried over calcium hydride, degassed by three freeze-pump-thaw cycles, and vacuum transferred prior to use. All other reagents were purchased from commercial sources in their anhydrous forms and used without further purification.

Synthetic Procedures

Synthesis of $[Et_4N][Tp^*WFe_3S_3(CH_3SiMe_3)_3]$ (2). $[Et_4N]_2[Tp^*WFe_3S_3(\mu_3\text{-}Cl)Cl_3]$ (100 mg, 0.087 mmol) was measured into a scintillation vial and suspended in THF (6 mL). $LiCH_2SiMe_3$ (0.37 ml of 0.7 M pentane solution, 0.261 mmol) was added to the stirring suspension dropwise at room temperature. The reaction suspension was allowed to stir at room temperature for 24 h. The suspension was filtered over a Celite pad and then dried *in-vacuo*. After trituration three times with Et_2O, the solids were washed with Et_2O and then C_6H_6 until the filtrate was colorless. The desired product was extracted into a minimum of THF and crystallization was set up with vapor diffusion of 2x volume of pentane to yield dark needle like crystals. Finally, the crystals were dried under vacuum to yield 79.4 mg of the final product (80% yield). ^{1}H NMR (400 MHz, THF): δ 16.1 (br s), 7.0 (br s), -18.3 (s) ppm. Anal. calcd. (%) for C35H75BFe3N7S3Si3W: C, 36.98; H, 6.65; N, 8.63. Found: C, 37.33; H, 6.85; N, 6.27.

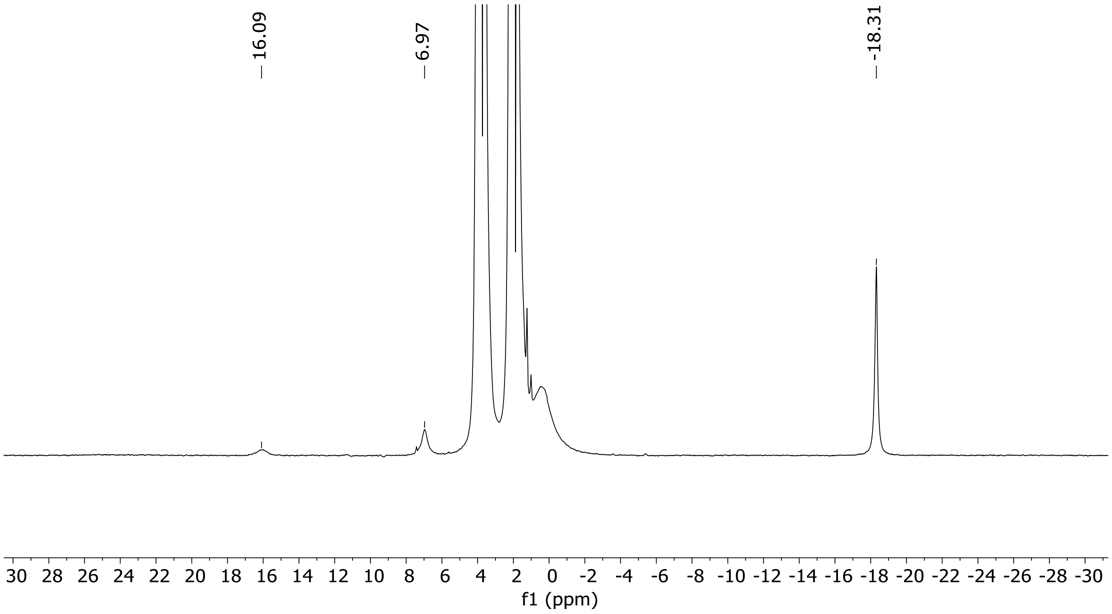

Figure S1: ^{1}H-NMR spectrum of $[Et_4N][Tp^*WFe_3S_3(CH_3SiMe_3)_3]$ in THF.

Synthesis of $[Et_4N][Tp^*MoFe_3S_3(CH_3SiMe_3)_3]$ (2-Mo). $[Et_4N]_2[Tp^*MoFe_3S_3(\mu_3\text{-}Cl)Cl_3]$ (100 mg, 0.095 mmol) was measured into a scintillation vial and suspended in THF (6 mL). $LiCH_2SiMe_3$ (0.41 ml of 0.7 M pentane solution, 0.285 mmol) was added to the stirring suspension dropwise at room temperature. The reaction suspension was allowed to stir at room temperature for 24 h. The suspension was filtered over a Celite pad and then dried *in-vacuo*. After trituration three times with Et_2O, the solids were washed with Et_2O and then C_6H_6 until the filtrate was colorless. The desired product was extracted into a minimum of THF and crystallization was set up with vapor diffusion of 2x volume of pentane to yield dark needle like crystals. Finally, the crystals were dried under vacuum to yield 64.8 mg of the final product (82% yield). ^{1}H NMR (400 MHz, THF): δ 19.7 (br s), 12.9 (s), -0.3 (s), -10.9 (s) ppm. Anal. calcd. (%) for C35H75BFe3N7S3Si3Mo: C, 40.08; H, 7.21; N, 9.35. Found: C, 40.11; H, 7.18; N, 9.08.

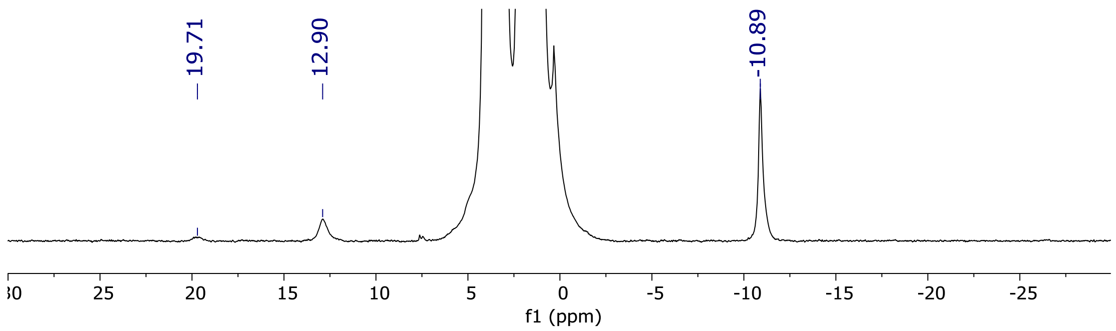

Figure S2: ^{1}H-NMR spectrum of $[Et_4N][Tp^*MoFe_3S_3(CH_3SiMe_3)_3]$ in THF.

Synthesis of $[Et_4N]_2[Tp^*WFe_3S_3(\mu_3\text{-}CSiMe_3)Cl_3]$ (3). **2** (100 mg, 0.088 mmol) was measured into a scintillation vial and dissolved in THF (6 mL). The solution was cooled to -78 °C and $[FeCp_2][BPh_4]$ (133.3 mg, 0.26 mmol) was added and the solution was maintained at -78 °C for 2 h. Et_4NCl (43.1 mg, 0.26 mmol) was added to the solution and the reaction was brought to room temperature and stirred at room temperature for 3 h. It was then filtered over a Celite pad and dried *in-vacuo*. After trituration three times with Et_2O, the solids were washed with pentane, Et_2O, and then C_6H_6 until the filtrate was colorless. The product was extracted into a minimum of THF and crystallization was set up with vapor diffusion of 2x volume of Et_2O to yield dark block like crystals. The crystals were then dissolved in a minimum of DMF and crystallization was set up with vapor diffusion of 3x volume of Et_2O. Finally, the crystals were dried under vacuum to yield 68.5 mg of the final product (65% yield). ^{1}H NMR silent except for solvent peaks. Anal. calcd. (%) for C35H71BCl3Fe3N8S3SiW: C, 35.13; H, 5.98; N, 9.36. Found: C, 34.97; H, 6.12; N, 8.42.

Synthesis of $[Et_4N][Tp^*WFe_3S_3(\mu_3\text{-}CSiMe_3)Cl_3]$ (5). **4** (100 mg, 0.084 mmol) was measured into a scintillation vial and dissolved in DMF (6 mL). The solution was cooled to -78 °C and $[(4\text{-}BrC_6H_4)_3N][OTf]$ (53.0 mg, 0.084 mmol) was added. The solution was stirred at room temperature for 30 minutes and then filtered over a Celite pad. 20x the volume of Et_2O was added and the solution was allowed to sit for at least 6 hours before dark needle like crystals formed. The crystals were dissolved in 2 mL of DMF and then filtered over a Celite pad and then 18 mL of Et_2O was added and the solution was allowed to sit for at least 6 hours before dark needle like crystals formed. This was performed 5x to achieve high purity. Finally, the crystals were dried under vacuum to yield 58.2 mg of the final product (65% yield).

Synthesis of [Et_4N][$Tp^*WFe_3S_3(\mu_3$-$CSiMe_3)HCl_3$] (4). **2** (100 mg, 0.088 mmol) was measured into a scintillation vial and dissolved in THF (6 mL). The solution was cooled to -78 °C and [$FeCp_2$][BPh_4] (133.3 mg, 0.26 mmol) was added and the solution was maintained at -78 °C for 2h. Et_4NCl (43.1 mg, 0.26 mmol) was added to the solution and the reaction was brought to room temperature and stirred at room temperature for 3 h. It was then filtered over a Celite pad and dried *in-vacuo*. After trituration three times with Et_2O, the solids were washed with pentane, Et_2O, and then C_6H_6 until the filtrate was colorless. The product was extracted into a minimum of THF and crystallization was set up with vapor diffusion of 2x volume of Et_2O to yield dark block like crystals. The crystals were re-dissolved in a minimum of MeCN, filtered over a Celite pad, and crystallization was set up with vapor diffusion of 2x volume of Et_2O to yield dark block like crystals. Finally, the crystals were dried under vacuum to yield 72.3 mg of the final product (77% yield). ^1H NMR silent except for solvent peaks. Anal. calcd. (%) for C27H52BCl3Fe3N7S3SiW: C, 30.38; H, 4.91; N, 9.18. Found: C, 30.19; H, 4.79; N, 7.35.

Synthesis of [Et_4N][$Tp^*WFe_3S_3(\mu_3$-$CSiMe_3)HBr_3$] (4-Br). **2** (100 mg, 0.088 mmol) was measured into a scintillation vial and dissolved in THF (6 mL). The solution was cooled to

-78 °C and $[FeCp_2][BPh_4]$ (133.3 mg, 0.26 mmol) was added and the solution was maintained at -78 °C for 2 h. Et_4NBr (54.6 mg, 0.26 mmol) was added to the solution and the reaction was brought to room temperature and stirred at room temperature for 3 h. It was then filtered over a Celite pad and dried *in-vacuo*. After trituration three times with Et_2O, the solids were washed with pentane, Et_2O, and then C_6H_6 until the filtrate was colorless. The product was extracted into a minimum of THF and crystallization was set up with vapor diffusion of 2x volume of Et_2O to yield dark block like crystals. The crystals were re-dissolved in a minimum of MeCN, filtered over a Celite pad, and crystallization was set up with vapor diffusion of 2x volume of Et_2O to yield dark block like crystals. Finally, the crystals were dried under vacuum to yield 78.1 mg of the final product (74% yield). ^1H NMR silent except for solvent peaks. Anal. calcd. (%) for C27H52BBr3Fe3N7S3SiW: C, 27.00; H, 4.36; N, 8.16. Found: C, 26.87; H, 4.21; N, 7.38.

Synthesis of $[Et_4N]_2[Tp^*MoFe_3S_3(\mu_3\text{-}CSiMe_3)Cl_3]$ (3-Mo). **2** (100 mg, 0.095 mmol) was measured into a scintillation vial and dissolved in THF (6 mL). The solution was cooled to -78 °C and $[FeCp_2][BPh_4]$ (133.3 mg, 0.29 mmol) was added and the solution was maintained at -78 °C for 2 h. Et_4NCl (43.1 mg, 0.29 mmol) was added to the solution and the reaction was brought to room temperature and stirred at room temperature for 3 h. It was then filtered over a Celite pad and dried *in-vacuo*. After trituration three times with Et_2O, the solids were washed with pentane, Et_2O, and then C_6H_6 until the filtrate was colorless. The product was extracted into a minimum of THF and crystallization was set up with vapor diffusion of 2x volume of Et_2O to yield dark block like crystals. The crystals were then dissolved in a minimum of DMF and crystallization was set up with vapor diffusion of 3x volume of Et_2O. Finally, the crystals were dried under vacuum to yield 68.5

mg of the final product (65% yield). ^{1}H NMR silent except for solvent peaks. Anal. calcd. (%) for C35H71BCl3Fe3N8S3SiMo: C, 37.91; H, 6.45; N, 10.

Synthesis of [Et$_4$N][Tp*MoFe$_3$S$_3$(μ_3-CSiMe$_3$)Cl$_3$] (5-Mo). **4** (100 mg, 0.090 mmol) was measured into a scintillation vial and dissolved in DMF (6 mL). The solution was cooled to -78 °C and [(4-BrC$_6$H$_4$)$_3$N][OTf] (56.9 mg, 0.090 mmol) was added. The solution was stirred at room temperature for 30 minutes and then filtered over a Celite pad. 20x the volume of Et$_2$O was added and the solution was allowed to sit for at least 6 hours before dark needle like crystals formed. The crystals were dissolved in 2 mL of DMF and then filtered over a Celite pad and then 18 mL of Et$_2$O was added and the solution was allowed to sit for at least 6 hours before dark needle like crystals formed. This was performed 5x to achieve high purity. Finally, the crystals were dried under vacuum to yield 59.8 mg of the final product (65% yield). ^{1}H NMR (400 MHz, CD$_3$CN): δ 6.01 (s, 3H), 3.6 (s, 9H), 3.2 (q, 9H), 2.3 (s, 9H), 1.2 (td, 12H), 0.6 (s, 9H) ppm. Anal. calcd. (%) for C27H51BCl3Fe3N7S3SiMo: C, 33.14; H, 5.25; N, 10.75.

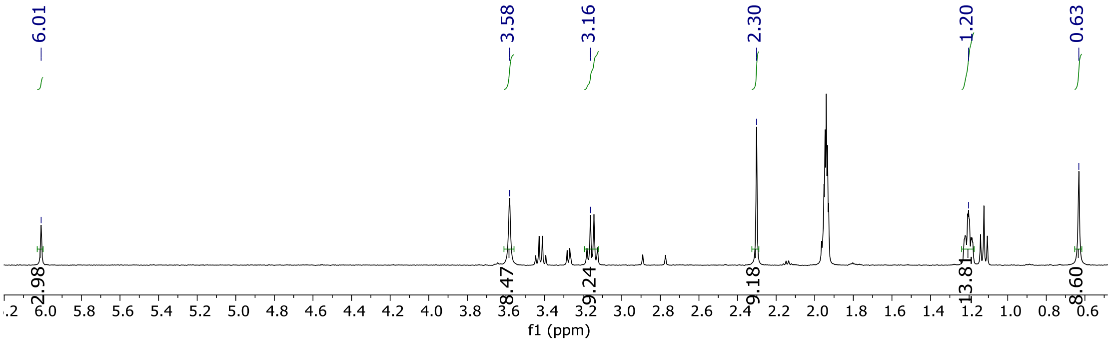

Synthesis of [Et$_4$N][Tp*MoFe$_3$S$_3$(μ_3-CSiMe$_3$)HCl$_3$] (4-Mo). **2** (100 mg, 0.090 mmol) was measured into a scintillation vial and dissolved in THF (6 mL). The solution was cooled to -78 °C and [FeCp$_2$][BPh$_4$] (133.3 mg, 0.26 mmol) was added and the solution was maintained at -78 °C for 2h. Et$_4$NCl (43.1 mg, 0.26 mmol) was added to the solution and the reaction was brought to room temperature and stirred at room temperature for 3 h. It was then filtered over a Celite pad and dried *in-vacuo*. After trituration three times with Et_2O, the solids were washed with pentane, Et_2O, and then C_6H_6 until the filtrate was colorless. The product was extracted into a minimum of THF and crystallization was set up with vapor diffusion of 2x volume of Et_2O to yield dark block like crystals. The crystals were re-dissolved in a minimum of MeCN, filtered over a Celite pad, and crystallization was set up with vapor diffusion of 2x volume of Et_2O to yield dark block like crystals. Finally, the crystals were dried under vacuum to yield 72.3 mg of the final product (77% yield). ^{1}H NMR silent except for solvent peaks. Anal. calcd. (%) for C27H52BCl3Fe3N7S3SiMo: C, 33.10; H, 5.35; N, 10.

^{1}H-NMR Experiments

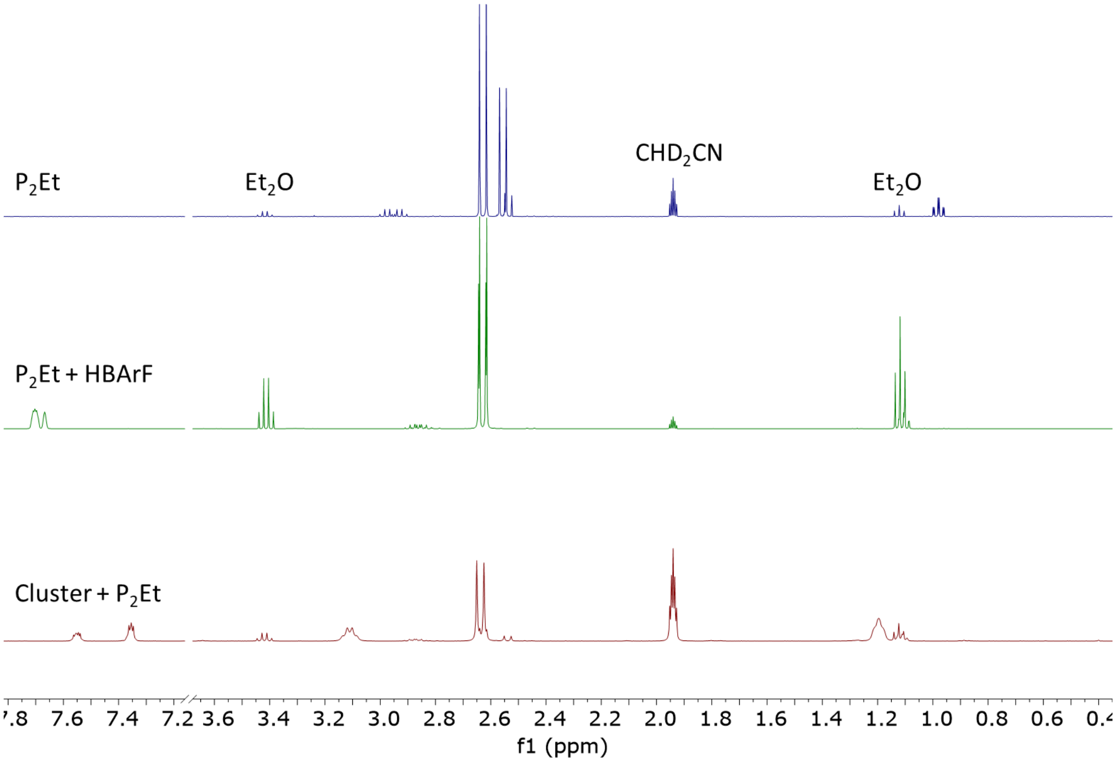

Figure S3: ^{1}H-NMR spectrum (CD_3CN) spectra of P_2Et, P_2Et plus acid, and P_2Et plus cluster **4**.

Electrochemistry Data

General

Cyclic voltammetry experiments were performed with a Pine Instrument Company AFCBP1 biopotentiostat with the AfterMathsoftware package. All measurements were performed in a three-electrode cell, which consisted of glassy carbon (working; ⌀= 3.0 mm), Ag wire (reference), and bare Pt wire (counter), in a N_2-filled MBraun glovebox at room temperature. Dry CH_3CN or DMF that contained ~0.2 M $[Bu_4N][PF_6]$ was used as the electrolyte solution. Redox potentials are reported relative to the ferrocene/ferrocenium redox wave (Fc/Fc^+;ferrocene added as an internal standard).The open circuit potential was measured prior to each voltammogram being collected. Voltammograms were scanned reductively in order to minimize the oxidative damage that was frequently observed on scanning more oxidatively.

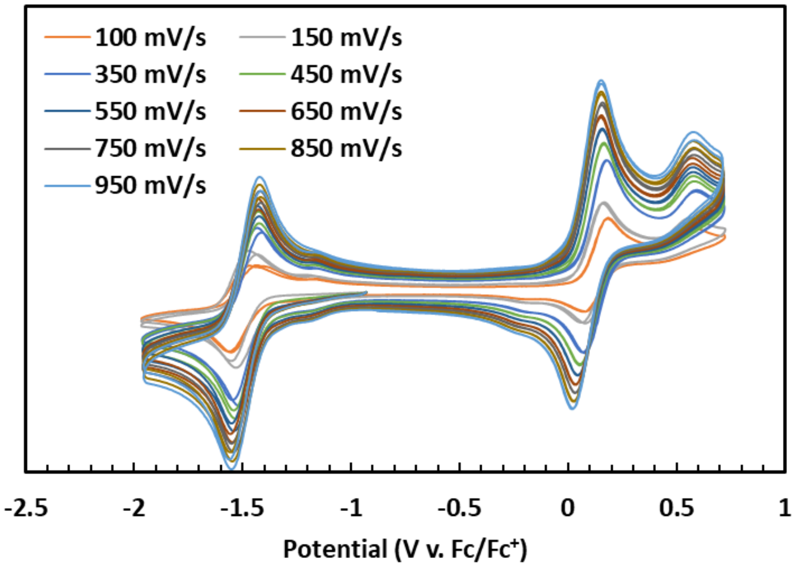

Figure S4: Cyclic voltammetry of $[Et_4N][Tp^*WFe_3S_3(\mu_3\text{-}CSiMe_3)HCl_3]$ **(4)** at different scan rates.

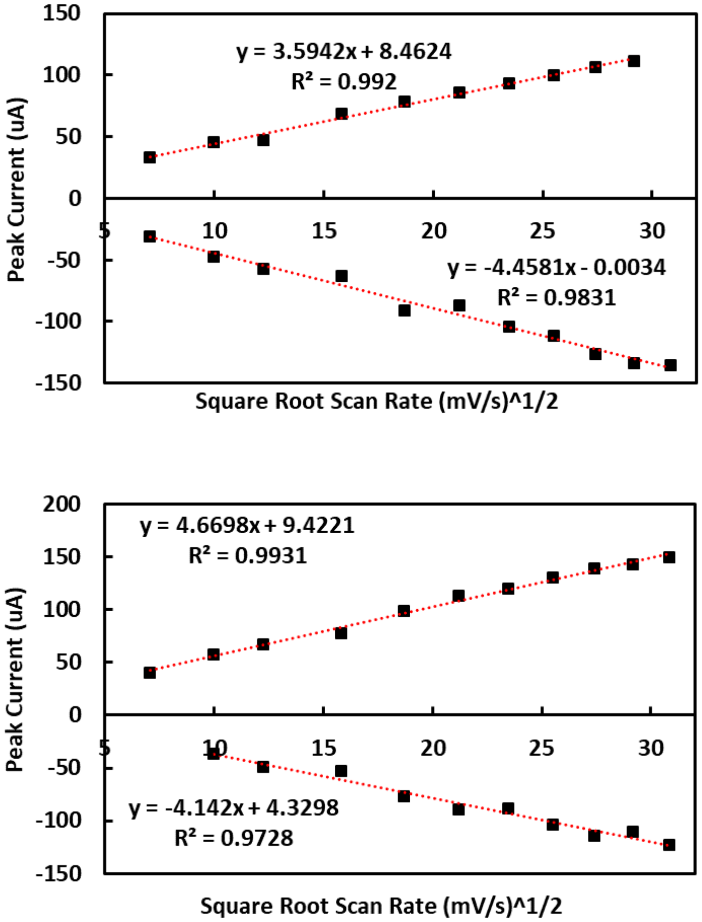

Figure S5: Peak current vs. square root of scan rate for the -1.46 V (top) and 0.15 V (bottom) redox features of [Et$_4$N][Tp*WFe$_3$S$_3$(μ_3-CSiMe$_3$)HCl$_3$] **(4)**.

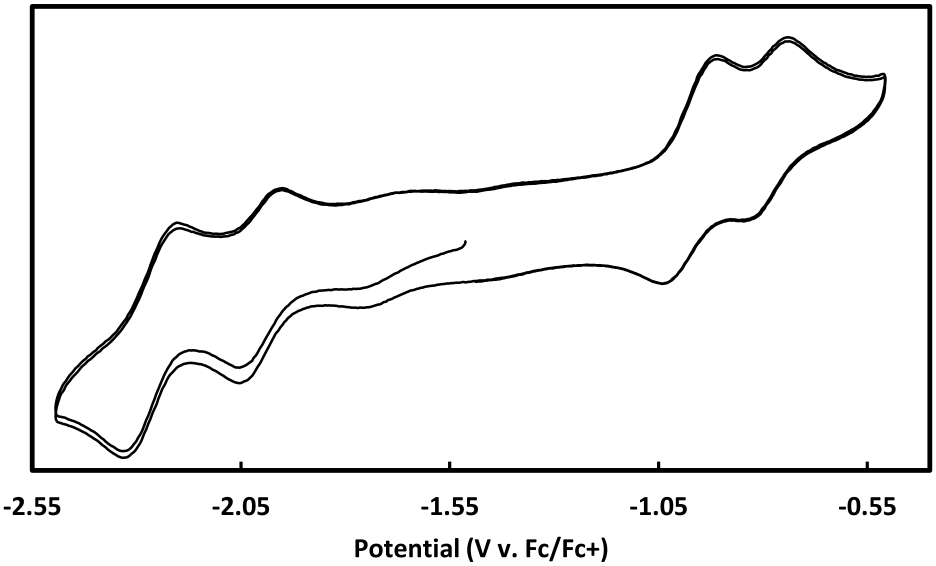

Figure S8: Cyclic voltammetry of [Et_4N][Tp*$MoFe_3S_3(CH_2SiMe_3)_3$] **(2-Mo)** at different scan rates.

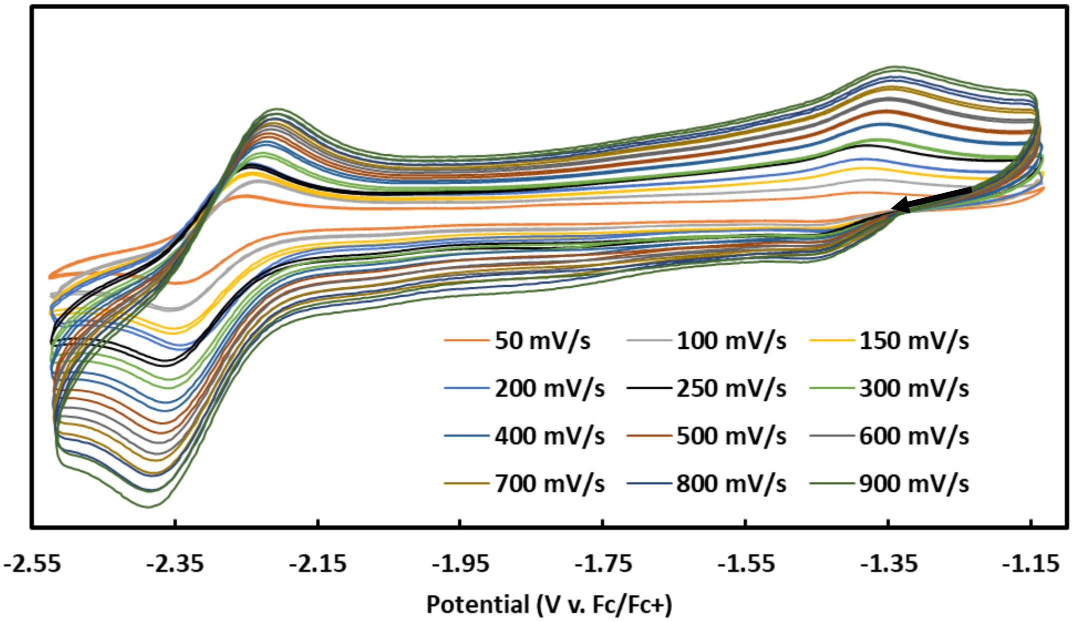

Figure S9: Cyclic voltammetry of [Et_4N][Tp*$MoFe_3S_3(\mu_3\text{-}CSiMe_3)HCl_3$] **(4-Mo)** at different scan rates.

Electron Paramagnetic Resonance (EPR) Data

General

Samples were prepared as solutions (c.a. 1 mM) and rapidly cooled in liquid nitrogen to form a frozen glass. All X-band CW-EPR experiments presented in this study were acquired at the Caltech EPR facility. X-band CW EPR spectra were acquired on a Bruker (Billerica, MA) EMX spectrometer using Bruker Win-EPR software (ver.3.0). Temperature control was achieved using liquid helium and an Oxford Instruments (Oxford, UK) ESR-900 cryogen flow cryostat and an ITC-503 temperature controller. Data were collected at T = 5 K. Spectra were simulated using EasySpin8(release 5.2.33) with Matlab R2020b.

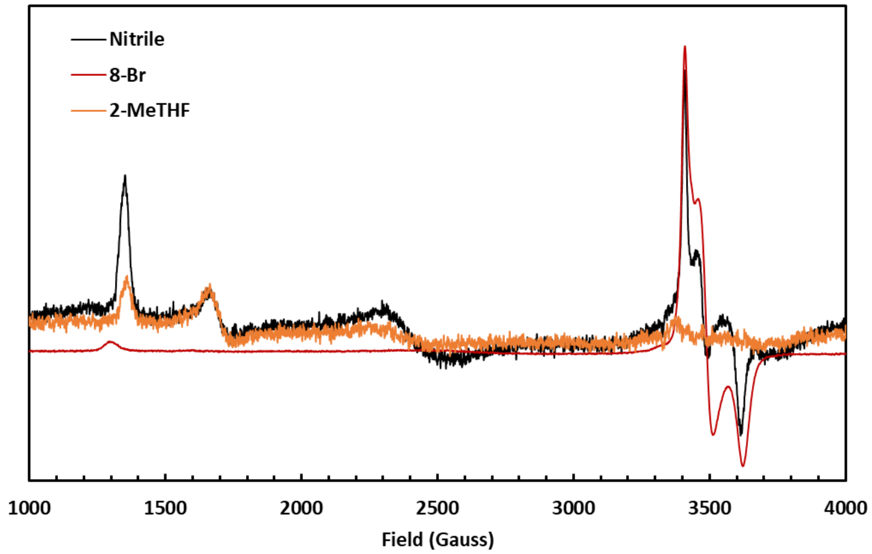

Figure S10: EPR spectrum of [Et_4N][$Tp^*WFe_3S_3(\mu_3\text{-}CSiMe_3)HCl_3$] **(7)** in 2-MeTHF and a 3:1 mixture of butyrlnitrile:propionitrile and [Et_4N][$Tp^*WFe_3S_3(\mu_3\text{-}CSiMe_3)HBr_3$] **(7-Br)** in a 3:1 mixture of butyrlnitrile:propionitrile.

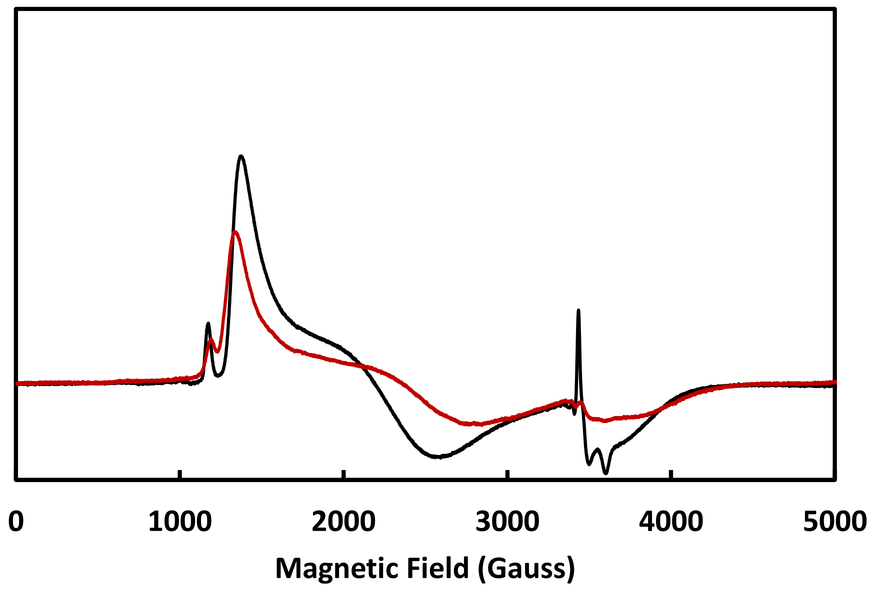

Figure S11: EPR spectra of $[Et_4N]_2[Tp^*MoFe_3S_3(\mu_3\text{-}CSiMe_3)Cl_3]$ **(3-Mo)** in DMF (black) and $[Et_4N][Tp^*MoFe_3S_3(\mu_3\text{-}CSiMe_3)HCl_3]$ **(4-Mo)** in a 3:1 mixture of butyrlnitrile:propionitrile (blue). Data acquisition parameters, respectively: frequency = 9.6375 MHz, 9.6385 MHz, and 9.6370 MHz; power = 2 mW, conversion time = 10.12 ms, and modulation amplitude = 8 G.

Mössbauer Measurements

General

Zero applied field ^{57}Fe Mossbauer spectra were recorded at 80 K in constant acceleration mode on a spectrometer from See Co (Edina, MN) equipped with an SVT- S6 400 cryostat (Janis, Wilmington, WA). The isomer shifts are relative to the centroid of an α-Fe foil signal at room temperature. Samples were prepared by mixing polycrystalline material (20 mg) with boron nitride in a cup fitted with a screw cap. The data were fit to Lorentzian lineshapes using WMOSS (www.wmoss.org).

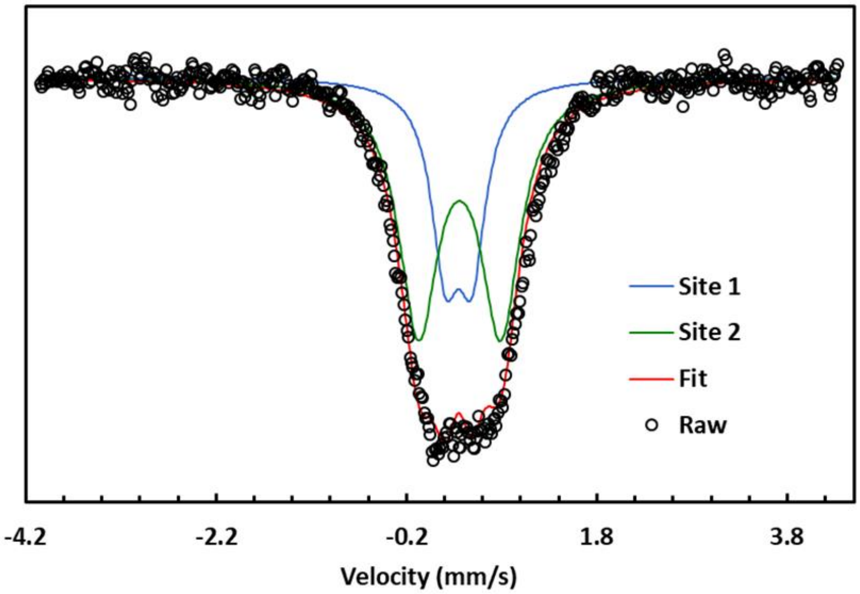

	δ (mm/s)	**ΔE_q (mm/s)**	**χ^2**	**Relative Fraction**
Site 1	0.36	1.00	0.63	2/3
Site 2	0.36	0.40		1/3
Average, 2 Site Fit	0.36	0.80		

Figure S15: Mössbauer spectrum of [Et_4N][Tp*W**H**Fe_3S_3(μ_3-$CSiMe_3$)Cl_3] (**4**) showing fit. Parameters are shown in table. Black circles are raw data.

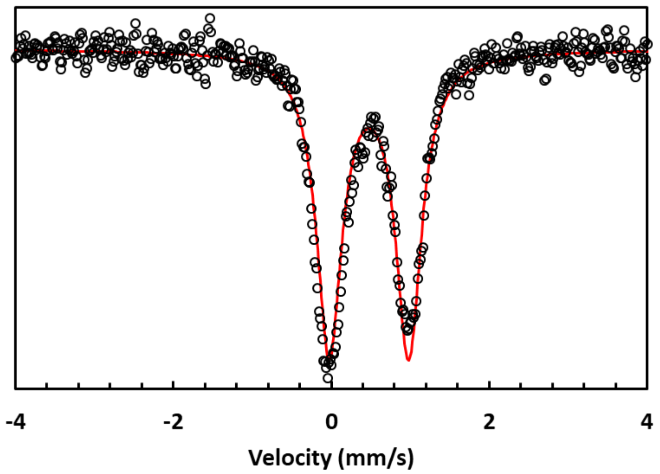

	δ (mm/s)	ΔE_q (mm/s)	χ^2	Relative Fraction
Fit	0.48	1.00	0.20	1

Figure S18: Mössbauer spectrum of [Et_4N][Tp*MoHFe$_3$S$_3$(μ_3-CSiMe$_3$) Cl$_3$] (**4-Mo**) showing fit. Parameters are shown in table. Black circles are raw data.

Single Crystal X-ray Diffraction Data

General

XRD data were collected at 100 K on a Bruker AXS D8 KAPPA or Bruker AXS D8 VENTURE diffractometer [microfocus sealed X-ray tube, λ(Mo Kα) = 0.71073 Å or λ(Cu Kα) = 1.54178 Å]. All manipulations, including data collection, integration, and scaling, were carried out using the Bruker APEX3 software.[35] Absorption corrections were applied using SADABS.[36] Structures were solved by direct methods using XS(incorporated into SHELXTL),[37] Sir92[38] or SUPERFLIP[39] and refined using full-matrix least-squares on Olex2[40] to convergence. All non-H atoms were refined using anisotropic displacement parameters. H atoms were placed in idealized positions and refined using a riding model.

Crystal Structures of Mo analogues

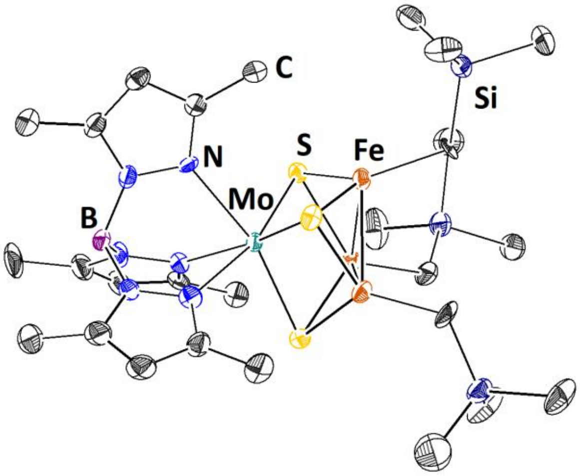

Figure S27: Crystal structure of **2-Mo**. Ellipsoids plotted at the 50% probability level. Hydrogen, solvent, and counterion atoms not shown for clarity.

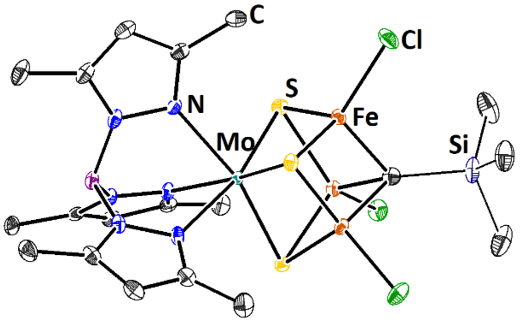

Figure S28: Crystal structure of **4-Mo**. Ellipsoids plotted at the 50% probability level. Hydrogen, solvent, and counterion atoms not shown for clarity.

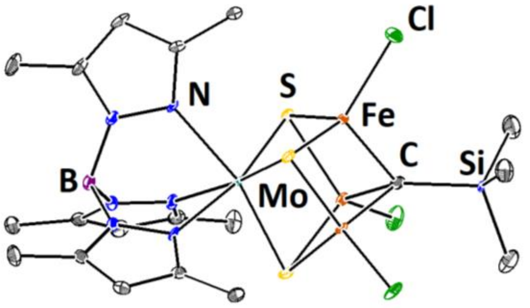

Figure S29: Crystal structure of **5-Mo**. Ellipsoids plotted at the 50% probability level. Hydrogen, solvent, and counterion atoms not shown for clarity.

Special Refinement Details

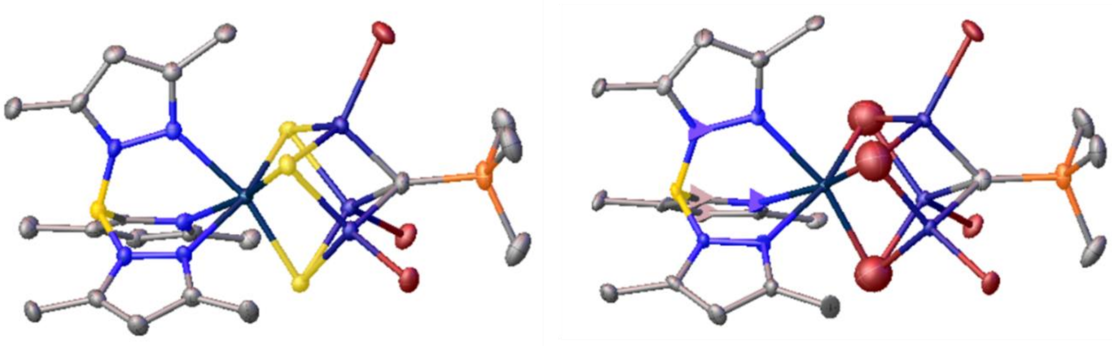

Figure S30: Refinement of **4-Br** showing ellipsoids when the bridging atoms are refined as sulfides (left) versus bromides (right). Ellipsoids are plotted at the 50% probability level.

Cluster	2	3	4
CCDC	2170937		
Empirical formula	$C_{35}H_{75}BFe_3N_7S_3WSi_3$	$C_{40}H_{82}BCl_3O_2Fe_3N_{10}S_3WSi$	$C_{44}H_{66}BCl_3Fe_3N_9S_3WSi$
Formula weight	1136.68	1316.68	1313.88
Temperature/K	100	100	100
Crystal system	Orthorhombic	Triclinic	Monoclinic
Space group	$P2_12_12_1$	P-1	$P2_1/c$
a/Å	10.5856(15)	10.7345(6)	10.7565(5)
b/Å	18.200(2)	15.6406(9)	19.0986(9)
c/Å	26.002(4)	17.7292(10)	19.3433(9)
α/°	90	84.975(3)	90
β/°	90	80.136(3)	90.878(2)
γ/°	90	80.913(3)	90
Volume/Å^3	5009.5(12)	2890.2(3)	3973.3(2)
Z	4	2	4
ρ_{calc}/g cm^{-3}	1.507	1.513	2.196
μ/mm^{-1}	3.369	12.300	17.869
F(000)	2324	1345	2652
Crystal size/mm^3	0.10 × 0.25 × 0.35	0.03 × 0.08 × 0.14	0.05 × 0.05 × 0.37
Radiation	Mo Kα	Cu Kα	Cu Kα
θ_{max}/°	38.238	72.72	72.40
Index ranges	$-17 \leq h \leq 18$ $-24 \leq k \leq 31$ $-38 \leq l \leq 44$	$-13 \leq h \leq 13$ $-19 \leq k \leq 19$ $-21 \leq l \leq 21$	$-13 \leq h \leq 13$ $-23 \leq k \leq 23$ $-23 \leq l \leq 23$
Reflections measured	26456	59466	41043
Independent reflections	9865	9901	9943
Restraints/Parameters	0/498	145/761	0/428
GOF on F^2	0.893	1.077	1.139
R-factor	0.0642	0.0355	0.0305
Weighted R-factor	0.0611	0.0880	0.0764
Largest diff. peak/hole/e Å^{-3}	2.144/-1.359	2.008/-1.377	1.159/-1.154

Cluster	**5**	**4-Br**	**2-Mo**
CCDC	2170935		2170936
Empirical formula	$C_{28}H_{51}BCl_3Fe_3N_6S_3WSi$	$C_{27}H_{51}BBr_3Fe_3N_7S_3SiW$	$C_{35}\ H_{75}\ B\ Fe_3\ Mo\ N_7\ S_3\ Si_3$
Formula weight	1064.57	1199.95	1048.77
Temperature/K	100	100	100
Crystal system	Monoclinic	Monoclinic	Orthorhombic
Space group	$P2_1/c$	$P2_1/c$	$P2_12_12_1$
a/Å	10.7471(6)	10.6656(5)	10.608(2)
b/Å	19.1398(10)	20.1629(9)	18.143(4)
c/Å	19.2949(10)	19.0066(8)	26.105(5)
α/°	90	90	90
β/°	90.712(2)	90.587(2)	90
γ/°	90	92.587(2)	90
Volume/Å^3	3968.6(4)	90	5023.9(17)
Z	4	4	4
ρ_{calc}/g cm^{-3}	1.782	1.952	1.387
μ/mm^{-1}	17.692	18.838	10.897
F(000)	21264	2344	2196
Crystal size/mm^3	0.05 × 0.10 × 0.30	0.04 x 0.07 x 0.15	0.03 × 0.13 × 0.17
Radiation	Cu Kα	Cu Kα	Cu Kα
θ_{max}/°	72.37	72.37	72.287
Index ranges	$-13 \leq h \leq 12$ $-23 \leq k \leq 23$ $-23 \leq l \leq 22$	$-11 \leq h \leq 12$ $-24 \leq k \leq 24$ $-23 \leq l \leq 23$	$-13 \leq h \leq 13$ $-22 \leq k \leq 22$ $-32 \leq l \leq 32$
Reflections measured	49643	45161	75346
Independent reflections	9816	9053	9459
Restraints/Parameters	0/428	0/428	0/498
GOF on F^2	1.070	1.044	1.074
R-factor	0.0342	0.0356	0.0528
Weighted R-factor	0.0932	0.0821	0.1222
Largest diff. peak/hole/e Å^{-3}	1.993/-1.199	2.512/-0.948	2.989/-1.422

Cluster	**3-Mo**	**4-Mo**	**5-Mo**

CCDC	2170937		
Empirical formula	$C_{35}H_{75}BFe_3N_7S_3WSi3$	C27 H51 B Cl3 Fe3 Mo N7 S3 Si	$C_{44}H_{66}BCl_3Fe_3N_9S_3WSi_3$
Formula weight	1136.68	978.66	1313.88
Temperature/K	100	100	100
Crystal system	Orthorhombic	Monoclinic	Monoclinic
Space group	$P2_12_12_1$	$P2_1/c$	$P2_1/c$
a/Å	10.5856(15)	10.7686(5)	10.7565(5)
b/Å	18.200(2)	19.1042(8)	19.0986(9)
c/Å	26.002(4)	19.3386(9)	19.3433(9)
α/°	90	90	90
β/°	90	90.852(2)	90.878(2)
γ/°	90	90	90
Volume/Å^3	5009.5(12)	3978.0(3)	3973.3(2)
Z	4	4	4
ρ_{calc}/g cm^{-3}	1.507	1.634	2.196
μ/mm^{-1}	3.369	14.974	17.869
F(000)	2324	2000	2652
Crystal size/mm^3	0.10 × 0.25 × 0.35	0.02 × 0.14 × 0.3	0.05 × 0.05 × 0.37
Radiation	Mo Kα	Cu Kα	Cu Kα
θ_{max}/°	38.238	72.441	72.40
Index ranges	$-17 \leq h \leq 18$ $-24 \leq k \leq 31$ $-38 \leq l \leq 44$	$-13 \leq h \leq 13$ $-23 \leq k \leq 23$ $-22 \leq l \leq 23$	$-13 \leq h \leq 13$ $-23 \leq k \leq 23$ $-23 \leq l \leq 23$
Reflections measured	26456	48732	48732
Independent reflections	9865	9239	9239
Restraints/Parameters	0/498	0/428	0/428
GOF on F^2	0.893	1.122	1.139
R-factor	0.0642	0.0326.	0.0305
Weighted R-factor	0.0611	0.0794	0.0764
Largest diff. peak/hole/e Å^{-3}	2.144/-1.359	1.093/-0.891	1.159/-1.154

References:

(1) Spatzal, T.; Aksoyoglu, M.; Zhang, L.; Andrade, S. L. A.; Schleicher, E.; Weber, S.; Rees, D. C.; Einsle, O. Evidence for Interstitial Carbon in Nitrogenase FeMo Cofactor. *Science* **2011**, *334* (6058), 940–940. https://doi.org/10.1126/science.1214025.

(2) Lancaster, K. M.; Roemelt, M.; Ettenhuber, P.; Hu, Y.; Ribbe, M. W.; Neese, F.; Bergmann, U.; DeBeer, S. X-Ray Emission Spectroscopy Evidences a Central Carbon in the Nitrogenase Iron-Molybdenum Cofactor. *Science* **2011**, *334* (6058), 974–977. https://doi.org/10.1126/science.1206445.

(3) Jasniewski, A. J.; Lee, C. C.; Ribbe, M. W.; Hu, Y. Reactivity, Mechanism, and Assembly of the Alternative Nitrogenases. *Chem. Rev.* **2020**. https://doi.org/10.1021/acs.chemrev.9b00704.

(4) Hoffman, B. M.; Lukoyanov, D.; Yang, Z.-Y.; Dean, D. R.; Seefeldt, L. C. Mechanism of Nitrogen Fixation by Nitrogenase: The next Stage. *Chemical reviews* **2014**, *114* (8), 4041–4062.

(5) Seefeldt, L. C.; Yang, Z.-Y.; Lukoyanov, D. A.; Harris, D. F.; Dean, D. R.; Raugei, S.; Hoffman, B. M. Reduction of Substrates by Nitrogenases. *Chem. Rev.* **2020**, *120* (12), 5082–5106. https://doi.org/10.1021/acs.chemrev.9b00556.

(6) Burgess, B. K.; Lowe, D. J. Mechanism of Molybdenum Nitrogenase. *Chem. Rev.* **1996**, *96* (7), 2983–3012. https://doi.org/10.1021/cr950055x.

(7) Lowe, D. J.; Thorneley, R. N. The Mechanism of Klebsiella Pneumoniae Nitrogenase Action. Pre-Steady-State Kinetics of H2 Formation. *Biochemical Journal* **1984**, *224* (3), 877–886. https://doi.org/10.1042/bj2240877.

(8) Thorneley, R. N. F.; Lowe, D. J. The Mechanism of Klebsiella Pneumoniae Nitrogenase Action. Simulation of the Dependences of H2-Evolution Rate on Component-Protein Concentration and Ratio and Sodium Dithionite Concentration. *Biochemical Journal* **1984**, *224* (3), 903–909. https://doi.org/10.1042/bj2240903.

(9) Thorneley, R. N. F.; Lowe, D. J. The Mechanism of Klebsiella Pneumoniae Nitrogenase Action. Pre-Steady-State Kinetics of an Enzyme-Bound Intermediate in N2 Reduction and of NH3 Formation. *Biochemical Journal* **1984**, *224* (3), 887–894. https://doi.org/10.1042/bj2240887.

(10) Hoffman, B. M.; Lukoyanov, D.; Dean, D. R.; Seefeldt, L. C. Nitrogenase: A Draft Mechanism. *Acc. Chem. Res.* **2013**, *46* (2), 587–595. https://doi.org/10.1021/ar300267m.

(11) Dos Santos, P. C.; Igarashi, R. Y.; Lee, H.-I.; Hoffman, B. M.; Seefeldt, L. C.; Dean, D. R. Substrate Interactions with the Nitrogenase Active Site. *Acc. Chem. Res.* **2005**, *38* (3), 208–214. https://doi.org/10.1021/ar040050z.

(12) Christiansen, J.; Dean, D. R.; Seefeldt, L. C. Mechanistic Features of the Mo-Containing Nitrogenase. *Annual Review of Plant Physiology and Plant Molecular Biology* **2001**, *52* (1), 269–295. https://doi.org/10.1146/annurev.arplant.52.1.269.

(13) Čorić, I.; Holland, P. L. Insight into the Iron–Molybdenum Cofactor of Nitrogenase from Synthetic Iron Complexes with Sulfur, Carbon, and Hydride Ligands. *Journal of the American Chemical Society* **2016**, *138* (23), 7200–7211.

(14) Igarashi, R. Y.; Laryukhin, M.; Dos Santos, P. C.; Lee, H.-I.; Dean, D. R.; Seefeldt, L. C.; Hoffman, B. M. Trapping H- Bound to the Nitrogenase FeMo-Cofactor Active Site during H2 Evolution: Characterization by ENDOR Spectroscopy. *J. Am. Chem. Soc.* **2005**, *127* (17), 6231–6241. https://doi.org/10.1021/ja043596p.

(15) Hoeke, V.; Tociu, L.; Case, D. A.; Seefeldt, L. C.; Raugei, S.; Hoffman, B. M. High-Resolution ENDOR Spectroscopy Combined with Quantum Chemical Calculations Reveals the Structure of Nitrogenase Janus Intermediate E4(4H). *J. Am. Chem. Soc.* **2019**, *141* (30), 11984–11996. https://doi.org/10.1021/jacs.9b04474.

(16) Lukoyanov, D.; Yang, Z.-Y.; Duval, S.; Danyal, K.; Dean, D. R.; Seefeldt, L. C.; Hoffman, B. M. A Confirmation of the Quench-Cryoannealing Relaxation Protocol for Identifying Reduction States of Freeze-Trapped Nitrogenase Intermediates. *Inorg. Chem.* **2014**, *53* (7), 3688–3693. https://doi.org/10.1021/ic500013c.

(17) Lukoyanov, D.; Barney, B. M.; Dean, D. R.; Seefeldt, L. C.; Hoffman, B. M. Connecting Nitrogenase Intermediates with the Kinetic Scheme for N2 Reduction by a Relaxation Protocol and Identification of the N2 Binding State. *Proceedings of the National Academy of Sciences* **2007**, *104* (5), 1451–1455. https://doi.org/10.1073/pnas.0610975104.

(18) Lukoyanov, D.; Khadka, N.; Yang, Z.-Y.; Dean, D. R.; Seefeldt, L. C.; Hoffman, B. M. Reductive Elimination of H2 Activates Nitrogenase to Reduce the N≡N Triple Bond: Characterization of the E4(4H) Janus Intermediate in Wild-Type Enzyme. *J. Am. Chem. Soc.* **2016**, *138* (33), 10674–10683. https://doi.org/10.1021/jacs.6b06362.

(19) Dugan, T. R.; Bill, E.; MacLeod, K. C.; Brennessel, W. W.; Holland, P. L. Synthesis, Spectroscopy, and Hydrogen/Deuterium Exchange in High-Spin Iron(II) Hydride Complexes. *Inorg. Chem.* **2014**, *53* (5), 2370–2380. https://doi.org/10.1021/ic4013137.

(20) Arnet, N. A.; Dugan, T. R.; Menges, F. S.; Mercado, B. Q.; Brennessel, W. W.; Bill, E.; Johnson, M. A.; Holland, P. L. Synthesis, Characterization, and Nitrogenase-Relevant Reactions of an Iron Sulfide Complex with a Bridging Hydride. *J. Am. Chem. Soc.* **2015**, *137* (41), 13220–13223. https://doi.org/10.1021/jacs.5b06841.

(21) Wang, C.-H.; DeBeer, S. Structure, Reactivity, and Spectroscopy of Nitrogenase-Related Synthetic and Biological Clusters. *Chemical Society Reviews* **2021**, *50* (15), 8743–8761. https://doi.org/10.1039/D1CS00381J.

(22) Yang, D.; Xu, S.; Zhang, Y.; Li, Y.; Li, Y.; Wang, B.; Qu, J. Reactivity toward Unsaturated Small Molecules of Thiolate-Bridged Diiron Hydride Complexes. *Inorg. Chem.* **2018**, *57* (24), 15198–15204. https://doi.org/10.1021/acs.inorgchem.8b02459.

(23) Speelman, A. L.; Holland, P. L. Sulfur-Supported Iron Complexes for Understanding N2 Reduction. In *Nitrogen Fixation*; Nishibayashi, Y., Ed.; Topics in Organometallic Chemistry; Springer International Publishing: Cham, 2017; pp 197–213. https://doi.org/10.1007/3418_2016_4.

(24) Arnet, N. A.; McWilliams, S. F.; DeRosha, D. E.; Mercado, B. Q.; Holland, P. L. Synthesis and Mechanism of Formation of Hydride–Sulfide Complexes of Iron.

Inorg. Chem. **2017**, *56* (15), 9185–9193. https://doi.org/10.1021/acs.inorgchem.7b01230.

(25) Bai, X.; Mei, T.; Yang, D.; Su, L.; Wang, B.; Qu, J. Synthesis, Characterization and Reactivity toward Small Molecules of a Diiron Tetrahydrido Bridged Complex. *Inorganic Chemistry Communications* **2020**, *122*, 108286. https://doi.org/10.1016/j.inoche.2020.108286.

(26) Creutz, S. E.; Peters, J. C. Diiron Bridged-Thiolate Complexes That Bind N2 at the FeIIFeII, FeIIFeI, and FeIFeI Redox States. *J. Am. Chem. Soc.* **2015**, *137* (23), 7310–7313. https://doi.org/10.1021/jacs.5b04738.

(27) Rittle, J.; McCrory, C. C. L.; Peters, J. C. A 106-Fold Enhancement in N2-Binding Affinity of an Fe2(μ-H)2 Core upon Reduction to a Mixed-Valence FeIIFeI State. *J. Am. Chem. Soc.* **2014**, *136* (39), 13853–13862. https://doi.org/10.1021/ja507217v.

(28) Arnett, C. H.; Bogacz, I.; Chatterjee, R.; Yano, J.; Oyala, P. H.; Agapie, T. Mixed-Valent Diiron μ-Carbyne, μ-Hydride Complexes: Implications for Nitrogenase. *J. Am. Chem. Soc.* **2020**, *142* (44), 18795–18813. https://doi.org/10.1021/jacs.0c05920.

(29) Yang, D.; Li, Y.; Wang, B.; Zhao, X.; Su, L.; Chen, S.; Tong, P.; Luo, Y.; Qu, J. Synthesis and Electrocatalytic Property of Diiron Hydride Complexes Derived from a Thiolate-Bridged Diiron Complex. *Inorg. Chem.* **2015**, *54* (21), 10243–10249. https://doi.org/10.1021/acs.inorgchem.5b01508.

(30) Saouma, C. T.; Morris, W. D.; Darcy, J. W.; Mayer, J. M. Protonation and Proton-Coupled Electron Transfer at S-Ligated [4Fe-4S] Clusters. *Chemistry – A European Journal* **2015**, *21* (25), 9256–9260. https://doi.org/10.1002/chem.201500152.

(31) Scott, A. G.; Agapie, T. Synthesis of a Fe3–Carbyne Motif by Oxidation of an Alkyl Ligated Iron–Sulfur (WFe3S3) Cluster. *J. Am. Chem. Soc.* **2023**, *145* (1), 2–6. https://doi.org/10.1021/jacs.2c04826.

(32) Xu, G.; Wang, Z.; Ling, R.; Zhou, J.; Chen, X.-D.; Holm, R. H. Ligand Metathesis as Rational Strategy for the Synthesis of Cubane-Type Heteroleptic Iron–Sulfur Clusters Relevant to the FeMo Cofactor. *Proceedings of the National Academy of Sciences* **2018**, *115* (20), 5089–5092.

(33) Le, L.; Bailey, G.; Scott, A.; Agapie, T. Cluster Models of FeMoco with Sulfide and Carbyne Ligands: Effect of Interstitial Atom in Nitrogenase Active Site. **2021**. https://doi.org/10.26434/chemrxiv.14614152.v1.

(34) Pangborn, A. B.; Giardello, M. A.; Grubbs, R. H.; Rosen, R. K.; Timmers, F. J. Safe and Convenient Procedure for Solvent Purification. *Organometallics* **1996**, *15* (5), 1518–1520. https://doi.org/10.1021/om9503712.

(35) Bruker, APEX3(Bruker AXS Inc., 2012).

(36) Bruker, SADABS(Bruker AXS Inc., 2001).

(37) Sheldrick, G. M. SHELXT – Integrated Space-Group and Crystal-Structure Determination. *Acta Cryst A* **2015**, *71* (1), 3–8. https://doi.org/10.1107/S2053273314026370.

(38) Altomare, A.; Cascarano, G.; Giacovazzo, C.; Guagliardi, A.; Burla, M. C.; Polidori, G.; Camalli, M. SIRPOW.92 – a Program for Automatic Solution of Crystal Structures by Direct Methods Optimized for Powder Data. *J Appl Cryst* **1994**, *27* (3), 435–436. https://doi.org/10.1107/S0021889894000221.

(39) Palatinus, L.; Chapuis, G. SUPERFLIP – a Computer Program for the Solution of Crystal Structures by Charge Flipping in Arbitrary Dimensions. *J Appl Cryst* **2007**, *40* (4), 786–790. https://doi.org/10.1107/S0021889807029238.

(40) Dolomanov, O. V.; Bourhis, L. J.; Gildea, R. J.; Howard, J. a. K.; Puschmann, H. OLEX2: A Complete Structure Solution, Refinement and Analysis Program. *J Appl Cryst* **2009**, *42* (2), 339–341. https://doi.org/10.1107/S0021889808042726.

Appendix B

SYNTHETIC PROTOCOLS FOR MISCELLANEOUS COMPOUNDS

Experimental

General Considerations: All synthetic procedures were carried out in a MBraun glovebox filled with purified nitrogen or using standard Schlenk techniques with nitrogen unless stated otherwise. All solvents were bought in their anhydrous form and passed over a column of activated A2 alumina under nitrogen for further drying. Solvents were then bump degassed on the Schlenk line. Solvents in the glovebox were stored over 3 Å molecular sieves. THF was dried further by storing over 3 Å molecular sieves for at least 48 hours before use. DMF was bought in its anhydrous form and stored over 3 Å molecular sieves for at least 48 hours before use. The NMR solvent CD_3CN was dried over calcium hydride and C_6D_6 was dried over Na/benzophenone and then vacuum transferred and degassed for use in the glovebox. All other NMR solvents were used as received outside of the glovebox. NMR spectra were recorded on either a Varian 300 MHz instrument or a Varian 400 MHz instrument. 31P NMR were referenced with a H_3PO_4 standard. All commercially available materials were used as received. $Cl_3PNSiMe_3$,[1] **Py_3TREN**,[2] compounds $HOPhP^iPr_2$ (**1**),[3] $HSPhP^iPr_2$ (**2**),[4] and $H_3CPhP^iPr_2$ (**3**)[5] were synthesized based on literature procedures.

Synthesis of Sodium (2-(diisopropylphosphaneyl)phenyl)oxide (4a) and Potassium (2-(diisopropylphosphaneyl)phenyl)oxide (4b)

4a and **4b** were synthesized analogously to **1**. 2-(diisopropylphosphaneyl)phenol (200 mg, 0.95 mmol) was reacted with either NaH (231 mg, 0.96 mmol) or KH (38.9 mg, 0.96 mmol) yielding

2a (0.2056 g, 93% yield) and **2b (**0.2104 g, 89% yield**)** as white powders. ^{1}H NMR (400 MHz, C_6D_6, 25 °C): δ (ppm) (**2a**) 1.03 (m, 7.0 Hz, 12H), 1.95 (m, 6.8 Hz, 2H), 6.65-6.74 (m, 2H), 7.21 (bm, 1H), 7.28 (t, 7.3 Hz, 1H) (**2b**) 1.15 (m, 12H), 2.02 (m, 2H), 6.18 (m, 1H), 6.69 (m, 1H), 7.25-7.32 (bm, 2H). ^{31}P NMR (400 MHz, C_6D_6, 25 °C): δ (ppm) (**2a**) -14.8 (s) (**2b)** -13.2 (s).

Synthesis of Sodium (2-(diisopropylphosphaneyl)phenyl)sulfide (5)

2-(diisopropylphosphaneyl)benzenethiol (200 mg, .88 mmol) was dissolved in benzene (4 mL). NaH (21.4 mg, 0.89 mmol) was added in portions and the solution was stirred at room temperature for 1 hour. The reaction solution was then filtered through celite and concentrated to dryness yielding **5** as a light yellow solid (0.2020 g, 92% yield). ^{1}H NMR (400 MHz, THF, 25 °C): δ (ppm) ^{31}P NMR (400 MHz, THF, 25 °C): δ (ppm) 1.03 (m, 12H), 2.09 (bm, 2H), 6.91 (bm, 2H), 7.06 (bm, 2H) .31P NMR (400 MHz, C_6D_6, 25 °C): δ (ppm) -15.4 (s).

Synthesis of (2-(diisopropylphosphaneyl)benzyl)potassium (6)

Diisopropyl(o-tolyl)phosphane (200 mg, 0.96 mmol) was dissolved in hexane (6 mL). nBuLi (0.57 mL, 1.71 M, 0.97 mmol) was added dropwise. K^{t}BuO (111 mg, 0.99 mmol) was then added portionwise. The reaction solution went from clear to a bright orange suspension. The orange solid was collected on a filter frit, washed with hexane, and concentrated to dryness. The bright orange solid **6** (0.2131 g, 90% yield) was stored at -30 °C. ^{1}H NMR (400 MHz, C6D6, 25 °C): δ (ppm) 0.94 (m, 6.9 Hz, 12H), 2.44 (m, 7.3 Hz, 2H), 4.77 (t, 6.6 Hz, 1H), 5.61 (m, 1H), 5.83 (m, 1H), 6.18 (t, 7.3 Hz, 1H), 6.18 (t, 7.3 Hz, 1H). ^{31}P NMR (400 MHz, C6D6, 25 °C): δ (ppm) -0.4 (s).

Synthesis of $[Et_4N][Tp^*{}_2W_2S_6Fe_4(\mu_3\text{-}Cl)_2Cl_2]$ (7)

$[Et_4N][Tp^*WS_3Fe_2(\mu\text{-}Cl)Cl_2]$ (100 mg, 0.10 mmol) and **5** (24.7 mg, 0.10 mmol) were mixed for 12 hours in THF (4 mL). The solution remained dark brown over the course of the reaction. The reaction was then filtered over celite and pumped to dryness. The sticky brown solid was triturated with Et_2O twice, pumping to dryness each time. Diffusion of Et_2O into concentrated benzene solution of **7** at room temperature yielded dark brown diamond X-ray quality crystals. 1H NMR (400 MHz, C_6D_6, 25 °C): δ (ppm) -32.57 (s, 1H), -15.50 (s, 6H), -7.86 (s, 1H), -5.62 (s, 6H), 11.49 (s, 1H).

Synthesis of $[Et_4N]_3[Tp^*{}_2W_2S_6Fe_6(\mu_6\text{-}Cl)(\mu\text{-}Cl)_2Cl_2]$ (8)

$[Et_4N]_2[Tp^*WS_3Fe_3(\mu_3\text{-}Cl)Cl_3]$ (100 mg, 0.08 mmol) and **6** (21.4 mg, 0.08 mmol) were mixed for 12 hours in THF/MeCN (7:3). The solution remained dark brown over the course of the reaction. The reaction was then filtered over celite and pumped to dryness. The black solid was washed with pentane (10 mL) and then extracted into Et_2O (20 mL), filtered over celite, and concentrated to dryness to yield **8** as a black solid (0.0135 g, 15% yield). Diffusion of Et_2O into a concentrated MeCN solution of **8** yielded dark brown diamond X-ray quality crystals. ^1H NMR (400 MHz, C_6D_6, 25 °C): δ (ppm) -7.56 (s), -4.07 (s), -1.06 (s), 0.84 (s), 1.11 (s), 1.23 (s).

Synthesis of $[Et_4N][Tp^*{}_2W_2S_6Fe_4(\mu\text{-}Cl)_2(S_2TerPhenTrans)_2]$ (9)

Di-^{t}Bu-bis-Mesitylterphenyldithiophenol (100 mg, 0.16 mmol) was dissolved in THF (4 mL). KBn (44.6 mg, 0.34 mmol) was dissolved in THF (2 mL) and added dropwise. The solution first turned light yellow and then dark brown. The reaction was allowed to stir for 30 min at room temperature. Reaction solution was added dropwise to THF (2 mL) solution of **$[Et_4N][Tp^*WS_3Fe_2(\mu\text{-}Cl)Cl_2]$** (156 mg, 0.16 mmol) and stirred for 12 hours at room temperature. Reaction was filtered over celite and pumped to dryness. Dark brown solid was washed with pentane (10 mL), extracted into Et_2O, filtered through celite, and concentrated to dryness to yield **9** as a dark brown solid (0.233 g, 20% yield). X-ray quality crystals were grown from concentrated toluene solutions with slow diffusion of Et_2O at room temperature. ^1H NMR (400 MHz, CD_3CN, 25 °C): δ (ppm) -26.88 (s), 39.38 (s), 47.88 (s).

Synthesis of $[Et_4N][Tp^*{}_2W_2S_6Fe_6(\mu_4\text{-}Cl)_2(S_2TerPhenCis)_2]$ (10)

Di-^{t}Bu-bis-Mesitylterphenyldithiophenol (100 mg, 0.16 mmol) was dissolved in THF (4 mL). KBn (44.6 mg, 0.34 mmol) was dissolved in THF (2 mL) and added dropwise. The solution first turned light yellow and then dark brown. The reaction was allowed to stir for 30 min at room temperature. Reaction solution was added dropwise to THF (2 mL) solution of **$[Et_4N]_2[Tp^*WS_3Fe_3(\mu_3\text{-}Cl)Cl_3]$** (178 mg, 0.16 mmol) and stirred for 12 h at room temperature. Reaction was filtered over celite and pumped to dryness. Dark brown solid was washed with pentane (10 mL), extracted into Et_2O, filtered through celite, and concentrated to dryness to yield **10** as a dark brown solid (g, 18% yield). X-ray quality crystals were grown from concentrated toluene solutions with slow diffusion of Et_2O. $_1H$ NMR (400 MHz, CD_3CN, 25 °C): δ (ppm) -17.97 (s), -11.65 (s), -9.88 (s), 15.69 (s), 24.29 (s), 64.61 (bs).

Synthesis of $[Et_4N][Tp^*WS_3Fe_2(\mu\text{-}Cl)(S_2TerPhenCis)]$ (11)

10 (50 mg, mmol) was dissolved in THF (2 mL). **6** () was dissolved in THF (2 mL) and added dropwise. The solution remained dark brown and was stirred for 8 h at room temperature. The reaction was then filtered through celite and concentrated to dryness. The black solid was washed with pentane (10 mL), extracted with Et_2O (20 mL), filtered through celite, and concentrated to dryness to yield **11** as a dark brown solid. X-ray quality crystals were grown from a concentrated Et_2O solution at -30 °C yielding black diamonds. ^1H NMR (400 MHz, CD_3CN, 25 °C): δ (ppm) -7.61 (s), -4.14 (s), -1.05 (s), 41.77 (s).

Synthesis of (Trimethylsilylimino)trispyridylTRENphosphorane (12)

11 (1.00 g) was dissolved in THF (10 mL) and a THF solution (4 mL) of KBn was added dropwise resulting in a brown solution. The solution was cooled to just before freezing and added dropwise to a thawing THF solution (10 mL) of $Cl_3PNSiMe_3$. The solution was stirred at room temperature for 5 h and then concentrated to dryness. The product was extracted in pentane (50 mL), filtered through celite, and concentrated to dryness yielding **12** as a light yellow powder (). ^1H NMR (400 MHz, C_6D_6, 25 °C): δ (ppm) -0.09 (s, 9H), 2.54 (dd, 6.0 Hz, 6H), 3.07 (m, 3H), 5.13 (m, 3H), 6.48 (qd, 3H), 7.12 (qd, 3H), 7.72 (dd, 8.7 Hz, 3H), 8.28 (m, 3H). ^{31}P NMR (400 MHz, C_6D_6, 25 °C): δ (ppm) -13.62 (s).

Synthesis of Imino-trispyridylTRENphosphorane (13)

12 (200 mg) was dissolved in MeOH and stirred at room temperature for 3 h. Solution was concentrated to dryness, re-suspended in benzene (10 mL), filtered over celite, and concentrated to dryness to yield **12** as an off white powder. ^1H NMR (400 MHz, C6D6, 25 °C): δ (ppm) 2.64 (t, 4.88 Hz, 6H), 3.91 (b, 6H), 6.46 (q, 3H), 7.11 (m, 3H), 8.13 (d, 8.13 Hz, 3H), 8.23 (d, 4.48 Hz, 3H). ^{31}P NMR (400 MHz, C6D6, 25 °C): δ (ppm) 24.06 (s).

Synthesis of Potassium Imino-trispyridylTRENphosphorate (14)

13 (200 mg) was dissolved in THF and K^{t}BuO was added portionwise. The reaction was filtered over cealite and concentrated to dryness to yield **14** as a white powder. ^{1}H NMR (400 MHz, C_6D_6, 25 °C): δ (ppm) 2.59 (dd, 14.7 Hz, 3H), 2.74 (td, 11.9 Hz, 3H), 3.10 (m, 3H), 4.80 (qd, 3H), 6.45 (t, 6.0 Hz, 3H), 7.08 (td, 7.6 Hz, 3H), 8.18 (d, 8.5 Hz, 3H), 8.24 (d, 4.2 Hz, 3H). ^{31}P NMR (400 MHz, C_6D_6, 25 °C): δ (ppm) 20.57 (s).

Synthesis of FeX$_3$FeX$_2$-TrispyridylTRENphosphoramine (15a and 15b)

14 (100 mg) was dissolved in THF (4 mL) and FeX$_2$ was added. The solution was allowed to stir for 6 h at room temperature. Reaction was concentrated to dryness and resulting brown powder was washed with benzene (10 mL), extracted in THF (10 mL). X-ray quality crystals were grown by Et$_2$O diffusion into a concentrated THF solution of **15a** and **15b** yielding dark yellow/brown rods. ^{1}H NMR (400 MHz, CD$_3$CN, 25 °C): δ (ppm) **(a)** -2.24 (s), 14.05 (s), 20.93 (s), 32.47 (s), 42.65 (s) **(b)** -9.45 (s), 14.58 (s), 25.54 (s), 35.17 (s), 39.67 (s).

Synthesis of VanadiumtrispyridylTREN (16)

14 (100 mg) was dissolved in THF (4 mL) and a solution of VMes$_3$THF (2 mL THF) was added dropwise. Reaction was stirred for 4 h at room temperature and then filtered through celite. Filtrate was diffused with Et$_2$O at room temperature to give black rhombic crystals that were characterized via X-ray crystallography. Crystals are insoluble in a range of solvents and so NMR characterization was not possible of crystals, but crude NMR of reaction solution is given. ^{1}H NMR (400 MHz, THF, 25 °C): δ (ppm) -25.76 (s), -5.88 (s), 14.00 (s), 41.65 (s), 57.64 (s).

References:

(1) Wang, B.; Rivard, E.; Manners, I. A New High-Yield Synthesis of Cl3P NSiMe3, a Monomeric Precursor for the Controlled Preparation of High Molecular Weight Polyphosphazenes. *Inorganic chemistry* **2002**, *41* (7), 1690–1691.

(2) Hohloch, S.; Pankhurst, J. R.; Jaekel, E. E.; Parker, B. F.; Lussier, D. J.; Garner, M. E.; Booth, C. H.; Love, J. B.; Arnold, J. Benzoquinonoid-Bridged Dinuclear Actinide Complexes. *Dalton Transactions* **2017**, *46* (35), 11615–11625.

(3) Barry, B. M.; Stein, B. W.; Larsen, C. A.; Wirtz, M. N.; Geiger, W. E.; Waterman, R.; Kemp, R. A. Metal Complexes (M = Zn, Sn, and Pb) of 2-Phosphinobenzenethiolates: Insights into Ligand Folding and Hemilability. *Inorganic Chemistry* **2013**, *52* (17), 9875–9884. https://doi.org/10.1021/ic400990n.

(4) Heinicke, J.; Kohler, M.; Peulecke, N.; He, M. Z.; Kindermann, M. K.; Keim, W.; Fink, G. 2-Phosphanylphenolate Nickel Catalysts for the Polymerization of Ethylene. *Chemistry-a European Journal* **2003**, *9* (24), 6093–6107. https://doi.org/10.1002/chem.200304888.

(5) Riihimaki, H.; Suomalainen, P.; Reinius, H. K.; Suutari, J.; Jaaskelainen, S.; Krause, A. O. I.; Pakkanen, T. A.; Pursiainen, J. T. O-Alkyl-Subsfituted Aromatic Phosphanes for Hydroformylation Studies: Synthesis, Spectroscopic Characterization and Ab Initio Investigations. *Journal of Molecular Catalysis a-Chemical* **2003**, *200* (1–2), 69–79. https://doi.org/10.1016/S1381-1169(03)00022-0.

Appendix C

MISCELLANEOUS CRYSTAL STRUCTURES

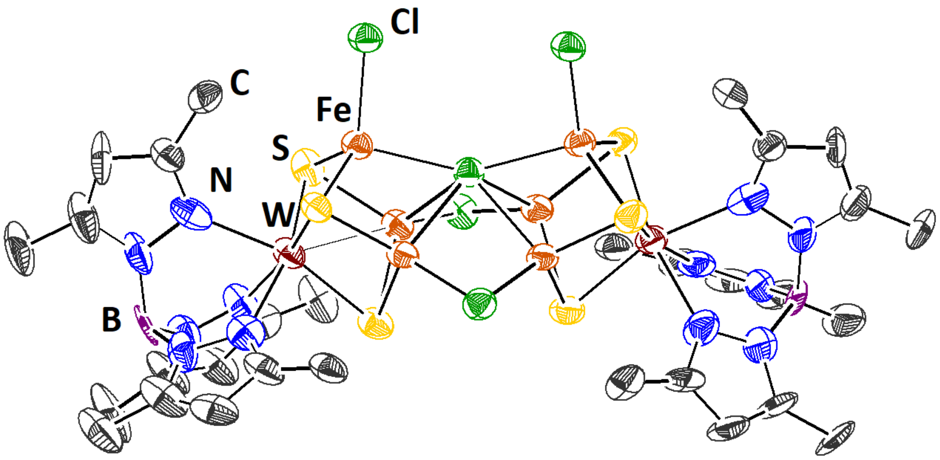

Figure 1: [Et$_4$N][Tp*$_2$W$_2$Fe$_6$S$_6$(μ-Cl)$_2$(u$_6$-Cl)Cl$_2$]

See Appendix B, **8**.

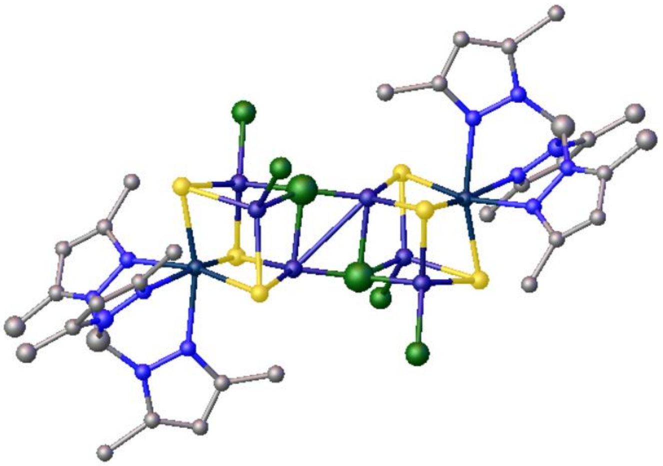

Figure 2: [Et$_4$N][Tp*$_2$W$_2$Fe$_6$S$_6$(μ$_4$-Cl)$_2$Cl$_4$]

See Appendix B, **7**.

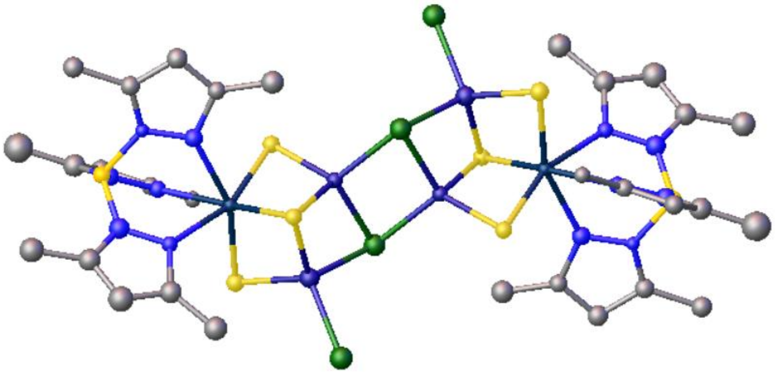

Figure 3: $[Et_4N][Tp^*_2W_2Fe_4S_6Cl_4]$

Crystallized from reaction of $[Et_4N][Tp^*WS_3Fe_2(\mu\text{-}Cl)Cl_2]$ with KC_8.

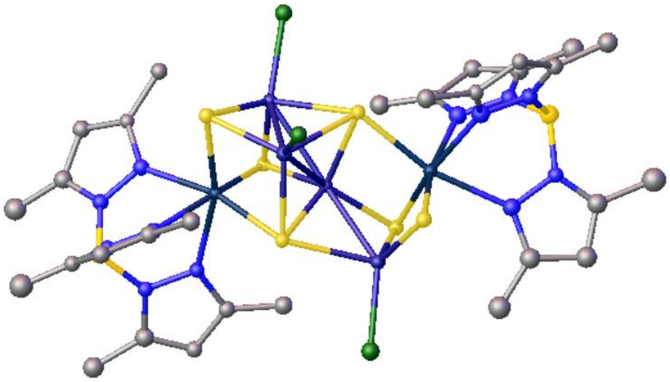

Figure 4: $[Et_4N]_2[Tp^*_2W_2Fe_3S_6Cl_3]$

Crystallized from reaction of $[Et_4N][Tp^*WS_3Fe_2(\mu\text{-}Cl)Cl_2]$ with KC_8.

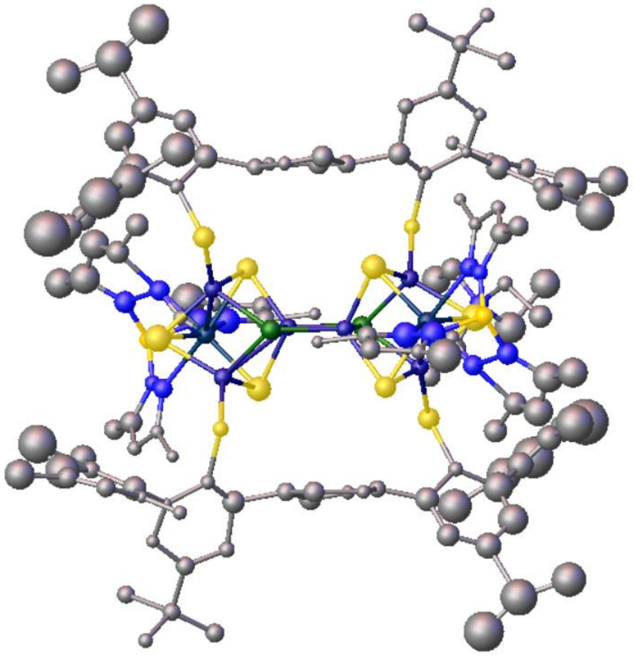

Figure 5: $[Et_4N][Tp^*{}_2W_2Fe_6S_6(\text{syn-dithiolate})_2Cl_2]$

See Appendix B, **10**.

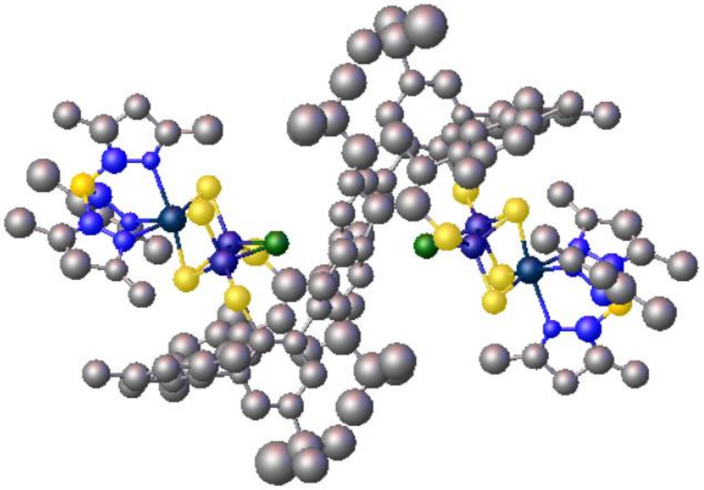

Figure 6: $[Et_4N][Tp^*{}_2W_2Fe_4S_6(\text{anti-dithiolate})_2Cl_2]$

See Appendix B, **9**.

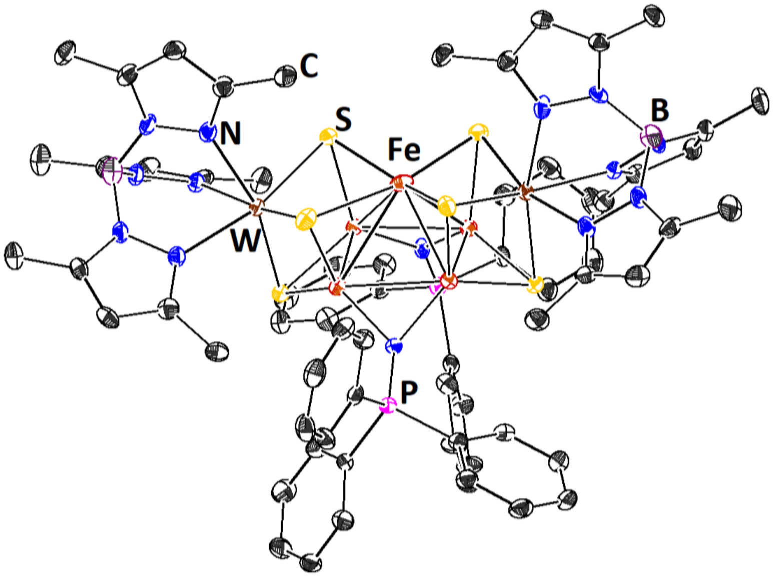

Figure 7: Tp*$_2$W$_2$Fe$_5$S$_6$(μ-NPPh$_3$)$_2$

Crystallized from reaction of [Et$_4$N][Tp*WS$_3$Fe$_3$(μ$_3$-NPPh$_3$)Cl$_3$] with Naketyl.

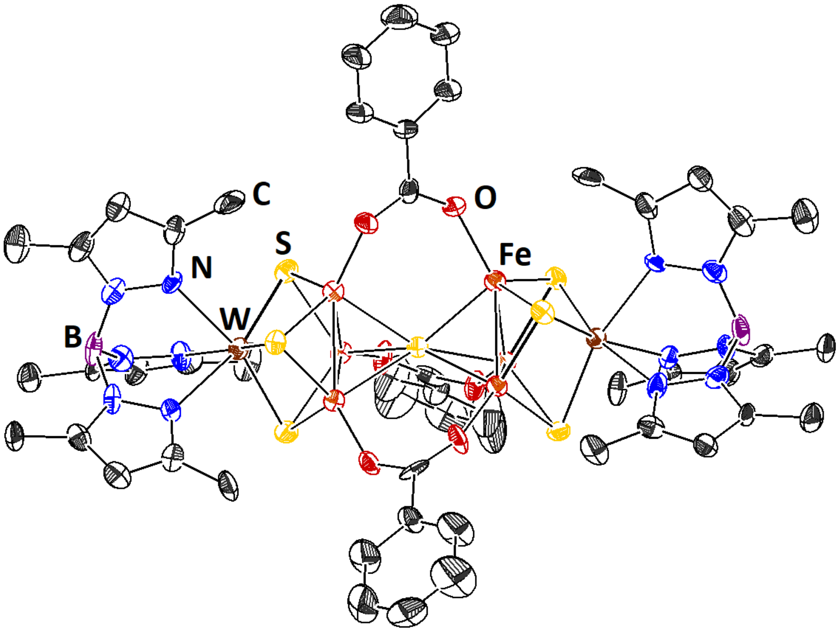

Figure 8: Tp*$_2$W$_2$Fe$_6$S$_7$(μ-O$_2$CPh)$_3$

Crystallized from reaction of Tp*$_4$W$_4$Fe$_{13}$S$_{12}$ with Me$_2$NOC(O)Ph.

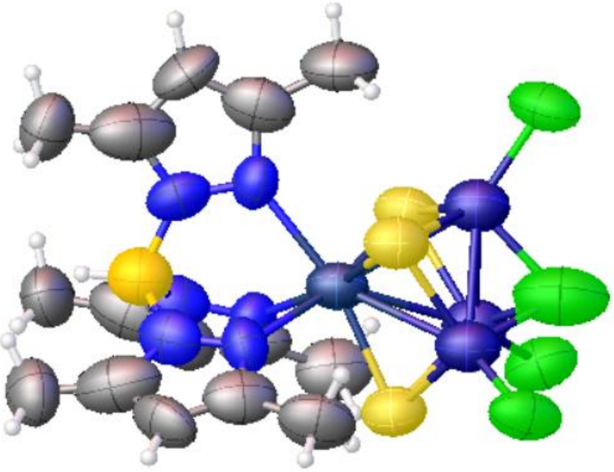

Figure 9: $[Et_4N][Tp^*WFe_3S_3(\mu_3\text{-}F)F_3]$

Crystallized from reaction of $[Et_4N][Tp^*WS_3Fe_3(\mu_3\text{-}CSiMe_3)Cl_3]$ with TBAF.

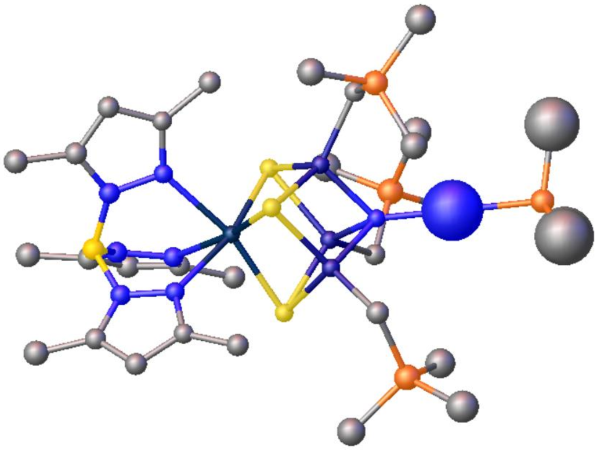

Figure 10: $Tp^*MoFe_3S_3(\mu_3\text{-}NxxSiMe_3)(CH_2Me_3)_3$

Crystallized from $[Et_4N][Tp^*WS_3Fe_3(\mu_3\text{-}CSiMe_3)Cl_3]$ with NaKetyl.

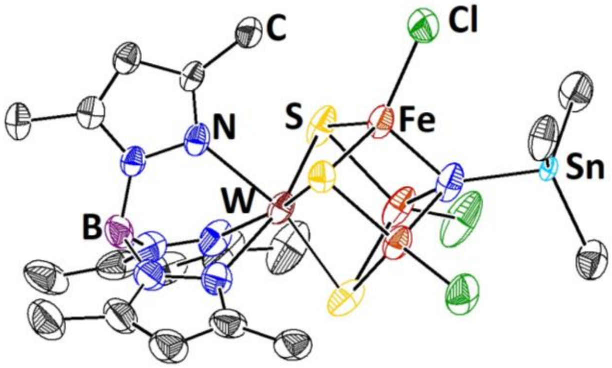

Figure 11: $[Et_4N][Tp^*WFe_3S_3(u_3\text{-}NSnMe_3)Cl_3]$

Crystallized from reaction of $[Et_4N]_2[Tp^*WS_3Fe_3(\mu_3\text{-}Cl)Cl_3]$ with N_3SnMe_3.

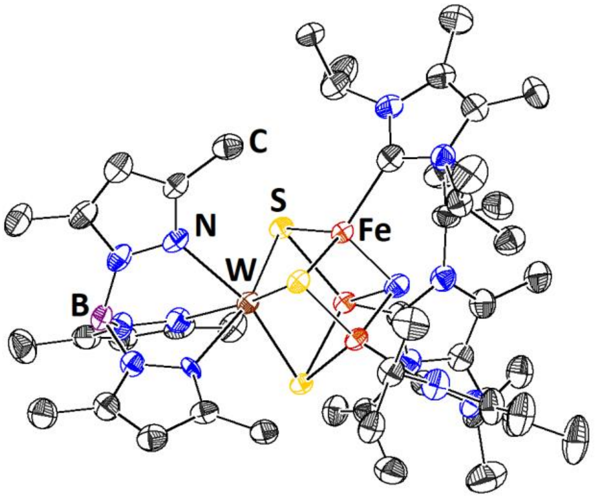

Figure 12: $[Tp^*MoFe_3S_3(u_3\text{-}NH)(^iPr_2Me_2NHC)_3][BPh_4]$

Synthesized using the same method as $[Tp^*WFe_3S_3(u_3\text{-}NH)(BAC)_3][BPh_4]$.

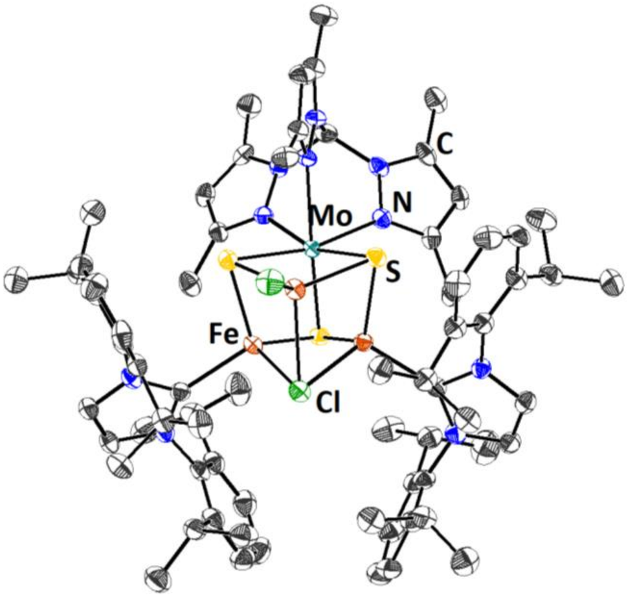

Figure 13: $[\mathrm{Et_4N}][\mathrm{Tp^*MoFe_3S_3(u_3\text{-}Cl)(IPr\text{-}NHC)_2Cl}]$

Synthesized from reaction of $[\mathrm{Et_4N}]_2[\mathrm{Tp^*WS_3Fe_3(\mu_3\text{-}Cl)Cl_3}]$ with 2 IPr-NHC and 2 $\mathrm{NaBPh_4}$.

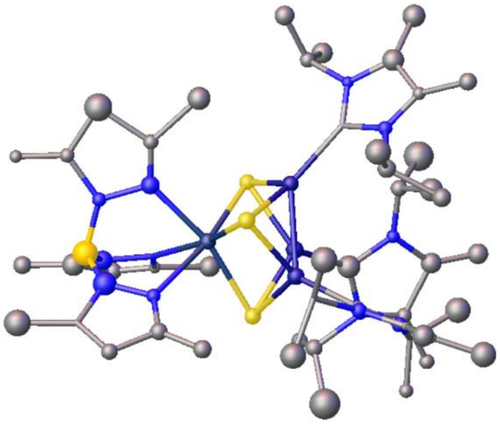

Figure 14: $[\mathrm{Tp^*MoFe_3S_3(^{i}Pr_2Me_2NHC)_3}][\mathrm{BPh_4}]$ Synthesized using the same procedure as for $[\mathrm{Tp^*WFe_3S_3(BAC)_3}][\mathrm{BPh_4}]$.

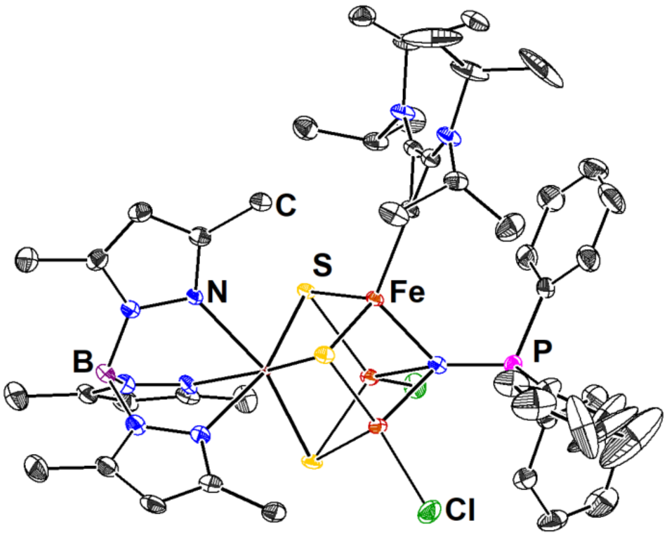

Figure 15: [Tp*WFe$_3$S$_3$(u$_3$-NPPh$_3$)(BAC)Cl$_2$][BPh$_4$]

Crystallized from reaction of [Et$_4$N][Tp*WS$_3$Fe$_3$(μ_3-NPPh$_3$)Cl$_3$] with BAC.

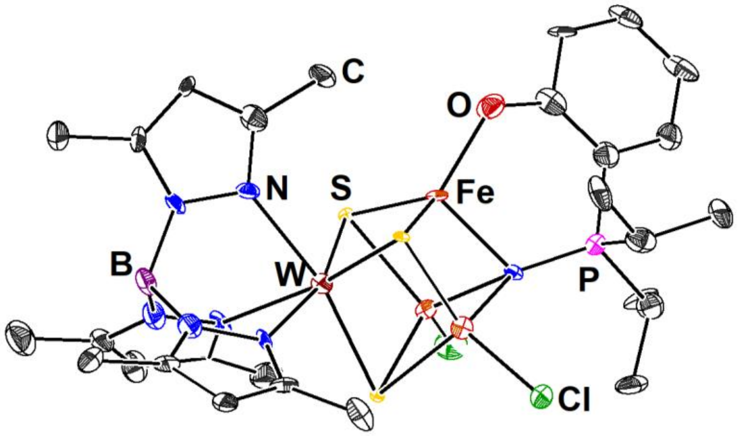

Figure 16: [Et$_4$N][Tp*WFe$_3$S$_3$(u$_3$-NP^{i}Pr$_2$PhO)Cl$_2$]

Synthesized using the same procedure as [Et$_4$N][Tp*WS$_3$Fe$_3$(μ_3-NPPh$_3$)Cl$_3$].

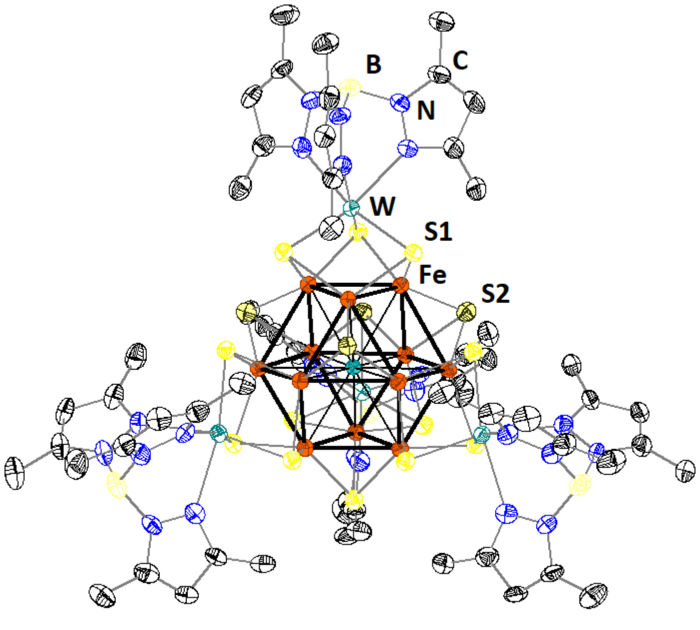

Figure 17: Tp*$_4$W$_5$Fe$_{12}$S$_{12}$

Crystallized from the synthesis of Tp*$_4$W$_3$Fe$_{13}$S$_{12}$ with added Naketyl.

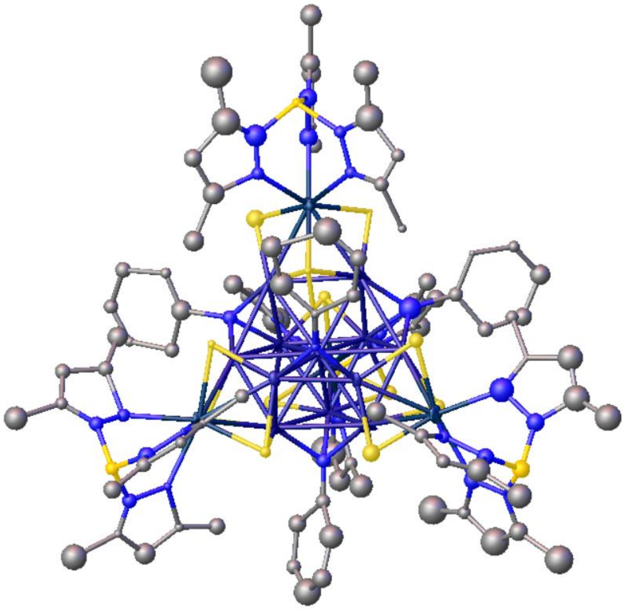

Figure 18: Tp*$_4$W$_4$Fe$_{11}$S$_{12}$(NPh)$_4$

Crystallized from reaction of Tp*$_4$W$_3$Fe$_{13}$S$_{12}$ with 5 N$_3$Ph.

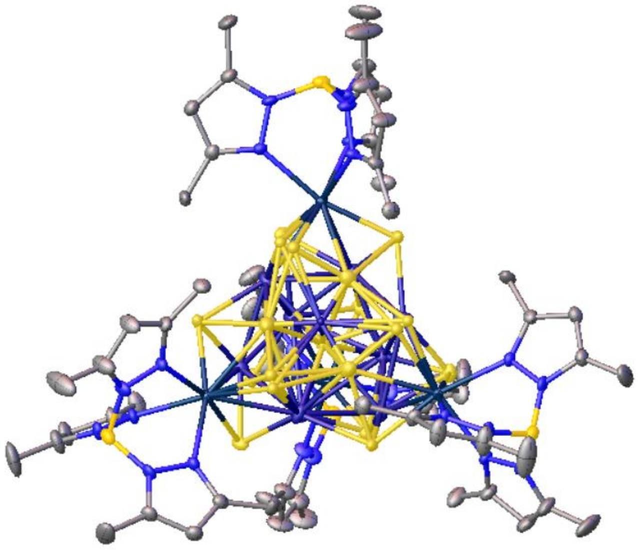

Figure 19: $Tp^{*}_4W_4Ni_9S_{15}$

Crystallized from reaction of $[Et_4N][Tp^{*}WS_3]$ with $Ni(COD)_2$ and Naketyl.

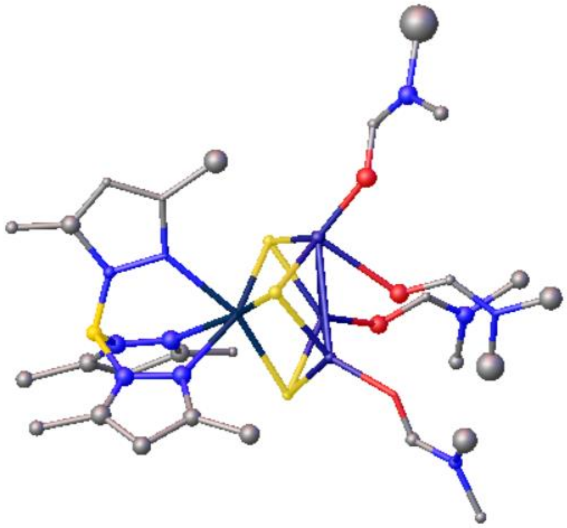

Figure 20: $[Tp^{*}MoCu_3S_3(DMF)_4][PF_6]_n$

Crystallized from reaction of $[Et_4N][Tp^{*}WS_3]$ with $Cu(OTf)_2$ and NaKetyl.

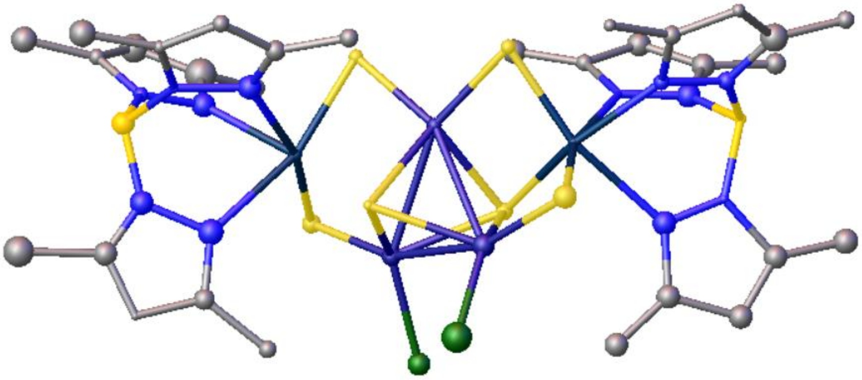

Figure 21: $[Et_4N][Tp^*{}_2W_2Ni_3S_6Cl_2]$

Crystallized from reaction of $[Et_4N][Tp^*WS_3]$ with $Ni(COD)_2$ and Naketyl.

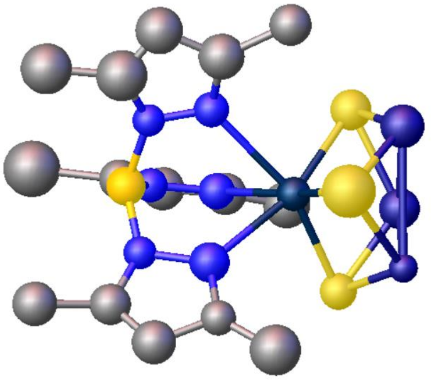

Figure 22: $[Et_4N][Tp^*WNi_3S_3]$

Ni atoms have partial occupancies.

Crystallized from reaction of $[Et_4N][Tp^*WS_3]$ with $Ni(COD)_2$ and Naketyl.

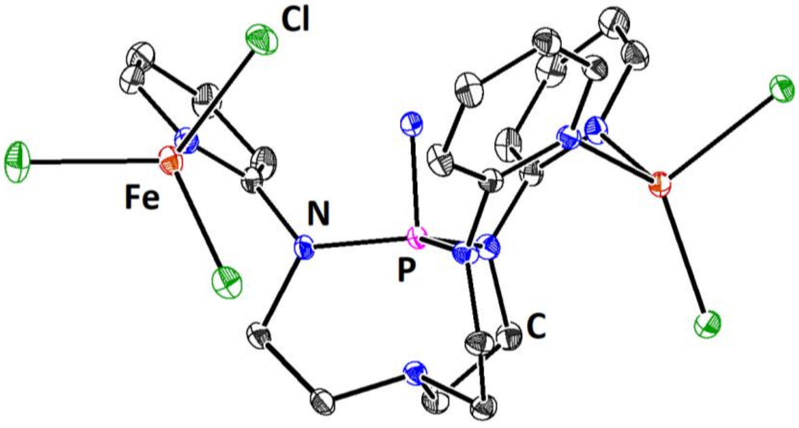

Figure 23: $Py_3TRENPNH_2FeCl_2FeCl_3$

See Appendix B, **15a**.

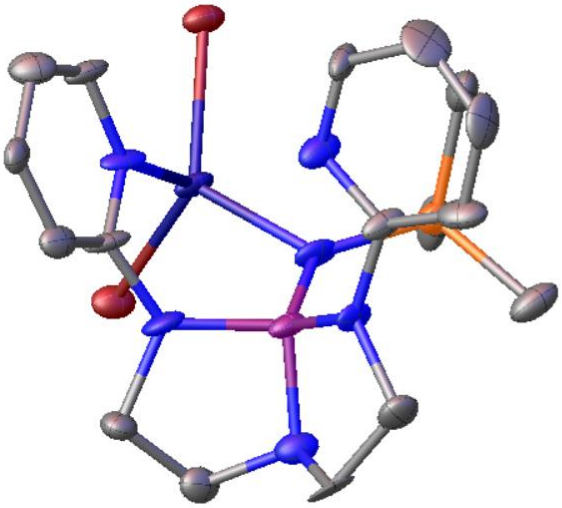

Figure 24: $Py_2TRENPNSiMe_3FeBr_2$

Crystallized from synthesis of **15b** (Appendix B).

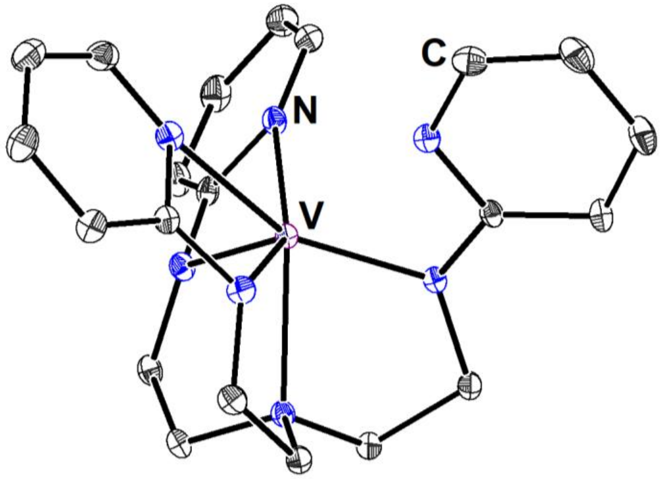

Figure 26: VPy_3TREN

See Appendix B, **16**.

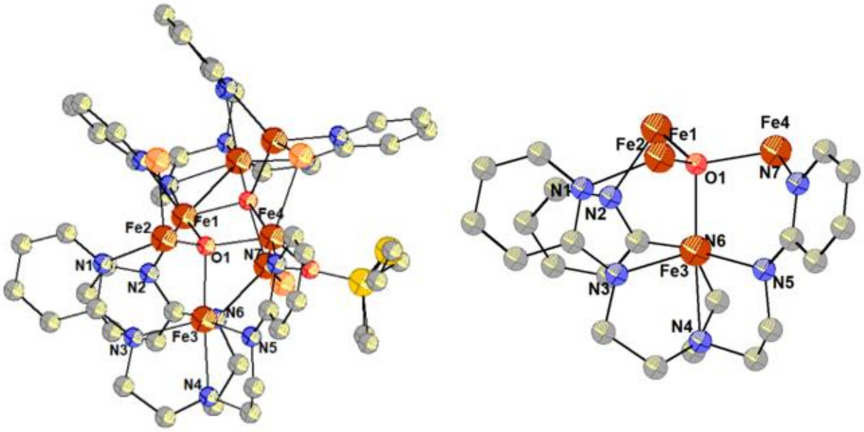

Figure 27: Fe_6Py_3TREN

Crystallized from synthesis of **15a** (Appendix B).

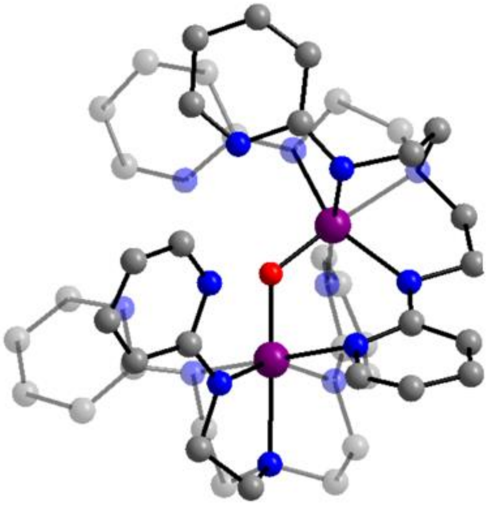

Figure 28: $V_2O(Py_3TREN)_2$

Crystallized from synthesis of **16** (Appendix B).

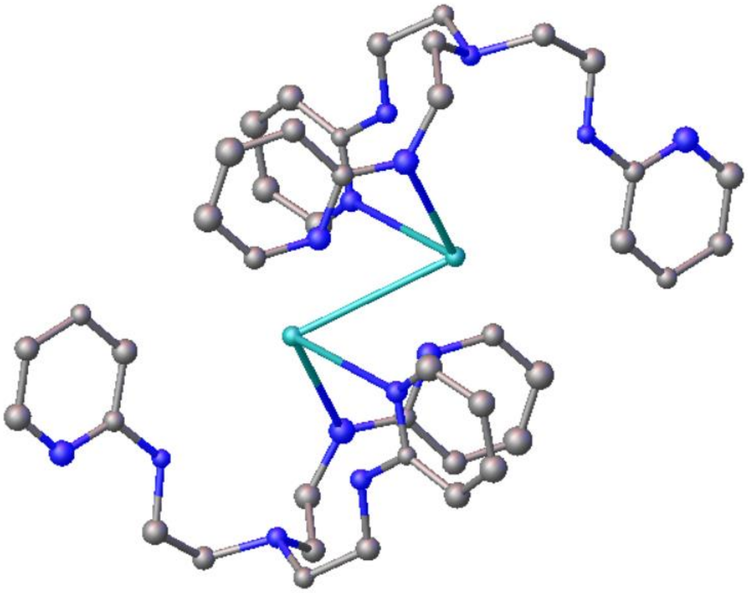

Figure 29: KPy_3TREN

Crystallized from the synthesis of **15a** (Appendix B).

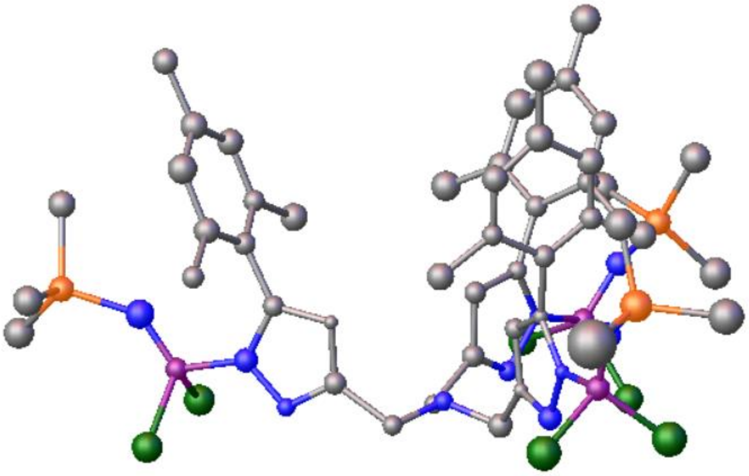

Figure 30: Trispyrazole(PCl_2NSiMe_3)$_3$

Crystallized from reaction of trispyrazole with PCl_3NiMe_3.

ABOUT THE AUTHOR

Anna G. Scott was born in Los Alamos, NM where she lived for 18 years before attending Montana State University. At MSU she developed her passion for studying multi-metallic clusters while investigating radical SAM enzymes in the Broderick group. During her time as an undgraduate she also participated in summer internships at LANL with Dr. Ken McClellan, NREL with Dr. David Mulder and Dr. Paul King, and at MIT with Dr. Stephen Lippard and Dr. Andrè Bessete. In 2015 she received a Goldwater Scholarship. Anna graduated from MSU in 2017, *summa cum laude*, with a B.S. in chemistry and a minor in mathematics and received the Outstanding Senior Award from the chemistry department. She then joined the Agapie group for her graduate studies and focused on studying synthetic FeS clusters. She was supported by a NSF Graduate Research Fellowship during her graduate studies. Anna completed her PhD studies at Caltech in 2023. Anna has accepted a postdoctoral position with Dr. Prof. Serena DeBeer at the Max Planck Institute for Chemical Energy Conversion in Germany. Outside the lab Anna loves being in the outdoors mountain biking, skiing, backpacking, and hiking.

“…there is more charm in one “mere” fact, confirmed by test and observation, linked to other facts through coherent theory into a rational system, than in a whole brainful of fancy and fantasy. I see more poetry in a chunk of quartzite than in a make-believe wood nymph, more beauty in the revelations of a verifiable intellectual construction than in whole misty empires of obsolete mythology.”

~ Edward Abbey, The Journey Home